

DISSERTATION

**RADIATION PROTECTION STUDIES FOR
CERN LINAC4/SPL ACCELERATOR COMPLEX**

EGIDIO MAURO

Directeur de thèse:

Prof. Aurelio Bay

Co-directeur de thèse:

Dr. Marco Silari

Contents

Introduction	5
1 Radiation protection at 'low' energy proton accelerators.....	7
1.1 Generation of prompt radiation	7
1.1.1 Interaction of protons with matter.....	7
1.1.2 Nuclear interactions	8
1.1.3 Characteristics of the prompt radiation field.....	10
1.1.4 Attenuation of the prompt radiation field.....	10
1.2 Environmental impact	14
1.2.1 Skyshine	14
1.2.2 Emission of radioactive effluents.....	16
1.3 Induced radioactivity	18
1.4 Radioactivity in air and water.....	20
1.4.1 Laminar flow model.....	20
1.4.2 Complete mixing model.....	21
2 Linac4 project	23
2.1 Linac4 and the CERN injector upgrade	23
2.2 The SPL and the next generation of physics facilities	25
2.3 Linac4 design	27
2.4 Facility layouts	29
2.5 H- source and low energy beam transfer	29
2.6 RFQ	32
2.7 DTL.....	33
2.8 CCDTL	36
2.9 PIMS	38
3 Monte Carlo codes and analytical models.....	41
3.1 The FLUKA radiation transport code.....	41
3.1.1 Electromagnetic and muon transport in FLUKA.....	42
3.1.2 Charged particle transport.....	42
3.1.3 FLUKA hadronic models.....	43
3.1.4 Shielding calculations and neutron transport description	46
3.1.5 Dosimetry	47

CONTENTS

3.2	FLUKA Monte Carlo simulations and gamma spectrometry measurements of induced radioactivity in a patient-specific collimator used in proton therapy.....	47
3.3	Prediction of transmission in ducts and labyrinths.....	54
3.3.1	Analytical models.....	55
3.3.2	Comparison of Monte Carlo simulations with the universal curves	57
4	Shielding design.....	69
4.1	Beam loss assumptions.....	69
4.2	Radiation shielding	71
4.3	Neutrons streaming through the waveguide ducts	72
4.3.1	First layouts: first duct close to the loss point	73
4.3.2	First layouts: ducts housing one waveguide	74
4.3.3	First layouts: ducts housing two waveguides.....	76
4.3.4	Final layout	78
4.4	Access maze, ventilation and cable ducts at the low-energy end of the linac	79
4.5	Low-energy section waveguide and cable duct studies.....	83
5	Induced radioactivity.....	87
5.1	Induced radioactivity in the main components of the accelerator.....	87
5.2	Air activation in the accelerator tunnel	99
5.3	Air activation in proximity of the dump.....	103
5.3.1	Simulation set-up.....	103
5.3.2	Residual dose rate	106
5.3.3	Air activation	108
5.3.4	Dose to the reference population group and to a worker intervening in the tunnel after the shutdown.....	109
6	Conclusions	115
	Acknowledgments.....	118
	Appendix A - Residual dose rate plots and radionuclide inventories	119
	Bibliography	145

Riassunto della tesi

Il CERN ha progettato una nuova catena di acceleratori allo scopo di sostituire l'attuale Proton Synchrotron (PS) complex: un acceleratore lineare di ioni H⁺ con un'energia di 160 MeV (Linac4) per sostituire l'attuale iniettore, un acceleratore lineare di protoni con un'energia di 50 MeV, un Superconducting Proton Linac con un'energia di 3.5 GeV (SPL) per sostituire il PS Booster (PSB) con un'energia di 1.4 GeV e un sincrotrone di 50 GeV (chiamato PS2) per sostituire il PS da 26 GeV. Il progetto Linac4 è stato finanziato ed i lavori di costruzione del tunnel che lo ospiterà e degli edifici annessi sono iniziati nell'ottobre 2008, mentre il progetto SPL è ad uno stadio avanzato del conceptual design. Oltre all' iniezione nel futuro PS da 50 GeV, l'obiettivo finale dell'SPL è quello di generare un fascio di 4 MW per la produzione di intensi fasci di neutrini. Gli studi radioprotezionistici saranno realizzati sulla base di quest'ultima esigenza. Questa tesi descrive gli studi di radioprotezione condotti per il Linac4. Sono state realizzate simulazioni Monte Carlo con il codice FLUKA e calcoli analitici 1) per stimare la propagazione dei neutroni attraverso i condotti per le guide d'onda, il sistema di ventilazione e i condotti per i cavi posti lungo l'acceleratore, 2) per valutare l'impatto radiologico dell'acceleratore nella sua sezione di bassa energia, dove è situata la zona di accesso, e 3) per calcolare la radioattività indotta nell'aria e nei componenti dell'acceleratore. Quest'ultimo studio è particolarmente importante per gli interventi di manutenzione e per la futura gestione dei rifiuti radioattivi. Due distinti progetti per la sezione CCDTL dell'acceleratore sono stati presi in considerazione per valutare la fattibilità, dal punto di vista radiologico, di sostituire i quadrupoli elettromagnetici con quadrupoli permanenti ad alto contenuto di cobalto. Questa tesi fornisce informazioni complete e dettagliate riguardo le assunzioni utilizzate per le perdite del fascio, la struttura dell'acceleratore e lo schema di condotti e labirinti, in modo che i risultati ottenuti possano essere di interesse generale e possano fornire delle linee guida per studi simili su acceleratori di protoni di energia simile.

In aggiunta agli studi specifici per il Linac4, questo lavoro di tesi ha anche realizzato simulazioni con il codice FLUKA per valutare la capacità del codice nel predire la radioattività indotta da protoni di energie intermedie, per applicazioni in protonterapia. La tesi ha anche implicato una rassegna dei modelli principalmente utilizzati per stimare il flusso neutronico attraverso condotti e labirinti, descrive le simulazioni realizzate per testare l'affidabilità di questi modelli e, sulla base delle simulazioni compiute, introduce un'espressione universale da utilizzare nel caso della trasmissione neutronica attraverso un condotto posto di fronte alla sorgente, modello ad oggi mancante in letteratura.

Keywords: Radiation protection, proton accelerators, induced radioactivity, shielding design, FLUKA code.

Abstract

CERN is presently designing a new chain of accelerators to replace the present Proton Synchrotron (PS) complex: a 160 MeV room-temperature H⁻ linac (Linac4) to replace the present 50 MeV proton linac injector, a 3.5 GeV Superconducting Proton Linac (SPL) to replace the 1.4 GeV PS booster (PSB) and a 50 GeV synchrotron (named PS2) to replace the 26 GeV PS. Linac4 has been funded and the civil engineering work started in October 2008, whilst the SPL is in an advanced stage of design. Beyond injecting into the future 50 GeV PS, the ultimate goal of the SPL is to generate a 4 MW beam for the production of intense neutrino beams. The radiation protection design is driven by the latter requirement. This thesis summarizes the radiation protection studies conducted for Linac4. FLUKA Monte Carlo simulations, complemented by analytical estimates, were performed 1) to evaluate the propagation of neutrons through the waveguide, ventilation and cable ducts placed along the accelerator, 2) to estimate the radiological impact of the accelerator in its low energy section, where the access area is located, and 3) to calculate the induced radioactivity in the air and in the components of the accelerator. The latter study is particularly important for maintenance interventions and final disposal of radioactive waste. Two possible layouts for the CCDTL section of the machine were considered in order to evaluate the feasibility, from the radiological standpoint, of replacing electromagnetic quadrupoles with permanent magnet quadrupoles with high content of cobalt. The present work provides complete information on beam loss assumptions, accelerator structure and duct and maze design, in order to make the present results of sufficiently general interest and provide guidelines for similar studies for intermediate energy proton accelerators.

In addition to the Linac4-specific studies, this thesis also discusses FLUKA simulations performed to test the capability of the code, in a proton therapy application, in predicting induced radioactivity from intermediate energy protons. The thesis also reviews the analytical models mostly used for the calculation of neutron streaming through penetration traversing shielding barriers, discusses the FLUKA simulations performed to test the reliability of these models and, on the basis of the simulations, derives a universal expression that can be used to estimate the neutron transmission through a straight duct in direct view of the source, model missing so far in the literature.

Keywords: Radiation protection, proton accelerators, induced radioactivity, shielding design, FLUKA code.

Introduction

The purpose of this thesis is to provide guidelines for radiation protection studies, and to delineate those aspects of radiological safety that are of major, or even unique, importance both in the operation and the maintenance of particle-accelerator installations and to suggest the most adequate tools and models to use in order to carry out these studies. The thesis is intended to assist as a guide to the planning of proton accelerators below an energy of few giga-electron volts.

Chapter 1 describes the main processes responsible for the production of the prompt radiation and the induced radioactivity in this energy range and some models useful to estimate the attenuation of the prompt radiation field and the radioactivity induced in the components of the accelerators, in air and in water.

The radiation protection studies will have as object a 160 MeV room temperature H- Linac, the so-called Linac4, designed at CERN in order to replace the present 50 MeV proton linac injector and to become the source of all protons at CERN in 2013. Linac4 has been funded and the civil engineering work started in October 2008. Chapter 2 describes the layouts that were considered for the installation of the facility and gives an overview of the machine and its accelerating structures.

The radiation protection studies for Linac4 were carried out through a combination of Monte Carlo simulations and predictions made via analytical models. Chapter 3 provides a description of the particle transport code FLUKA and its benchmarks, and of the analytical models commonly used for the evaluation of the radiation streaming through ducts and labyrinths. Section 3.1 describes the FLUKA code, its applications and the most relevant benchmarks reported in literature; Section 3.2 discusses the FLUKA simulations performed to test the capability of the code, in a proton therapy application, in predicting induced radioactivity from intermediate energy protons; Section 3.3 reviews the analytical models mostly used for the calculation of neutron streaming through penetration traversing shielding barriers, discusses the FLUKA simulations performed to test the reliability of these models and, on the basis of the simulations, derives a universal expression that can be used to estimate the neutron transmission through a straight duct in direct view of the source.

Chapter 4 discusses the radiation protection studies concerning the shielding design. Particular attention was devoted to evaluating the propagation of neutrons through the waveguide and cable ducts, and through the access area at the low-energy end of the linac.

Chapter 5 discussed the Monte Carlo simulations performed for the assessment of the induced radioactivity in the accelerator components (Section 5.1) and for the determination of air activation in the Linac4 tunnel (Section 5.2) and in proximity of the dump (Section 5.3).

INTRODUCTION

1 Radiation protection at 'low' energy proton accelerators

Accelerators, first designed and constructed as research instruments, have now entered the very fabric of our life. In addition to their continued application to fundamental research in cosmology and particle physics, they are now widely applied in, e.g. medicine, material science and solid-state physics, polymerization of plastics, sterilization of toxic biological wastes and food preservation. The radiological protection aspects of these facilities are extremely important in the design of these machines. There are many parameters by which particle accelerators may be classified. For example, they may be classified in terms of the technology by which acceleration is achieved, such as power source or acceleration path geometry. Also they may be classified by their application, but the classifications of greatest relevance in radiological physics are the types of particle accelerated, the maximal energy, the maximal intensity and the duty factor of the accelerated particle beams (1).

This work is focused on radiation protection at 'low' energy proton accelerators, where low energy is taken to mean less than 1 GeV and, therefore, includes so-called intermediate energy accelerators. This chapter describes the main processes responsible for the production of the prompt radiation and the induced radioactivity in this energy range and some models useful to estimate the attenuation of the prompt radiation field and the radioactivity induced in the components of the accelerators, in air and in water. Some of these models in combination with Monte Carlo simulations will be used in this work for the radiological studies for a 160 MeV H⁻ Linac.

1.1 Generation of prompt radiation

It is the interaction of the accelerated protons with matter that leads to the primary radiological hazard associated with proton accelerators. These interactions produce both 'prompt' radiation that persists only while the accelerator is in operation and induced radioactivity that continues to emit radiation after the accelerator is shut off.

1.1.1 Interaction of protons with matter

The interactions of protons with matter degrade the energy of the protons and at the same time result in production of prompt radiation in the form of a spray of secondary particles. At the lowest proton energy the energy loss is primarily due to ionization of the stopping medium. The specific ionization is in fact greatest for the lowest energy protons and results in the characteristic Bragg peak at the end of the proton range. This property of the energy loss curve for protons has been used effectively to treat deep-seated tumours with protons in the energy range of 100 - 250 MeV. Because the energy required for creating an ion pair is small when compared to the lowest energy accelerated protons, the energy loss appears almost continuous and the protons, except for minor straggling effects, have a definite range. An approximate expression for the range in iron is (2)

$$R_{Fe} = 1.1 \times 10^{-3} E^{1.6} \quad (1)$$

where R is in cm and E is in MeV. For materials other than iron the Bragg-Kleeman rule (3) may be used to scale the range from that for iron

$$R = R_{Fe} \frac{\rho_{Fe}}{\rho} \frac{\sqrt{A}}{\sqrt{A_{Fe}}} \quad (2)$$

For protons whose kinetic energy is sufficiently high so that they are able to penetrate the Coulomb barrier of the target nuclei, nuclear reactions other than simple Coulomb scattering become possible. The nuclear reactions compete with the electromagnetic interactions as the energy of the protons is increased. When the energy of the protons approaches the upper limit of the range that we are considering, the probability of a nuclear interaction rises to nearly unity and is more or less independent of the stopping medium (Figure 1). At the highest energies the proton range is no longer a useful concept as the primary protons are effectively removed from the particle stream but are at the same time to some extent replenished by the secondary protons produced by nuclear interactions.

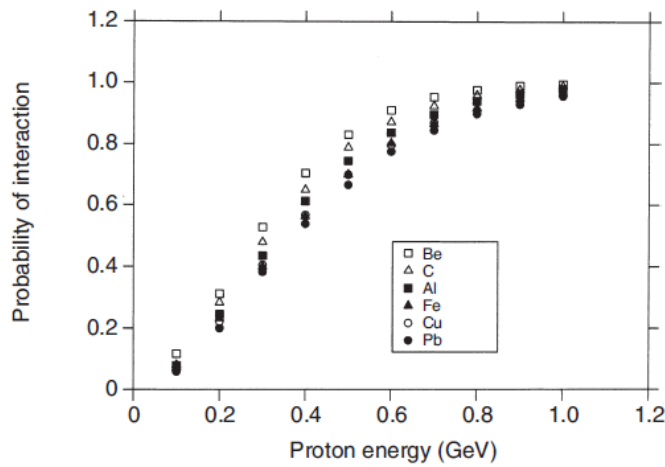


Figure 1 : The fraction $f_n(E_p)$ of protons incident on a stopping target that participate in nuclear reactions as a function of proton energy for a number of target materials (4).

1.1.2 Nuclear interactions

An understanding of the prompt radiation (and induced radioactivity) requires a basic knowledge of the nuclear reaction mechanisms that apply in the energy range under consideration. The incident proton, or more generally nucleon, may simply enter the nucleus, be deflected by the nuclear potential and emerge again at a different angle but with the same energy. This is *direct elastic scattering*. On the other hand, it can collide directly with a target nucleon and excite it above the Fermi sea forming a *compound state*. Two alternatives are now possible: either one or both nucleons have energy greater than their separation energy or neither has. In the former case, the nucleon(s) whose energy exceeds the separation energy may leave the nucleus without further interaction other than its deflection by the average potential. This is described as a *direct reaction*. In those cases where the change in mass number is $\Delta A = 0$, the reaction is either *inelastic scattering* (the outgoing particle is the same type as the incident particle) or a *charge-exchange reaction*. Where $\Delta A \neq 0$, we refer to transfer reactions (either *stripping* or *pickup*) and *knockout reactions*. The angular distribution of the scattered particles is characteristically anisotropic, peaking in the forward direction.

In the latter case, each nucleon will undergo further collisions, gradually spreading its excitation energy over the whole nucleus. For a certain time (during the pre-equilibrium phase) the nuclear state will become increasingly complex, but, after a certain relaxation time, statistical equilibrium will be reached. A certain fraction of the resultant complicated mixture of nuclear states consists of configurations in which sufficient energy is concentrated on one nucleon so that it may

escape from the nucleus. Similarly, kinetic energy may be concentrated on groups of particles and lead to the emission of α particles, tritons, deuterons etc. This process is similar to evaporation and may be characterized by a nuclear temperature $\Theta \approx 2-8$ MeV, so that the spectrum of the emitted neutrons may be described by the following Maxwellian distribution:

$$d\phi(E_n) \propto \frac{E_n}{\Theta^2} \exp\left(\frac{-E_n}{\Theta}\right) dE_n \quad (3)$$

Compound reactions may occur during the ‘pre-equilibrium’ phase, before statistical equilibrium is achieved. In such cases the angle of emission may still be strongly correlated with the direction of the incident particle. On the other hand, once statistical equilibrium has been reached, the emitted or ‘evaporated’ particles have no memory of the direction of the incident particles and the angular distribution is isotropic. The evaporated particles are emitted isotropically and the energy distribution of the ‘evaporated’ neutrons extends up to about 8 MeV. If the evaporated particles are charged the Coulomb barrier suppresses the emission of low energy particles.

All the scattered and emitted particles can again participate in similar reactions resulting in an intranuclear cascade. The intranuclear cascade develops through the interaction of individual nucleons inside the nucleus; the probability for these interactions is determined by the interaction cross-section that apply in free space and by the Pauli exclusion Principle (5; 6; 7).

Tesch has evaluated three measurements (8; 9; 10) and two calculations (11; 12) of the neutron spectra emitted from thick targets (here it is assumed that the incident protons are completely stopped in the target). “In all calculated and measured spectra both production processes can be distinguished; neutron emission by evaporation from compound nucleus, and the neutrons of higher energy from the intranuclear cascade. The angular distribution of the “evaporation neutrons” is isotropic. Their energy distribution reaches about 8 MeV. In the interesting angular interval from 75° to 105°, the “cascade neutrons”, defined as neutrons with energy above 8 MeV, are only a few per cent of the total neutron yield. Their contribution to the dose at 90° with respect to the proton beam rises with increasing proton energy from 5% to about 20%.” (13)

Bertini has reported calculations of the production of particles from protons interacting with several target nuclei: C, O, Al, Cr, Cu, Ru, Ce, W, Pb and U. Protons of 25 MeV and 50 – 400 MeV were selected and both evaporation and intranuclear cascades were included in the calculations. The particle yields were determined for four angular ranges: 0° - 30°, 30° - 60°, 60° - 90° and 90° - 180° (5). Alsmiller et al. (14) have conveniently summarized the calculated spectra of Bertini by fitting them by fifth and sixth order polynomials. The number of neutrons per MeV per steradian per interaction of a proton of kinetic energy E_0 (expressed in MeV) may then be represented by:

$$n(E) = \frac{1}{E_0} \exp \left| \sum_{i=0}^5 a_i \left| \frac{E}{E_0} \right|^i \right| + \frac{1}{4\pi} \frac{1}{25} \exp \left| \sum_{j=0}^4 a_j \left| \frac{E}{25} \right|^j \right| \quad (4)$$

the first term referring to the yield from the intranuclear cascade, and the second from the evaporation. Values of the coefficients a_i and a_j are given so that the energy distribution, for both evaporation and cascade neutrons produced at each of the incident energies and for each angular region, may be calculated.

For high atomic mass nuclei, proton or neutron induced fission becomes a possible reaction. Although there are some low energy neutrons emitted as a result of the photon-induced fission of

heavy nuclei, the prime radiological significance is that fission may lead to the production of some of the more radiotoxic isotopes such as the radioactive species of iodine.

1.1.3 Characteristics of the prompt radiation field

From the description above it is evident that the prompt radiation field near a point of interaction of accelerated protons with matter is complex and becomes more complex as the energy of the protons is increased. The field consists of a mixture of charged and neutral particles as well as photons. Several simulation codes are now available which include all the interactions described above and which allow estimates of the radiation field near the interaction points, such as those required for calculating energy deposition in targets and beam dumps.

At proton energies lower than 1 GeV a simplification occurs, because the range of the charged particles produced in nuclear reactions are such that they are always ranged out in a shielding that is sufficiently thick to provide protection against neutrons. This means that in this energy range the radiation field outside an accelerator shielding is always determined and dominated by neutrons. Neutrons are nevertheless not the only contribution to the radiation field, because the degraded neutrons may be captured by the nuclei of the shielding material with the consequent emission of neutron capture gamma rays.

1.1.4 Attenuation of the prompt radiation field

As we have seen above, neutrons always dominate the prompt radiation field outside sufficiently thick shielding of proton accelerators in this energy range. The attenuation length of neutrons in the shielding material therefore determines the attenuation of the dose equivalent provided by the shielding. Shielding for neutrons must satisfy two criteria: interpose sufficient mass between the source and the field point and attenuate effectively neutrons of all energies. The first criterion is most easily met by dense material of high atomic mass, whereas the second is most easily met by hydrogen, which effectively attenuates neutrons of all energies via elastic scattering. The two criteria, and the additional one of having to provide stable shielding at minimum cost, are simultaneously and most easily met by concrete because of its relatively high hydrogen content in the form of water of hydration. If higher density is required, steel is often used as shielding near the source point. However, because the total cross section for neutrons incident on iron shows a series of dips between 0.2 – 0.3 MeV (Figure 2), steel is essentially ‘transparent’ to neutrons at this energy. An outer layer of a material containing hydrogen must therefore always follow steel.

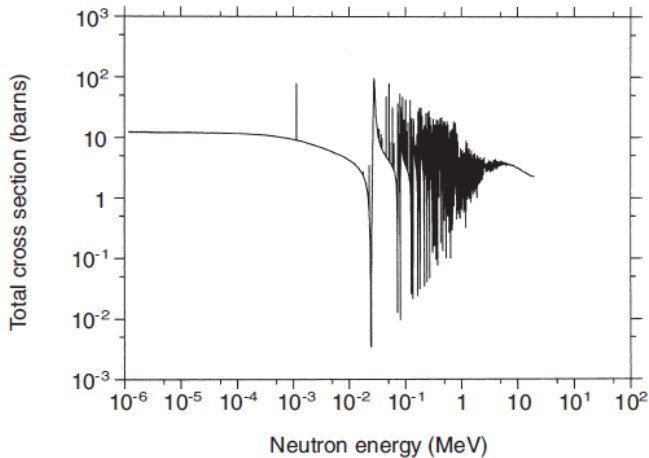


Figure 2 : The $^{56}\text{Fe}(n,\text{tot})$ cross section as a function of neutron energy. The width of the gaps between 0.01 MeV and 0.1 MeV are greater than the mean energy loss per scatter and hence neutrons with energy just above the gaps build up in iron shielding.

Figure 3 shows the variation of the mass attenuation length, $\rho\lambda$, for monoenergetic neutrons in concrete as a function of neutron energy. Below about 20 MeV, $\rho\lambda$ has the value 200 kg/m^2 . Above this energy there is an increase in the attenuation length that reflects the change from the regime where neutrons interact with the target nuclei as a whole, and largely by direct elastic scattering, to the regime where the interaction is most likely with individual constituent nucleons of the target nuclei and may lead to an intranuclear cascade. The attenuation length reaches a limiting value of 1170 kg/m^2 above about 150 MeV.

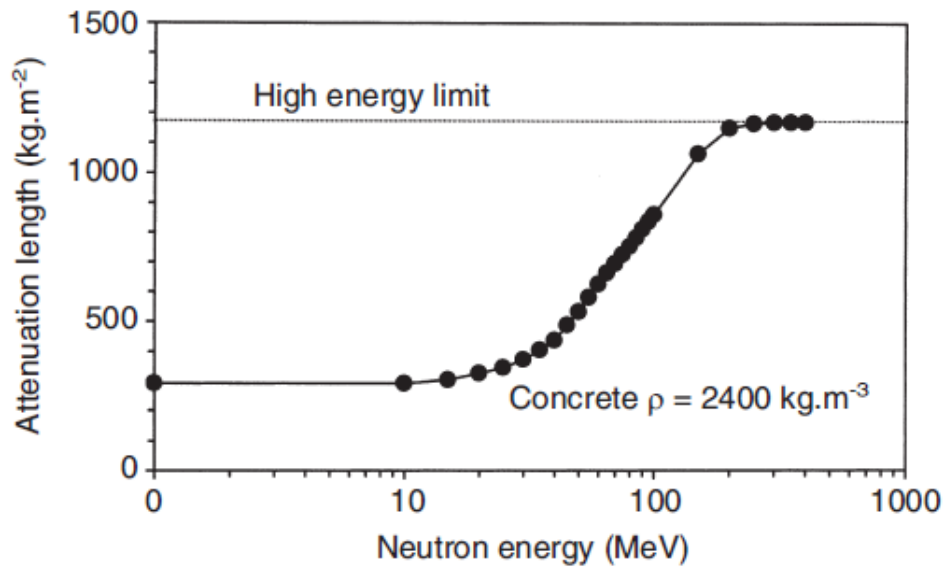


Figure 3 : The variation with energy of the attenuation length $\rho\lambda$ of monoenergetic neutrons in concrete of density $\rho = 2400 \text{ kg/m}^3$. The high energy limit is 1170 kg/m^2 .

For low energy accelerators the attenuation of shielding in concrete may therefore be estimated by a simple exponential function, using the attenuation length appropriate for the neutrons with energy in the peak of the Maxwellian distribution, i.e. at the nuclear temperature Θ . Attenuation curves for monoenergetic neutrons in this energy range have been tabulated in NCRP

Report No 38 (15). The attenuation length of 200 kg/m^2 for a concrete density of 2400 kg/m^3 corresponds to a tenth value layer of about 30 cm. Proton accelerators with energy above 50 MeV tend to be rather compact and thus the shielding cost for an additional 10 – 30 cm of concrete is not a major factor in the overall cost.

Above proton energies of a few hundred MeV, neutrons with energy above 100 MeV propagate the neutron field through shielding because of their longer attenuation length (Figure 3). The lower energy neutrons and charged particles are regenerated at all depths in the shield by the inelastic interactions of the neutrons with the shielding material. In other words, at any field point outside the shielding, the highest energy neutrons will be those that have come directly from the source without interaction, or that have undergone only elastic scattering or direct inelastic scattering with little loss of energy and only small angular deflection. Any low energy neutrons and charged particles detected outside the shielding will have been generated by the intranuclear cascade near the outer surface of the shield. The yield of high energy neutrons ($E_n > 100 \text{ MeV}$) in the primary collision of the incident protons with the target material therefore determines the magnitude of the prompt radiation field outside the shield for proton accelerators with energy above a few hundred MeV. Figure 4 shows the variation with proton energy of the yield of neutrons with energy greater than 100 MeV for protons stopping in a number of materials. These yields were calculated (16) using the FLUKA Monte Carlo code (17; 18). The neutron yield is normalized per interacting proton and has a simple dependence on the proton bombarding energy of the form

$$n(E_p) = n_0 E_p^m \quad (5)$$

Table 1 lists the parameters n_0 and m obtained by at least square fit to the points in Figure 4 and it is evident that, except for the lightest elements, the yield is largely independent of the target materials.

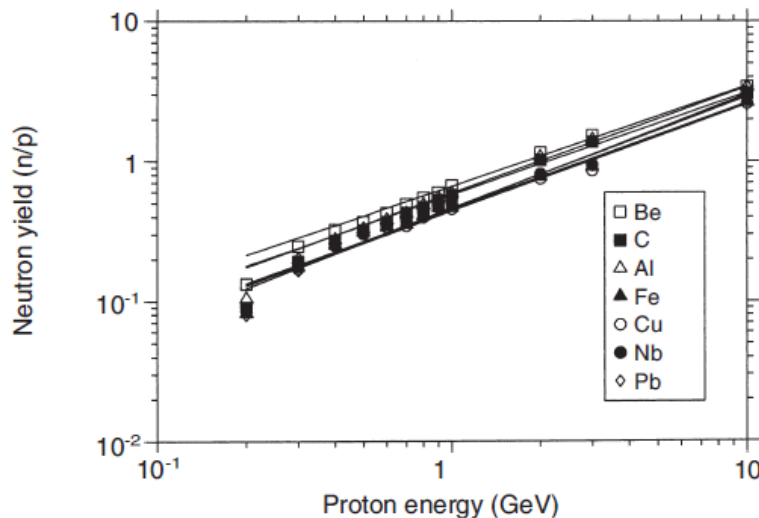


Figure 4 : The yield of neutrons with energy $E_n > 100 \text{ MeV}$ per interacting protons in stopping targets of a number of materials as a function of proton energy. The points are the results of calculations with the FLUKA Monte Carlo code and the lines are best fits to these points to the relation $n(E_p) = n_0 E_p^m$.

Table 1 : Values of parameters n_0 and m for the production of neutrons ($E_n > 100$ MeV) of the form $n = n_0 E_p^m$ as a function of proton energy E_p . The parameters have been obtained as best fits to the points calculated using the FLUKA Monte Carlo code and shown in Figure 4. The number of neutrons n is normalized to the number of interacting protons.

Material	n_0	m
Be	0.66 ± 0.02	0.71 ± 0.01
C	0.59 ± 0.02	0.73 ± 0.02
Al	0.58 ± 0.01	0.76 ± 0.01
Fe	0.46 ± 0.02	0.76 ± 0.02
Cu	0.44 ± 0.02	0.76 ± 0.02
Nb	0.46 ± 0.02	0.80 ± 0.02
Pb	0.46 ± 0.03	0.82 ± 0.03

Although the ready accessibility of powerful simulation codes allows us to calculate detailed spatial distributions of any of the radiological quantities of interest, even for complex geometries, nevertheless there is still considerable interest in doing simple point-kernel calculations if for no other reason than to provide a ‘reality check’ on the more detailed Monte Carlo results. In general one would like to have an equation of the type:

$$H(E_p, \theta, d/\lambda) = H_0(E_p, \theta) \exp(-d/\lambda)/r^2 \quad (6)$$

where $H(E_p, \theta, d/\lambda)$ is the dose equivalent at a point outside the shielding, E_p is the energy of the incident protons, r is the distance from the source point to the field point, θ is the angle between the line of sight from the source to the field point and the direction of the proton beam, d is the thickness of the shielding and λ is a suitably defined attenuation length for dose equivalent. If we restrict ourselves to proton energies above a few hundred MeV (being 150 MeV the neutron energy above which the attenuation length reaches an approximately constant plateau value, see fig. 3), it would appear that the energy dependence of $H_0(E_p, \theta)$ ought to follow the form of equation 5 above, as long as its value is normalized to the number of protons interacting in the target. Also the attenuation of the dose rate should follow that of the high energy neutrons, as these are the neutrons that propagate the cascade. The angular distribution of the high energy neutrons was investigated in the interval $60^\circ < \theta < 120^\circ$ using the Monte Carlo code FLUKA99 and it can be expressed quite well as an exponential in θ of the form $\exp(-\beta\theta)$. The angular relaxation parameter, β , depends on the bombarding proton energy and on the target material.

The dose equivalent at a point of interest which is at a radial distance r from the beam axis and the position vector of which (with the target as origin) makes an angle θ is given then by the relation

$$H(E_p, \theta, d/\lambda) = f_n(E_p) h_0 E_p^m \exp\left(-\frac{d}{\lambda}\right) \exp(-\beta\theta) / r^2 \quad (7)$$

where $f_n(E_p)$ is the fraction of protons participating in nuclear reactions (Figure 1) and h_0 is the source term. This expression merges smoothly into the Moyer model (19) used at proton energies above 1 GeV, where $f_n(E_p) \rightarrow 1$, $h_0 \rightarrow 0.28$ pSv m², $m \rightarrow 0.8$ and $\beta \rightarrow 2.3$.

1.2 Environmental impact

The environmental impact of proton accelerator operation is due to the prompt or direct radiation as well as to the possibility of the emission of radioactive effluents, each of which may have an off-site radiological impact.

1.2.1 *Skyshine*

The off-site component of the prompt radiation field is usually referred to as ‘skyshine’, because in most cases sufficient shielding must be provided in the horizontal direction (often by having the accelerator located below ground level) to protect the personnel working at the facility. However, the shielding in the vertical direction is not always constrained in this way so that more radiation (usually neutrons) may be emitted from the roof shielding of an accelerator at levels that may have an off-site impact.

Because the thresholds for nuclear reactions for neutrons with the constituents of air all lie near or above 20 MeV, the interactions below this energy are restricted to elastic scattering. The high energy nuclear interaction length for N₂ and O₂ are of the order of 90 g cm⁻², which for the density of air ($\rho=1.2 \times 10^{-3}$ g cm⁻³) is of the order of 750 m and hence the high energy neutrons effectively escape to great distances. Because only low energy neutrons can be scattered into the backward direction, near the source it is only these neutrons that are important. At distances that may be reached by a small angle scatter, i.e. distances comparable to the nuclear interaction length, the high energy neutrons will predominate. Due to the mass ratio of neutrons to nitrogen and oxygen nuclei, many elastic scatters are needed in order to reduce the neutron energy significantly. It follows that, as a first approximation, there is no effective attenuation of neutrons in air and the primary reduction in fluence out to a few hundred metres derives from geometrical factors. The dependence of neutron dose on distance from the source is therefore in the first instance a purely geometrical effect. As particle number must be conserved, the dose is inversely proportional to the area over which the particles are dispersed

$$H = \frac{Q}{2\pi r^2} \quad (8)$$

where $Q=h_a A$ is the dose h_a averaged over the roof area A and r is the distance from the source to the field point of interest. For largest distances there is some attenuation characterized by an attenuation length λ that is of the order of several hundred to 800 m. A more complete expression is therefore

$$H(r) = \frac{Q}{2\pi r^2} \exp(-\frac{r}{\lambda}) \quad (9)$$

This simple expression ignores the fact that the neutron spectrum will be affected by the scattering off the air. The high energy neutrons will disappear to great distances and the lower energy neutrons will be further degraded. A number of authors have investigated the variation of the source term Q and the attenuation length λ as a function of the energy spectrum of the neutrons emerging from the area A . The most complete analysis is that due to Stapleton et al (20) who have used the importance functions calculated by Alsmiller et al. (21) and folded them with a composite spectrum that approximates the sea-level cosmic ray neutron spectrum and has an angular distribution that

varies as $\cos(\theta)$. They determined the dose equivalent as a function of distance from the source point and use a function of the form

$$H(r) = \frac{a \exp(-r/\lambda(E_c))}{(b+r)^2} \quad \text{per skyshine neutron} \quad (10)$$

to represent their results. They claim that the factor b accounts for the fact that skyshine will produce a virtual source in the air at same height above the ground. They chose $a = 2 \text{ fSv m}^2$ and $b = 40 \text{ m}$ to be appropriate values to give a reasonable representation of their results. However, a detailed analysis that determines the parameters as a best fit to their results (Figure 5) yields the values for a , b and λ listed in Table 2.

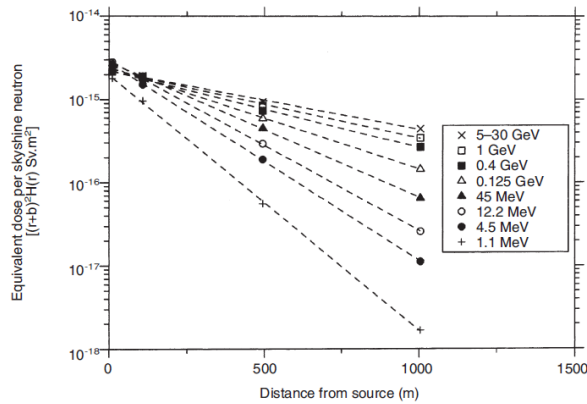


Figure 5 : The results for the calculation by Stapleton et al of dose equivalent due to skyshine as a function of horizontal distance from the source. The dashed lines are best fit to the data points of Equation 10.

Table 2 : The parameters a , b and λ to be used in Equation 10. They were obtained as best fits to the skyshine calculation of Stapleton et al. (20).

E_c (MeV)	a (fSv.m ²)	b (m)	λ (m)	g (fSv.m ²)
1.1	1.96 ± 0.28	47.1 ± 5.4	142 ± 4	4.0
4.5	2.78 ± 0.16	53.1 ± 2.5	183 ± 2	5.7
12.2	2.94 ± 0.15	54.2 ± 2.2	213 ± 3	7.4
45	2.81 ± 0.14	53.1 ± 2.1	267 ± 4	9.6
125	2.44 ± 0.11	49.2 ± 1.8	355 ± 7	11.3
400	2.24 ± 0.27	47.1 ± 4.5	467 ± 33	13.2
1000	2.24 ± 0.18	47.3 ± 3.0	532 ± 28	14.1
5000	2.23 ± 0.18	46.8 ± 3.1	597 ± 36	14.6
10,000	2.23 ± 0.24	46.8 ± 4.0	604 ± 49	14.7
30,000	2.22 ± 0.26	46.4 ± 4.4	617 ± 57	14.7

The average value for a is $(2.41 \pm 0.29) \text{ fSv m}^2$ and for b it is $(49.1 \pm 3.7) \text{ m}$; the values for λ are plotted as a function of maximum neutron energy in Figure 6.

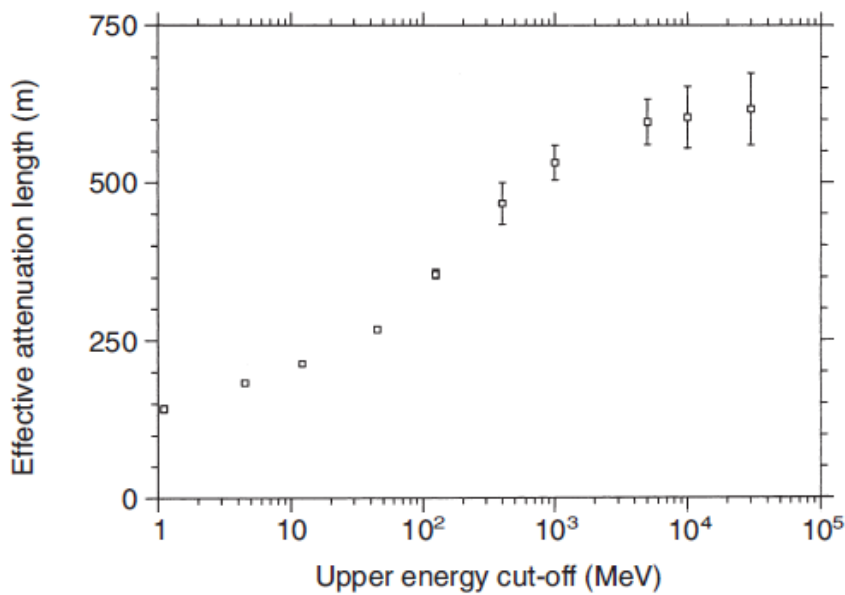


Figure 6 : The effective attenuation length for skyshine neutron as a function of maximum neutron energy.

In this method, if the source Q is known only in terms of the dose equivalent, then it must be converted to neutrons using the g factors of the last column of Table 2. These factors are the averaged dose equivalent over the composite spectrum with cut-off energy E_c . For low energy accelerators, which are compact and sited such that boundaries are often within less than 100 m from the source, the geometrical factors always dominate the reduction in dose equivalent with distance and it is usually not necessary to include the exponential attenuation term.

1.2.2 Emission of radioactive effluents

Because of their compact size and location in built-up urban areas, radioactive emissions to the atmosphere can dominate the radiological off-site impact of high power, low energy proton accelerators. This is especially true if the target materials being bombarded include high-Z materials that may produce exotic radioactive species such as radioactive isotopes of iodine or α -emitters. On the other hand, releases to ground and surface water can often be mitigated by minimising water inventories and holding up the effluent until such time that the radioactivity content has decayed below the levels of concern.

The NCRP has produced a guide (22) that can be used to screen the magnitude of the potential off-site impact of the release of radioactive effluents to the environment and to select a model for estimating that impact. In this approach one starts with a crude model that assumes that a member of the public is continuously ingesting or inhaling the maximum concentration at the point of the release. If this crude estimate does not yield a significant dose then the process stops. On the other hand if this estimate fails to meet the regulatory requirements of the local jurisdiction then one proceeds through a series of even more detailed calculations, at each stage verifying whether the regulatory limits can be met. In this way one needs to refine the calculation only to the extent required by the identified risk.

The transport of the radioactive releases may be modelled using an environmental pathway model. A generic model is illustrated in Figure 7. The release proceeds from the source through a number of environmental compartments to produce a dose in a typical member of the ‘critical group’ of the population, i.e. the most exposed homogeneous group of people of the general public. The

transfer of radioactive material between compartments is modelled by evaluating the transfer factors P_{ij} that determine the fraction of radioactivity transferred from compartment i to compartment j. For the short-lived positron emitters and noble gases (e.g. ^{41}Ar) that are usually the products of direct air activation at accelerators, only the external dose via the immersion pathway determined by $P(e)_{19}$ is significant. For long-lived and biological active isotopes, all possible pathways need to be considered.

For example, in the release of an airborne radionuclide, the calculation of the transfer of radioactivity from the source to the environment at the point of interest would proceed as follows:

$$X_1 = P_{01}X_0(a) \quad (11)$$

$$X_3 = P_{13}X_1 \quad (12)$$

$$X_4 = P_{14}X_1 + P_{34}X_3 = P_{01}(P_{14} + P_{13}P_{34})X_0(a) \quad (13)$$

where $X_0(a)$ is the source release rate, and X_i is the radioactivity concentration in compartment i. We have neglected here the contribution via irrigation of contaminated surface water. The equivalent dose to a member of the critical group from this pathway would then be given by $X_9 = P_{49}X_4$, where P_{49} is the dose equivalent per unit intake multiplied by the quantity of vegetation consumed per person per year. Methods for calculating the various transfer factors are given in NCRP Report No 123 (22). A number of countries have revised their own specific pathway models that include the preferred values or method for calculating these factors.

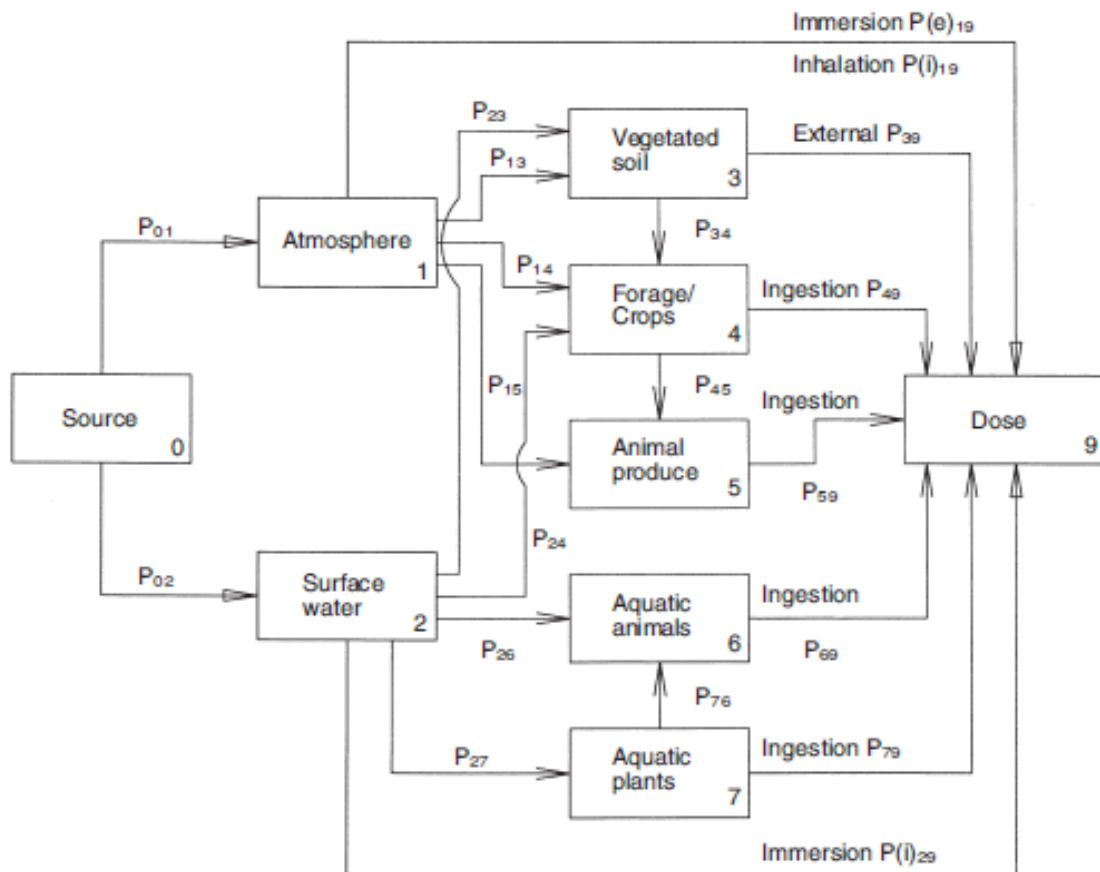


Figure 7 : An example of an environmental pathway model for the release of radioactive effluents from an accelerator facility. Compartment 0 is the source and compartment 9 is the dose to a member of the critical group.

1.3 Induced radioactivity

At lower incident energies ($E \leq 30$ MeV) radionuclide production by direct reactions such as single- and multi-nucleon transfer as well as processes such as (p, γ) are of principal concern. The systematic and approximate energy dependences of these processes are generally well understood. The majority of reactions of concern are endoergic nuclear reactions that have threshold E_{th} below which the process is forbidden by conservation of energy. E_{th} is related to the mass of the projectile, m_p , the mass of the target nucleus, M , and the energy released in the reaction, Q , by

$$E_{th} = \frac{m_p + M}{M} |Q| \quad (14)$$

The Q -value is the difference between the separation energy of the in-going and out-going particles in the absence of excitation energy in either the entrance or the exit channels.

It is also quite common for thermal neutrons to produce significant levels of induced radioactivity in the accelerator room. Such radioactivity results from thermal neutron capture reactions that sometimes can have relatively large cross sections. As the energy of the incident radiation increases, the number of possible reaction channels increases, with a corresponding increase in the number of radionuclides produced. The variety of radionuclides that can be produced increases as one raises the bombarding energy because more reaction thresholds are exceeded.

A very useful summary of the production of radioactivity at particle accelerators (Table 3) and four simple rules for approximate radioactivity estimates have been given by Gollon (23).

- **Rule 1:** the absorbed-dose rate, dD/dt (Gy/h), at a distance r (meters) from a “point” source of typical activation gamma rays is given in terms of source strength [S (Becquerel)] and the photon energy [E_γ (MeV)] by:

$$\frac{dD}{dt} = \Gamma \sum E_\gamma \left(\frac{S}{r^2} \right), \quad (15)$$

where the summation is over all gamma rays present. The constant, Γ , has a value of $1.08 \times 10^{-13} \text{ m}^2 \text{ Gy h}^{-1} \text{ MeV}^{-1} \text{ Bq}^{-1}$

- **Rule 2:** in many common materials, about 50% of the nuclear interactions produce a nuclide with a half-life longer than a few minutes, with about 50% of these having a half-life longer than 1 d.
- **Rule 3:** for most common shielding materials, the approximate dose rate dD/dt due to constant irradiation is given by Sullivan and Overton (24) as:

$$\frac{dD}{dt} = b \phi \ln[(t_i + t_c)t_c], \quad (16)$$

where b is a factor that depend on geometry and target material, ϕ is the fluence rate of incident particles, the variable t_i is the irradiation time and t_c is the cooling time since the cessation of the irradiation.

- **Rule 4:** in an hadronic cascade, a proton produces about four interactions for each GeV of energy

Table 3 : a summary of radionuclides commonly identified in materials irradiated in radiation environments.

Irradiated Material	Radionuclides Produced	Half-Life
Water, plastics, oils	^7Be ^{11}C	53.3 d 20.3 min
Aluminum	All of those above plus: ^{18}F ^{22}Na ^{24}Na	110 min 2.60 y 15.0 h
Steel	All of those above plus: ^{42}K ^{43}K ^{44}Sc $^{44\text{m}}\text{Sc}$ ^{46}Sc ^{47}Sc ^{48}Sc ^{48}V ^{51}Cr ^{52}Mn $^{52\text{m}}\text{Mn}$ ^{54}Mn ^{56}Co ^{57}Co ^{58}Co ^{55}Fe ^{59}Fe	12.4 h 22.3 h 3.93 h 2.44 d 83.8 d 3.35 d 1.82 d 16.0 d 27.7 d 5.59 d 21.1 min 312 d 77.3 d 272 d 70.9 d 2.73 y 44.5 d
Stainless steel	All of those above plus: ^{60}Co ^{57}Ni ^{60}Cu	5.27 y 35.6 h 23.7 min
Copper	All of those above plus: ^{65}Ni ^{61}Cu ^{62}Cu ^{64}Cu ^{63}Zn ^{65}Zn	2.52 h 3.35 h 9.74 min 12.7 h 38.5 min 244 d

1.4 Radioactivity in air and water

The yield P_i of a radionuclide i , produced by a hadronic cascade in air or water can be calculated by integrating the product of the production cross sections with the particle track-length spectrum:

$$P_i = \sum_{i,j} n_j \int \sigma_{i,j,k} (E) \Lambda_k (E) dE \quad (17)$$

where the summation is performed over all possible participant elements j and all hadron components k in the cascade, n_j is the atomic concentration of the element j in air and water per cm^{-3} and Λ_k is the track-length spectrum in cm of hadrons of type k and energy E , as obtained from a proper simulation, $\sigma_{i,j,k}$ is the cross section for production of the radionuclide i in the reaction of the particle of type k and energy E on the nucleus j . The 39 radionuclides of interest for air and water activation together with their energy-dependent production cross sections are given by Huhtinen (25).

However, the main problem in assessing the environmental impact of the activation of fluids lies in choosing the correct model for the fluid movement during activation and in transit to the release point. The simplest activation model assumes that the fluid is stationary during activation and then moves directly to the release point after irradiation. Since this involves simple exponentials, the mathematics of this model will not be considered further. More interesting are the cases firstly where the fluid passes at a uniform speed through the irradiation region without turbulence and, secondly, where there is complete mixing of the fluid in the irradiation region and a small fraction of the fluid is removed regularly. A very detailed description of these two cases is given by Stevenson (26) and briefly summarized in Sections 1.4.1 and 1.4.2.

1.4.1 Laminar flow model

Let the number of beam particles (protons) intercepted per second by the activating system (target) be n_p , which is a function of time, and let L be the length of the accelerator tunnel or water pipe. If the total volume of the air or water circuit is V_{irr} cm^3 and the flow rate of air (or water) through the circuit is $Q \text{ cm}^3 \text{ s}^{-1}$, the linear velocity of the fluid in the tunnel or pipe, v (cm s^{-1}), is:

$$v = \frac{QL}{V_{\text{irr}}} \quad (18)$$

If the transit time of the fluid past the activating region is very short when compared with the time variations of the proton beam intensity, one can make considerable simplifications in the following calculations of release and concentration of radioactivity.

Release

The number of nuclei of a given radionuclide produced during a time dt in an elemental length dx of the activation region, at a distance x from the end of the activating region, is $n_p P dt dx/l$, where P is the total number of nuclei of the radionuclide produced in the fluid by the loss of one proton and l is the length of the activation region. The transit time for the fluid in this elemental volume to reach the end of the activating region is x/v , and so the number of radioactive nuclei reaching the end of the activation region is $n_p P dt dx \exp(-x/v\tau)/l$, where τ is the mean lifetime of the

radionuclide. The total activity, A , produced in the time dt in the whole activation region and which reaches the end of this region is then:

$$A = \frac{1}{\tau l} \int_0^l n_p P dt \exp(-x/v\tau) dx = \frac{n_p P dt}{t_{\text{irr}}} [1 - \exp(-t_{\text{irr}}/\tau)] \quad (19)$$

where $t_{\text{irr}}=l/v$ is the transit time for the fluid to traverse the activation region.

If it takes a time t_d for the fluid to reach the release point, the amount of radioactivity, A_{Rel} , produced in the time dt and which escapes to the environment is:

$$A_{\text{rel}} = A \exp\left(-\frac{t_d}{\tau}\right) = \frac{n_p P dt}{t_{\text{irr}}} [1 - \exp(-t_{\text{irr}}/\tau)] \exp\left(-\frac{t_d}{\tau}\right) \quad (20)$$

The total amount of radioactivity released during one operation period, A_{tot} , is then simply:

$$A_{\text{tot}} = \frac{N_p P}{t_{\text{irr}}} [1 - \exp(-t_{\text{irr}}/\tau)] \exp\left(-\frac{t_d}{\tau}\right) \quad (21)$$

where N_p is the total number of protons intercepted by the target during an operation period.

Concentration

The concentration of a given radionuclide in the fluid at the end of the activation region is A , taken from equation 19, divided by the volume of the fluid flowing past in the time dt . If t_{tot} is the duration of the operating period, the average concentration during operation, a_{ave} is then:

$$a_{\text{ave}} = \frac{N_p P}{Q t_{\text{irr}} t_{\text{tot}}} \left[1 - \exp\left(-\frac{t_{\text{irr}}}{\tau}\right) \right] \quad (22)$$

1.4.2 Complete mixing model

In this model the activity is produced in a region where there is complete mixing of the air inside the region. There is a supply of air to and an extraction of air from the region, and it is assumed that an activated nucleus has the same probability of being removed from the region no matter where it is produced. Let the volume of air cycled through the region per second be Q and the volume of the region V_{irr} . Thus the change in the number, N , of radionuclides of a given species per unit time is the difference between the production rate and the sum of its decay and extraction rates:

$$\frac{dN}{dt} = P \nu_p(t) - \left(\frac{N}{\tau} + \frac{Q}{V_{\text{irr}}} N \right) \quad (23)$$

P is the production per unit proton of the radionuclide, whose mean life-time is τ , by the hadronic cascade in air and can be calculated by integrating the production cross sections with the particle track-length spectrum following the usual formula. ν_p is the proton interaction rate which can vary with time. For the sake of convenience, in the following the decay constant λ will be used instead of $1/\tau$ and Q/V_{irr} will be defined as the air-exchange rate in the cavern m . The above equation then becomes:

$$\frac{dN}{dt} + (\lambda + m) N = P \nu_p(t) \quad (24)$$

which has the solution

$$N = \exp[-(\lambda + m)t] P \int \nu_p(t) \exp[(\lambda + m)t] dt + \text{constant} \quad (25)$$

In the simple case where $N=0$ at $t=0$ and the proton interaction rate has constant value ν , then after a time t the number of nuclei is given by the relation:

$$N = \nu P \frac{1}{\lambda+m} (1 - \exp[-(\lambda+m)t]) \quad (26)$$

In the more general case where N_i radionuclides remain at the start of the i^{th} period of operation, $t=0$, from previous periods :

$$N = \exp[-(\lambda+m)t] \left(\left(N_i + P \int_0^t \nu_p(t) \exp[(\lambda+m)t] dt \right) \right) \quad (27)$$

Concentration

The total activity in the volume of the region is thus λN and its concentration $\lambda N / V_{\text{irr}}$.

Release

The activity of a given radionuclide extracted from the activation region is $m\lambda N$, where N is given by Equation 25. Thus the rate of release in Bq per second of the radionuclide is:

$$R = m\lambda N \exp(-\lambda t_d) \quad (28)$$

where t_d is the decay time during which the activated fluid passes through the ducts from the activation region to the external environment.

The total activity released during the i^{th} operation period which lasts for a time t_{on} is obtained by integrating the above equation:

$$Y_i^{\text{on}} = \int_0^{t_{\text{on}}} R dt \quad (29)$$

At the end of the operation period, the number of radionuclides in the activation region, N'_i is given by substituting t_{on} into Equation 27. If the time between operation periods is t_{off} , the number remaining at the start of the next period of operation is simply:

$$N_{i+1} = N'_i \exp[-(\lambda + m_{\text{off}})t_{\text{off}}] \quad (30)$$

where the air-exchange rate during the down-time between operation periods, m_{off} , could well be different from the value of m during operation because of a different ventilation rate Q_{off} .

The total activity vented after the i^{th} operation period during the time between periods is:

$$Y_i^{\text{off}} = m \lambda \exp(-\lambda t_d^{\text{off}}) \int_0^{t_{\text{off}}} N'_i \exp[-(\lambda + m_{\text{off}})t] dt = \frac{m\lambda}{m+\lambda} \exp(-\lambda t_d^{\text{off}}) N'_i (1 - \exp[-(\lambda + m_{\text{off}})t_{\text{off}}]) \quad (31)$$

In the calculation of the total release in one year of operation the contributions from successive periods are summed up:

$$Y^{\text{tot}} = \sum_i (Y_i^{\text{on}} + Y_i^{\text{off}}) \quad (32)$$

remembering that after the final air exchange the integration in Equation 31 has to be taken to infinity rather than to t_{off} .

2 Linac4 project

A programme for the progressive replacement or upgrade of the LHC injectors has been recently defined at CERN (27). The first goal of this programme is to increase the LHC luminosity beyond the nominal value by improving the beam brightness from the injector complex, which is now the main limiting factor towards higher luminosity. A second motivation is the replacement of the present cascade of injectors, which has been built between 1959 and 1978 and in the past few years has raised concerns for its long-term reliability, with a more modern, reliable and easier to maintain system, where transfer energies and beam parameters are optimized for the LHC needs. Moreover, new low energy accelerators can be made compatible with operation at higher beam power that could be required by future physics needs.

Linac4, a 160 MeV H^- Linac, is an essential component in this project of renovation of the LHC injector chain. It will replace Linac2 and inject beam directly in the present PS Booster (PSB) and will become the source of all protons at CERN in 2013. This chapter provides a description of the layouts considered for the installation of the facility and it gives an overview of the machine and its accelerating structures.

2.1 Linac4 and the CERN injector upgrade

The present sequence of accelerators used as LHC injectors is based on a proton linac of a relatively low final energy (Linac2, 50 MeV) followed by the 1.4 GeV PS Booster (PSB), by the 26 GeV Proton Synchrotron (PS) and finally by the 450 GeV Super Proton Synchrotron (SPS). The new injector sequence would use an H^- high-energy linear accelerator, the 4 GeV Low-Power Superconducting Proton Linac (LP-SPL). Its normal-conducting section of 160 MeV, to be built in a preliminary stage, is called Linac4 (28). The LP-SPL can be eventually upgraded to a High-Power SPL (HP-SPL) operating at multi-MW beam power (29). The SPL is followed by a new 50 GeV Proton Synchrotron (PS2). The last of the LHC injectors, the 450 GeV Super Proton Synchrotron (SPS), would be upgraded to cope with the higher brightness from its injectors. The scheme of the old and new injection complex is shown in Fig. 8.

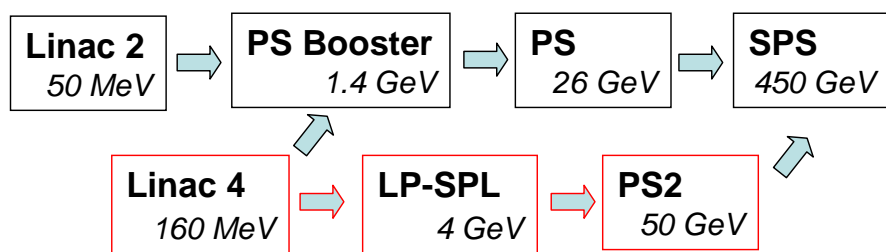


Figure 8 : Scheme of the old and new LHC injectors.

A staged construction is possible because Linac4 can inject in a preliminary phase H^- ions into the existing PSB. The higher injection energy coupled with the benefits of H^- charge exchange injection are expected to increase brightness out of the PSB by a factor of 2, making possible a first increase in the LHC luminosity around 2013, when the nominal luminosity should have been attained in the LHC and a programme of upgrades to the ring and to the experiments aiming at higher luminosity could be implemented.

Linac4 will be housed in a 12 m deep underground tunnel, connected to the Linac2-PSB line. A surface equipment building will house klystrons and other ancillary equipment. The Linac4 tunnel

can be later on extended to the SPL. Figure 9 shows a view of the CERN Linac-PSB-PS complex, indicating the position of Linac4 and of the future extension to the SPL. Figure 10 presents the layout of the Linac4 infrastructure. Civil engineering works started in October 2008 and are foreseen to be completed by November 2010.

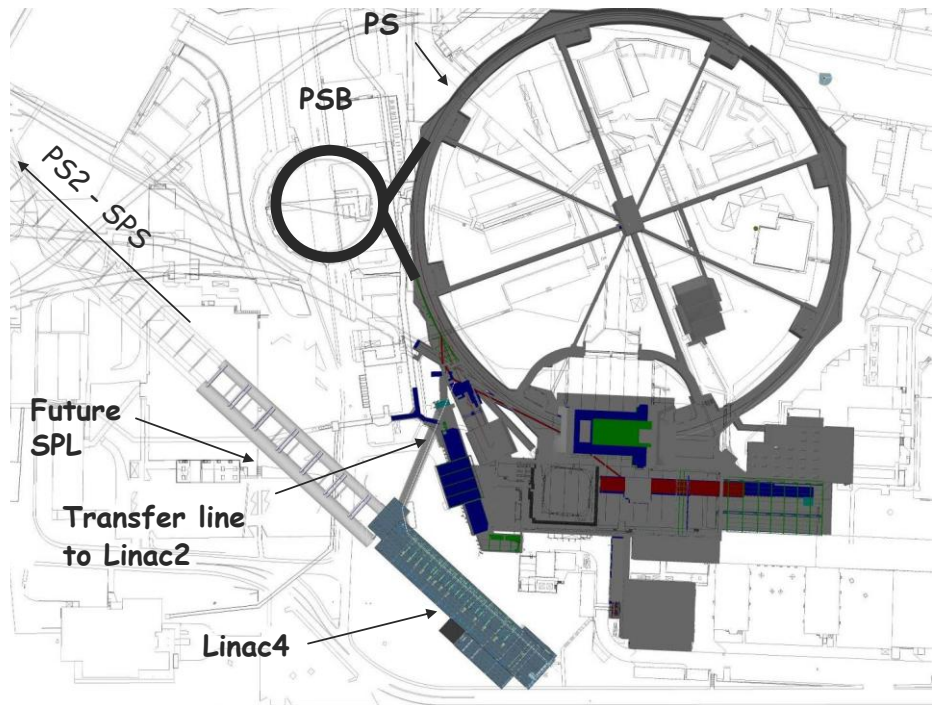


Figure 9 : View of the PS Complex at CERN, showing the position of Linac4.

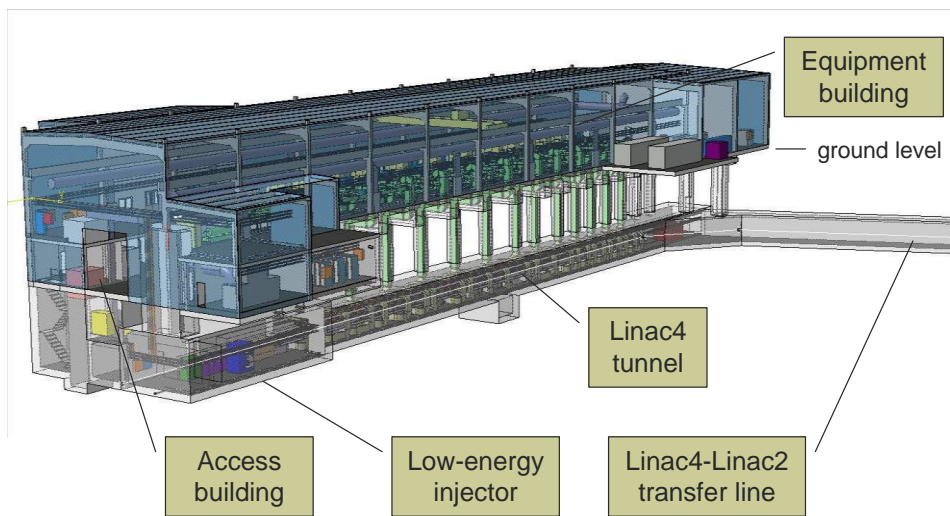


Figure 10 : The Linac4 layout (released in September 2007).

In June 2007 the CERN Council, while approving the construction of Linac4 as a high-priority project for the period 2008-2013, has approved the detailed design of SPL and PS2, the construction of which could start in 2012 and be terminated between 2015 and 2017.

2.2 The SPL and the next generation of physics facilities

The preparation of the CERN injectors for the Large Hadron Collider (LHC), which took place in the years 1995 – 2000 (30), allowed reaching the LHC goals but at the same time showed clearly that the present injectors are at the limit of their capabilities in terms of both brightness (for LHC) and intensity (for other users).

During the same years, the foreseen decommissioning of the LEP collider with its powerful 352 MHz RF system triggered the proposal to build a modern high-energy high-intensity linear accelerator at 352 MHz based on the LEP RF technology. The first designs were addresses at energy production applications (31), but soon came a proposal to build a 2 GeV linac at CERN to inject directly into the Proton Synchrotron (PS) ring (32). After some studies, this idea materialized into the conceptual design of a 2.2 GeV H^- linac called the Superconducting Proton Linac (SPL) published in 2000 (33). This machine was meant to produce a low-intensity and high-brightness beam in the PS for the LHC, and at the same time generate high-intensity beams for other potential users, like a neutrino factory, or a radioactive ion beam facility. In its original design as well as in the recent design updates (29) (34), the SPL is a modern H^- linac, equipped with a chopping section and with a sophisticated beam dynamics design. The low-energy front-end of the SPL uses normal-conducting accelerating structures up to an energy of 180 MeV. The section up to 160 MeV is the above-mentioned Linac4.

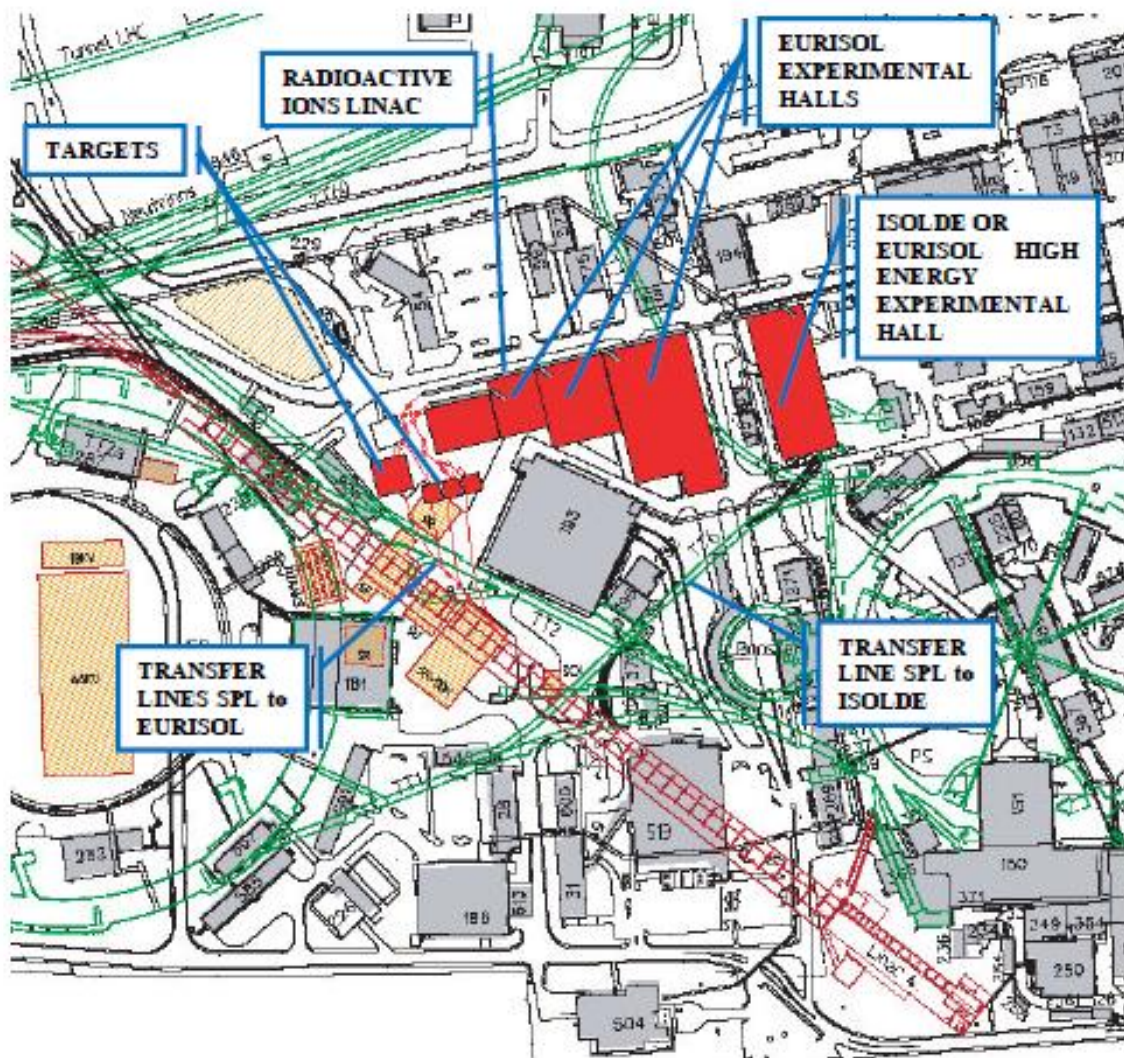
Future facilities requiring multi-MW of beam power at a few GeV are the subject of intensive studies:

- A radioactive ion beam facility based on the ISOL technique (“EURISOL”) (35). The SPL can be equipped with a deflection system at about 2.5 GeV to send beam through a new transfer line to a new hall located close to the building 193. The area available in this part of the Meyrin site is adequate to host the EURISOL facility (Figure 11). A second underground location between the SM18 buildings and the PS2, for which the TT2/TT10 transfer lines would be used to transport the beam, is also being considered.
- A neutrino factory. The possibility to install a Neutrino Factory at CERN has been considered a few years ago (36) (37). A recent study has confirmed the capability of the SPL, when combined with an accumulator and a compressor ring, to meet the specifications of the proton driver of such a facility (38). The foreseen layout is also compatible with the position of the new accelerators (Figure 12).

Additional investments in infrastructures (electrical power, cryo-cooling capacity, replacement of klystron power supplies ...) can transform the 4 GeV, 200 kW LP-SPL into the 5 GeV, 4 MW SPL. The Linac4 tunnel and equipment building are dimensioned for high beam power operation, as well as the Linac4 accelerating structures and klystrons. Power converters and infrastructure (water, electricity) are dimensioned only for low beam power operation and will need to be replaced when going to high beam power. However, adequate space has been foreseen in the equipment building for the larger high-duty power converters and in the machine tunnel for larger cooling pipes, which could be easily installed during machine shut-downs. The additional external electrical and cooling installations required for the high-power operation can be integrated to those needed for the SPL and housed in the remaining space outside of Linac4 or in the old buildings of the PS complex, which will be free after the decommissioning of the PS.

In the same way, the conversion of the LP-SPL to high-beam power operation will require the replacement of the power converters and the installation of additional klystrons in the space that has

been foreseen in the klystron tunnel. The LP-SPL tunnels will be made long enough to host the additional accelerating structures and klystrons necessary for increasing the beam energy up to 5 GeV.



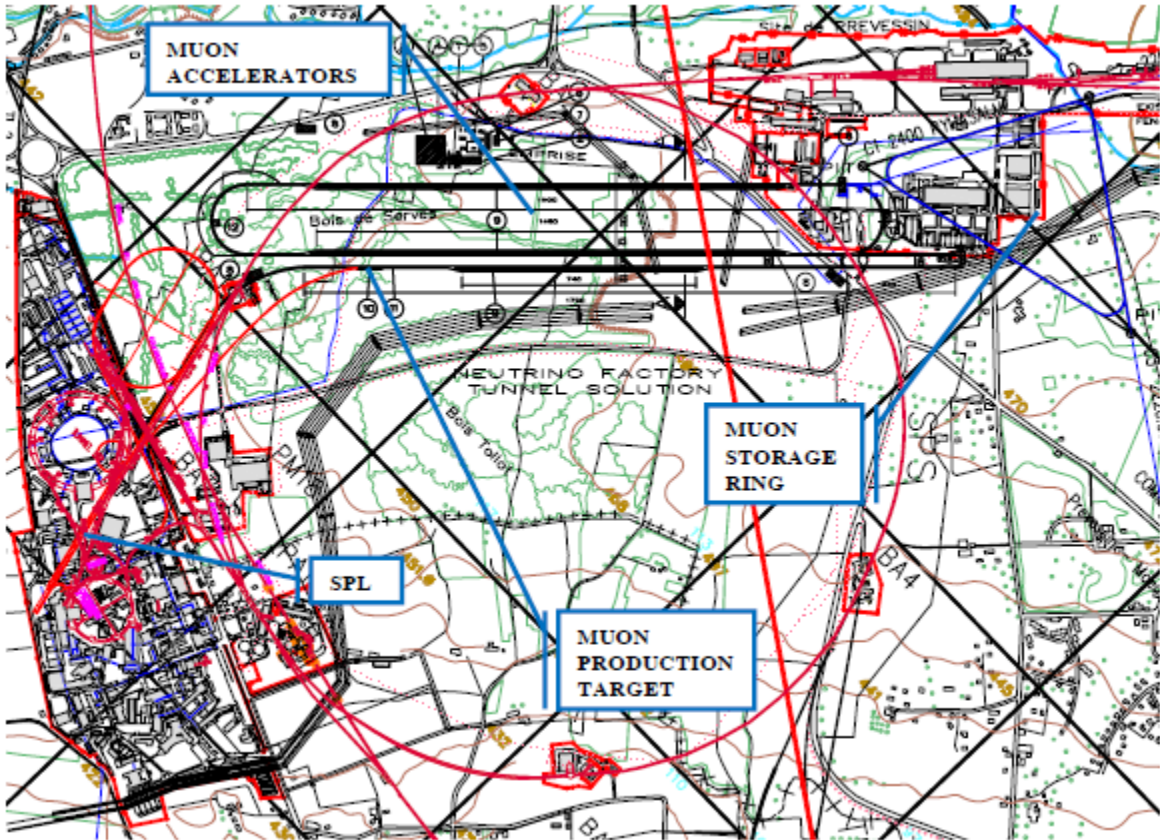


Figure 12 : Connection with a neutrino factory.

2.3 Linac4 design

The design of Linac4 is dictated by the requirement to operate in three different modes during its lifetime, depending on the characteristics (repetition frequency, pulse current and pulse duration) of the machine that it has to supply with beam:

1. PSB injector, 2013-2017: 1.1 Hz, 40 mA, 400 μ s.
2. LP-SPL injector, from 2017: 2 Hz, 20 mA, 1.2 ms.
3. HP-SPL injector, after 2020: 50 Hz, 40 mA, 400 μ s.

After a first phase as PSB injector the Linac4 beam pulse length will increase to 1.2 ms, whereas its current will go down by a factor of 2. At a later stage, if the high-power programme is approved, Linac4 would operate at 50 Hz with a beam current going up again to 40 mA.

The main consequence on the Linac4 design is that civil engineering and in particular radiation shielding have to be dimensioned from the beginning for high-power operation. Accelerating structures and klystrons will be specified as well for high duty operation, whereas power supplies, electronics, and all electrical and cooling infrastructures will be dimensioned only for low beam power operation and will be replaced or upgraded when required for the HP-SPL. Additional space has been foreseen in the surface building for larger power supplies and for the additional SPL equipment.

In the design of machine and infrastructure particular care has been given to solutions providing the high reliability required for the first accelerator in the injection chain. Fault rate should be comparable to that of Linac2, about 1.5% of the scheduled beam time. Particular attention has been given to the control of transverse and longitudinal emittance growth, for clean PSB and SPL

injection, and of losses along the machine, to limit activation for the full-SPL mode of operation) (39). The main Linac4 design parameters are listed in Table 4.

Table 4 : Linac4 beam parameters.

Ion species	H^-
Output Energy	160 MeV
Bunch Frequency	352.2 MHz
Maximum Repetition Rate	2 Hz
Beam Pulse Length	400 μ s
Chopping scheme	222/133 transmitted bunches/empty buckets
Mean pulse current	40 mA
Beam Power	5.1 kW
Number of particles per pulse	$1.0 \cdot 10^{14}$
Number of particles per bunch	$1.14 \cdot 10^9$
Beam transverse emittance	$0.4\pi \text{ mm mrad (rms)}$

Three different accelerating structures are used in Linac4 after the RFQ, all working at 352 MHz frequency (40). In particular, the Side Coupled Linac (SCL) at 704 MHz foreseen in a previous design has been replaced with a Pi-Mode Structure (PIMS) operating at the basic linac frequency (41). The basic scheme with the transition energies is shown in Fig. 13.

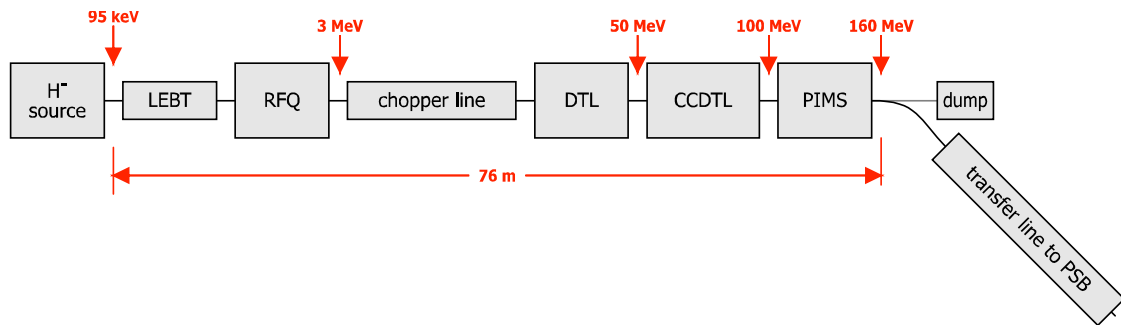


Figure 13 : Scheme of the Linac4.

Some 352 MHz klystrons and other equipment from the old LEP accelerator will be re-used for Linac4. In the first stage (Fig. 14, top), 13 old LEP klystrons at 1.3 MW and 6 new pulsed klystrons at 2.6 MW will feed the accelerating structures. Most of the LEP klystrons will be connected in pairs to a single modulator, allowing for the progressive replacement of pairs of LEP klystrons with one klystron of the new type. In the final configuration (Fig. 14, bottom) 9 new klystrons will feed two RF cavities each.

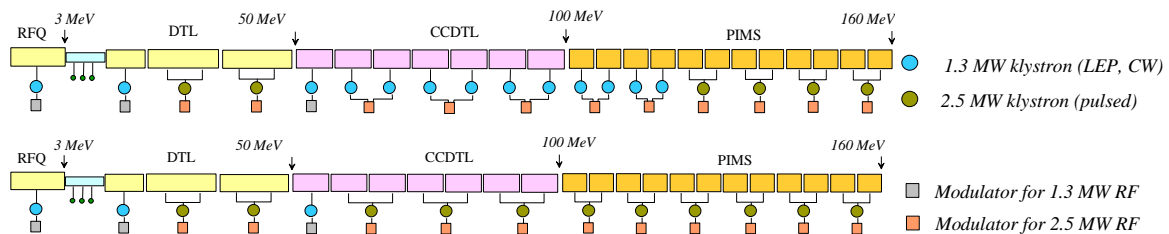


Figure 14 : RF power distribution at installation (top) and after the end of the stock of LEP klystrons (bottom).

2.4 Facility layouts

Different locations for the new accelerators have been analyzed and compared. For Linac4, the preferred site is South-West of the PS, under a small artificial hill made with excavation materials dating from the PS construction. This location allows for a short and simple connection to the present Linac2 to the PSB transfer line and for an extension to a long underground tunnel housing the LP-SPL followed by a straight transfer line to the PS2 machine, nearly tangential to the SPS. The precise position of Linac4 is dictated by the needs to have a stable foundation of the equipment building on the surface (the site presents an important slope towards the PS area) and to keep sufficient distance between this building and the Swiss-French border, where constructions are forbidden by international laws. Other sites considered for Linac4 were (i) the existing PS South Hall, economic but impossible to extend to SPL and with a difficult connection to the PSB through the PS (28), (ii) the present Linac2 location, impossible to extend to SPL and forcing to a long interruption for switching between the two machines (28), and finally (iii) the SPS West Hall, which offers a limited option for an extension but requires a long and expensive transfer line to the PSB.

Apart from the easy connection to the PSB and to the LP-SPL, the selected location is one of the few areas on the Meyrin site which is free from constructions. The Linac4 tunnel can be built with a “cut-and-cover” technique, less expensive than tunneling, at nearly the same level as the PSB and PS machines. The remaining layer of earth between the accelerator tunnel and the surface provides an effective radiation shielding that allows a minimum thickness of the accelerator walls, when compared to solutions above ground or within existing halls. The LP-SPL is located in an underground extension of the Linac4 tunnel having a length of 460 m and a slope of about 1.7 %. The klystrons and power supplies will be housed in a gallery parallel to the accelerator tunnel at 9 m distance (42).

The depth of Linac4 and LP-SPL is defined by radiation protection requirements, taking into account that these machines could later be upgraded to the high beam power required by potential future physics facilities. For the needs of hands-on maintenance, activation must be minimized and tightly controlled. The new accelerator complex will therefore be designed for and will have to be operated with a maximum of 1 W/m of uncontrolled beam loss (43). The combination concrete-earth shielding of the Linac4 tunnel and the depth of the SPL have been defined in order to keep the estimated dose in public access areas (surface buildings and infrastructure, service tunnels, etc.) below the limits defined by Radiation Protection. The result is that the Linac4 beam axis must be 2.5 m below the present PSB-PS level. The studies performed to assess the interferences between the SPL and various existing tunnels and the closest surface buildings are reported in ref. (44).

2.5 H⁻ source and low energy beam transfer

The linac project requires a high performance and high reliability H⁻ ion source. A collaboration with DESY allows CERN to construct a modified version of the DESY-HERA source (45). The source parameters for the different CERN H⁻ linac design phases and the conceptual design are published in (46). The 2 MHz DESY RF volume source, proving its high reliability and high current capability over the past years, comes close to the requirements and shows a promising potential for improving its performance. H⁻ currents up to 70 mA without cesium have been reached (47).

A first goal was to develop a RF H⁻ source at an extraction voltage of 95 kV. The basic idea was that the entire source infrastructure, which is kept at ground potential at DESY, floats on an intermediate 60 kV HV platform (see fig. 15). The beam is extracted from the source at 35 kV, providing the needed beam energy of 95 keV. The 2 MHz RF generator and the vacuum pumps stay

also at ground potential. The entire extraction electrode system is coupled to the source body, which is suspended onto the vacuum tank by a ceramic insulator. The source is aligned with respect to the vacuum tank. After the extraction and the deflection of the electrons by a set of permanent magnets the H- ions are post-accelerated with a diode gap.

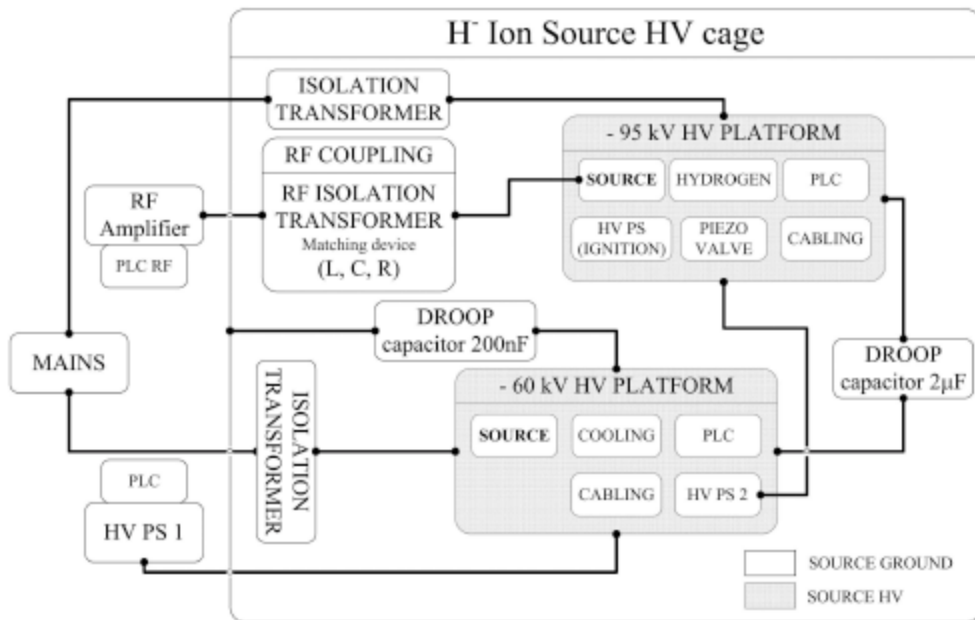


Figure 15 : Source schema for the 95 kV option (passive droop compensation): the source is operated on two HV platforms and the RF power is brought up to the 95 kV one by a RF transformer.

The possible use of a RFQ with lower injection energy (45 keV), optimized for Linac4, made it necessary to design a 45 kV H^- source. Numerical simulations indicated that the post-acceleration could not be adapted for a 45 kV solution, because the beam explodes. Therefore a single stage extraction concept has been thought of. The main ceramic will be replaced by a standard stainless steel shell and the post-acceleration will be omitted. The gain of space allows shifting the source closer to the first low energy beam transfer (LEBT) solenoid. The electrons are dumped on ground potential. Firstly the CERN source will be commissioned at 35 kV and its emittance will be re-measured. Then the high voltage will be changed to its nominal level. Adaptations of the source in case of voltage holding problems are feasible. The distance between ground electrode and the plasma electrode can be modified by changing the spacers that hold the entire electrode system. Fig. 16 shows the inside of the 45 kV H^- source.

The Low-Energy Beam Transport (LEBT) line provides the beam matching from the source to the RFQ and contains the diagnostics to monitor the source. The scheme of the LEBT for Linac4 is given in Fig. 17. The beam emerging from the source post-acceleration system will be more than 30 mm in diameter, with a total divergence of approximately 100 mrad. Therefore large diameter solenoids are required for the focusing. The emittance of the LEBT is optimized with a short distance between PAS (PAS: post-acceleration system) and solenoid. The space charge compensation will be optimized with gas injection.

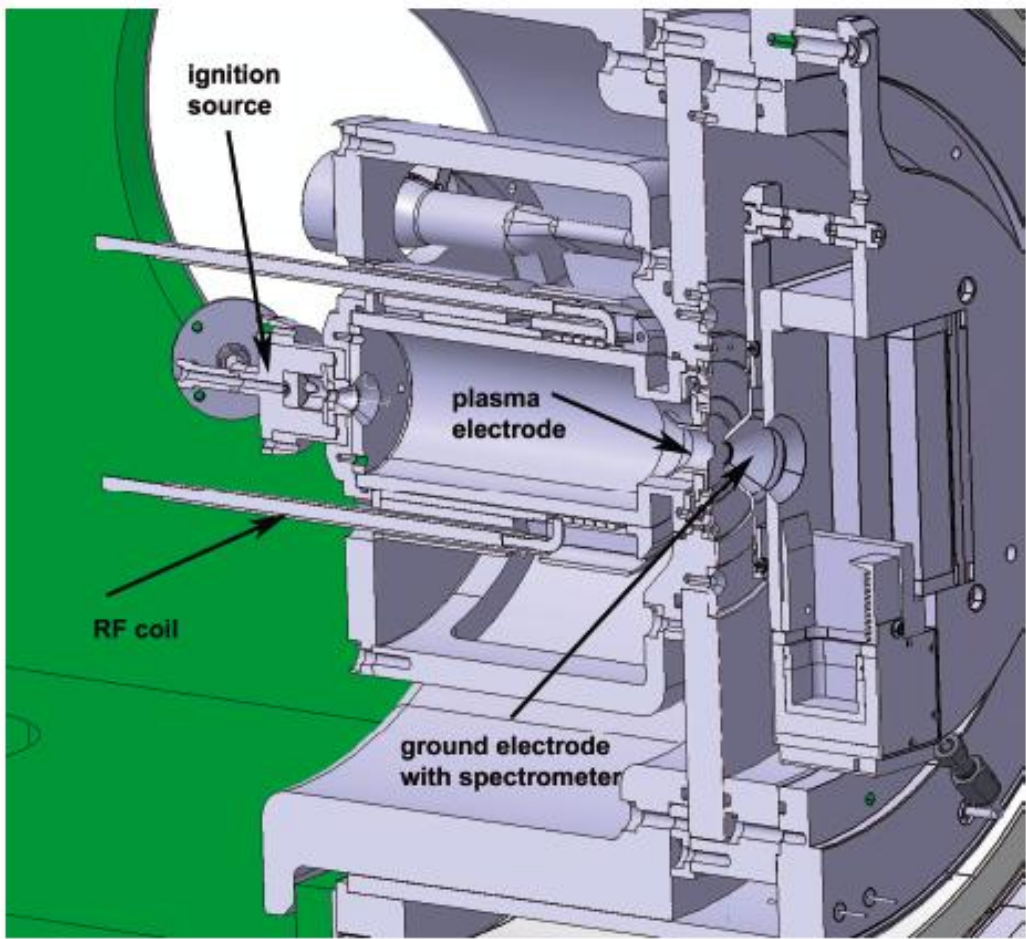


Figure 16 : Sectional view of the 45 kV CERN source: ignition source, RF coil, plasma electrode and spectrometer.

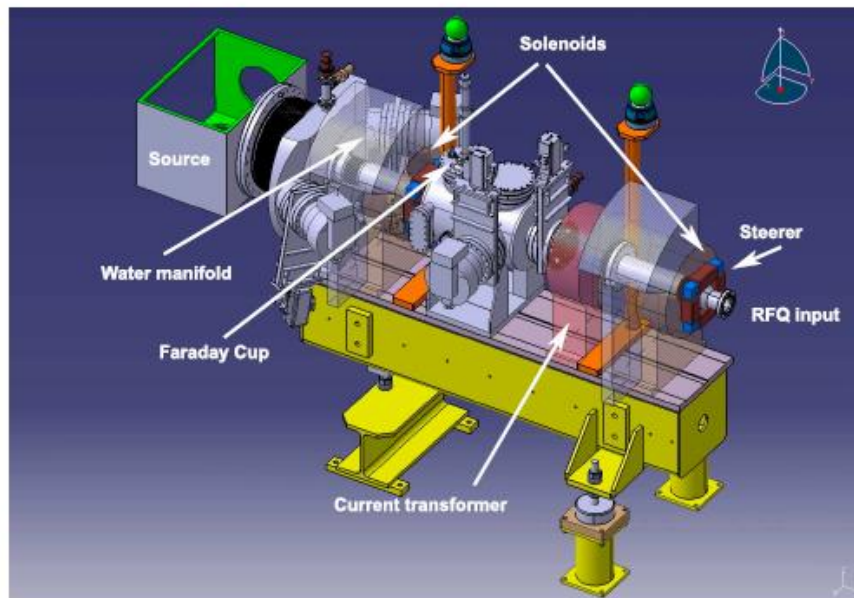


Figure 17 : 1.8 m long LEBT consisting of 2 solenoids and a diagnostic box in-between for beam analysis and an injection valve for space charge compensation.

2.6 RFQ

The first stage of acceleration in Linac4 is a 352 MHz, 3-m long Radiofrequency Quadrupole (RFQ) accelerator. The RFQ (48) will capture a 70 mA, 45 keV beam from the RF source and accelerate it to 3 MeV, an energy suitable for chopping and injecting the beam in a conventional Drift Tube Linac. The RFQ must initially be able to operate in Linac4 to fill the PS Booster, delivering beam pulses of 400 μ s at 1.1 Hz, and, at a later stage, to fill a Superconducting Proton Linac (SPL) operated as LHC injector (1.2 ms, 2 Hz). In case a high intensity beam programme would be approved, the option is left open to operate with 400 μ s, 50 Hz pulses. These different requirements represent an additional complication to the design. The specification parameters are listed in Table 5.

Table 5: Main design specification for the Linac4 RFQ, with rms values of emittance in the two planes.

Linac4 RFQ Parameter	Min	Max	Units
Beam energy	3.0	3.0	MeV
Operating frequency	352.2		MHz
Peak beam current (pulse)	10	80	mA
RF duty cycle	0.08	7.5	%
Transverse emittance (in)	0.20	0.35	π mm mrad
Longitudinal emittance (out)	0.11	0.20	π deg MeV

Other constraints on the design are the requirement to limit the RF power to 0.8 MW peak, corresponding to a single LEP klystron with a sufficient safety margin, and to keep the RFQ length around 3 m. This allows dividing the RFQ into 3 segments of 1 meter while keeping the overall length at 3.5λ , thus allowing the direct coupling of the three RFQ sections without using coupling cells between sections. The result of this design is a compact RFQ with an intra-vane voltage of 78 kV and a peak surface field of 34 MV/m. The main design parameters are shown in Figure 18.

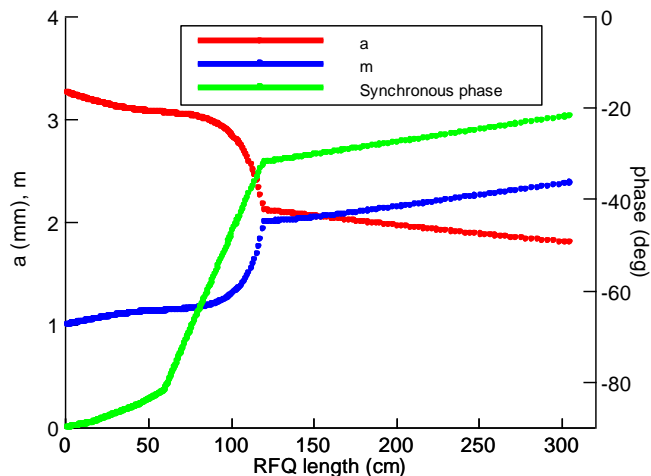


Figure 18 : Graph of the synchronous phase, with the RFQ aperture a and modulation parameter m.

The RFQ cavity is made of three sections, each one-meter long, directly coupled. Each of the three sections results from the assembly of two major vanes and two minor vanes. A CAD picture of the RFQ is shown in Figure 19.

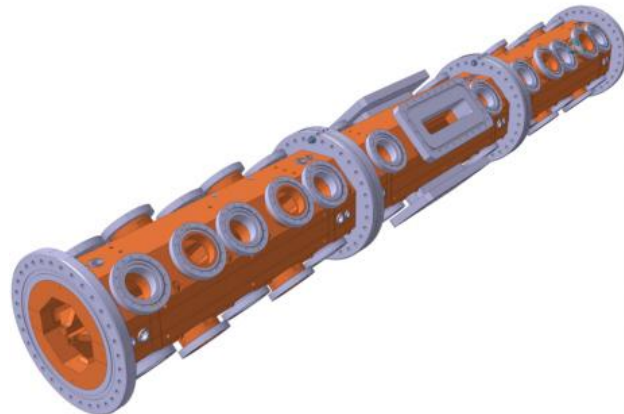


Figure 19 : Linac4 RFQ.

The structure is equipped with a total of thirty-two circular apertures, 82 mm in diameter, to host the fixed tuners; four rectangular apertures have been designed in the central section for the RF input(s). The first and last section holds eight circular apertures that have been designed to host the vacuum pumping ports. The design of the vacuum system takes into account that the main gas load is coming from the LEBT gas injection used for neutralization and is estimated at $1.1 \cdot 10^{-3}$ mbar l/s, whereas the gas load from out-gassing is only $1.5 \cdot 10^{-5}$ mbar l/s. By using eight diode ion pumps and four turbo molecular pumps an effective pumping speed of 2700 l/s is obtained, which allows to keep the dynamic vacuum level of the RFQ in the range of 10^{-7} mbar.

The vane modulation is achieved by a milling machine using a wheel shaped cutting tool. The assembly of the RFQ cavity will be performed by means of a two-step brazing procedure that has been developed at CERN during the fabrication of the IPHI and TRASCO RFQs (49). The first assembly step of the four poles is made by brazing in the horizontal position, at 825 °C, which allows a uniform diffusion of the brazing material, by capillary action. The second assembly step, performed in a vertical oven at 790 °C, brings the stainless steel flanges and end-flanges onto the RFQ cavity. The OFE copper used for fabrication has been submitted to a severe 3D forging, in order to obtain the maximum of homogeneity in the raw material. A detailed procedure, alternating machining phases to thermal annealing cycles has been established in order to stabilize the material and avoid deformations and possible displacements of the vanes, especially on the occasion of the first brazing step. The machining and assembly tolerances have been defined following an error study simulation campaign, which showed that the beam dynamics design adopted is relatively insensitive to errors. The most important contributions come from section tilts and electromagnetic field errors.

2.7 DTL

The Linac4 DTL (50) will accelerate H⁻-ion beams of up to 40 mA average pulse current from 3 MeV to 50 MeV in 3 accelerating cavities over a length of 18.7 m. The RF cavities operating at 352.2 MHz and at duty cycles of up to 10% are 520 mm in diameter with drift tubes of 90 mm diameter and 20 mm beam aperture. The 3 DTL cavities consist of 2, 4 and 4 section of about 1.8 m each, are equipped with 35, 41 and 29 drift tubes respectively, and are stabilized with postcouplers. The drift tubes are

equipped with permanent magnet quadrupoles (PMQ), used as focusing elements, with an FFDD lattice in cavity 1 and an FD lattice in cavity 2 and 3. PMQs have the advantage of small size at medium magnetic gradients without the need for current supply wires or power converters. To ease matching for beam currents below nominal, electromagnetic quadrupoles are placed in each of the intertank sections. The latest design parameters are shown in Table 6.

The DTL cavities consist of a steel cavity, an aluminum girder, drift tubes assembled from pre-machined copper pieces, and accessories for mounting drift tubes in girders as well as for tuning, stabilization, support, vacuum pumping and alignment of the structures (Fig. 20). The cavities are made from 50 mm thick mild steel cylinders that provide the rigidity to achieve the required tolerances when placed on supports. The cavity is segmented into 2 sections in the first cavity, and 4 sections in the second and third cavity that are aligned with precisely machined rings after assembly of each section. Mild steel is the material of choice due to its thermal conductivity, mechanical strength, and comparably low price (51). The steel cylinders of about 1.8 m length are precision machined in order to correctly position rectangular aluminum girders on top. The girders are pre-machined for each drift tube and stainless steel rings are inserted into the openings from above and below. The steel rings are re-machined for precise drift tube positioning.

Table 6 : DTL cavity parameters.

Parameter	Cavity 1 / 2 / 3
Cells per cavity	36 / 42 / 30
Maximum surface field	1.6 / 1.4 / 1.3 Kilp
Synchronous phase	-30 to -20 / -20 / -20 deg
RF peak power per cavity	0.95 / 1.92 / 1.85 MW
RF beam/peak power	1.88 MW / 4.7 MW
Focusing scheme	FFDD / FD / FD
Quadrupole length	45 / 80 / 80 mm
Number of sections	2 / 4 / 4
Length per cavity	3.63 / 7.38 / 7.25 m

The electro-magnetic design aims at accelerating with high constant average field E_0 of 3.2 MV/m over all gaps with high effective shunt impedance per unit length ZT^2 . While it is a typical DTL concept to ramp E_0 in the first cavity in order to adiabatically capture the beam longitudinally (51), the choice of high constant E_0 aims at maximizing the energy acceptance to the incoming beam and leads to a more compact design (39).

A particular advantage of ramping E_0 is lower peak fields at lower beam energies where earlier designs showed increased breakdowns (52). Several parameters might be of influence: comparably

large surfaces of flat opposing faces on consecutive drift tubes, more outgassing due to larger overall surfaces including the cavity end-wall, an incoming beam with a higher number of stray particles, magnetic fields close to surfaces of shorter drift tubes. Recent studies for muon cooling where strong accelerating and magnetic fields have to be combined, emphasize the importance of the latter (53). The PMQs that will be used for the DTL design have a peak magnetic surface field of 0.5 T which in the shortest drift tubes falls close to the area of peak electric fields. In order to reduce breakdown probability in the first cells, the peak electric field therefore has been reduced by 30% by increasing the gap length. The cells are tuned by the face angle. At longer drift tubes the peak electric field can be ramped to values that allow for optimum effective shunt impedance (Fig. 21). In this way, the same advantage of lower peak fields in the first cells is achieved as when ramping E_0 .

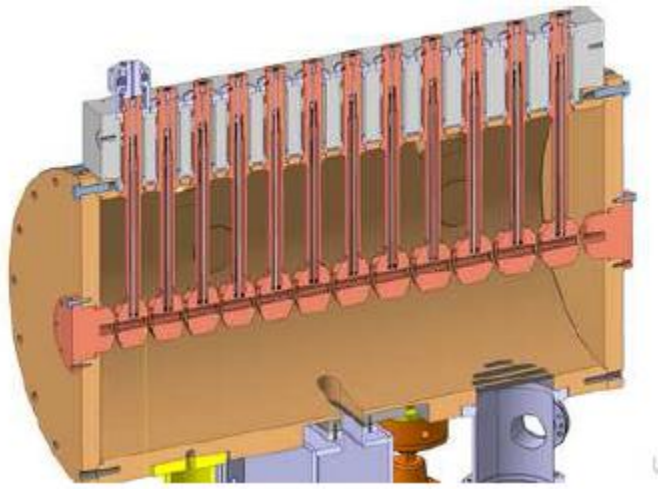


Figure 20: DTL prototype cut along the beam axis.

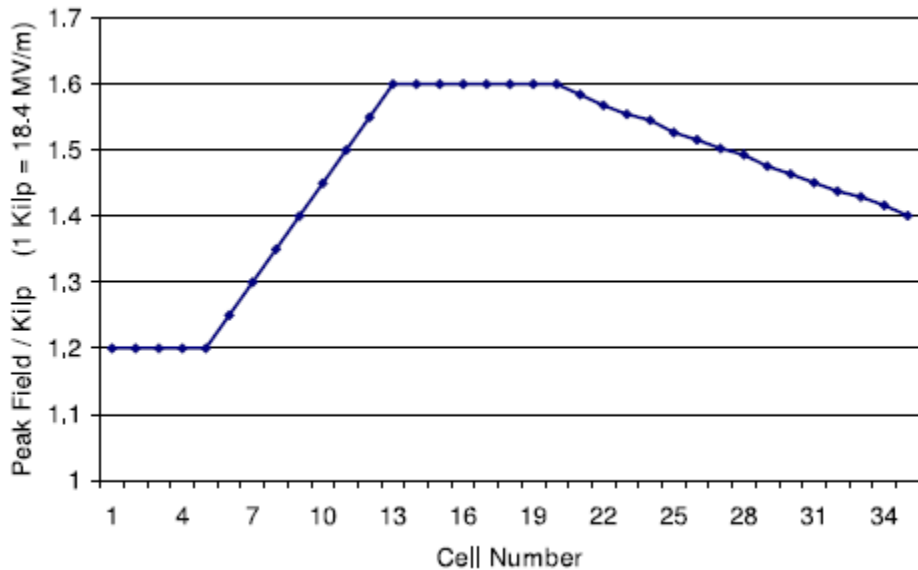


Figure 21 : The peak field is reduced in the first cells.

Currently a full-scale prototype of a half section with 12 drift tubes without PMQs is being constructed at CERN (Fig. 22).



Figure 22 : DTL prototype in the assembly stage.

2.8CCDTL

The 352 MHz CCDTL (54) will accelerate the Linac4 beam from 50 to 102 MeV. It is the first structure of this kind that will be used in a proton linac. The Cell-Coupled Drift Tube Linac (CCDTL) was originally developed at LANL as a structure providing higher shunt impedance than conventional Drift Tube Linacs (DTL) for intermediate-velocity particles (55). In the original design the CCDTL was used at twice the basic linac frequency (800 MHz) and when the principle was tested on a CW prototype it appeared that the surface power density was too large for stable operation. To avoid these problems, CERN started to develop a CCDTL at the basic linac frequency of 352 MHz and for applications as the Superconducting Proton Linac (SPL), limited at a duty cycle of less than 10% (29). Different combinations were analyzed and tested, to finally adopt for the Linac4 project the CCDTL configuration shown in Fig. 23. This CCDTL is made of 3-gap DTL-like accelerating tanks, connected by off-axis coupling cells bridging the focusing quadrupoles. Whereas the shunt impedance of this CCDTL configuration remains similar to that of a DTL with permanent quadrupoles, its main advantages are the easy access, alignment and cooling of the quadrupoles and the simpler construction and alignment of the tanks, the drift tube alignment tolerances being no longer dominated by the tight requirements of the quadrupoles.

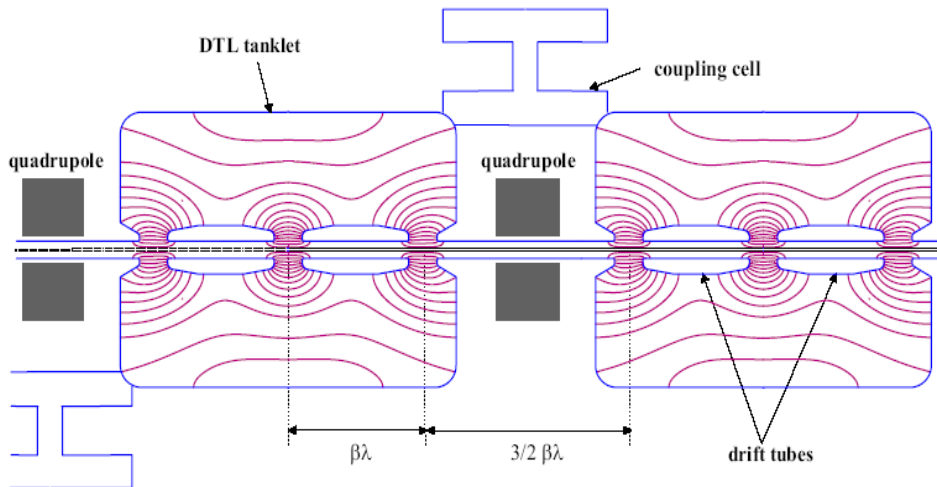


Figure 23: Linac4 CCDTL structure with indication of the electric field lines.

The RF configuration of Linac4 limits the peak power per resonator to about 1 MW. For this reason, the CCDTL tanks are grouped in modules of 3 tanks connected by two coupling cells (Fig. 24). The basic Linac4 CCDTL resonator is therefore made of 5 coupled cells operating in the $\pi/2$ mode. The CCDTL starts at 50 MeV, an energy that allows placing quadrupoles within the $3/2 \beta\lambda$ distance between neighboring gaps. The geometry of the coupling cell and coupling slot is kept constant for all modules to simplify construction. This is achieved by shifting the end-walls of the tanks.

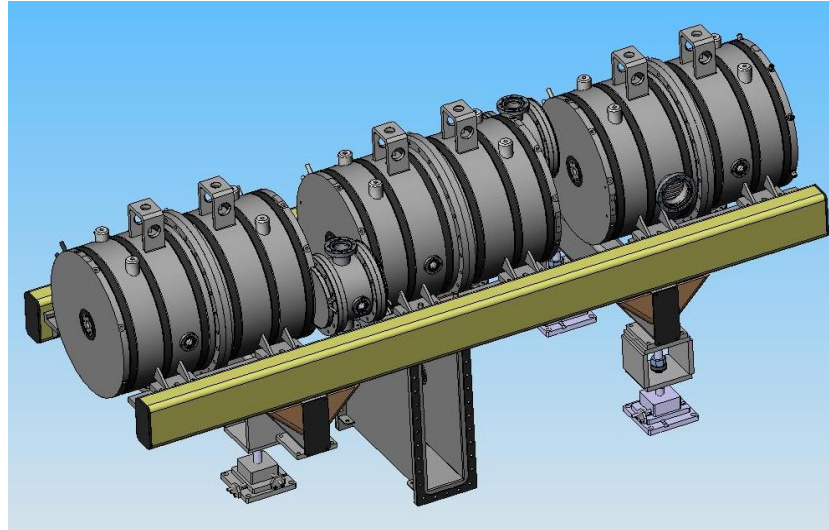


Figure 24 : 3D view of a Linac4 CCDTL module with support structure and rectangular RF port.

At higher energies the shunt impedance of the CCDTL falls considerably, together with the coupling factor between CCDTL cells, inversely proportional to the stored energy per tank. Both these factors impose an upper limit of about 100 MeV for this structure. The main parameters of the seven CCDTL modules are given in Table 7. The calculated copper power takes into account the effect of stems and slots and is then increased by a safety factor of 20%. The overall length of the CCDTL section is 23.38 m.

Table 7 : Linac4 CCDTL modules.

	E_{out} [MeV]	G_{acc} [MV/m]	P_{RF} [MW]	length [m]	E_{max} [Kilp.]
1	57.1	4.00	0.96	2.64	1.6
2	64.6	4.10	1.0	2.82	1.6
3	72.1	4.20	1.0	2.98	1.6
4	79.9	4.30	1.0	3.14	1.7
5	87.8	4.23	1.0	3.29	1.7
6	95.6	4.16	1.0	3.43	1.6
7	102.9	4.10	1.0	3.57	1.6

2.9 PIMS

The high-energy section of Linac4, between 102 and 160 MeV, is made of a sequence of 12 seven-cell accelerating cavities of the Pi-Mode Structure (PIMS) type, resonating at 352 MHz. The PIMS (41) replaces a Side Coupled Linac (SCL), which was originally foreseen in the high energy section of Linac4 (28). The SCL was using a total of 468 cells (220 accelerating cells plus coupling cells) operating at 704 MHz to accelerate beam from 90 to 160 MeV, while the PIMS now covers 102 to 160 MeV using only 84 cells (12 cavities of 7 cells). Since the construction and tuning of pi-mode cavities is already well known at CERN, and since the SCL entails the use of 2 different RF frequencies in Linac4 it was decided to give preference to the PIMS (40) despite the $\approx 12\%$ lower shunt impedance (see Fig. 25). The basic design is a scaled (geometrically) version of the normal conducting LEP accelerating structure (56), which was then modified for higher cell-to-cell coupling.

The structure consists of discs and cylinders which are machined out of solid copper blocks. About 40% less copper is needed for the PIMS with respect to the SCL. Cooling channels are drilled from the outside into the discs, preventing any risk of water leaking into the vacuum of the cavity. After the brazing of tubes for RF pick-ups, power coupler and tuners onto the cylinders the structure will be electron-beam welded. The welded cavities are tuned by five fixed and two movable tuners to provide the necessary field flatness. Figure 26 shows a sketch of the foreseen 7-cell structure at 100MeV. The cells are coupled by two coupling slots, which are turned by 90 deg from cell to cell to minimize the 2nd neighbour coupling. A minimum coupling factor of 3%, which provides the same field stability as in the case of the 5-cell LEP cavities (1.5% coupling), is easily achieved.

The cell length is the same within a cavity, but changes from cavity to cavity according to the beam velocity profile. Compared to other structures used in this energy range, pi-mode cavities with a low number of cells have the advantage of simplified construction and tuning, compensating for the fact that the shunt impedance is about 10% lower because of the lower frequency. Field stability in steady state and in presence of transients is assured by the low number of cells and by the relatively high coupling factor of 5%. Standardizing the linac RF system to a single frequency is considered as an additional economical and operational advantage.

The accelerating gradient in the first 10 cavities has been adjusted to a relatively high value of 4 MV/m, resulting in a maximum power of about 1 MW per cavity. Using a high gradient limits the number of cells per cavity to 7, and thus makes it easier to obtain a flat field distribution. The last 2 cavities are used not only for acceleration but also for energy painting for injection into the subsequent Proton Synchrotron Booster (PSB). In order to achieve a high ramping speed in these

cavities (about 2 MeV/10 μ s), the nominal accelerating gradient was lowered to 3.1 MV/m. An overview of the main parameters is given in Table 8.

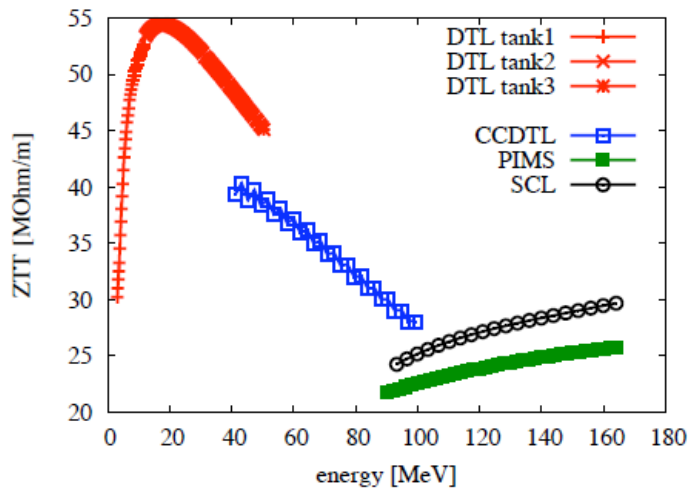


Figure 25 : Shunt impedance (ZT^2) for the Linac4 accelerating structures (80% of simulated values, including additional losses on stems, coupling holes, tuning rings).

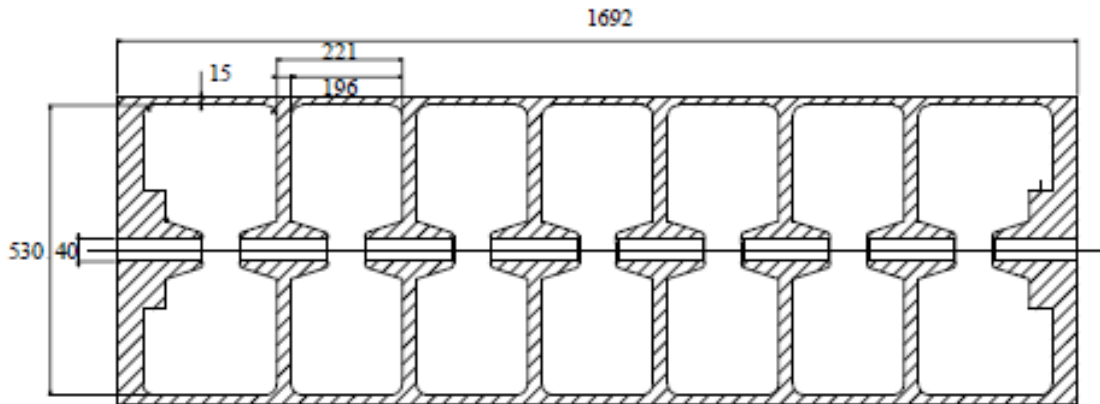


Figure 26 : 7-cell pi-mode structure.

Table 8: Main PIMS (57) parameters.

Parameter	value
Frequency	352.2 MHz
Input energy	102 MeV
Output energy	160 MeV
Electric gradient	4 MV/m
Peak power/cav.	1 MW
Max. surface field	1.8 Kilpatrick
Design duty cycle	10%
Max. expected d. c.	6%
Linac4 d. c.	0.1%
Cells/cavity	7
Number of cavities	12
Beam aperture	40 mm

3 Monte Carlo codes and analytical models

The radiation protection studies for Linac4 were carried out through a combination of Monte Carlo simulations and predictions made via analytical models. This chapter provides a description of the particle transport code FLUKA and its benchmarks, and of the analytical models commonly used for the evaluation of the radiation streaming through ducts and labyrinths. Section 3.1 describes the FLUKA code, its applications and the most relevant benchmarks reported in literature; Section 3.2 and 3.3 are original work of this thesis. Section 3.2 discusses the FLUKA simulations performed to test the capability of the code, in a proton therapy application, in predicting induced radioactivity from intermediate energy protons. Section 3.3 reviews the analytical models mostly used for the calculation of neutron streaming through penetration traversing shielding barriers, discusses the FLUKA simulations performed to test the reliability of these models and, on the basis of the simulations, derives a universal expression that can be used to estimate the neutron transmission through a straight duct in direct view of the source, model missing so far in the literature.

3.1 The FLUKA radiation transport code

The beginning of the FLUKA history (see (58)) is back to 1964 when Johannes Ranft started to develop Monte Carlo codes for high energy beams, as required at CERN for many accelerator-related tasks. The name FLUKA came around 1970, when first attempts were made to predict calorimeter fluctuations on an event-by-event basis (FLUKA = FLUctuating KAskades). The present code is mostly an effort started in 1990 in order to get a suitable tool for the LHC era, and has little or no remnants of older versions. The main link with the past is Johannes Ranft, mostly in the development of the high energy generator part. The code is in wide use at CERN and in other laboratories, and is *the* tool used for all radiation calculations and for the neutrino beam studies at CERN. It is the Monte Carlo code used in the ICARUS/ICANOE neutrino and rare event experiments, as well as for the spallation part of the Energy Amplifier studies (activities chaired by C. Rubbia).

The modern FLUKA [(17), (18) and (59)] is a general purpose tool for calculations of particle transport and interactions with matter, covering an extended range of applications spanning from proton and electron accelerator shielding to target design, calorimetry, activation, dosimetry, detector design, Accelerator Driven Systems, cosmic rays, neutrino physics, radiotherapy etc.

FLUKA can simulate with high accuracy the interaction and propagation in matter of about 60 different particles, including photons and electrons from 1 keV to thousands of TeV, neutrinos, muons of any energy, hadrons of energies up to 20 TeV (up to 10 PeV by linking FLUKA with the DPMJET code) and all the corresponding antiparticles, neutrons down to thermal energies and heavy ions. The program can also transport polarised photons (e.g., synchrotron radiation) and optical photons. Time evolution and tracking of emitted radiation from unstable residual nuclei can be performed online. FLUKA can handle even very complex geometries, using an improved version of the well-known Combinatorial Geometry (CG) package. The FLUKA CG has been designed to track correctly also charged particles (even in the presence of magnetic or electric fields). Various visualisation and debugging tools are also available. Another feature of FLUKA, probably not found in any other Monte Carlo program, is its double capability to be used in a biased mode as well as a fully analogue code. That means that while it can be used to predict fluctuations, signal coincidences and other correlated events, a wide choice of statistical techniques are also available to investigate punch through or other rare events in connection with attenuations by many orders of magnitude.

3.1.1 Electromagnetic and muon transport in FLUKA

For historical reasons, FLUKA is best known for its hadron event generators, but since more than 17 years it can handle with similar or better accuracy electromagnetic (e.m.) effects. Briefly, the energy range covered by this sector of FLUKA is very wide: the program can transport photons and electrons over about 12 energy decades, from 1 PeV down to 1 keV. The e.m. part is fully coupled with the hadron sector, including the low energy (i.e. < 20 MeV) neutrons. The simulation of the electromagnetic cascade in FLUKA is very accurate, including the Landau-Pomeranchuk-Migdal effect and a special treatment of the tip of the bremsstrahlung spectrum. Electron pairs and bremsstrahlung are sampled from the proper double differential energy-angular distributions improving the common practice of using average angles. In a similar way, the three-dimensional shape of the e.m. cascades is reproduced in detail by a rigorous sampling of correlated energy and angles in decay, scattering, and multiple Coulomb scattering. Recently, since the FLUKA2005.6 version, the need for an external cross section preprocessor has been eliminated, integrating all the needed functionalities into the initialization stage. At the same time, data from the EPDL97 (60) photon cross section library have become the source for pair production, photoelectric and total coherent cross-section tabulations, as well as for atomic form factor data. Bremsstrahlung and direct pair production by muons are modeled according to state-of-the-art theoretical description and have been checked against experimental data [(61), (62)]. Muon photonuclear interactions are also modeled.

3.1.2 Charged particle transport

Transport of charged particles is performed through an original Multiple Coulomb scattering algorithm (63), supplemented by an optional single scattering method. The treatment of ionization energy loss is based on a statistical approach alternative to the standard Landau and Vavilov ones that provides a very good reproduction of average ionization and of fluctuations (64). Multiple scattering with inclusion of nuclear form factors is applied also to heavy ion transport. Up-to-date effective charge parameterizations are employed, and straggling of ion energy loss is described in “normal” first Born approximation with inclusion of charge exchange effects.

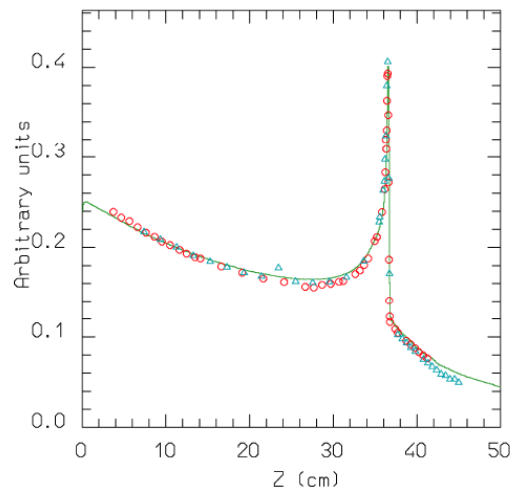


Figure 27 : Dose versus depth distribution for 670 MeV/n ^{20}Ne ions on a water phantom. The symbols represent LBL (circles) and GSI (triangles) experimental data (65), the line is the prediction of FLUKA including the new BME interface. For the profile reproduction at large depths, nuclear interactions below 100 MeV/n play an important role.

The precise determination of ion range and ionization losses is of utmost importance in dosimetry and in therapeutic applications. For this reason, FLUKA is being heavily benchmarked (66) against models and experimental data concerning ions beams of interest for hadrontherapy. In fig. 27 an example of very nice agreement between Bragg peak calculations and data is shown. The contribution of fragmented ions is also evident after the peak.

3.1.3 FLUKA hadronic models

A basic description of hadronic interactions in FLUKA and of their most recent developments can be found in [(67) and (68)]. Hadron-nucleon interactions at energies below a few GeV are simulated in FLUKA by the isobar model, through resonance production and decay, and by taking into account elastic, charge and strangeness exchange. Elementary hadron-hadron collisions at energies above a few GeV are described thanks to an implementation of the Dual Parton Model (DPM) (69), coupled to a hadronization scheme. This model allows a successful description of soft collision processes that cannot be addressed by perturbative QCD. Hadron-hadron collisions are the main building blocks of hadron-nucleus collisions. Multiple collisions of each hadron with the nuclear constituents are taken into account by means of the Glauber-Gribov calculus [(70) and (71)]. Particular efforts are devoted to the study of nuclear effects on hadron propagation. These are treated by the FLUKA nuclear interaction model called PEANUT [(72), (68) and (67)]. This model includes a Generalized IntraNuclear Cascade (GINC) with smooth transition to a pre-equilibrium stage performed with standard assumptions on exciton number or excitation energy. GINC modeling in PEANUT is highly sophisticated. Different nuclear densities are adopted for neutrons and protons, Fermi motion is defined locally including wave packet-like uncertainty smearing, the curvature of particle trajectories due to the nuclear potential is taken into account, binding energies are obtained from mass tables and updated after each particle emission, energy-momentum conservation including the recoil of the residual nucleus is ensured. Quantum effects are explicitly included: Pauli blocking, formation zone, nucleon anti-symmetrization, nucleon-nucleon hard-core correlations, coherence length.

The GINC step goes on until all nucleons are below a smooth threshold around 50 MeV, and all particles but nucleons (typically pions) have been emitted or absorbed. At the end of the GINC stage a few particles may have been emitted and the input configuration for the pre-equilibrium stage is characterized by the total number of protons and neutrons, by the number of particle-like excitons (nucleons excited above the Fermi level), and of hole-like excitons (holes created in the Fermi sea by the INC interactions), by the nucleus excitation energy and momentum. All the above quantities can be derived by proper counting of what occurred during the INC stage. For further details see ref. (67).

PEANUT has proved to be a precise and reliable tool for intermediate energy hadron-nucleus reactions. Its “nuclear environment” is also used in the modelization of (real and virtual) photonuclear reactions, neutrino interactions, nucleon decays, muon captures. Examples of PEANUT results on neutron production from low energy proton interactions are shown in fig. 28. These benchmarks are of high relevance for, for instance, calorimetry. Indeed, even in showers initiated by high energy projectiles, most of the interactions occur at medium-low energies, and the amount of visible energy depends critically on the energy balance and neutron balance in low energy reactions. Emission of energetic light fragments through the coalescence process is included all along the PEANUT reaction chain. This allows to reproduce the high energy tail of the light fragment spectra, as in fig. 29.

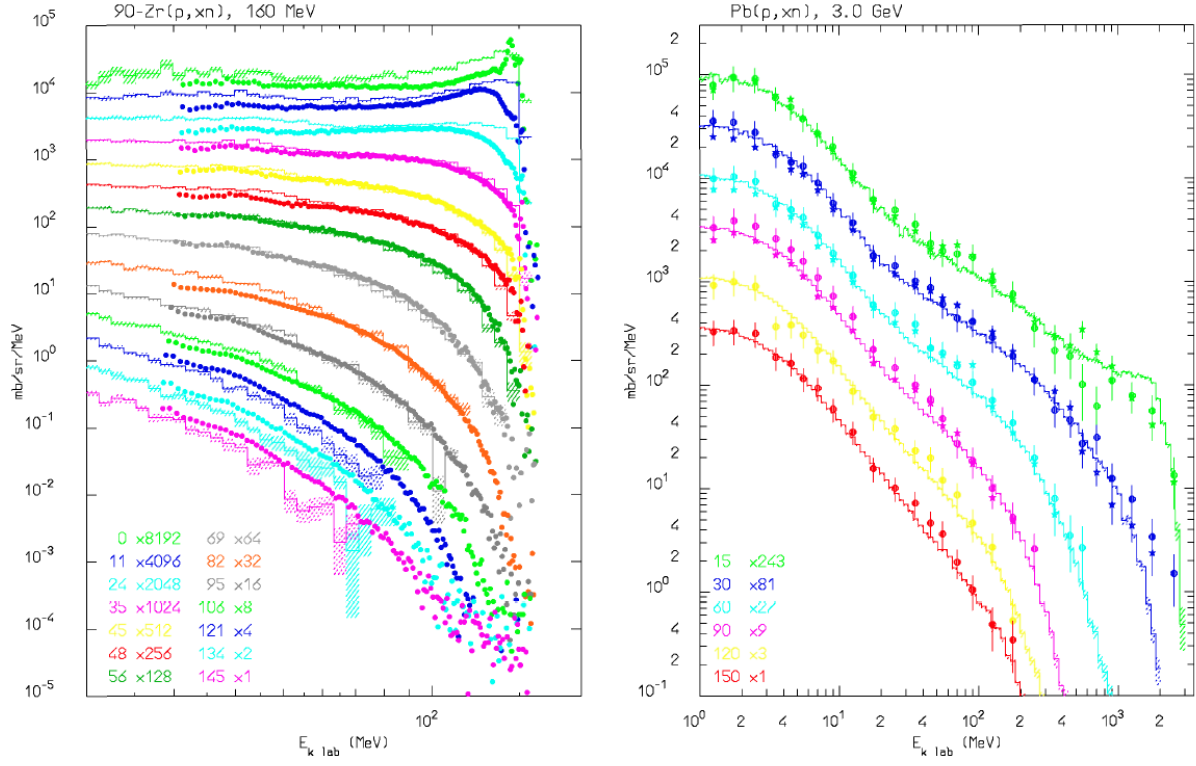


Figure 28 : Emitted neutron spectra at different angles, from 160 MeV protons on Zr (left) and 3 GeV protons on Pb (right). Histograms are FLUKA results, points are experimental data from [(73) and (74)].

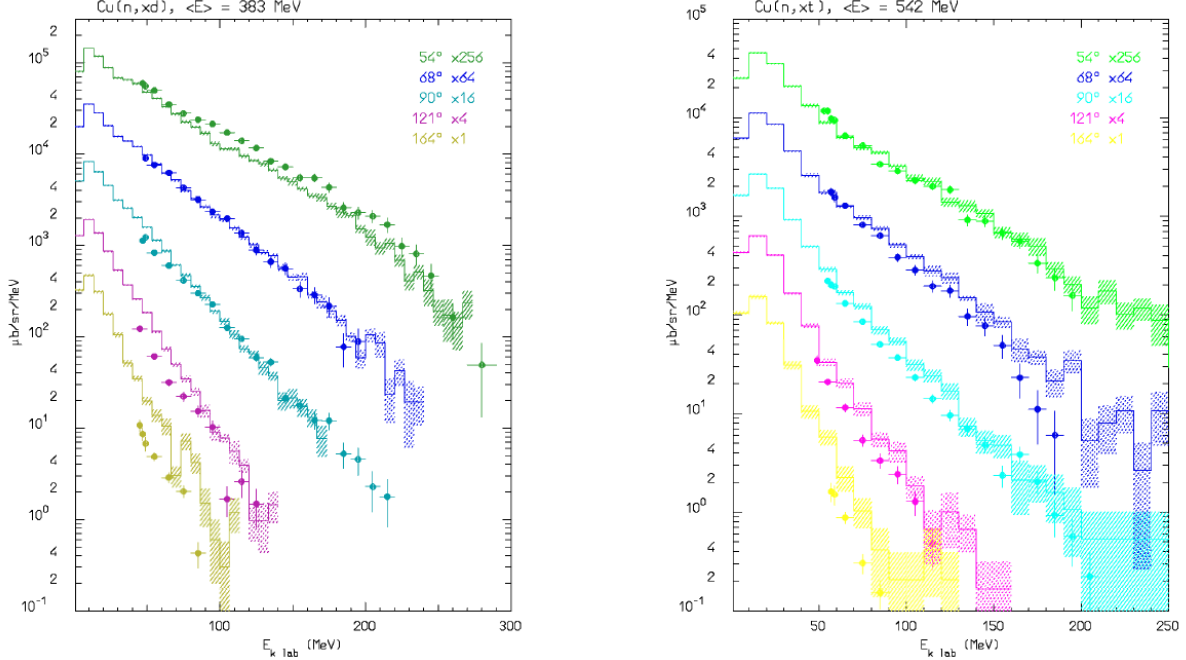


Figure 29 : Deuteron (left) and triton (right) emission from 383 MeV and 542 MeV neutrons on Cu respectively (exp data from (75))

The final steps of the reaction include evaporation in competition with fission and gamma deexcitation. For light nuclei, a Fermi break-up model is implemented. These equilibrium processes are critical for a correct calculation of residual nuclei distributions. This topic is obviously important for activation and residual dose rate studies, and it is also indirectly important for calorimetry: since the energy spent in breaking nuclear bonds is a major source of non-compensation and spread in

energy deposition, a correct reproduction of residual nuclei distribution is a proof that binding energy losses are correctly taken into account. The FLUKA evaporation model, which is based on the Weisskopf-Ewing approach, has been continuously updated along the years, with the inclusion, for instance, of sub-barrier emission, full level density formula, analytic solution of the emission widths, evaporation of nuclear fragments up to $A < 24$. Recent improvements in the treatment of fission and in the adopted level densities were particularly effective for the description of residual nuclei production from heavy targets. An example of the present code capabilities is shown in fig. 30.

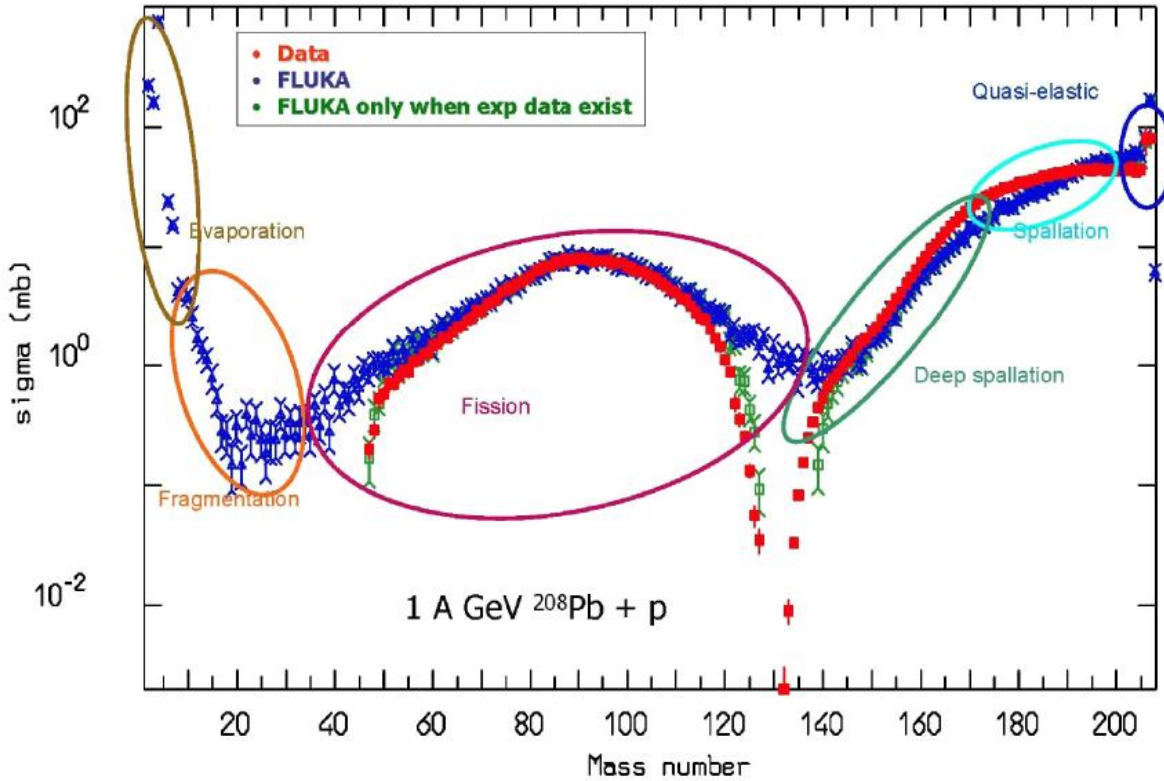


Figure 30 : Residual nuclei production from 1 GeV protons on lead. Data from (76).

More complex benchmarks have been carried out at the CERF (77) facility at CERN. The CERN-EU high energy reference field (CERF) Facility has been used for many years to investigate the performance of radiation detectors in mixed fields. It is well-characterized, for example, the structure of beam line and shielding is comparatively simple, and the source term is clearly defined. It is therefore suitable for benchmark studies outside hadron accelerator shielding. The CERF secondary radiation field is generated by a positively charged hadron beam consisting of a mixture of protons (34.8%), pions (60.7%) and kaons (4.5%) with a momentum of 120 GeV/c impacting on a 50 cm thick, 7 cm diameter copper target.

Teams of physicists from several countries are involved both in the measurements and in the intercomparison of their results with simulations. The agreement between the two appeared so convincing that the spectra calculated with FLUKA are considered as reference for the installation. Samples of different materials have also been irradiated in the mixed hadron field with broad energy spectrum of CERF. Comparison of experimental activation and dose rate curves with FLUKA simulations (78) show a very nice agreement, as for example in fig. 31.

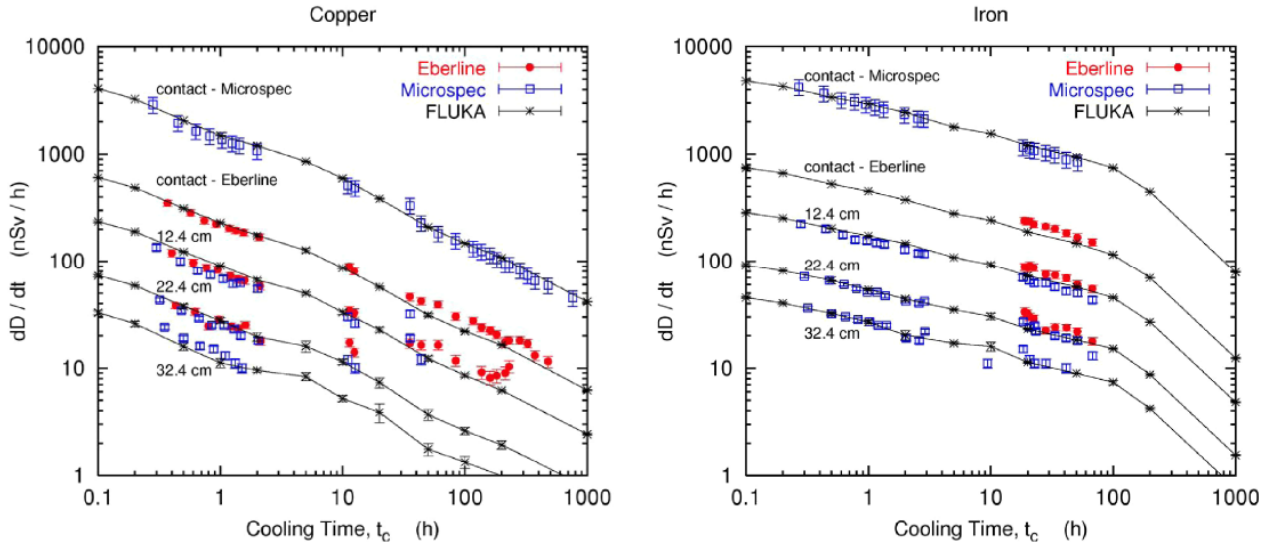


Figure 31 : Dose rate as a function of cooling time for different distances between sample and detector. Left: Copper sample. Right: iron sample, both irradiated at the CERF facility at CERN. Adapted from (78).

3.1.4 Shielding calculations and neutron transport description

The longitudinal and lateral development of the hadron cascades is an essential characteristic which must be correctly reproduced in order to obtain a result usable for shielding calculations, particularly if broad attenuation factors are involved. In several studies of lateral shield, after the entire development of the hadron cascade, neutrons represent the main component of the radiation field emerging from the shield. The neutron energy spectrum is an equilibrium spectrum with a shape that depends on the type of shielding and on the attenuation factor defined by that of the neutrons in an energy range between 50 and 200 MeV. FLUKA proved to be very powerful in reproducing, with a high degree of accuracy and in a very broad range in energy, the spectra of particles (particularly of the neutrons) emerging from the shield.

An example illustrating the capability of the code to predict correctly the space and energy distributions of the hadron flux, as well as the energy deposition profile can be found in (79), where the results of the code are compared with those obtained during the Rösti experiments. The objective of these experiments was the measurement of the longitudinal and radial profile of the hadron cascades induced by a beam of particles of 24 and 200 GeV interacting with an iron or lead structure, thanks to the use of various detectors with thresholds of reaction covering a broad range in energy. The profile of the energy deposition was also evaluated by means of RPL dosimeters. The capability of the code to describe the production and the transport of neutrons in heavy materials was also tested in a very satisfactory way during the FEAT (80) and TARC [(81) and (82)] experiments at CERN.

Few years ago, the transport of intermediate energy neutrons in concrete or iron shield was the topic of an international benchmark which concluded that FLUKA was the best code for this type of exercise (83). Probably the most revealing example of the capabilities of the code in the field of radiation protection is the comparison between calculations and the experimental results obtained over several years at CERN.

Examples of comparisons of measurements to the results of simulations can be found in [(84), (85), (86)]. A number even more significant of experimental data compared with the predictions of the code can be found in (87). During the experiments mentioned in [(84), (85) and (87)], FLUKA

was used not only to simulate the installation, but also to characterize the response function of the various apparatus used for the neutron detection.

3.1.5 Dosimetry

FLUKA has been widely tested in the field of dosimetry. FLUKA has been used for the calculation of the fluence-to-dose conversion coefficients for all the particles in a broad energy range [(88), (89), (90), (91), (92), (93) and (94)]. In recent times, the code has also been used (and compared with physical and radiobiological data from the PSI) in the attempt of merging physical and biophysical models in therapeutical applications and space problems [(95), (96) and (97)].

3.2 FLUKA Monte Carlo simulations and gamma spectrometry measurements of induced radioactivity in a patient-specific collimator used in proton therapy

FLUKA Monte Carlo simulations were performed to test the capability of the code in predicting induced radioactivity. A piece of a patient-specific collimator used at the MD Anderson Cancer Center (MDACC) in Houston, USA was supplied (see Fig. 32). The piece, which has been used for a prostate cancer treatment, is 22 cm × 22 cm wide and 2 cm thick. It was the most upstream section (closest to the nozzle) of three identical pieces, stacked together. The central aperture has the irregular shape shown in the figure, with approximate dimensions 6.5 cm × 7 cm. The piece received 0.91 Gy (1 CGE, Cobalt Gray Equivalent¹) per day for a total of 38 fractions, one fraction per day, at the rate of approximately 1.3 Gy per minute. The energy of the beam entering the nozzle was about 250 MeV. The beam size was 18 cm x 18 cm at isocentre, shaped in the terminal part of the nozzle about 20 cm upstream of the collimator. The piece was used over the period 22 January to 13 March 2008.



Figure 32 : The patient-specific collimator used for a prostate treatment at the MD Anderson Cancer Center in Houston. The piece (22 cm × 22 cm wide, 2 cm thick) is the upstream section of a unit made up of three identical pieces stacked together.

¹ The Cobalt Gray equivalent is the dose in Gy multiplied by the Relative Biological Effectiveness (1.1) for modulated protons relative to ⁶⁰Co radiation.

Eight samples were cut on one side of the collimator, from the central aperture to its edge (along the mid-plane on the right-end side of Figure 32). The first seven samples had about the same size, approximately 1 cm × 1 cm in transverse dimensions and 2 cm thick. As the last sample (the one closer to the edge) was considerably smaller than the others, the measurement results were affected by too large uncertainties and are therefore not reported here. The seven samples were analyzed at the Polytechnic of Milan by gamma spectrometry with an HPGe detector manufactured by EG&EG ORTEC, with 25% efficiency relative to 3" x 3" NaI and FWHM of 1.8 keV at 1.332 MeV, in a low-background cryostat, inside an OFHC shield. Data were acquired and processed with the Canberra Genie 2000 software. The energy calibration was 0.77 keV/ADC-channel and the lower and upper limits of energy spectrum were 35 keV and 3150 keV, respectively. The measurement time was about one day. The exact dimensions and mass of each sample and the measurement time per each sample are listed in Table 9. Sample no. 1 (the sample closest to the central aperture) was counted a second time 12 days after the first measurement.

Table 9 : Mass, dimensions and measurement time of each sample.

Sample number	Mass (g)	Dimensions (cm)	Measurement time (s)
1 (inner)	18.49	1 × 1.95 × 1.05	87041 / 360249
2	14.99	0.89 × 1.95 × 1.05	86000
3	15.78	0.89 × 1.95 × 1.05	93616
4	15.23	0.89 × 1.95 × 1.05	86000
5	15.58	0.89 × 1.95 × 1.05	84017
6	15.78	0.89 × 1.95 × 1.05	95156
7 (outer)	15.74	0.89 × 1.95 × 1.05	101553

The radionuclides that have been identified are listed in Table 10 along with the gamma emissions used for their identification. The samples were measured in contact with the detector, and the counting efficiency estimated assuming the radioactivity as uniformly distributed within the material. For calculating the self-absorption of the emitted photons, the following material composition was considered: 83% Cu, 7% Pb, 5% Sn and 5% Zn, with 8.91 g cm⁻³ density. The measured specific activity (activity per unit mass) of each radionuclide has been referred back to the date of 14 January 2009 (for a total decay time following the last irradiation of 307 days).

The simulations were performed with FLUKA (17), version 2008.3.7 (released on 25 September 2008). The collimator material is bearing bronze SAE 660 (98), with density $\rho = 8.9129$ g cm⁻³. The material composition is given in Table 11. The complete collimator made up of the three pieces was modelled in the simulations. The central aperture was represented as a rectangle with dimensions 6.6 cm × 7 cm, with area approximately equivalent to that of the real one (Figure 33).

Table 10 : Radionuclides identified by gamma spectrometry and their main photon emissions (99).

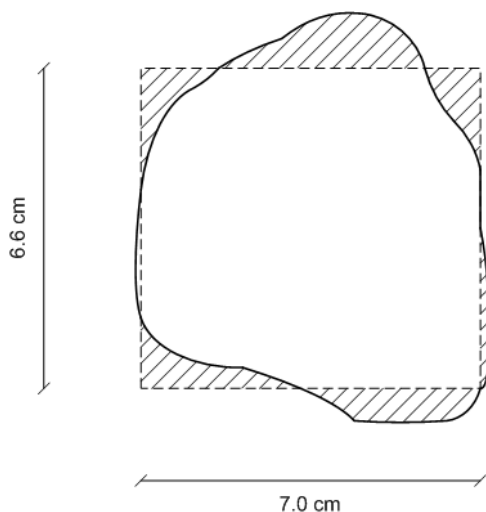
Radionuclide	$E\gamma$ (keV)	$T_{1/2}$ (d)	$I\gamma$ (%)
^{57}Co	122.06	271.79	85.60
^{58}Co	810.77	70.82	99.45
^{54}Mn	834.85	312.3	99.98
^{56}Co	846.78	77.27	99.94
^{113}Sn	391.70	115.09	64.0
^{65}Zn	1115.5	244.26	50.60
^{60}Co	1173.2 1332.5	1924.06	99.90 99.98

Table 11 : Material composition of bearing bronze SAE 660 (98) (percent by weight).

	Cu (a)	Al	Sb	Fe	Pb	Ni (b)	P	Si	S	Sn	Zn
min/max	81 – 85	0.005	0.35	0.20	6 – 8	1	0.15	0.005	0.08	6.3 – 7.5	1 – 4
Nominal	83.0	–	–	–	7.0	–	–	–	–	6.9	2.5

(a) In determining Cu min, Cu may be calculated as Cu + Ni

(b) Ni value includes Co. For the simulations 0.5 Ni + 0.5 Co has been used

**Figure 33 : Central aperture of the collimator: actual shape (see Figure 32) and how it was modelled in FLUKA (a rectangle with dimensions 6.6 cm x 7 cm). The shaded areas approximately compensate for each other. The right and top sides of the rectangle are at a distance of 7.5 cm and 7.9 cm from the right and top edges of the collimator, respectively.**

The seven samples measured by gamma spectrometry were modelled with identical dimensions of $1 \times 1 \times 2 \text{ cm}^3$ and an individual mass of 17.83 g. This mass value was used to normalize the activity of each scored radionuclide in order to obtain specific activity (Bq g^{-1}). The rest of the block has a mass of 7670.4 g, which was used to obtain the average specific activities in the bulk material.

The incoming beam was a monoenergetic proton beam with 200 MeV energy and flat transverse particle distribution over an 18 cm \times 18 cm area. The energy of the proton beam leaving the nozzle and impinging on the collimator was assumed to be 200 MeV to account for the energy degradation in the nozzle components of the original 250 MeV beam. This is a reasonable assumption as the range of 200 MeV protons in copper is 43 cm (62.5 cm for 250 MeV). In the plateau region the energy loss is anyhow rather constant and therefore the induced radioactivity does not depend much on the initial energy of the beam (see also the propagation of the proton fluence within the collimator as shown below).

An approximate and conservative estimate of the number of protons expected to hit a patient-specific collimator for a typical treatment of a deep-seated tumour was derived in ref. (100). The number of protons required to deliver a dose of 1 Gy in one litre volume was conservatively estimated at 2.1×10^{11} . A more precise albeit approximate algorithm is discussed in ref. (101), which would yield a more realistic figure in the range $0.6 - 1.4 \times 10^{11}$ according to the shape of the treatment volume. For the present simulations the figure of 2.1×10^{11} was used, scaled to the value required to deliver 0.91 Gy, as monitored by the MDACC dose monitor in the nozzle, and to the MDACC rate of 1.3 Gy per minute (see section 1). It is probably a conservative value for the actual beam intensity exiting the nozzle and striking the collimator. The irradiation profile (set with the IRRPROFI card of FLUKA) was thus made up of 38 daily irradiations each lasting 42 s and interspaced by 24 hours. The beam intensity impinging on the collimator was 4.5×10^9 protons per second.

Scoring of radionuclides (with the RESNUCLE card) in each of the seven samples and in the entire upstream piece, and of ambient dose equivalent rate $H^*(10)^2$ (with the DOSE-EQ option in the USRBIN card recently implemented in FLUKA) were done for a decay time of 307 days (defined with the DCYTIMES card) after the end of the last irradiation. The fluence of primary protons impinging on and exiting from the collimator and at 2 cm depth was also scored.

Thirty simulations were run, each with 1,000,000 primary protons, and the results are the average of the 30 runs. The statistical uncertainty on the values of specific activity is typically in the range 5% to 10%, except for a few cases as indicated in the next section. The statistical uncertainty on the fluence is around 2%, whilst on the dose rate is in the range 5% to 15%.

The proton fluences incident on the collimator, at 2 cm depth (i.e. emerging from the upstream piece) and exiting the collimator are plotted in Figures 34 – 36. One sees that the fluence remains practically constant in the first 2 cm (apart for a few scattered protons), whilst at the back only the protons going through the aperture survive. About 85% of the incoming beam is stopped by the collimator and only 15% goes through the central aperture.

The ambient dose equivalent rate, $H^*(10)$ along the central axis (cutting through the central aperture) of the collimator on its front face is shown in Figures 37 and 38. After more than 300 days

² The ambient dose equivalent, $H^*(d)$ is an operational quantity for area monitoring and is defined as the dose equivalent that would be produced by the corresponding expanded and aligned field in the ICRU sphere at the depth d , on the radius opposing the direction of the aligned field. The recommended value of d is 10 mm for penetrating radiation and 0.07 mm for low-penetrating radiation.

of decay, the residual dose rate has decreased to values largely below (about 1/10) the natural background radiation.

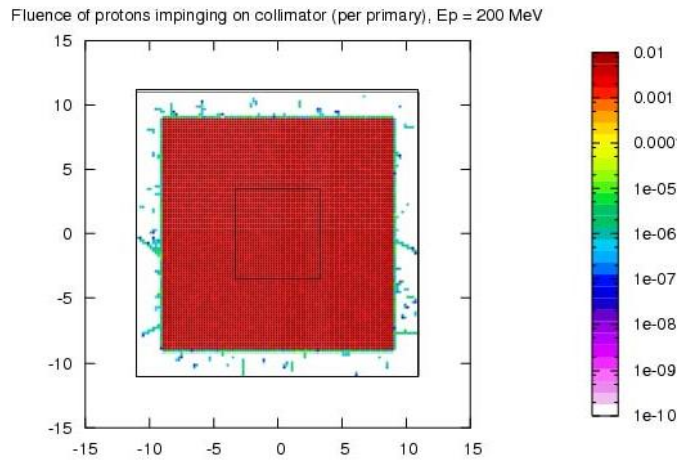


Figure 34 : Fluence of 200 MeV protons impinging on the collimator.

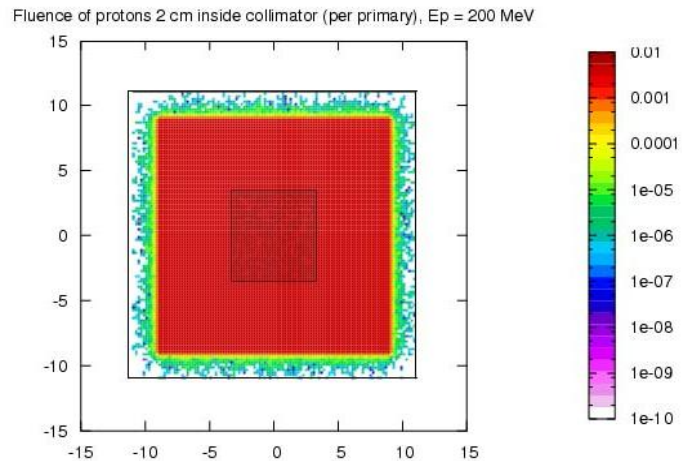


Figure 35 : Fluence of 200 MeV protons at a depth of 2 cm in the collimator.

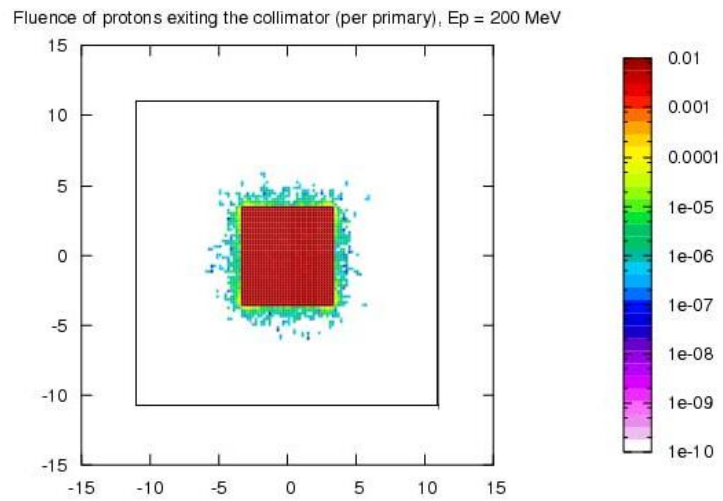


Figure 36 : Fluence of 200 MeV protons emerging from the collimator.

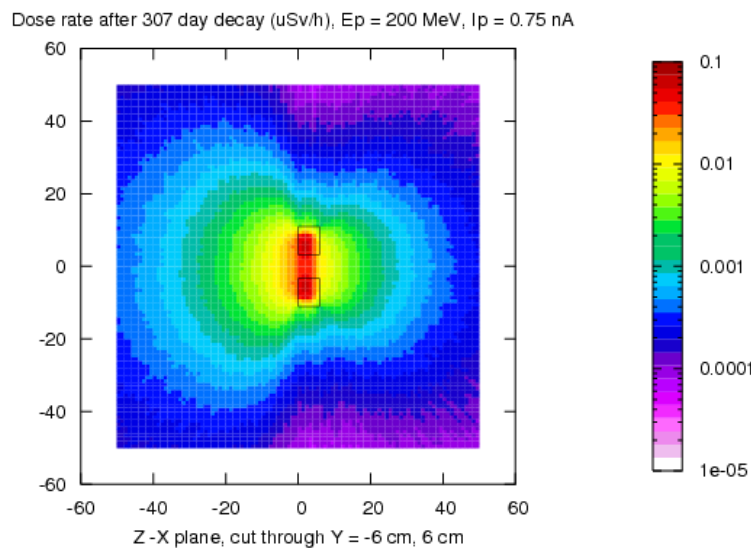


Figure 37 : Ambient dose equivalent rate, $H^*(10)$, along the central axis (Z-X plane) of the collimator. On the Y axis the $H^*(10)$ is integrated over the radius -6 cm to 6 cm cutting through the central aperture.

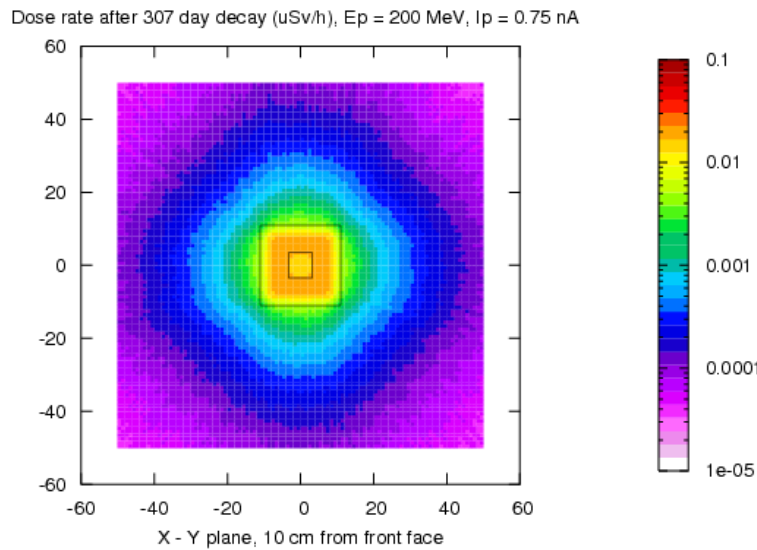


Figure 38 : Ambient dose equivalent rate at 1 cm from the entrance face of the collimator.

The results of the gamma spectrometry measurements are compared with the results of the Monte Carlo simulations in Table 12. The experimental results for sample no. 1 are those obtained with the longer measurement time (360249 s). The uncertainties associated to the experimental data include the error on the peak area as provided by the Genie2000 software and the error on the peak efficiency as determined by calibration sources. The uncertainties on I_γ and on sample mass are not considered. In sample no. 7 most of the identified radionuclides were close to or below the LLD.

Table 12 : Specific activity (in units of 10^{-3} Bq g $^{-1}$) of the seven samples measured by gamma spectrometry and calculated by Monte Carlo simulations. The last column gives the average value computed by Monte Carlo over the entire unit (mass of the samples excluded). LLD = lower limit of detection of the gamma spectrometry measurement. The three values for which the Monte Carlo uncertainties exceed 20% are in bold italics.

		Specific activity (mBq g $^{-1}$)							
		Sample number							Average
Radionuclide		1	2	3	4	5	6	7	
^{57}Co	Exp	116.4 \pm 11.6	128.5 \pm 13.2	121.9 \pm 12.5	127.7 \pm 13.1	126.3 \pm 13.0	130.9 \pm 13.4	30.4 \pm 3.7	
	MC	75.1 \pm 4.3	75.7 \pm 3.7	77.4 \pm 3.6	73.5 \pm 3.5	70.1 \pm 2.8	38.7 \pm 2.4	<1	47.2 \pm 0.1
^{113}Sn	Exp	5.2 \pm 0.5	4.3 \pm 1.2	5.5 \pm 1.5	3.7 \pm 1.0	4.5 \pm 1.2	3.9 \pm 1.1	< LLD	
	MC	5.7 \pm 0.8	5.6 \pm 0.8	6.9 \pm 1.1	5.4 \pm 0.9	6.1 \pm 1.0	2.4\pm0.5	–	3.4 \pm 0.03
^{58}Co	Exp	28.5 \pm 1.8	30.4 \pm 1.9	27.9 \pm 1.8	29.9 \pm 1.9	31.4 \pm 2.0	30.8 \pm 2.0	9.0 \pm 1.0	
	MC	27.6 \pm 1.2	24.2 \pm 1.0	26.2 \pm 1.4	29.3 \pm 1.4	26.9 \pm 1.6	13.1 \pm 0.9	<1	16.7 \pm 0.1
^{54}Mn	Exp	24.0 \pm 1.5	24.7 \pm 1.6	23.6 \pm 1.5	23.1 \pm 1.5	21.5 \pm 1.4	24.2 \pm 1.5	6.6 \pm 0.9	
	MC	30.2 \pm 1.9	23.6 \pm 2.4	33.0 \pm 2.1	31.0 \pm 2.3	27.3 \pm 2.1	14.6 \pm 1.5	<1	18.0 \pm 0.1
^{56}Co	Exp	6.7 \pm 0.5	7.2 \pm 1.0	6.2 \pm 0.9	8.8 \pm 1.2	8.6 \pm 1.2	7.1 \pm 1.0	< LLD	
	MC	12.5 \pm 1.0	11.4 \pm 0.9	13.1 \pm 0.9	12.2 \pm 0.8	11.7 \pm 0.9	5.9 \pm 0.6	–	7.7 \pm 0.04
^{65}Zn	Exp	18.0 \pm 2.0	19.5 \pm 2.1	20.7 \pm 2.3	17.1 \pm 1.9	21.4 \pm 2.4	19.3 \pm 2.1	10.3 \pm 1.6	
	MC	3.8\pm1.0	9.1 \pm 1.3	6.1 \pm 1.0	6.1 \pm 1.0	5.6 \pm 1.0	4.2\pm1.0	–	4.1 \pm 0.04
^{60}Co	Exp	6.9 \pm 0.7	6.3 \pm 0.9	6.7 \pm 0.9	6.9 \pm 0.9	8.1 \pm 1.1	6.9 \pm 0.9	< LLD	
	MC	4.5 \pm 0.4	4.6 \pm 0.5	4.7 \pm 0.5	4.8 \pm 0.6	3.8 \pm 0.4	2.6 \pm 0.3	<1	3.0 \pm 0.02

The statistical uncertainty of the Monte Carlo results is typically in the range 5% to 10%, except for a few cases listed below for which it exceeds about 15%:

sample 1, Zn-65: 25.3%; sample 2, Zn-65: 14.6%, Sn-113: 15.3%; sample 3, Zn-65: 17.0%, Sn-113: 15.2%; sample 4, Zn-65: 17.0%, Sn-113: 16.3%; sample 5, Zn-65: 17.4%, Sn-113: 15.8%; Sample 6: Zn-65: 23.5%, Sn-113: 22%.

The three values for which the Monte Carlo uncertainties exceed 20% are in bold italics in Table 12. In sample number 7 all radionuclides predicted in the other samples were either absent or present with a specific activity lower than 10^{-3} Bq g $^{-1}$.

A few additional radionuclides were predicted by the Monte Carlo simulations (Table 13) but were not identified by gamma spectrometry: ^3H is a pure β emitter, ^{55}Fe , ^{49}V and ^{109}Cd emit low energy photons (below the energy lower limit) and for ^{195}Au the LLD is $20 \cdot 10^{-3}$ Bq g $^{-1}$.

Table 13 : Radionuclides predicted by the Monte Carlo simulations but not identified by gamma spectrometry (in units of 10^{-3} Bq g $^{-1}$). The last column gives the average value computed by Monte Carlo over the entire unit (mass of the samples excluded). The eight values for which the uncertainties exceed 20% are in bold italics.

	Specific activity (mBq g $^{-1}$)							Average
	Sample number							
Radionuclide	1	2	3	4	5	6	7	
^{55}Fe	34.8 \pm 1.5	30.2 \pm 1.7	34.4 \pm 2.2	34.7 \pm 1.7	33.3 \pm 2.0	17.0 \pm 0.9	<1	20.9 \pm 0.1
^{49}V	10.1 \pm 1.2	12.7 \pm 1.3	11.1 \pm 1.4	10.3 \pm 1.4	12.1 \pm 1.3	6.7 \pm 1.1	–	7.3 \pm 0.05
^{109}Cd	2.7 \pm 0.5	2.3 ± 0.5	4.1 \pm 0.7	3.3 ± 0.7	3.6 ± 0.7	2.2 ± 0.6	–	2.1 \pm 0.03
^3H	7.8 \pm 0.4	7.4 \pm 0.4	7.4 \pm 0.4	8.7 \pm 0.4	7.3 \pm 0.4	3.9 \pm 0.3	<1	5.0 \pm 0.01
^{195}Au	4.3 \pm 0.7	2.6 ± 0.6	2.5 ± 0.8	3.2 \pm 0.6	3.2 ± 0.9	1.2 ± 0.4	–	2.1 \pm 0.03

The statistical uncertainties of the Monte Carlo results of Table 13 are also in the range 5% to 10%, except for a few cases listed below for which it exceeds 15%:

sample 1, Au-195: 16% ; sample 2, Au-195: 21.6%, Cd-109: 21.5% ; sample 3, Au-195: 31.7%, Cd-109: 16.1% ; sample 4, Au-195: 19.3%, Cd-109: 22.3% ; sample 5, Au-195: 27.8%, Cd-109: 20% ; sample 6, V-49: 16.3%, Au-195: 33.7%, Cd-109: 26.7%.

The eight values for which the uncertainties exceed 20% are in bold italics in Table 13.

The agreement between the results of the gamma spectrometry measurements and the Monte Carlo predictions is rather good, except for ^{65}Zn . This is explained by the fact that presently the FLUKA library does not include the cross sections for neutron activation on zinc below 20 MeV. In addition, two of the Monte Carlo values are affected by a statistical uncertainty larger than 20% and are therefore not much reliable. All radionuclides predicted by the simulations were detected by gamma spectrometry, except those which have low-energy photon emissions or are below the experimental LLD.

The simulation set-up was such that the first five samples were included in the irradiation field, only about half of the sixth sample was in the field, whilst the seventh sample was outside the field. This is clearly seen in the simulation results, where the specific activity of the sixth sample is approximately half of that of the first five samples, while the activity of the last sample is negligible. This is not seen with the gamma spectrometry, for which the specific activity for each radionuclide is similar in all samples, with the exception of the last one. This may be due to a slight misalignment of the beam.

Small variations between dimension and mass of the actual samples and their Monte Carlo modelling should not have a major influence on the results. The approximation introduced in the simulations by modelling the central aperture as a rectangle rather than using its real shape should also not introduce major uncertainties. The major source of uncertainty is probably the actual beam intensity hitting the collimator, as the number of protons per unit time was derived from the reading of a dose monitor upstream of the collimator. This uncertainty can be estimated to be up to 30%.

3.3 Prediction of transmission in ducts and labyrinths

Accelerator shielding is not limited to the calculation of barriers, but includes assessment of groundshine, skyshine and roof shielding, as well as design of ducts and mazes (labyrinths)

penetrating the shielding walls. Ducts and labyrinths serve as access path for control and power cables, ventilation pipes, waveguides for RF power, cooling and cryogenic lines, as well as for personnel and equipment access. At the same time they also represent a leakage path for radiation, especially neutrons, and must be properly designed in order not to compromise the shielding effectiveness of the barriers. Ducts and mazes can be very large: an example of an extreme case is represented by the access shafts leading to the underground areas of the Large Hadron Collider (LHC) of CERN, which are up to 20 m in diameter and more than 100 m in depth. Monte Carlo simulations are the best tool for calculating radiation streaming through ducts and labyrinths. However, the design of labyrinths with right-angle bends (curved tunnels are less common and are not addressed in this paper) can often be performed to a sufficient level of accuracy by simple analytical expressions or so-called universal transmission curves. Nonetheless, whereas the simple models available in the literature often provide sufficiently accurate results for cases in which the radiation source is not in direct view of the duct mouth, this is not the case for point-sources located in front of the mouth. This paper compares results from Monte Carlo simulations and from analytical expressions available in the literature for a number of practical cases. The aim is to confirm the suitability of the simple models for plane sources and point sources off-axis, and to propose a better expression for estimating the attenuation for neutrons sources located in direct view of the duct mouth.

3.3.1 *Analytical models*

Universal transmission curves are so-called as the depth in a duct or in a maze leg d , is normalized to its cross-sectional area A , and thus expressed as a function of $d/A^{1/2}$. They were obtained in the 1970's with the aim to evaluate the dose rates due to neutron leakage through the access tunnels of the CERN Super Proton Synchrotron (SPS) and other similar access ways to the experimental areas [(102) and (103)]. The tunnel penetration was estimated using the codes SAM-CE (104), AMC (105) and ZEUS (106) and experimental data were used both to check the results of the computations and for extrapolating directly to tunnels of roughly similar dimensions.

A parametric form of the transmission curves has later been derived by Stevenson and Fassò (107) for the case of an off-axis source, to facilitate pocket-calculator estimations. The transmission T in the first and second leg is given by:

$$T = 1 / (1 + 2.5 D^{1/2} + 0.17D^{1.7} + 0.79D^3) \quad (33)$$

and

$$T = 1 / [1 + 2.8 D (1.57)^{d+2}] \quad (34)$$

where $D = d/A^{1/2}$.

Tesch (108) has developed a very simple approach to the problem of dose equivalent rate attenuation by multi-legged labyrinths at proton accelerators that are typical of personnel passageways of approximately 2 m^2 cross section. Based on experimental data for the transmission of Am-Be neutrons in concrete-lined labyrinths, and on the similarity between the neutron spectra in the second leg of a labyrinth from either an Am-Be source and from high-energy protons stopped in a target, he proposed an empirical formula for describing the transmission of the dose-equivalent. The equation for the first leg (as presented in ref. (1)) is an inverse-square law, modified by a simple in-scattering factor of two, in the section of the labyrinth in direct view of the source:

$$H(r_1) = 2H_0(a)a^2r_1^{-2} \quad (35)$$

where $H(r_1)$ is the dose equivalent, in the first leg, at a distance r_1 from the source, a is the distance from the source to the mouth of the first leg and $H_0(a)$ is the dose equivalent at the mouth of the first leg. This formula does not accommodate the expected scaling with the square root of the tunnel aperture and is best used for labyrinths with relatively large cross-sectional areas (about 2 m^2) used for personnel access. The expression for the succeeding legs is the sum of two exponentials:

$$H(r_i) = \left(\frac{e^{-r_i/0.45} + 0.022 A_i^{1.3} e^{-r_i/2.35}}{1 + 0.022 A_i^{1.3}} \right) H_{oi} \quad (36)$$

in which r_i is the distance into the i th leg in meters, H_{oi} is the dose equivalent at the entrance of the i th leg and A_i is the cross-sectional area of the maze in m^2 .

NCRP Report 51 (109) provides guidelines for designing ducts and labyrinths for proton accelerators of energies below 100 MeV, using an empirical and conservative approach based on the work of Maerker and Muckenthaler [(110) and (111)] built on the use of the albedo concept, where the reflecting properties of the concrete are determined in great detail. In practice, for a multi-legged maze it is assumed that beyond the second leg all neutrons at the entrance of the duct have thermal energies. Transmission factors are given for thermal neutrons through a straight duct and for two- and three-legged ducts, from which one can calculate the dose equivalent at the exit once the neutron fluence rate incident on the inner aperture of the maze is known.

Gollon and Awschalom (112) have reported a number of Monte Carlo calculations of the attenuation of the neutron fluence in labyrinths using the albedo program ZEUS (106). In this program monoenergetic neutrons (3 or 4 MeV) were scattered at random angles from the walls of "typical" labyrinths using the albedo parameters of Maerker and Muckenthaler [(110) and (113)]. The calculations were used for a three-legged labyrinth and the calculated labyrinth attenuation resulted to be insensitive to the neutron energy.

Cossairt et al. (114) made measurements at the Tevatron at Fermilab in a four-legged labyrinth. The labyrinth gave access to the accelerator tunnel in which 400 GeV protons struck an aluminum target located in front of the mouth of the first leg, which was perpendicular to the beam direction. In ref. (115), the experimental measurement of ref. (114) were compared with calculations based on the work of Goebel (102), Gollon and Awschalom (112) and Tesch (108). The calculated transmission curves are in fair agreement with the measured data. Neutron spectral measurements also showed that the spectrum in the second leg of the labyrinth is dominated by thermal neutrons.

A good summary of calculations and measurements of the transmission of neutrons through ducts and labyrinths at higher energy accelerator can be found in refs. [(1) and (103)]. According to several experiments most of the dose equivalent transmitted is due to 1 – 20 MeV source neutrons. If the tunnel is to be designed from known or expected beam losses, instead of a defined dose equivalent rate at the tunnel entrance, one has to determine the neutron yield in the 1 – 20 MeV range from the effective source. This yield may then be converted to dose equivalent using appropriate conversion coefficients. When a point source is in full view of the back end of the duct, a simple inverse square law can be used to determine the neutron fluence at the duct exit. An appropriate coefficient to convert the apparent neutron fluence to dose equivalent is 20 fSv m^2 (103). It should nonetheless be stressed that the $1/r^2$ law for the attenuation of neutrons from a point-source in front of a duct is only approximately true. How close it is actually followed also

depends on the scattering material around the source (the beam loss point), e.g. the presence of nearby or back walls, and on the cross-sectional area of the duct, as it will be shown below.

The geometric and angular distribution of the neutrons source and its position with respect to the maze mouth, considerably affect the attenuation factor provided by the first leg of the maze. However, after the first bend the neutrons essentially lose “memory” of their original spectrum. For the second and subsequent legs of a labyrinth the position of the source (plane or point off-axis, linear or point on-axis) is no longer relevant. This reflects into a single universal curve (ref. (103), figure 4.39 on page 276). The energy of the proton beam causing the neutron emission is also not much relevant when considering the attenuation provided by the second and subsequent legs of the maze, especially for emission at 90 degrees.

The latest generation of Monte Carlo codes allows fast and accurate calculation of particle transport and interaction with matter. In this paper the reliability of the analytical or semi-empirical curves of Goebel et al. [(102) and (103)] and Tesch (108) was tested through comparisons with simulations made with the latest version (2006.3b, March 2007) of the particle transport code FLUKA [(17) and (59)]. The accuracy of this code for radiation protection applications and in particular for shielding design has been demonstrated through several benchmarks (see, for examples, refs. [(59) and (116)]).

3.3.2 Comparison of Monte Carlo simulations with the universal curves

The recent radiation protection studies performed for Linac4 required designing various types of penetrations for RF waveguides, cables and ventilation pipes. These penetrations were partly designed by Monte Carlo simulations with the FLUKA code [(17) and (59)] and partly with the universal curves of refs. [(102) and (103)]. These studies were subsequently extended and employed for a detailed comparison of the attenuation provided by these curves and the Monte Carlo predictions, for point and plane or point off-axis sources, which is the aim of this section of the thesis. More details on this comparison can be found in ref. (117).

Plane or point off-axis source

Three configurations were investigated: a single, straight duct made of four sections of variable size and shape (rectangular and circular), and two types of three-legged labyrinths. The duct geometries as implemented in the FLUKA simulations are shown in Figures 39 – 41 taken from (118) and are described in Tables 14 – 16. The first configuration (Figures 39 and 42 and Table 14), which we call low-energy waveguide duct, is for housing the 3 MeV waveguides for the RFQ (Radio Frequency Quadrupole): the neutron source was generated by a 11 MeV proton beam lost on a $5 \times 5 \times 5 \text{ cm}^3$ copper block placed 2.65 m downstream of the mouth of the duct and 3.8 m off-axis. The second configuration (Figures 40 and 43 and Table 15) is a labyrinth housing the ventilation duct at the high-energy end of the linac. Here neutrons were produced by a 160 MeV proton beam lost on a $5 \times 5 \times 5 \text{ cm}^3$ copper block placed 5.35 m upstream of the mouth of the maze and 80 cm off-axis. The third configuration (Figure 41 and Table 16, see also ref. (118)) is a maze for housing the waveguides at the high-energy end of the linac. The neutron source was generated by 160 MeV protons lost on a $5 \times 5 \times 5 \text{ cm}^3$ copper block placed at the same longitudinal distance in the tunnel as the maze mouth, but 1.8 m off-axis. Importance biasing techniques were used to improve the transport of the neutrons through the three legs of the labyrinths and to kill those crossing the bulk shield in order to save computing time (see (118) for more details).

Figures 39 – 41 plot the neutron transport through the ducts and labyrinths as simulated by FLUKA. The value of the ambient dose equivalent rate from the FLUKA simulations at the mouth of the ducts was used as source value for estimating the attenuation provided by the duct and labyrinths via the universal transmission curves of Goebel et al. (see ref. (103), figures 4.38 on page 274 and 4.39 on page 276). The transmission curve for the first leg of a labyrinth, for a plane (or point off-axis) source was used for the four sections of the low-energy waveguide duct. Figure 44 compares the transmission calculated with the universal curves and the FLUKA simulations, as a function of the total normalized distance in the duct. For the three-legged configurations, the transmission curves for the first (plane source model) and the subsequent legs were used. The comparison between universal curves and Monte Carlo simulations is shown in Figures 45 and 46. In all cases the agreement between simple model and Monte Carlo simulations is rather good.

Table 14 : Layout of the low-energy waveguide ducts.

Section of the duct	Length
Rectangular (30 cm x 70 cm)	0 - 50 cm
Cylindrical with diameter of 85 cm	50 - 250 cm
Rectangular (30 cm x 70 cm)	250 - 720 cm
Rectangular (40 cm x 70 cm)	720 - 750 cm

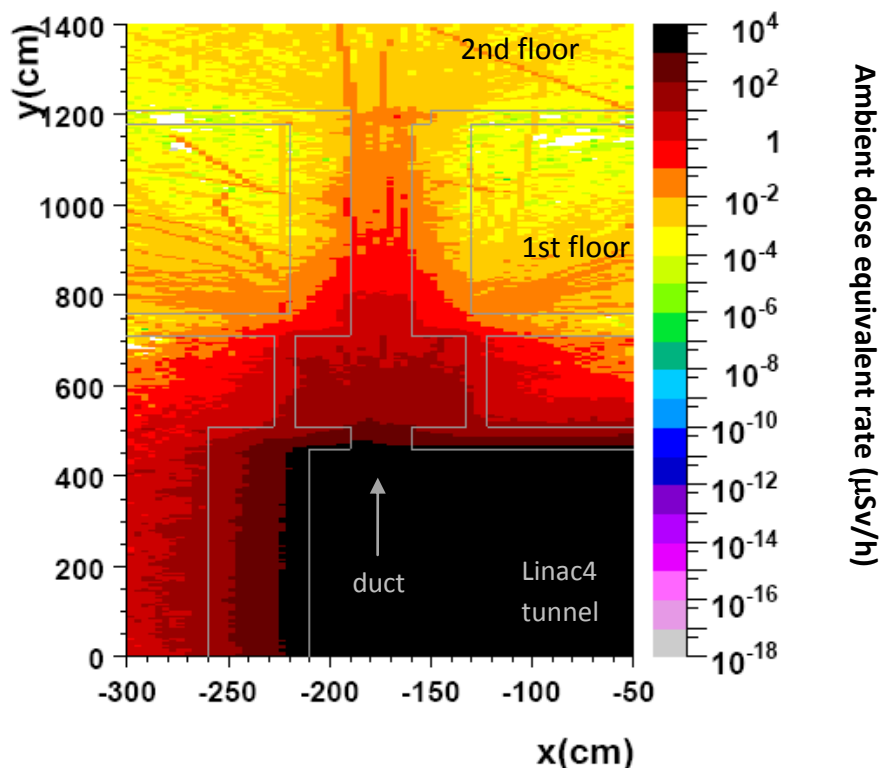


Figure 39 : Neutron streaming through the low-energy waveguide duct (see Table 14) calculated with FLUKA.

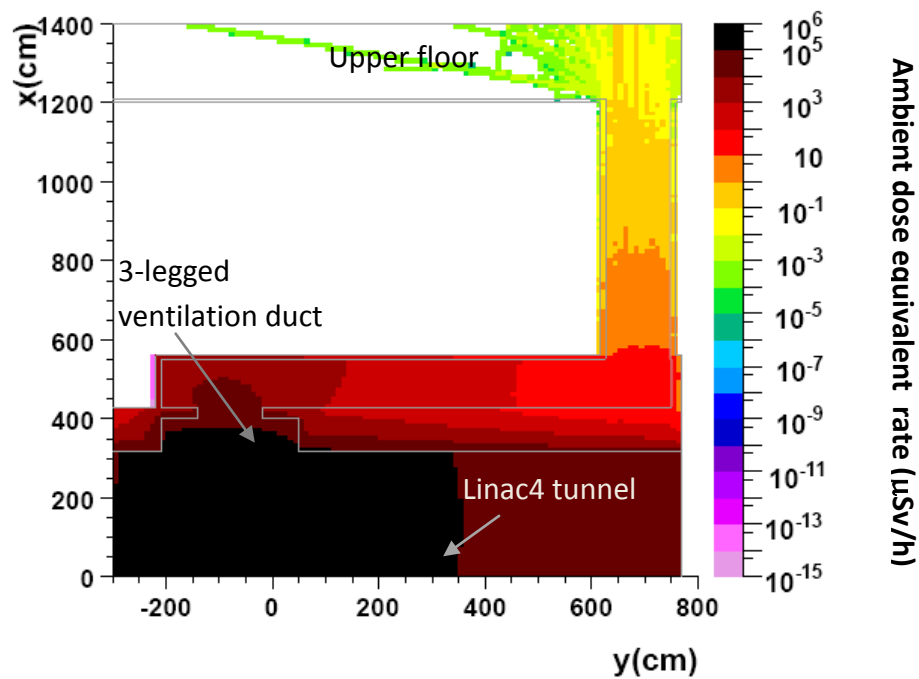


Figure 40 : Neutron streaming through the ventilation ducts (see Table 15) calculated with FLUKA.

Table 15 : Layout of the ventilation duct.

	Section	Length
First leg (vertical)	Circular with diameter of 125 cm	0.2 m
Second leg (horizontal)	Squared with a side of 120 cm	7.67 m
Third leg (vertical)	Circular with diameter of 125 cm	7.2 m

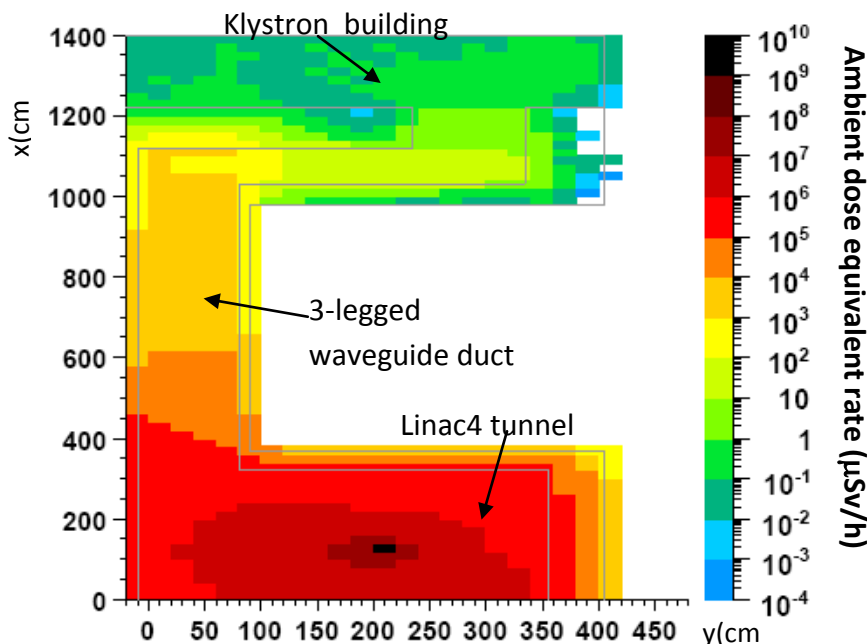


Figure 41 : Neutron streaming through the high-energy waveguide ducts (see Table 16) calculated with FLUKA.

Table 16 : Layout of the high-energy waveguide ducts.

	Section (cm ²)	Length (cm)
First leg (vertical)	90 x 90	755
Second leg (horizontal)	90 x 90	250
Third leg (vertical)	100 x 90	145

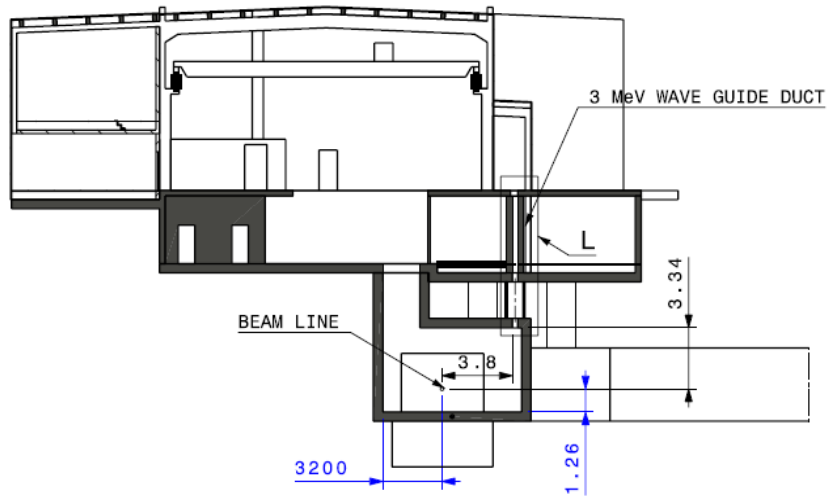


Figure 42 : Cross sectional view of the low-energy end of the Linac4 tunnel, the 3 MeV waveguide duct and the two upper floors (looking downstream in the tunnel).

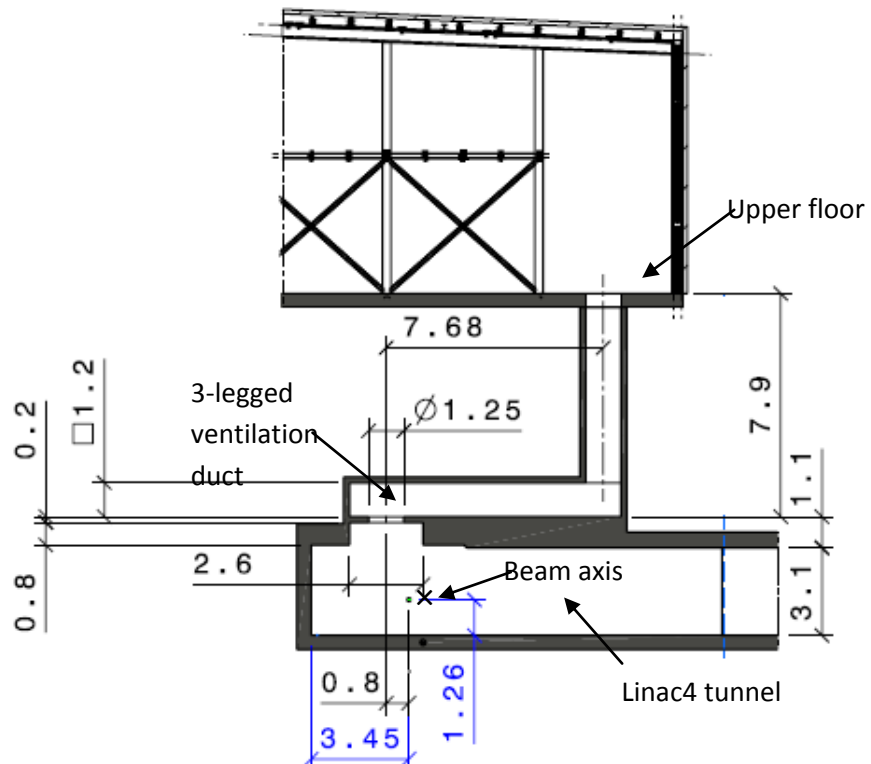


Figure 43 : Cross sectional view of the Linac4 tunnel, the three-legged ventilation duct and the ventilation building on top.

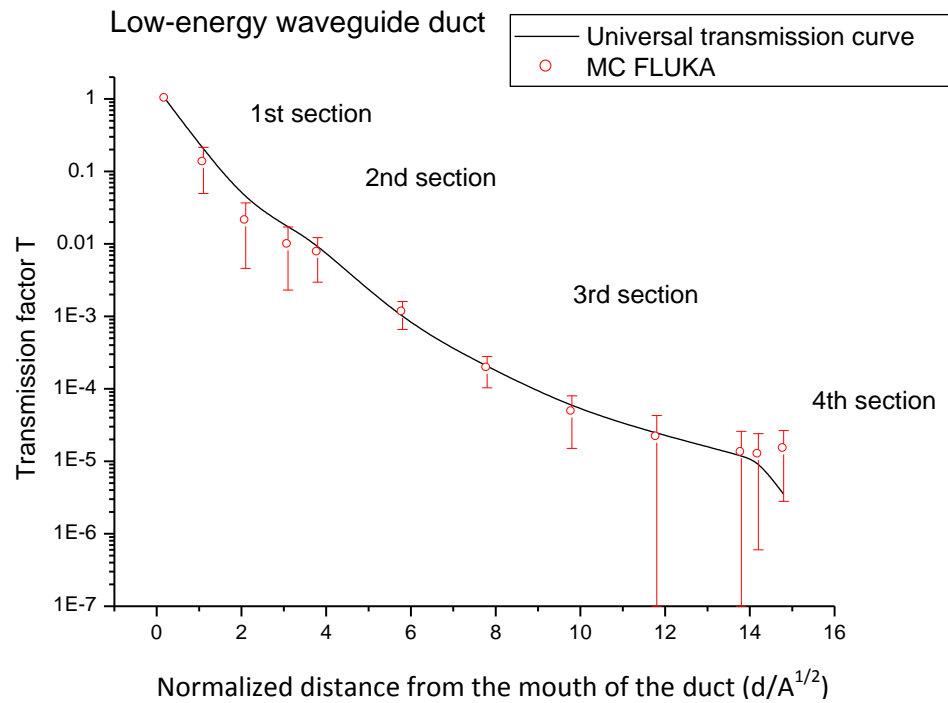


Figure 44 : Transmission of neutrons through a straight duct made of four sections of variable size, calculated with the universal transmission curve of refs. [(102) and (103)] and by Monte Carlo simulations (see Table 14 and Figure 39).

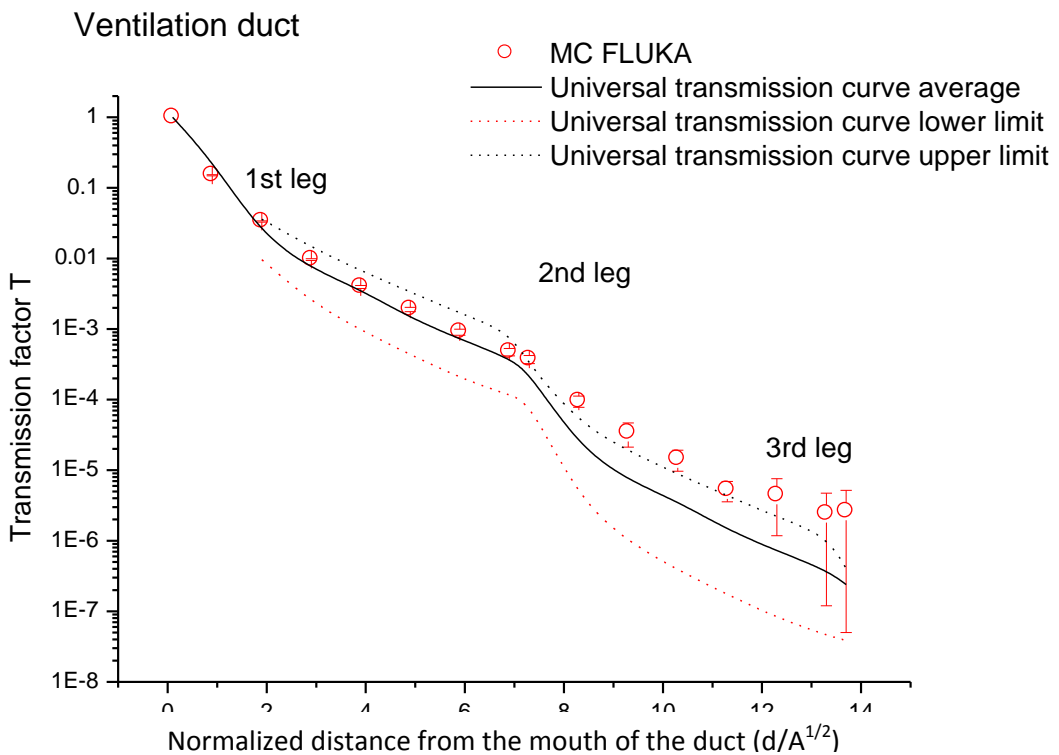


Figure 45 : Transmission of neutrons through a three-legged labyrinth (Table 15 and Figure 40) calculated with the universal transmission curve of refs. [(102) and (103)] and by Monte Carlo simulations.

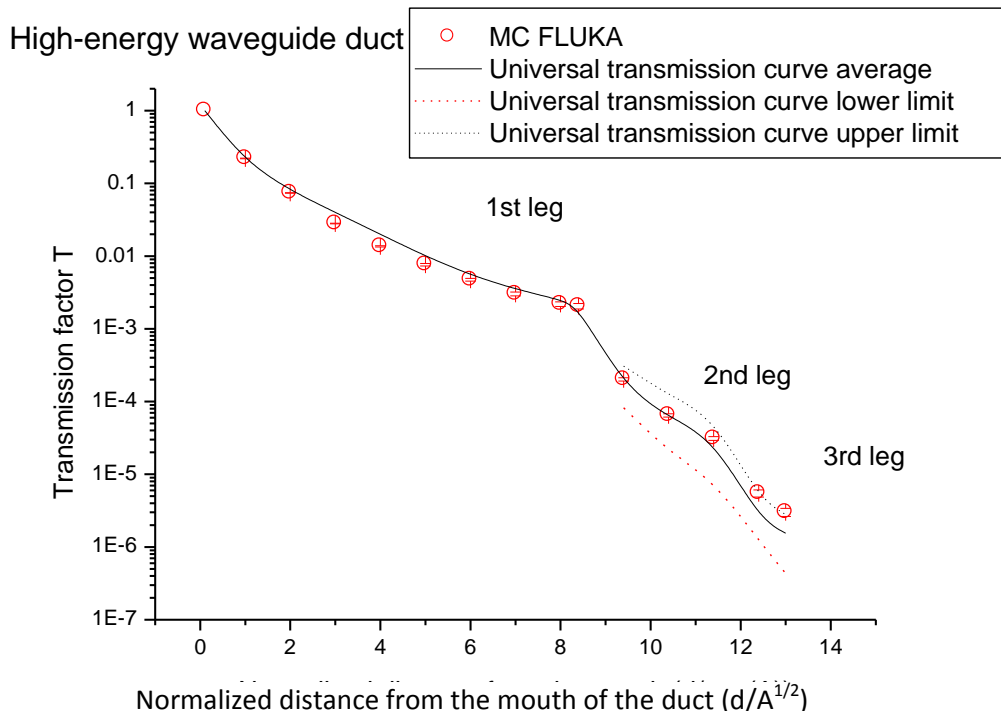


Figure 46 : Transmission of neutrons through a three-legged labyrinth (Table 16 and Figure 41) calculated with the universal transmission curve of refs. [(102) and (103)] and by Monte Carlo simulations.

The same universal curves are also appropriate for much larger ducts. An example is the attenuation of neutrons generated by high-energy electrons and positrons by one of the access shafts of the former CERN Electron Positron Collider (LEP). Figure 47 from ref. (119) shows the attenuation of neutron radiation in the LEP PM18 shaft (80 m deep and 14 m in diameter, $\max d/A^{1/2} = 6.5$) determined experimentally at three LEP energies (94.5, 100 and 103 GeV). PM18 was located on top of the positron injection region, where neutrons were produced by beam losses on the injection components. The dose attenuation measurements were performed with bubble detectors (model BD PND from Bubble Technology Industries, Chalk River, Ontario, Canada) suspended on the shaft axis, from the surface all the way down to the bottom. The experimental values are compared with the transmission curves for a neutron plane source and a neutron line source. The latter better seems to fit the experimental data, which is coherent with the beam loss scheme. The beam losses at injection remained constant over the years, as shown by the relative similarity of the data points at the three energies.

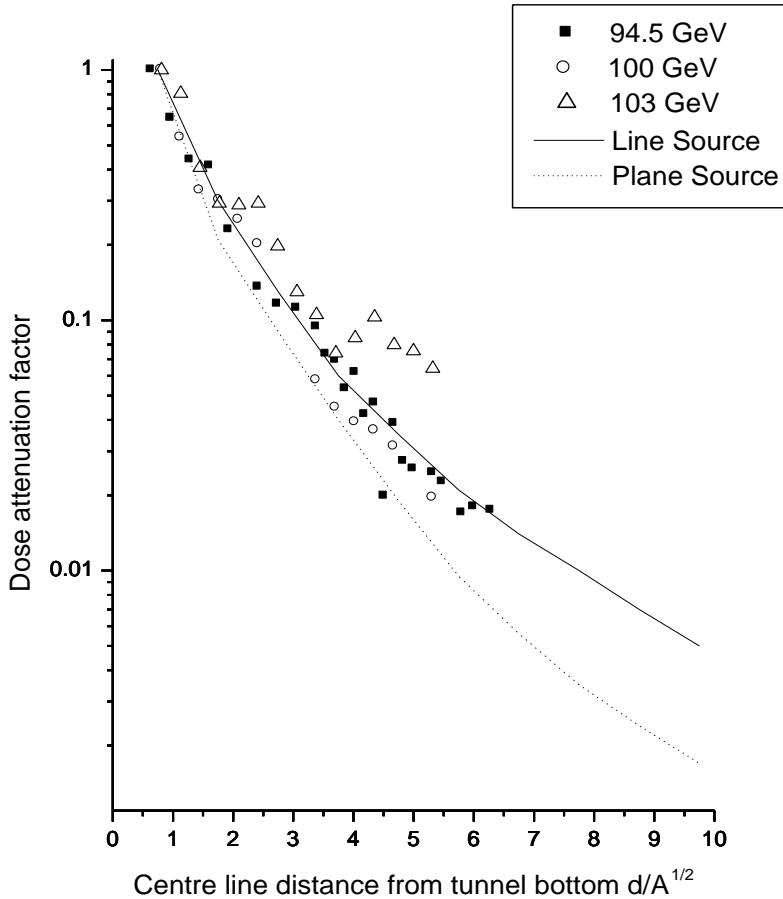


Figure 47 : Attenuation of neutron radiation in the access shaft PM18 (14 m in diameter and 80 m in depth) of the CERN Large Electron Positron collider (LEP) measured at three electron beam energies (94.5, 100 and 103 GeV per beam); d is the distance from the bottom end of the pit and A is the cross sectional area of the pit. The uncertainty on the measurements is $\pm 30\%$. The attenuation for a neutron plane source and a neutron line source is shown for comparison (from ref. (119)).

Point source

A point source on-axis, i.e. a localized beam loss in direct view of the duct aperture, represents a worst case and, although it may be less of a common situation than the previous case, it must also be considered. The results of Monte Carlo simulations of the propagation of neutrons through a long duct were compared with predictions made by the model of Tesch (108) and Goebel et al. [(102) and (103)].

First, the dependence of the transmission factor on the shape of the cross-sectional area of the duct and on the energy of the protons impinging on the neutron-production target was investigated. For the former study, a 160 MeV proton beam hit a cylindrical copper target (5 cm long and 5 cm in radius) placed at 2 m distance from the duct, with the beam direction perpendicular to the duct. For the same cross-sectional area (1 m^2) a circular and a squared aperture were considered, scoring the ambient dose equivalent rate along the duct. The transmission factor as a function of the normalized distance inside the duct is plotted in Figure 48. There is no appreciable difference between the two curves. The present result is in agreement with older calculations made, with a

different code, by Gollon and Awschalom (112), who estimated the attenuation of the neutron fluence by straight ducts with the same cross-sectional area and different aspect ratio.

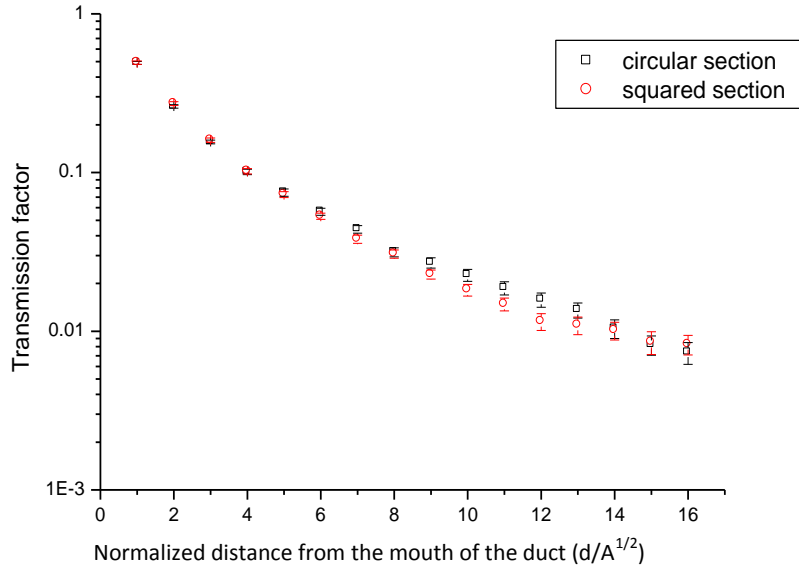


Figure 48 : Transmission factor as a function of normalized distance in ducts with the same cross-sectional area and different shape.

Keeping constant the shape of the duct, Monte Carlo simulations were then performed at three proton energies (50, 160 and 300 MeV). The proton beam hit a cylindrical copper target (5 cm in radius, 5 cm long for 50 and 160 MeV, 10 cm long for 300 MeV) placed at 2 m distance from the mouth of the duct. Figure 49 shows the transmission factor as a function of the normalized distance inside the duct for the three proton energies. Again the curves show no appreciable difference, confirming that the energy of the proton beam has no major influence on the attenuation of the secondary neutrons in the duct, as mentioned above.

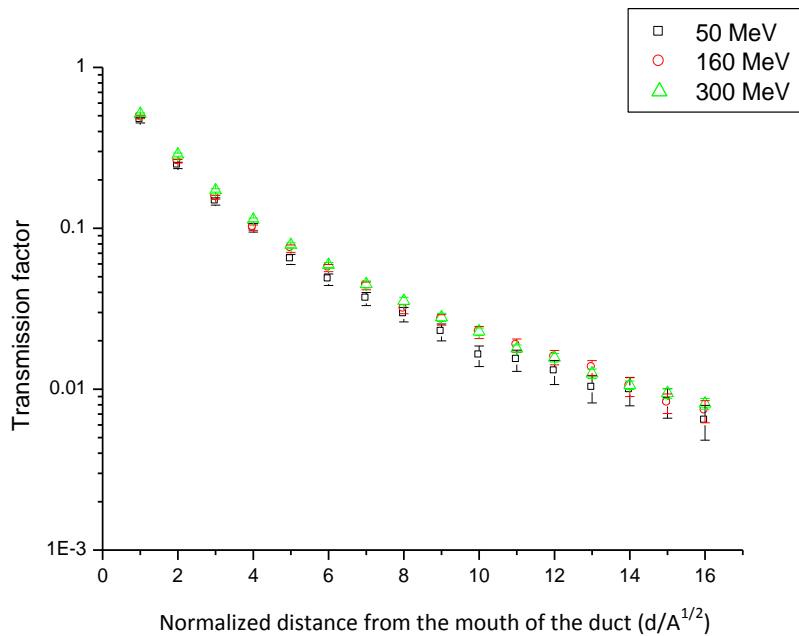


Figure 49 : Attenuation by a straight duct of neutrons produced by proton beams of different energy.

Finally, FLUKA simulations were performed to estimate the attenuation of the ambient dose equivalent rate inside circular ducts of different size (Table 17), representative of typical situations

found in radiation protection. A localized loss was assumed in front of the mouth of the duct. The comparison among the transmission factors for the five ducts as predicted by the FLUKA simulations, evaluated by the universal curves for a point source of ref. (103), by the inverse-square law and by the equation proposed by Tesch (108) is shown in Figure 50.

Table 17 : Typical cross-sectional area for circular ducts and mazes according to their use.

Cross-section (m ²)	A ^{1/2} (m)	Diameter (cm)	Use
0.07	0.26	30	Cables, cooling, cryogenics
0.28	0.53	60	RF waveguides, cooling, cryogenics
1	1.0	110	RF waveguides, ventilation
4	2.0	225	Access of personnel and services
9	3.0	340	Access of personnel and equipment

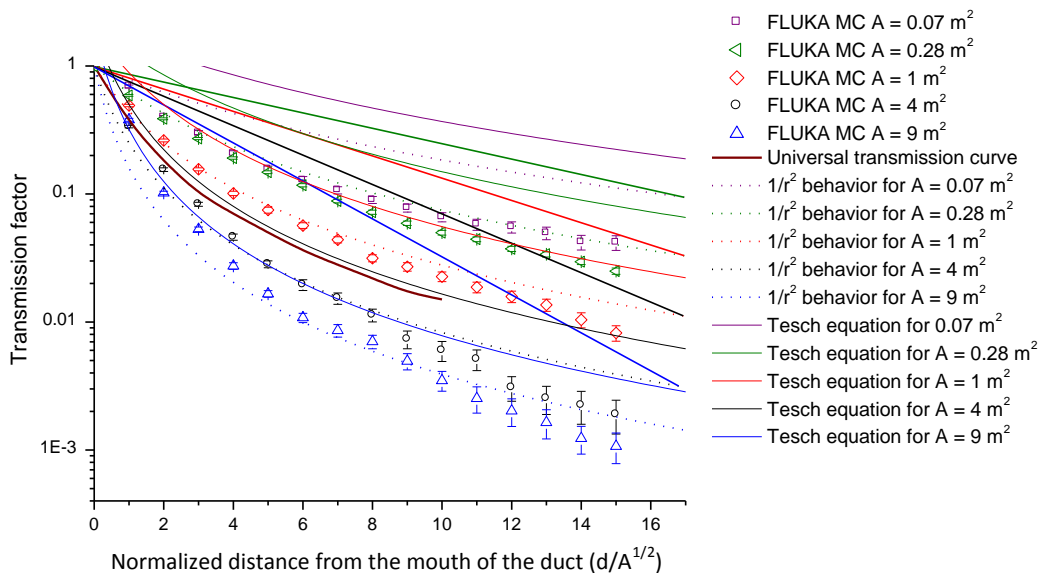


Figure 50 : Transmission of neutrons through a single duct for a point source on-axis, calculated with the universal transmission curves of refs. [(102) and (103)], the Tesch equation (eq. 35), the inverse-square-law and by FLUKA Monte Carlo simulations for five different cross sections.

The results of Figure 50 clearly show that it is not possible to define a generic transmission curve for the point source case. The inverse-square law completely fails for ducts of small cross-sectional area, is approximately correct for the 1 m² case up to a depth of about 7 d/A^{1/2} and overestimates at larger depths for ducts of larger cross-sectional areas. This is possibly because this law does not take into account the varying contribution of the scattered neutrons along the duct. With increasing distance, this scattering contribution first increases and then decreases because of the absorption in air. The equation proposed by Tesch (108) overestimates the contribution to the ambient dose equivalent from scattered neutrons. In fact, Tesch's equation seems to be applicable only far inside the duct and is totally inconsistent at the mouth.

The five transmission curves obtained from the Monte Carlo simulations can be fitted by the equation:

$$T = a (d/A^{1/2})^{-b} \quad (37)$$

where a and b are the free parameters of the fits.

In order to emphasize the dependence of the attenuation in the duct on the duct size, the parameters a and b can be expressed as

$$a = k A^{1/2} \quad (38a)$$

and

$$b = 2 h A^{1/2} \quad (38b)$$

where $A^{1/2}$ is in meters. The parameters k and h are given in Table 18.

Table 18 : Fit parameters k and h calculated for five cross sections of the duct.

	$A^{1/2}$ (m)				
	0.26	0.53	1.0	2.0	3.0
k (m^{-1})	4.18	1.70	0.76	0.39	0.17
h (m^{-1})	2.38	1.18	0.78	0.56	0.36

Both k and h decrease with increasing $A^{1/2}$. The dependence of k and h on $A^{1/2}$ is rather regular and can be represented by the fits shown in Figures 51 and 52:

$$k = k_1 A^{-k_2/2} \quad (39a)$$

$$h = h_1 A^{-h_2/2} \quad (39b)$$

and k_1, k_2, h_1, h_2 are given in Table 19. The neutron transmission through a straight duct of length d and cross-sectional area A in direct view of the source can thus be estimated from the expression:

$$T = (k A^{1/2}) (d / A^{1/2})^{-2hA^{1/2}} \quad (40)$$

in which the parameters k and h are calculated by expressions (39) and Table 19 for any given cross-sectional area A .

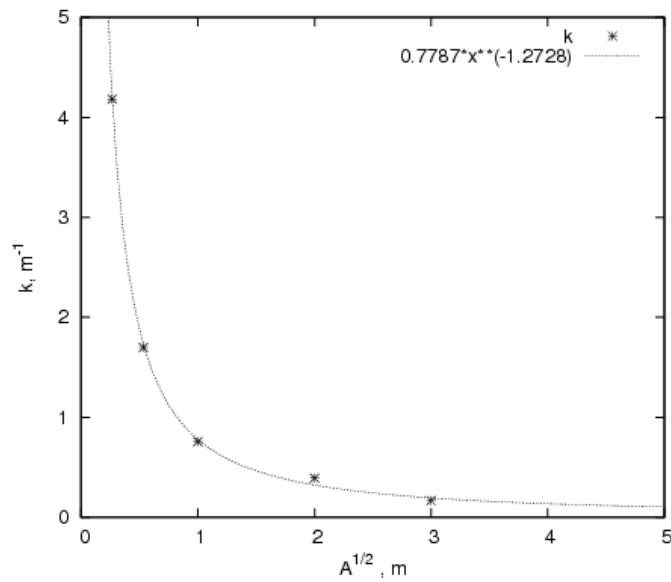


Figure 51 : Fit parameter k as a function of $A^{1/2}$ fitted through the equation $y = 0.7787 x^{1.2728}$.

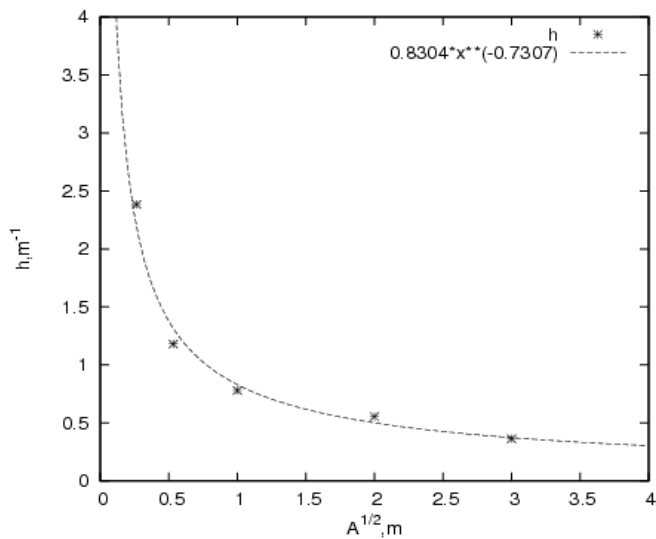


Figure 52 : Fit parameter h as a function of $A^{1/2}$ fitted through the equation $y = 0.8304 x^{-0.7307}$.

Table 19 : Fit parameters k_1 , k_2 , h_1 , h_2 to be used in equation 39a and 39b.

k_1	k_2	h_1	h_2
1.7787	1.2728	0.8304	0.7307

Discussion

Expression (40) can be used directly with the parameters of Table 18 for straight ducts with dimensions as given in Table 17, or together with the parameters given by expressions (39) and Table 19 for ducts of intermediate size. A penetration in a shield is usually orthogonal to the circulating beam direction (as e.g. for both linear and circular accelerators installed in a tunnel), and thus the neutron component generated by the beam loss and streaming through the duct is mainly the evaporation component rather than the direct neutron component. Therefore expression (40) is expected to be valid over a wide range of energies, and be applicable at both low (MeV), intermediate (tens or hundreds of MeV) and high-energy (GeV) particle accelerator facilities.

It is maybe redundant but still worth stressing that neutron attenuation data *cannot* be used to estimate the attenuation of electromagnetic radiation. A duct or a labyrinth is much more effective in attenuating photon radiation than neutrons. As an example, measurements of the attenuation by the LEP PM18 shaft of photons produced by electrons/positrons beams with energy varying from 45 GeV to 103 GeV have shown that the same duct is orders of magnitude more effective to attenuate photons than neutrons (see figure 12 of ref. [119]). The measurements also indicated a constant reduction of the photon attenuation factor (in other words, a constant increase in the transmission of radiation) with increasing electron beam energy, i.e. with increasingly harder photon spectra. As discussed above, this dependence on the original spectrum is much less pronounced with neutrons, in particular for the second and subsequent legs.

Although the present study has focused on the transmission of neutrons produced by proton accelerators, we have seen that the information on the original energy distribution is lost rather rapidly during the propagation in the first leg – because of scattering and attenuation – and is no longer relevant from the second leg onwards. Therefore it can reasonably be expected that these same attenuation data are equally applicable to neutrons produced at electron accelerators (where a large fraction of the neutrons are expected from the giant dipole resonance in the few MeV region), certainly for the second and subsequent legs, and most likely also in the first leg (as shown in Figure 47), or at least after a sufficient depth.

4 Shielding design

Over the past few years, four possible locations were investigated for the site of Linac4:

- 1) an existing hall (the radiation protection aspects are discussed in refs. (120), (121), (122) and (123));
- 2) the building housing the present Linac2 with a substantial reinforcement of the existing shielding (solution soon abandoned for cost reasons);
- 3) the building housing the present Linac2 with little additional shielding to the existing structure [(124) and (125)];
- 4) a future purpose-built tunnel, for which various options were investigated. The radiation protection aspects of an earlier scheme are discussed in ref. (125).

This chapter discusses the radiation protection aspects of the final configuration of the fourth scenario, the solution finally adopted and which is now under construction. Particular attention was devoted to evaluating the propagation of neutrons through the waveguide and cable ducts, and through the access area at the low-energy end of the linac. The present work provides complete information on beam loss assumptions, accelerator structure and duct and maze design, in order to make the present results of sufficiently general interest and provide guidelines for similar studies for intermediate energy proton accelerators.

4.1 Beam loss assumptions

In modern linear accelerators the design maximum beam loss is normally below 1 W/m. Losses below this threshold usually generate values of induced radioactivity such that hands-on maintenance on the machine is still possible. The beam dynamics and the apertures in Linac4 have been optimised to keep losses below 1 W/m at the SPL duty cycle of 5%. The same loss level was also taken as guideline for the shielding calculations of Linac4 as injector for the PSB. Since the accelerator designers expect that losses scale proportionally with duty cycle, this assumption leads to a large safety factor of about 50 (the ratio of the SPL and PSB duty cycles). Therefore the proposed shielding design is appropriate for Linac4 used as front-end of the SPL and it is rather conservative as injector to the PSB.

In reality beam losses will not be equally distributed along the machine, but will typically occur in the aperture restrictions of quadrupoles. In order to have a realistic loss configuration, in the following it is assumed that constant losses of 10 W every 10 m occur at selected points along the machine. In terms of shielding requirements this loss distribution is approximately equivalent to a uniform loss of 1 W/m. The validity of this approximation can be proved through a simplified model in which the 1 W/m continuous loss is represented through ten aligned 1 W loss points equally spaced over a total distance of 10 m and the localized 10 W loss point is placed in the middle of this ideal line (Fig. 53). As an example, the contributions to the ambient dose equivalent rate at point P beyond the shield of the ten 1 W losses and of the 10 W localized loss are compared at the proton energy of 150 MeV. Let us consider a distance of the localized source from the inner surface of the concrete wall equal to 1 m and a 1 m thick shield. The attenuation through the shield of the ambient dose equivalent is described through the classical two-parameter formula (see, for example, ref. (103) and (126)):

$$H(E_p, \theta, d / \lambda) = \frac{H_0(E_p, \theta)}{r^2} \exp \left[-\frac{d}{\lambda(\theta) g(\alpha)} \right] \quad (41)$$

where H is the ambient dose equivalent beyond the shield, E_p is the proton energy, r is the distance between the radiation source (the target stopping the protons) and the scoring position, θ is the angle between the direction \vec{r} and the beam axis, H_0 is the source term, d is the shield thickness, $\lambda(\theta)$ is the attenuation length for the given shielding material at emission angle θ , and α is the angle between the direction \vec{r} and the normal to the shield surface. The function $g(\alpha) = 1$ for a spherical geometry and $g(\alpha) = \cos \alpha$ in all other cases. The ambient dose equivalent rate can be calculated multiplying the ambient dose equivalent by the number of protons per hour. At the energy of 150 MeV the number of lost protons per hour is 1.5×10^{14} for 1 W beam loss. Attenuation lengths and source terms as a function of proton energy E_p and emission angle θ were taken from ref. (126). As shown in Table 20, the contributions to the ambient dose equivalent rate in point P of the 10 W losses and of the localized 10 W loss are 1.10×10^{-4} Sv/h and 1.02×10^{-4} Sv/h, respectively. Therefore, the approximation used in the present study is correct.

Table 20 : Ambient dose equivalent rates for a continuous beam loss of 1 W/m and a localized loss of 10 W.

Loss point	Distance source-scoring point P (m)	Effective Shield thickness d (cm)	Angle (degrees)	λ for concrete (cm)	Source term (Sv m ² /proton)	Ambient dose equivalent H (Sv/proton)	Ambient dose equivalent rate H*(10) (Sv/h)
A	6.10	174	35.01	32.42	5.52E-16	6.84E-20	1.03E-05
B	5.23	150	42.00	32.01	3.73E-16	1.28E-19	1.93E-05
C	4.47	128	51.57	31.44	2.19E-16	1.88E-19	2.85E-05
D	3.88	111	64.52	30.67	1.06E-16	1.90E-19	2.88E-05
E	3.54	101	80.95	29.69	4.24E-17	1.11E-19	1.68E-05
F	3.54	101	99.09	28.61	1.54E-17	3.55E-20	5.37E-06
G	3.88	111	115.52	27.63	6.14E-18	7.40E-21	1.12E-06
H	4.47	128	128.48	26.86	2.98E-18	1.28E-21	1.94E-07
I	5.23	150	138.05	26.29	1.74E-18	2.16E-22	3.26E-08
J	6.10	174	145.04	25.87	1.18E-18	3.75E-23	5.67E-09
Total ambient dose equivalent and dose eq. rate from the ten 1 W loss points						7.30E-19	1.10E-04
10 W loss point	3.5	100	90.00	29.15	2.56E-17	6.75E-20	1.02E-04

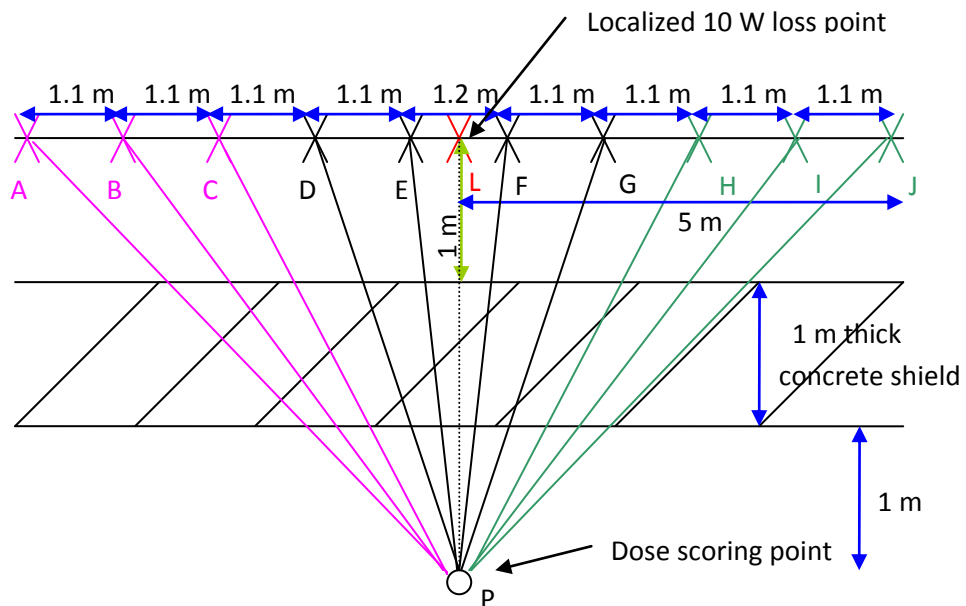


Figure 53 : Simplified model for the comparison between a continuous beam loss and a localized beam loss 10 times higher.

4.2 Radiation shielding

The Linac4 tunnel will be located underground, at a depth sufficient to shield the direct stray radiation produced during the accelerator operation. In the first design the linac was at a depth such that it was effectively shielded by 430 cm of earth plus about 1 m of concrete. Subsequently, with the aim to minimize the interference of the future SPL with surface buildings and existing tunnels nearby (44), the Linac4 and SPL tunnels were lowered by 2.5 m (see Section 2.4 and Fig. 10 showing the final layout). The klystrons will be installed in an auxiliary building located on the surface on top of the linac tunnel and will be connected to the linac by waveguides running through ducts traversing the shielding.

The basic assumptions for the shielding design are the classification of radiation areas (Table 21) and the beam loss pattern (position and intensity of the losses) for routine operation and accidental conditions.

Table 21 : Classification of radiation areas according to CERN Radiation Safety Code.

Type of area	Maximum annual effective dose	Maximum ambient dose equivalent rate
Non-designated	1 mSv	0.5 μ Sv/h
Supervised	6 mSv	3 μ Sv/h
Simple controlled	20 mSv	10 μ Sv/h

The linac tunnel is underground, while the klystron building is on the surface on top of the tunnel. The klystron building will be classified as a supervised radiation area (3 μ Sv/h guideline value for the dose rate) according to CERN Radiation Safety Code (127) but, because of the thin walls separating this building from the public area, 1 μ Sv/h has been taken as design value for the calculations. The

shielding calculations were performed for the worst-case scenario for routine operation (160 MeV, 10 W point losses every 10 m). Because the linac is at such a depth, one can verify by using a simple point-source line-of-sight model that the earth thickness between the machine tunnel and the klystron building is indeed sufficient as bulk shield. For a point source and 90 degree emission expression (41) approximates to

$$H = \frac{H_{\pi/2} \exp(-d/\lambda)}{r^2} \quad (42)$$

where r is the distance from the radiation source to the exposure point of interest, $H_{\pi/2}$ and λ are the source term and attenuation length of the shielding material for 90 degrees emission, and d is the shield thickness. Both $H_{\pi/2}$ and λ increase with increasing beam energy. The distance r is about 8 m. Data from refs. (103) and (126) were used to estimate the source term and the attenuation length in ordinary concrete at 160 MeV. The estimated concrete thicknesses required to reduce the dose equivalent rate down to 1 $\mu\text{Sv}/\text{h}$ are 250 cm and 190 cm, respectively. The 25% discrepancy is acceptable considering that the two sets of data are derived from totally independent assumptions and calculation approaches (data from ref. (103) are based on analytical models, data from ref. (126) from Monte Carlo simulations with the latest version of the FLUKA code) and 20 years apart. The “real” thickness required for the shielding is probably closer to the value estimated from ref. (126), but the thickest shield was here chosen as a conservative assumption. A safety factor of 3 in a shielding design is usually recommended. This can be obtained by increasing the concrete shielding by 1.1λ , which leads to a 280 cm thickness of concrete. The equivalent earth thickness can approximately be assessed by simply scaling the thickness for concrete by the ratio of the densities of the two materials, taken as 1.8 g/cm^3 for earth and 2.35 g/cm^3 for concrete. This value of earth density should be regarded as conservative for CERN local soil, a density of 2 g/cm^3 being probably a more realistic figure. With this simplification, 280 cm of concrete are approximately equivalent to 370 cm of earth, from the point of view of radiation attenuation. Thus even the original 430 cm of earth plus 100 cm of concrete are largely sufficient to reduce the ambient dose equivalent rate due to stray radiation through the shield to well below the value for public exposure of 0.5 $\mu\text{Sv}/\text{h}$. Given the fact that the linac tunnel was further lowered by 2.5 m, it was decided that detailed Monte Carlo simulations were not necessary to confirm the adequacy of the bulk shielding.

4.3 Neutrons streaming through the waveguide ducts

The first radiological study was focused on the propagation of neutrons through the waveguide ducts from the linac tunnel to the surface klystron building. Along the accelerator the distance between the waveguides decreases with increasing energy. The worst case scenario in the high-energy section was studied. The stray radiation in the klystron building is mainly given by the addition of two terms, the radiation traversing the shield and the radiation streaming through the waveguides ducts. As the bulk shield is largely sufficient to shield the direct radiation, in the simulations the particles were not transported through the earth in order to optimize the computing time. Several simulations were performed to optimize the number, cross sectional area and length of the legs of the ducts. The first calculations for the waveguide ducts were performed before the linac tunnel was finally lowered by 2.5 m. Sections 4.3.1, 4.3.2 and 4.3.3 discuss these first studies, while section 4.3.4 refers to the final layout.

4.3.1 First layouts: first duct close to the loss point

The ducts housing the waveguides were originally designed according to the three-leg configuration shown in Fig. 54 and described in Table 22, dictated by an early design of the facility in which the klystrons were located in an underground tunnel just below ground level.

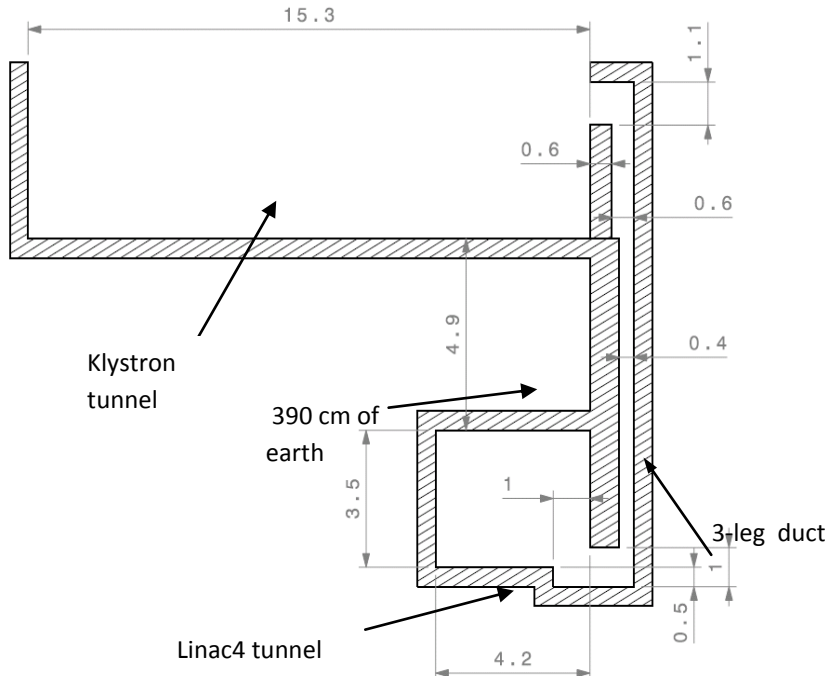


Figure 54 : Layout of the geometry implemented in the simulation (linac tunnel, three-leg waveguide ducts and klystron tunnel).

Table 22 : Layout of the waveguide duct for two possible scenarios: a duct housing two waveguides and a long well housing all the 18 waveguides (section 4.3.1 of text).

	Height (cm)	Length (cm)	Width in beam direction (cm)
First leg (horizontal)	40	100	200 or 9000
Second leg (vertical)	40 in the lower section and 60 in the upper section	1150	200 or 9000
Third leg (horizontal)	40	110	200 or 9000

The cross-sectional area of the waveguides is $700 \times 250 \text{ mm}^2$ and two possible layouts for the ducts were investigated:

- 1) several 200 cm long (in the beam direction) ducts, each one housing 2 waveguides;
- 2) one single 90 m long rectangular well housing all the 18 waveguides.

The target where the beam is lost was simulated by a $5 \times 5 \times 5 \text{ cm}^3$ copper block placed at beam height, 126 cm above the floor of the tunnel and 86 cm above the opening of the duct. A beam loss of 10 W at the maximum energy (160 MeV) was assumed. The importance biasing technique was used to improve the transport of the neutrons through the three legs of the duct and to kill those crossing the bulk shield.

As shown in Fig. 55 (left), for the 200 cm long duct in the most critical case the radiation streaming into the klystron tunnel is between 0.1 and 0.5 $\mu\text{Sv}/\text{h}$. For the 90 m long rectangular well the dose streaming into the klystron tunnel can reach a maximum value between 1 and 3 $\mu\text{Sv}/\text{h}$ (Fig. 55, right).

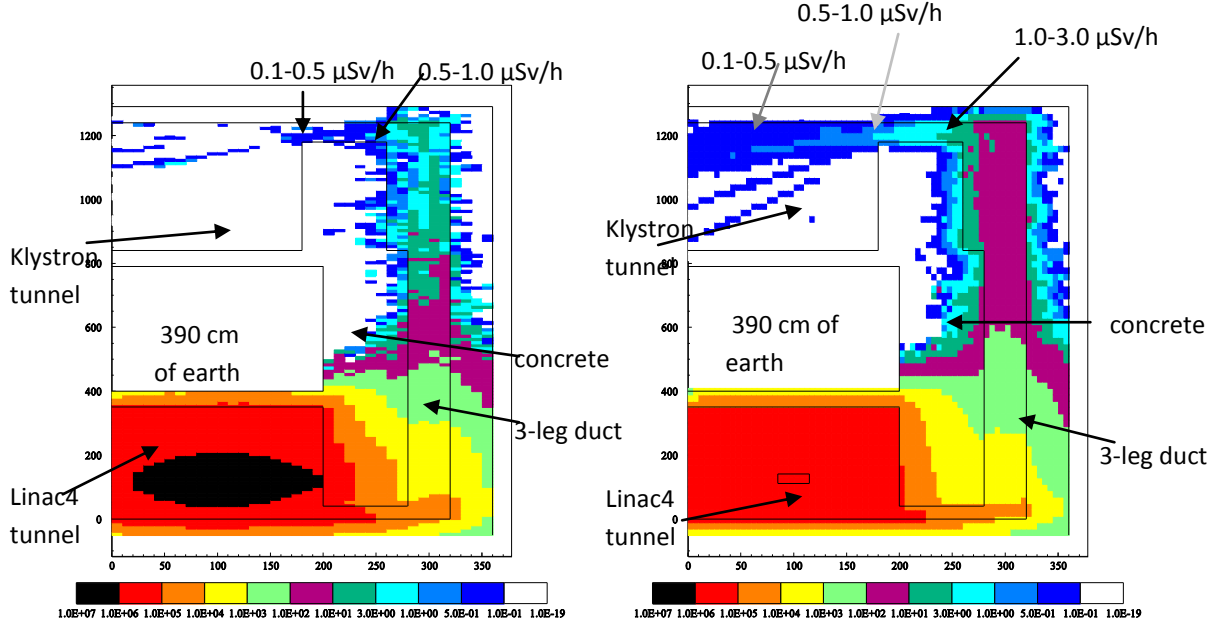


Figure 55 : Beam loss in a $5 \times 5 \times 5 \text{ cm}^3$ copper target, 10 W, 160 MeV. Left: cross sectional view of the Linac4 tunnel, the 2 m long duct housing two waveguides and the klystron tunnel. Right: cross sectional view of the Linac4 tunnel, the 90 m long well housing all the waveguides and the klystron tunnel. $H^*(10)$ in $\mu\text{Sv}/\text{h}$.

4.3.2 First layouts: ducts housing one waveguide

In the next design phase, the klystrons were moved to a surface building (the configuration finally adopted). The ducts housing the waveguides connecting the klystrons to the RF cavities were designed according to the three-leg configuration described in Table 23. The ducts have two reductions in size, at the beginning and at the end of the first vertical leg, respectively, where the width is reduced from 75 cm to 30 cm.

Table 23 : Layout of the waveguide ducts (section 4.3.2 of text).

	Section (cm^2)	Length (cm)
First leg (vertical)	75 x 75	460
Second leg (horizontal)	25 x 70	400
Third leg (vertical)	25 x 70	50

In correspondence to the waveguides the shield is made of 100 cm of concrete plus 360 cm of earth with an additional 50 cm thick concrete layer over the horizontal leg (the vertical dimension of the duct is 25 cm) (Fig. 56). The geometry implemented in the simulation includes two parallel ducts separated by 100 cm of earth plus 20 cm of concrete corresponding to the thickness of the duct walls (Fig. 56, right). The target where the beam is lost was simulated by a $5 \times 5 \times 5 \text{ cm}^3$ copper block placed in front of the mouth of the second (downstream) duct. A beam loss of 10 W at the maximum energy of 160 MeV was assumed.

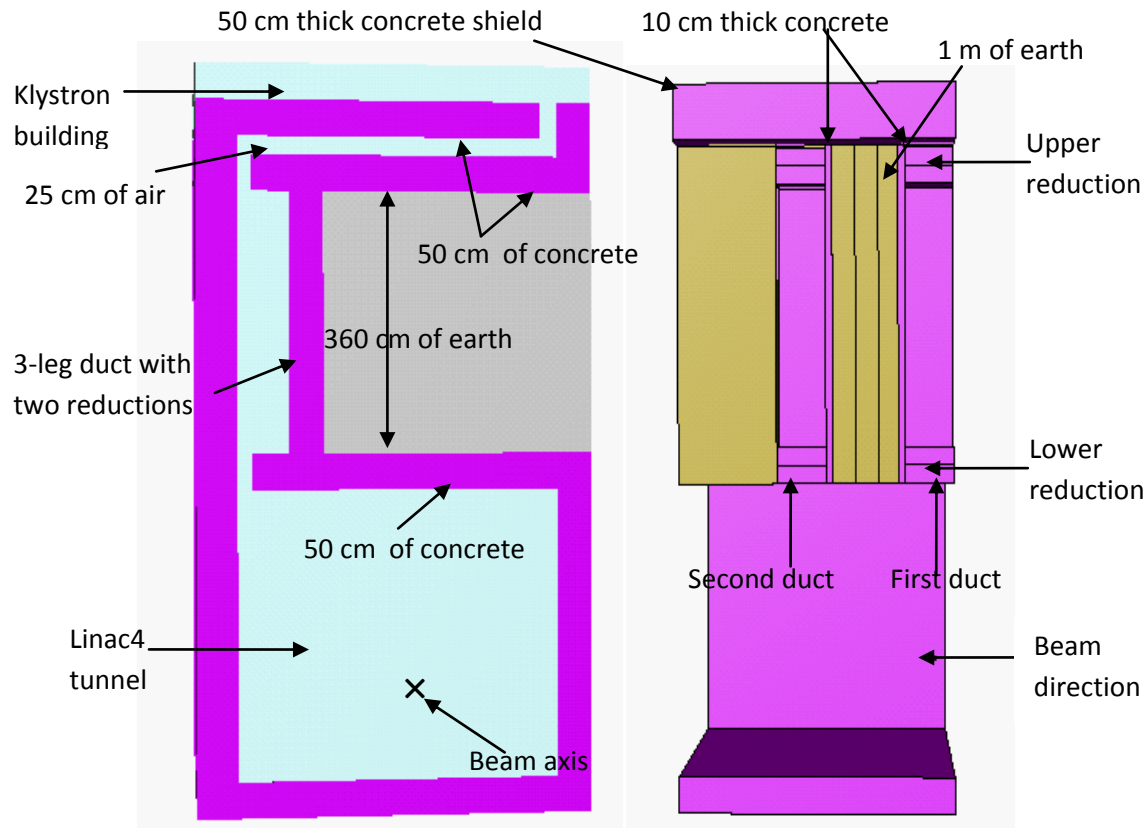
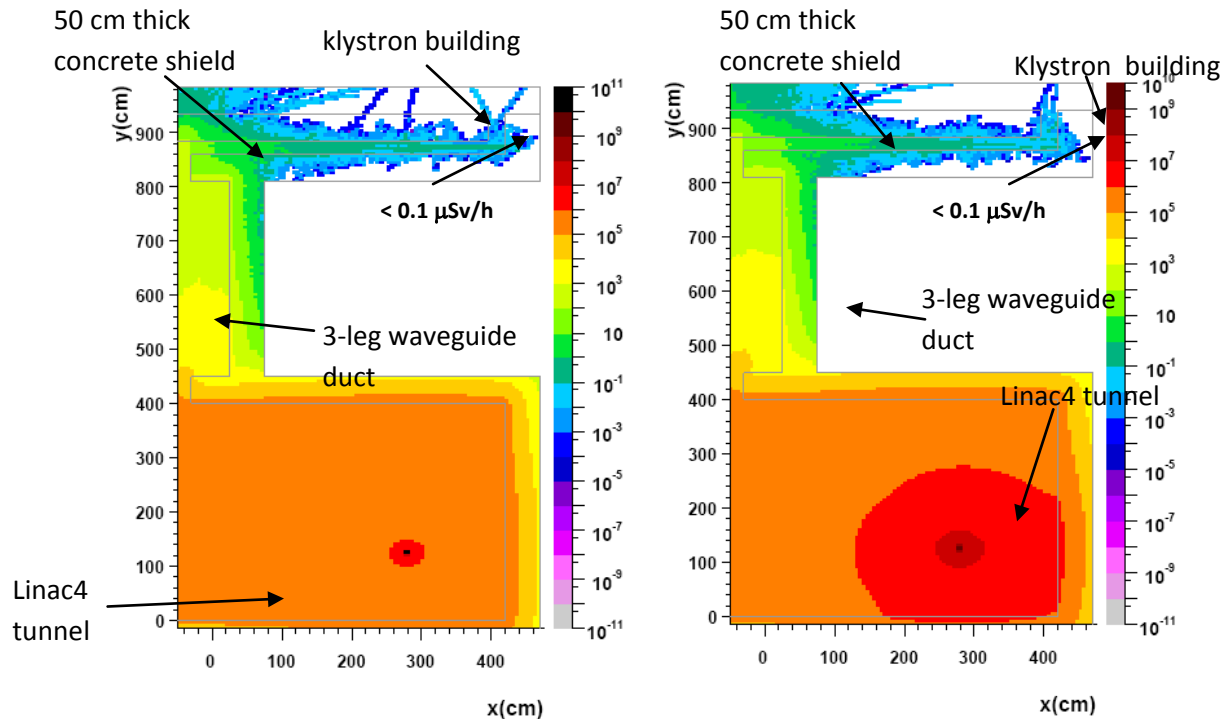


Figure 56 : FLUKA geometry plotted with SimpleGeo (128): cross sectional and lateral views of the Linac4 tunnel, the two 3-leg ducts and the floor of the klystron building.



Ambient dose equivalent rate ($\mu\text{Sv}/\text{h}$)

Figure 57 : Neutrons streaming through a pair of waveguide ducts spaced by 1 m. Beam loss in a $5 \times 5 \times 5 \text{ cm}^3$ copper target, 10 W, 160 MeV, placed in front of the downstream duct. Cross sectional view of the Linac4 tunnel, the 3-leg duct and the floor of the klystron building. $H^*(10)$ in $\mu\text{Sv}/\text{h}$. Left: Dose rate in the upstream duct. Right: Dose rate in the downstream duct. Note the different scale for x and y directions.

The simulations showed that the radiation streaming into the klystron building directly from the first leg of the first duct, beyond the 50 cm thick concrete shield, is expected to be between 0.1 and 1 $\mu\text{Sv}/\text{h}$. For both ducts the radiation streaming out of the third leg is less than 0.1 $\mu\text{Sv}/\text{h}$ (Fig. 57). However, the radiation streaming into the klystron building from the first leg of the second duct beyond the 50 cm thick concrete shield is expected between 1 and 10 $\mu\text{Sv}/\text{h}$. This radiation level is too high so that a different solution had to be studied.

4.3.3 First layouts: ducts housing two waveguides

With the aim of grouping two waveguides in a single duct a new three-leg configuration was designed (Table 24). The concrete shield over the horizontal leg was increased from 50 cm to 100 cm. Two parallel waveguide ducts are now spaced by 2.80 m of earth plus 20 cm of concrete corresponding to the thickness of the duct walls (Fig. 58).

Table 24 : Layout of the waveguide ducts (section 4.3.3 of text).

	Section (cm^2)	Length (cm)
First leg (vertical)	80 x 70	500
Second leg (horizontal)	80 x 70	285
Third leg (vertical)	100 x 90	140

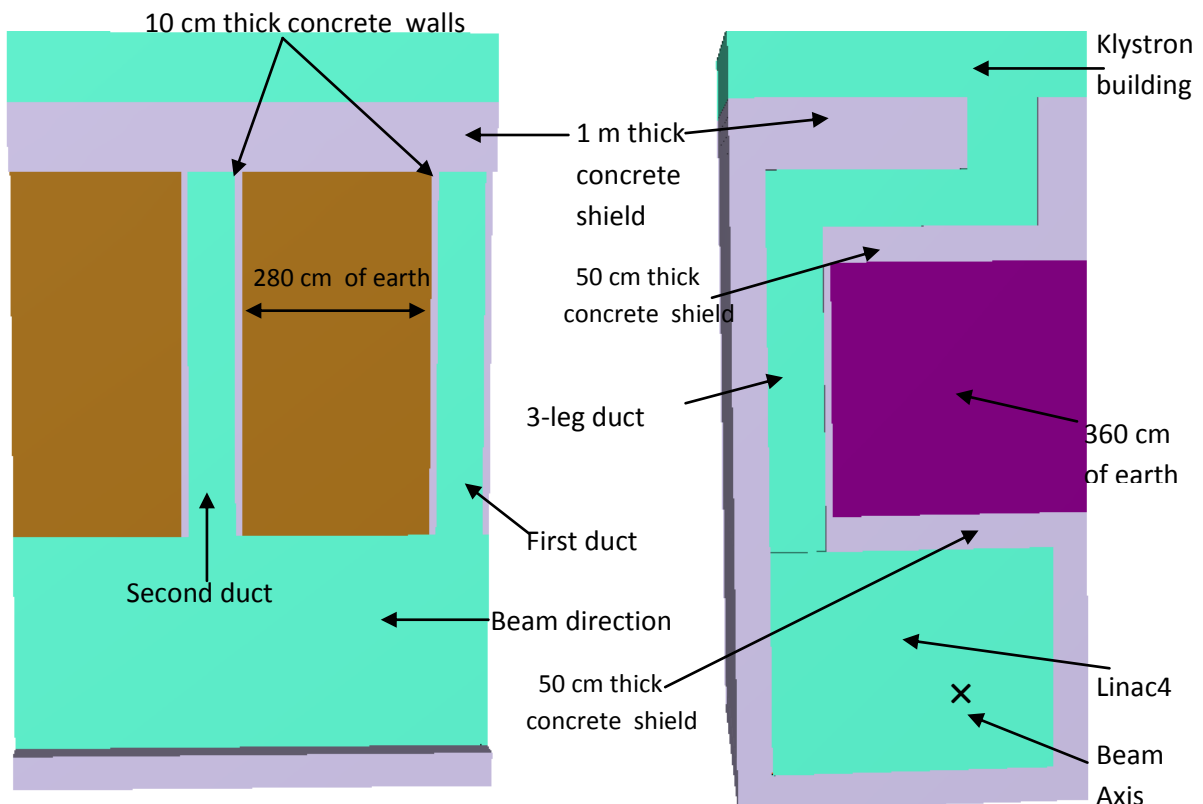


Figure 58 : FLUKA geometry plotted with SimpleGeo (128): lateral and cross sectional views of the Linac4 tunnel, the two 3-leg ducts housing two waveguides and the klystron building.

Several configurations concerning the size, the material and the position of the target were studied by FLUKA simulations: the resulting radiation levels are given in Table 25.

The results are comparable and the level of radiation is acceptable for the classification of the klystron building as a supervised area. The results for the last scenario described in Table 25 are also depicted in Fig. 59.

Table 25 : Dose rates for several configurations of size, material and position of the target in the waveguide duct studies (section 4.3.3 of text).

Target dimension	Target material	Position of the target	Dose rate streaming out of the 1 st leg (1 st duct)	Dose rate streaming out of the 3 rd leg (1 st duct)	Dose rate streaming out of the 1 st leg (2 nd duct)	Dose rate streaming out of the 3 rd leg (2 nd duct)
5 cm x 5 cm x 5 cm	copper	In between the two ducts	< 0.1 μ Sv/h	0.1 – 1 μ Sv/h	0.1 – 1 μ Sv/h	0.1 – 1 μ Sv/h
5 cm x 5 cm x 30 cm (beam direction)	iron	In between the two ducts	< 0.1 μ Sv/h	0.1 – 1 μ Sv/h	0.1 – 1 μ Sv/h	0.1 – 1 μ Sv/h
5 cm x 5 cm x 5 cm	copper	In front of the second duct mouth	< 0.1 μ Sv/h	0.1 – 1 μ Sv/h	0.1 – 1 μ Sv/h	0.1 – 1 μ Sv/h
20 cm x 20 cm x 5 cm	copper	In front of the second duct mouth	< 0.1 μ Sv/h	0.1 – 1 μ Sv/h	0.1 – 1 μ Sv/h	0.1 – 1 μ Sv/h

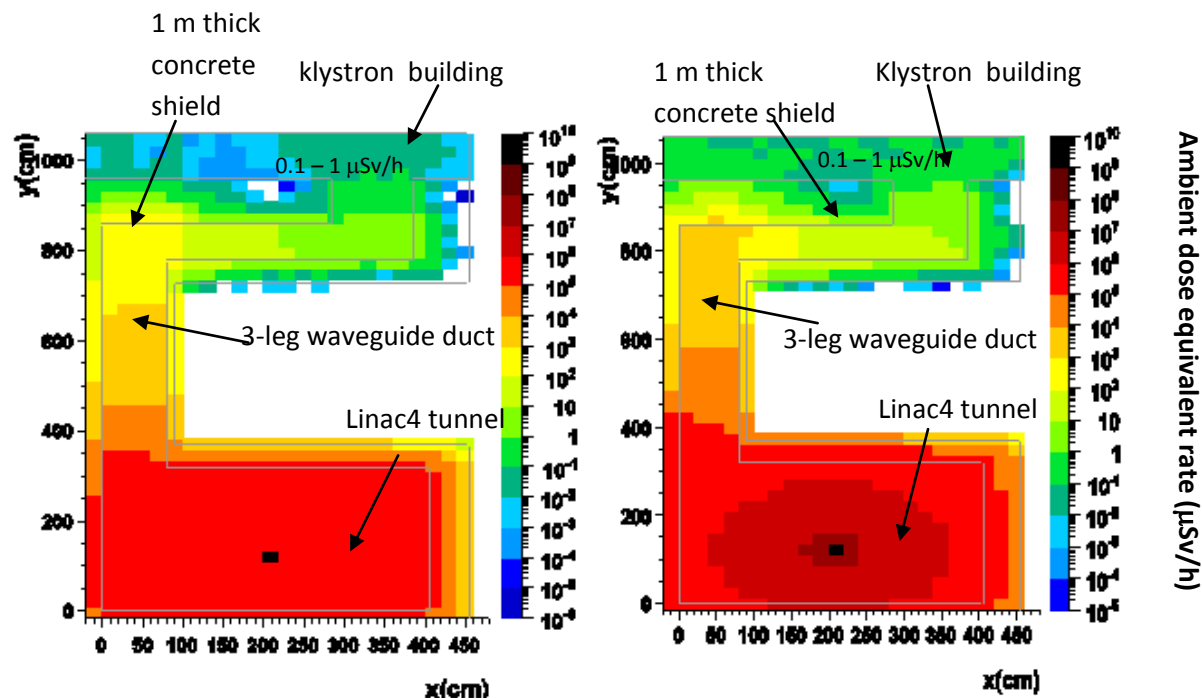


Figure 59 : Neutrons streaming through a pair of waveguide ducts spaced by 2.8 m. Beam loss in a 20 x 20 x 5 cm³ copper target, 10 W, 160 MeV, placed in front of the downstream duct. Cross sectional view of the Linac4 tunnel and the 3-leg duct. H*(10) in μ Sv/h. Left: Dose rate in the upstream duct. Right: Dose rate in the downstream duct. Note the different scale for x and y directions.

4.3.4 Final layout

The civil engineering design has been subsequently modified lowering the linac4 tunnel by 2.5 m because of radiation safety aspects related to the future SPL (44). The waveguide duct design has also been changed, increasing the length of the first leg by 2.5 m, increasing the cross-section of the first two legs and shortening the horizontal leg by 50 cm. The new three-leg configuration is described in Table 26.

The target, a cube of 5 cm side made of copper, was placed in front of the mouth of the second (downstream) duct. The simulations showed that the stray radiation in the klystron building on top of the first leg is expected to be less than 0.1 $\mu\text{Sv}/\text{h}$, while the radiation streaming out of the third leg is between 0.1 and 1 $\mu\text{Sv}/\text{h}$. The radiation on top of the first leg of the second duct and that streaming out of the third leg are both expected between 0.1 and 1 $\mu\text{Sv}/\text{h}$ (Fig. 60).

Table 26 : Layout of the waveguide ducts (section 4.3.4 of text).

	Section (cm^2)	Length (cm)
First leg (vertical)	90 x 90	755
Second leg (horizontal)	90 x 90	250
Third leg (vertical)	100 x 90	145

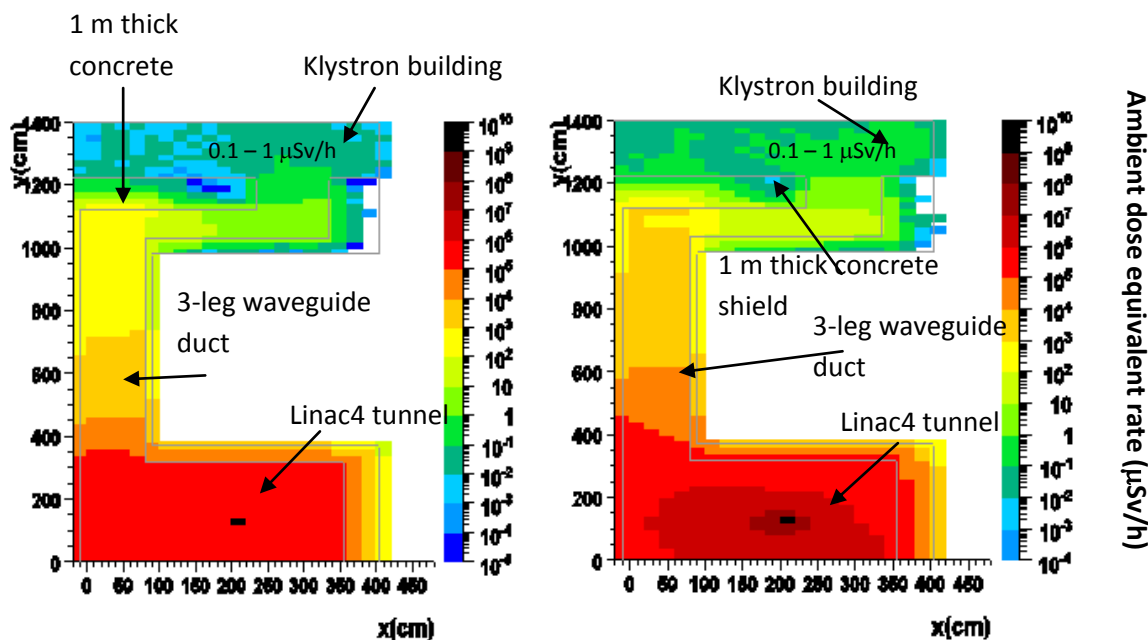


Figure 60: Neutrons streaming through a pair of waveguide ducts spaced by 2.8 m. Beam loss in a $5 \times 5 \times 5 \text{ cm}^3$ copper target, 10 W, 160 MeV, place in front of the downstream duct. Cross sectional view of the Linac4 tunnel and the 3-leg duct. $H^*(10)$ in $\mu\text{Sv}/\text{h}$. Left: Dose rate in the upstream duct. Right: Dose rate in the downstream duct. Note the different scale for x and y directions.

4.4 Access maze, ventilation and cable ducts at the low-energy end of the linac

A detailed geometry was implemented in the FLUKA simulation to study the radiological impact in the low-energy section of the accelerator. This part of the Linac4 tunnel is particularly important for two reasons: first it includes the shafts housing the cables and the ventilation system, and second it is close to the access shaft containing the staircases and the lift. An initial simulation was performed to estimate the radiation backscattered from a beam loss point at the end of the low-energy section (10 W, 11 MeV) into the access area, where the lift and the staircases are located, and to evaluate the need for an access maze. The geometry implemented in the simulation includes a simplified model of the accelerator tunnel and of the access area. The simulations showed that without maze the radiation streaming into the access area is expected between 10 and 100 $\mu\text{Sv/h}$ (Fig. 61). A 100 cm thick concrete wall was thus added in this area to create a maze and to reduce the radiation streaming through the lift and the staircases and reaching the surface.

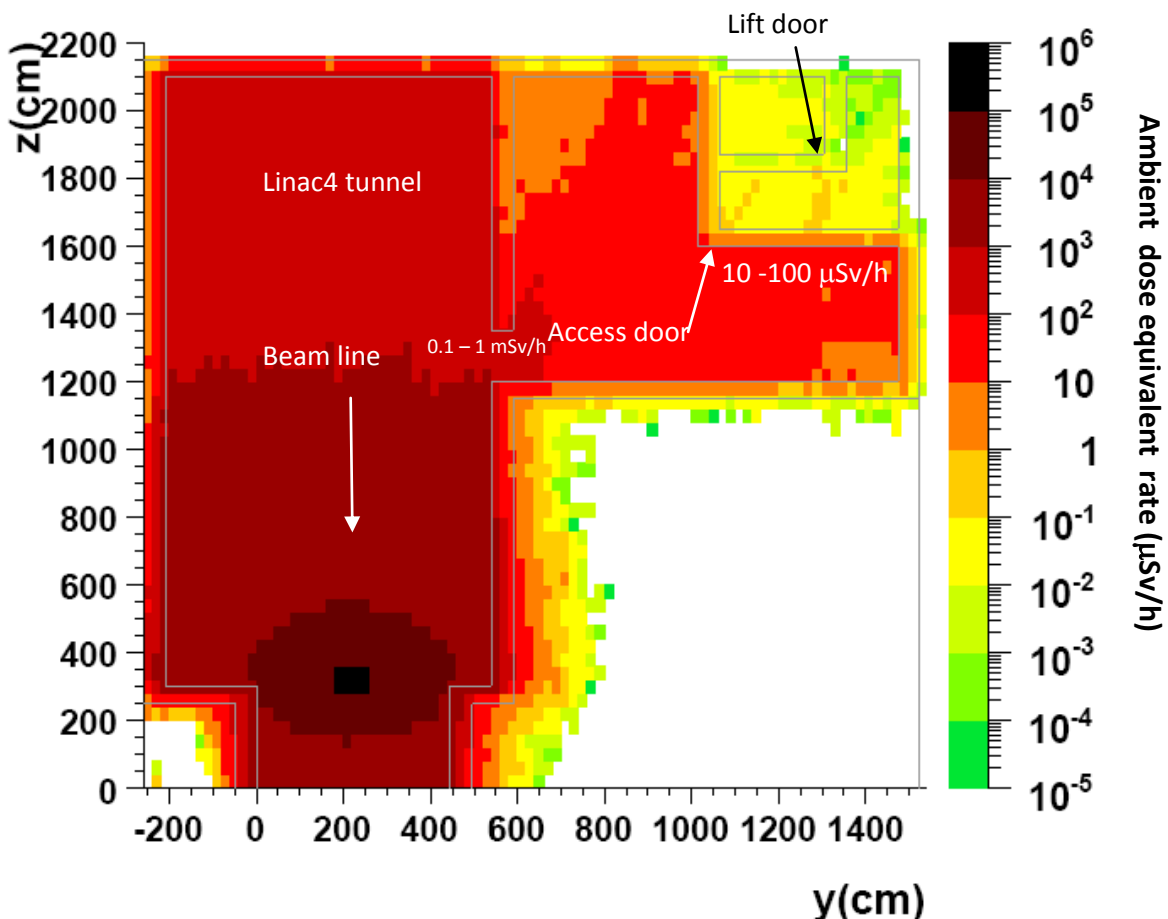


Figure 61 : Neutrons streaming on the ground floor of the Linac4 tunnel. Beam loss in a $5 \times 5 \times 5 \text{ cm}^3$ copper target, 10 W, 11 MeV, placed at the end of the low-energy section of the accelerator. Cross sectional view of the Linac4 tunnel and of the access area. $H^*(10)$ in $\mu\text{Sv/h}$.

A second simulation, including this maze in the geometry, was performed to estimate the radiation in the occupied areas nearby the low-energy section of Linac4. The layout of the simulation (Fig. 62) includes the following structures (heights are given with reference to the tunnel floor):

- the accelerator tunnel;
- the so-called “safe room” at a height of 3.5 m;
- the galleries on the first and second floor located at a height of 7.6 m and 12.1 m, respectively;

- the ventilation shaft and the cable duct located at the beginning of the accelerator tunnel;
- the access area with the lift, the staircases and the maze designed to reduce the radiation streaming through these shafts;
- the target, a 5 cm side cube, made of copper and located at the end of the low-energy section (energy of 11 MeV).

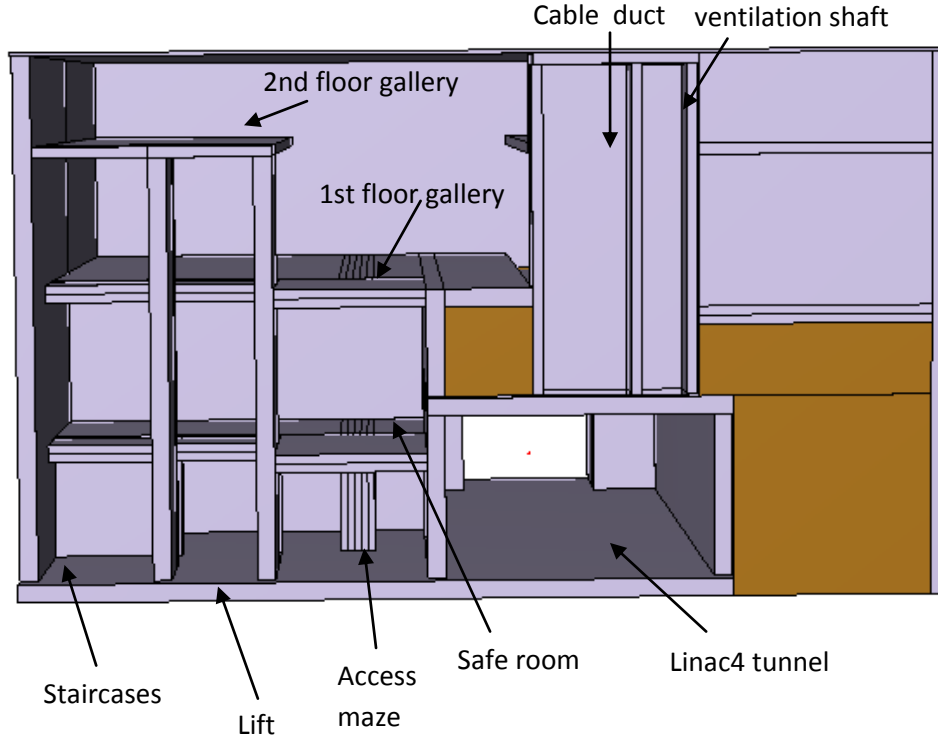


Figure 62 : FLUKA geometry plotted with SimpleGeo (128). Cross sectional view of the low-energy section of Linac4. The view looks downstream in the tunnel, towards the high-energy end of the accelerator.

A beam loss of 10 W at the energy of 11 MeV was simulated and the backscattered radiation estimated. The setup of an access maze by the addition of the 100 cm thick wall reduces the dose rate in the access area to less than 0.1 $\mu\text{Sv}/\text{h}$ (Fig. 63). The radiation in the “safe room” is expected to be between 1 and 10 $\mu\text{Sv}/\text{h}$ just in proximity of the 50 cm thick lateral wall of the room, while everywhere else in the room is less than 1 $\mu\text{Sv}/\text{h}$ (Fig. 64). The radiation in the gallery on the first floor is well below 1 $\mu\text{Sv}/\text{h}$ (Fig. 65). The radiation level along the cable duct was estimated (Figs. 66 and 67). In proximity of the gallery on the second floor at the height of 1180 cm the ambient dose equivalent rate is expected to be 2.4 $\mu\text{Sv}/\text{h}$, while on the top of the cable duct at the height of 1430 cm is expected to be 1.2 $\mu\text{Sv}/\text{h}$. According to these radiation levels the cables should be pulled through the top of the cable duct and not through a hole drilled in the shield.

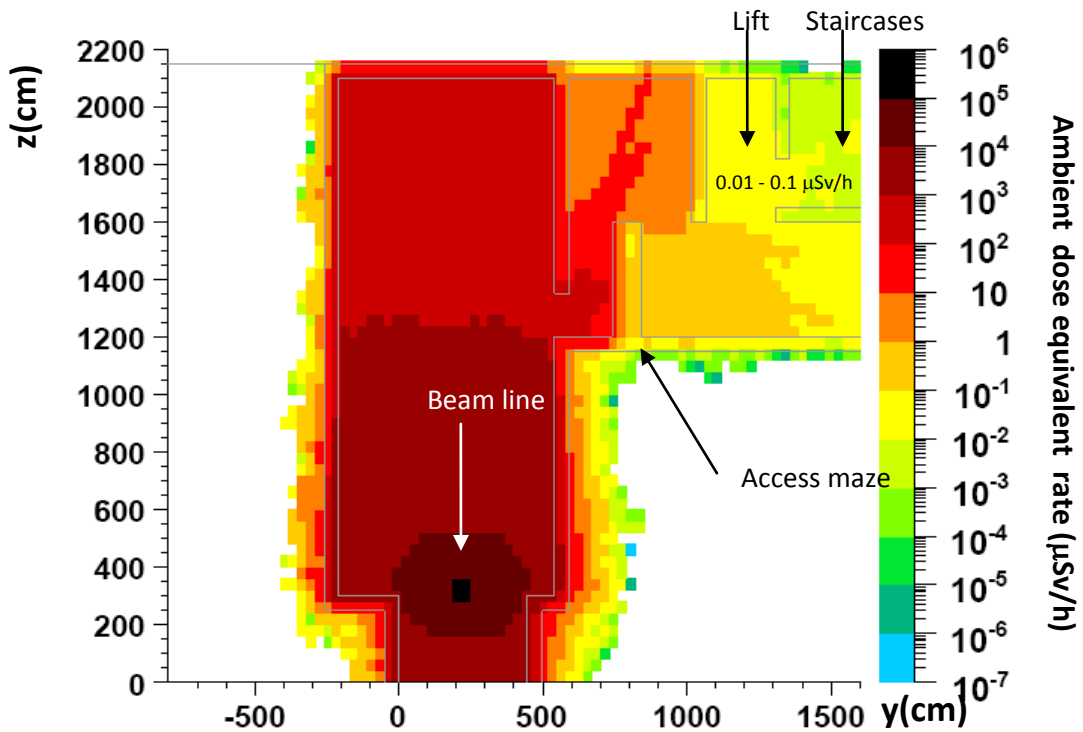


Figure 63 : Neutrons streaming into the ground floor of the Linac4 tunnel. Beam loss in a $5 \times 5 \times 5 \text{ cm}^3$ copper target, 10 W, 11 MeV, placed at the end of the low-energy section of the accelerator. Cross sectional view of the Linac4 tunnel and of the access area with the addition of the maze. $H^*(10)$ in $\mu\text{Sv}/\text{h}$.

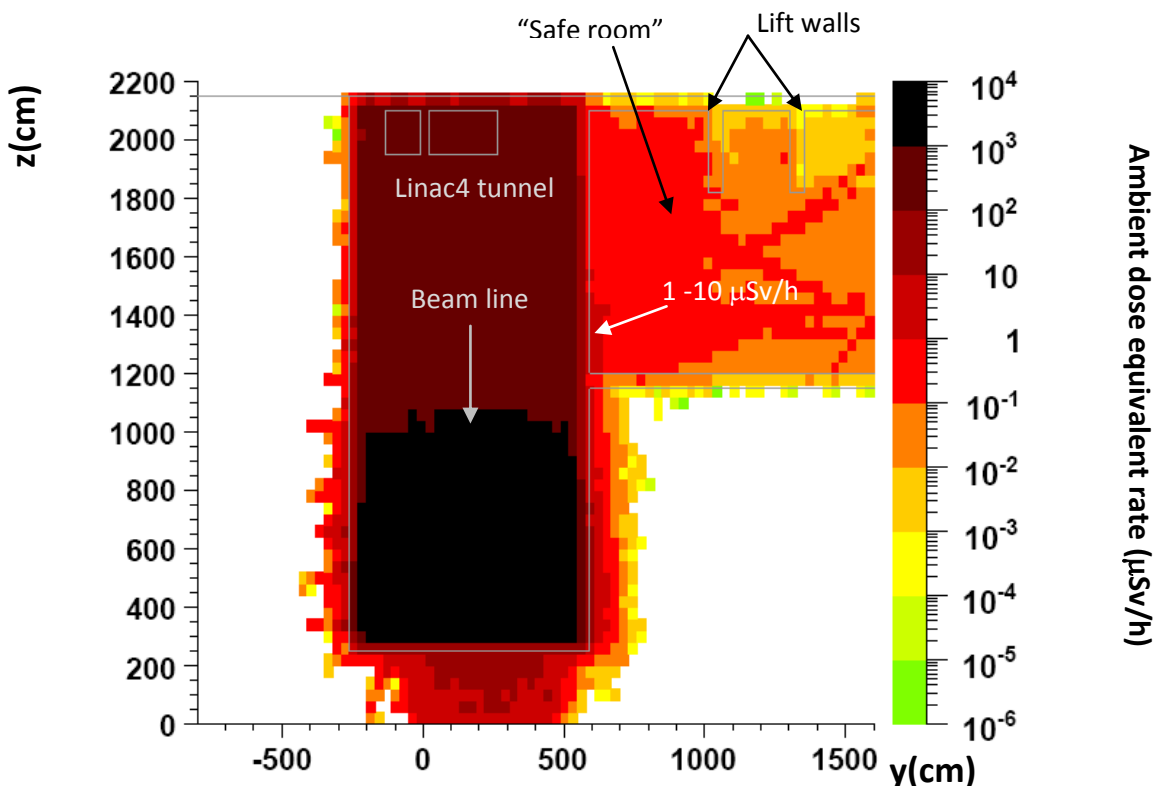


Figure 64 : Neutrons streaming into the “safe room”. Beam loss in a $5 \times 5 \times 5 \text{ cm}^3$ copper target, 10 W, 11 MeV, placed at the end of the low-energy section of the accelerator. Top-cross sectional view of the “safe room” at the height of 3.5 m with respect to the tunnel floor. $H^*(10)$ in $\mu\text{Sv}/\text{h}$.

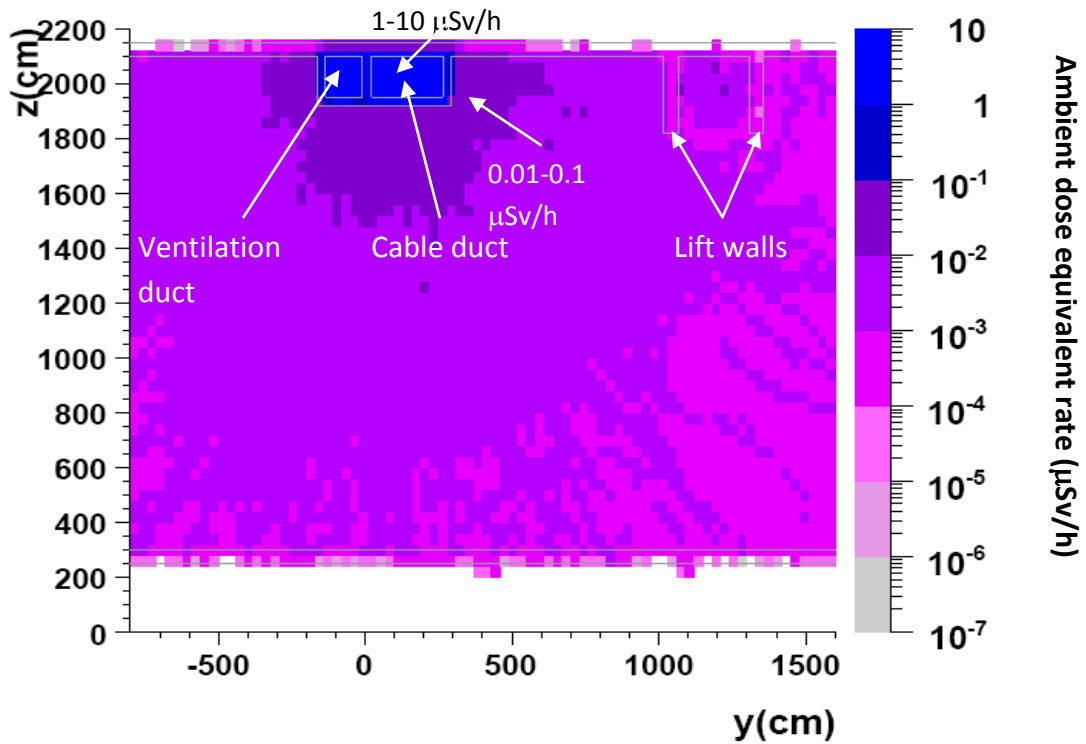


Figure 65 : Neutrons streaming into the gallery on the first floor. Beam loss in a $5 \times 5 \times 5 \text{ cm}^3$ copper target, 10 W, 11 MeV, placed at the end of the low-energy section of the accelerator. Top-cross sectional view of the gallery on the first floor in the Linac4 tunnel at a height of 7.6 m. $H^*(10)$ in $\mu\text{Sv/h}$.

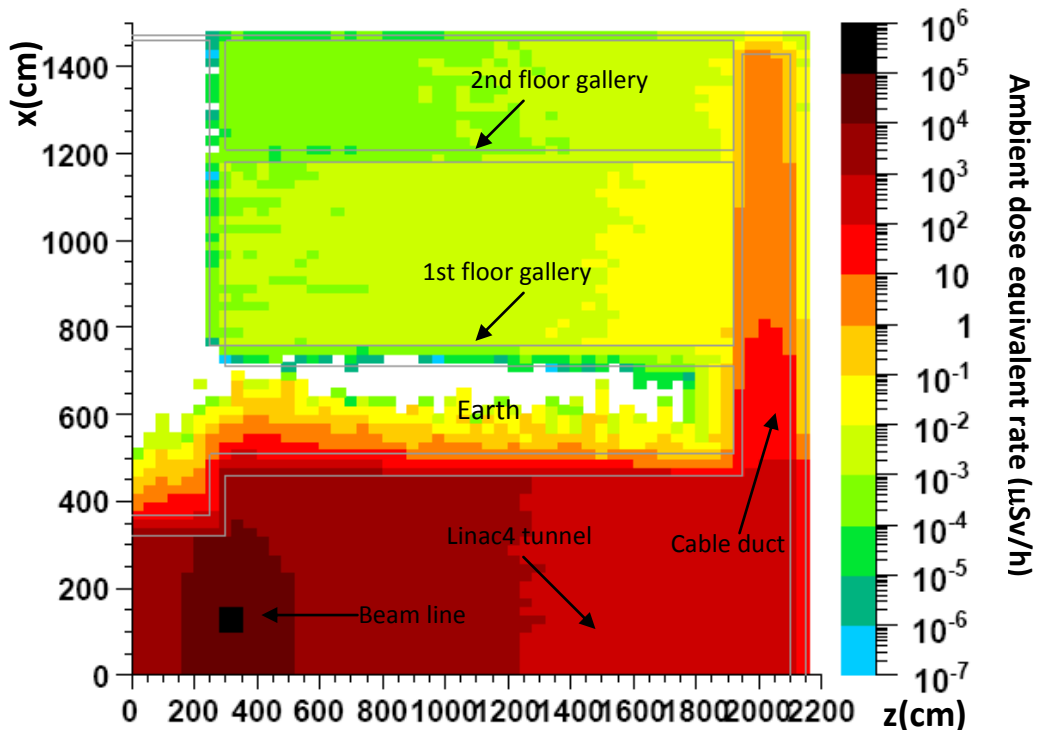
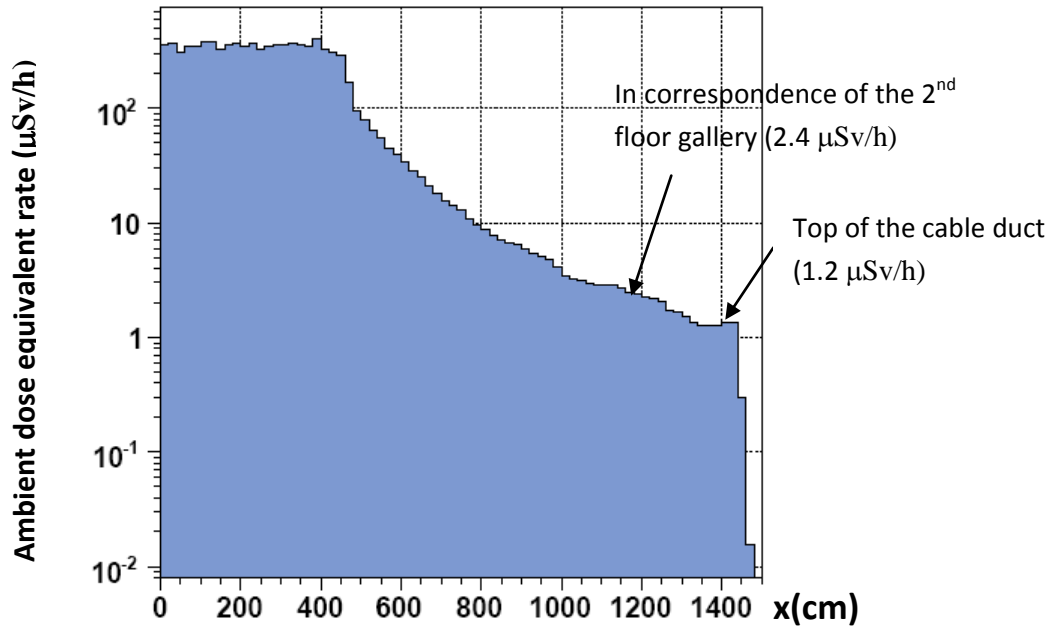


Figure 66 : Neutrons streaming into the cable duct. Beam loss in a $5 \times 5 \times 5 \text{ cm}^3$ copper target, 10 W, 11 MeV, placed at the end of the low-energy section of the accelerator. Cross sectional view of the low-energy section of the Linac4 tunnel. $H^*(10)$ in $\mu\text{Sv/h}$. Note the different scale for x and z directions.

Figure 67 : Radiation level along the length of the cable duct. $H^*(10)$ in $\mu\text{Sv}/\text{h}$.

4.5 Low-energy section waveguide and cable duct studies

In the RFQ section of the accelerator two waveguide ducts have been designed according to a different layout with respect to the remaining part of the tunnel (Figs. 68 and 69). They are made of a single, straight duct, the section and shape of which change along its length according to the configuration shown in Table 27. The dose rate must be estimated in the two galleries, nearby these ducts, located on top of the linac tunnel, at a height of 7.6 and 12.1 m respectively, with respect to the tunnel floor. A 10 W beam loss at the end of the low-energy section of the accelerator, where the linac energy is 11 MeV, was taken into account and the backscattered radiation transmitted through the ducts was estimated. The duct mouth is 2.65 m upstream of the beam loss point. The simulations showed that the radiation in both tunnels is expected to be less than 0.1 $\mu\text{Sv}/\text{h}$ (Fig. 70).

A cable duct with the same section of the 3 MeV waveguide ducts was added at the end of the low-energy section of the accelerator, as shown in Fig. 71. According to the 3 MeV waveguide studies, the ambient dose equivalent rate at the entrance of the 3 MeV waveguide ducts and of the cable duct are comparable (Fig. 72) and, consequently, also the level of radiation on the upper floors.

Table 27 : Layout of the 3 MeV waveguide ducts.

Section of the duct	Length
Rectangular (30 cm x 70 cm)	0 - 50 cm
Cylindrical with diameter of 85 cm	50 - 250 cm
Rectangular (30 cm x 70 cm)	250 - 720 cm
Rectangular (40 cm x 70 cm)	720 - 750 cm

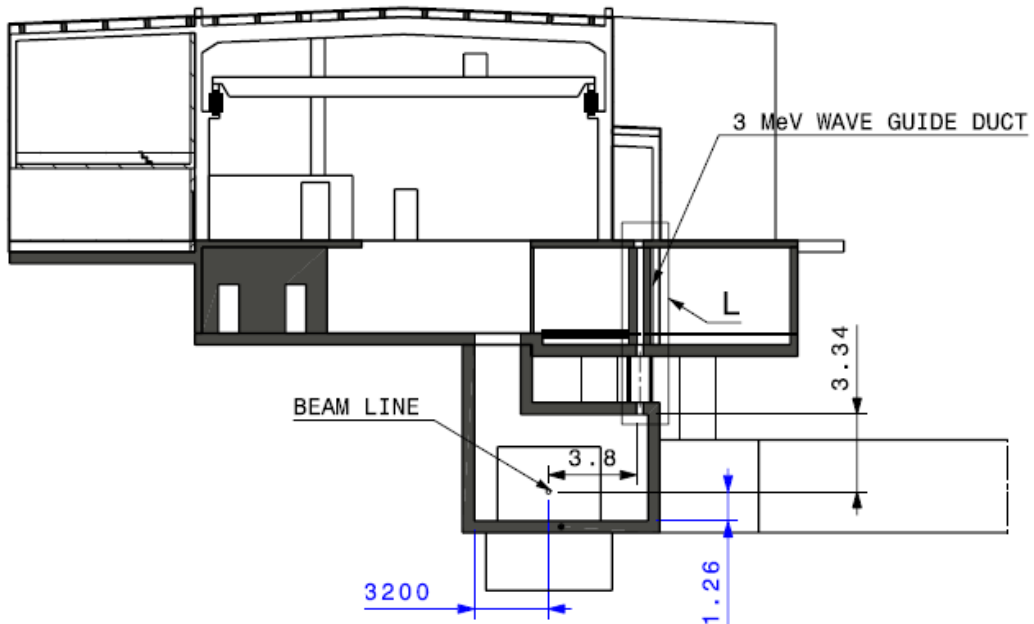


Figure 68 : Cross sectional view of the low-energy end of the linac tunnel, the 3 MeV waveguide duct and the two upper floors (looking downstream).

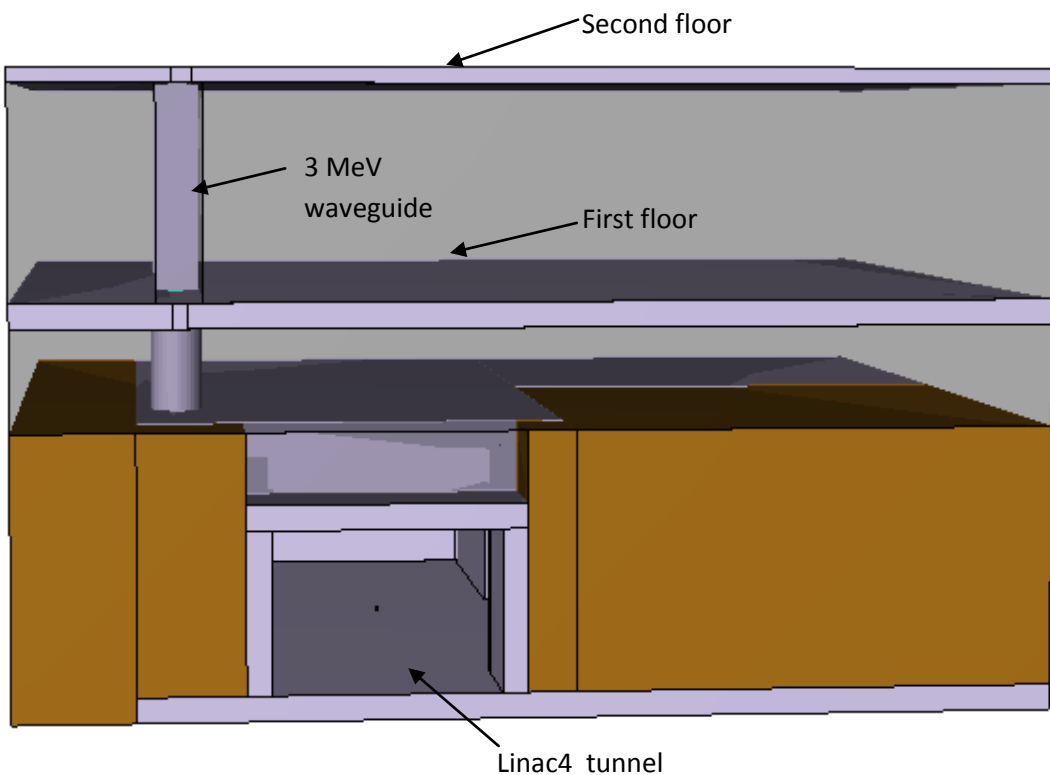


Figure 69 : FLUKA geometry plotted with SimpleGeo (128): cross sectional view of the low-energy section of the Linac4 building. The view looks upstream of the tunnel, towards the beginning of the accelerator.

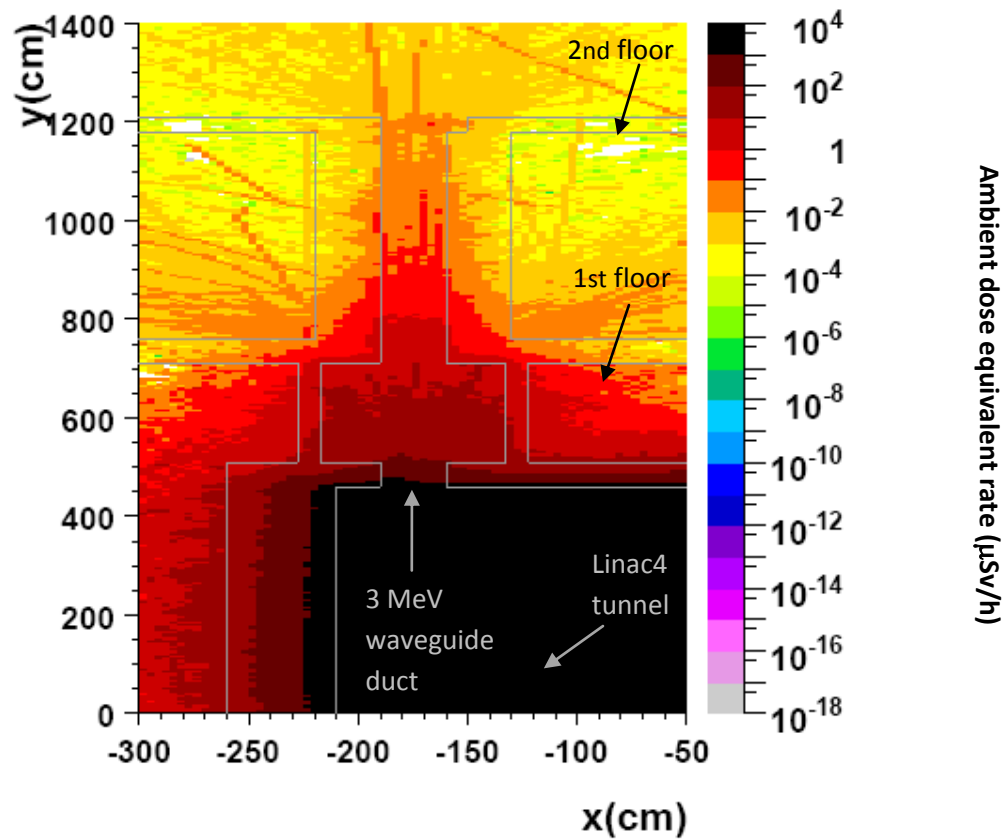


Figure 70 : Neutrons streaming through the 3 MeV waveguide duct. Beam loss in a $5 \times 5 \times 5 \text{ cm}^3$ copper target, 10 W, 11 MeV, placed at the end of the low-energy section of the accelerator. Cross sectional view of the Linac4 tunnel, the 3 MeV waveguide duct and the two upper floors. $H^*(10)$ in $\mu\text{Sv}/\text{h}$. note the different scale for x and y directions.

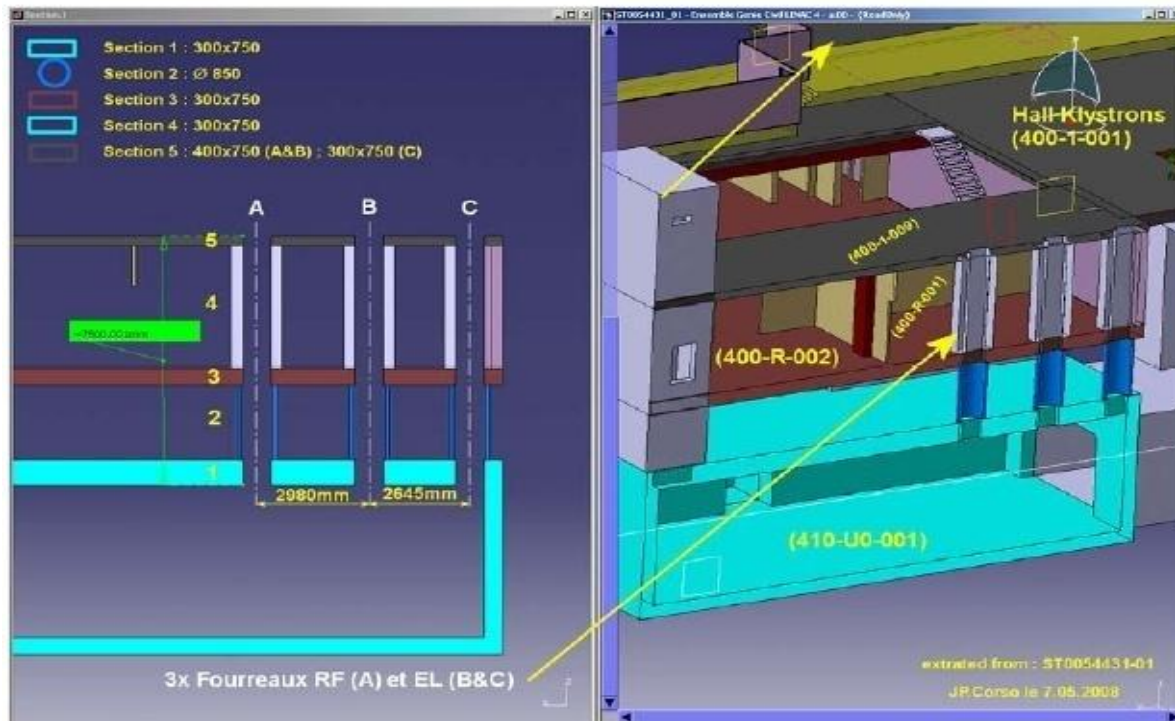


Figure 71 : View of the two 3 MeV waveguide ducts and of the cable duct in the low-energy section of the accelerator.

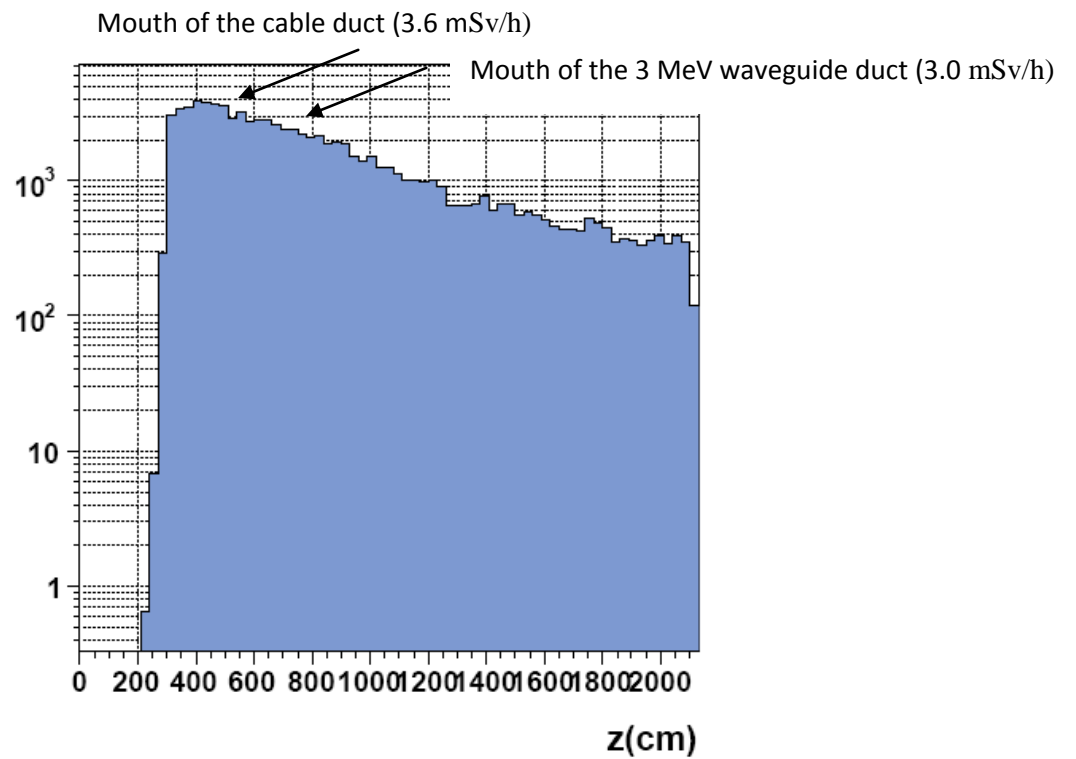


Figure 72 : Radiation level in correspondence of the mouths of the 3 MeV waveguide and cable duct. $H^*(10)$ in $\mu\text{Sv/h}$.

5 Induced radioactivity

Three methods are commonly used for estimating induced radioactivity: 1) multiplication of the density of inelastic interactions (“stars”) with appropriate conversion factors, 2) folding of particle track-length spectra with evaluated isotope production cross sections and 3) explicit Monte Carlo calculations of isotope production from hadronic interaction models. The choice of the method depends on the case to be studied. Conversion factors from star densities are typically used for preliminary estimates and for bulk materials. Folding of track-lengths with energy-dependent cross sections is usually applied to low-density (e.g. gaseous) materials, as long as reliable experimental cross sections are available. Monte Carlo calculations, which are rather time-consuming, can assess the self-absorption in solids with complex geometry and the build-up and decay of radioactivity under arbitrary irradiation cycles. However, they fail in predicting induced radioactivity in gases due to the very low interaction probability. The Monte Carlo technique was used for assessing the induced radioactivity in the accelerator components (Section 5.1), whilst the second approach was retained for the determination of air activation in the Linac4 tunnel (Section 5.2) and in proximity of the dump (Section 5.3).

5.1 Induced radioactivity in the main components of the accelerator

The estimation of the induced radioactivity in the components of the accelerator is particularly important for maintenance interventions and final disposal of radioactive waste. Equipment activation in the Linac4 area will be produced by particle losses. The main cause of particle loss in a linear accelerator are collisions between accelerated particles escaping from the fields generated for controlling the focusing and the acceleration, and the metallic walls of the vacuum chamber. The analysis of particle losses (carried out by the Linac4 design team) and induced radioactivity was done at the highest possible operating beam current, corresponding to the full SPL duty cycle. Several measures have been applied in the design of Linac4 to minimize the beam losses [(43) and (129)]. After the optimization process, a set of multiparticle calculations with random errors have been performed in order to determine the particle loss distribution and their values expected in Linac4. The results for the worst case computation are shown in Fig. 73 extracted from refs. [(43) and (129)].

The beam losses are concentrated in 22 “hot spots” along the machine. The lost beam power ranges from 0.03 W to 0.92 W (worst case, at the end of the CCDTL section). The actual error distribution in the real machine is unpredictable, and the number, position and intensity of the hot spots will be different from the simulated ones. However, taking the worst case over 1500 (for the DTL) and 700 (for the rest of the machine) random error distributions instead of the average, is considered a conservative assumption covering against all possible real cases.

To assess the residual dose rates in the Linac4 tunnel, a series of FLUKA calculations were performed, using a detailed geometrical model of the accelerating structures, based on the current linac layout.

Power lost (watt) vs z (m),
 40 mA, 6% duty cycle, worst case, steerers on
 quad alignment 0.1 mm **1sigma gaussian**, beam error 0.3mm 0.3mrad gaussian

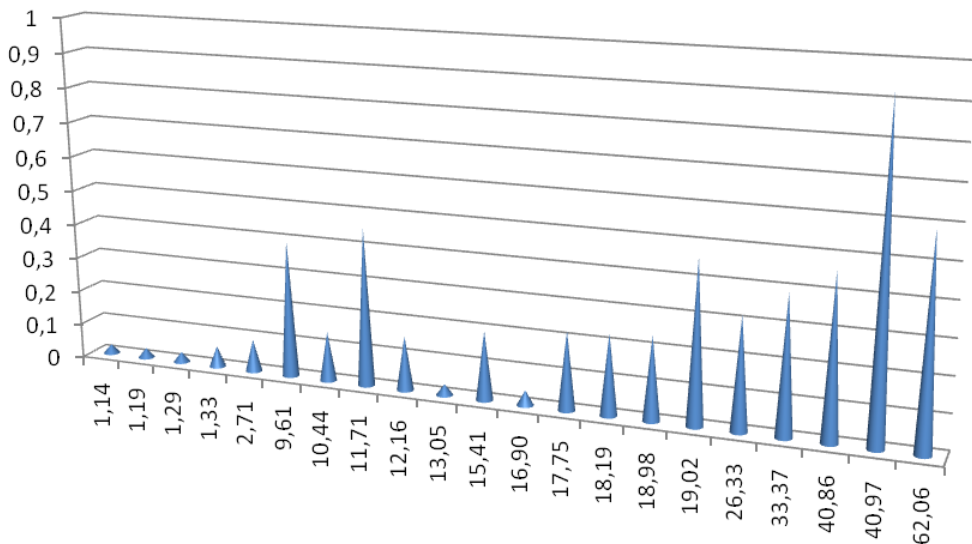


Figure 73 : Lost beam power along Linac4, from the entrance of the DTL (3 MeV) to the end of the PIMS (160 MeV). Losses are localized; the plot shows position and intensity of the loss points in presence of errors, for the worst case, at 6% duty cycle [(43) and (129)].

The geometry implemented in the simulations includes the following structures:

- The DTL (Figs. 74 – 75) consisting of
 - three 5 cm thick tanks made of stainless steel (ST-52)
 - the drift tubes made of copper housing the permanent magnet quadrupoles (PMQs). The quadrupoles of the first tank of the DTL are modeled as cylinders with 90% magnetic material (a samarium-cobalt alloy) and 10% aluminum holder, whereas the quadrupoles of the second and third tank have 50% magnetic material and 50% aluminum. The PMQs are cylinders with inner bore diameter equal to 22 mm and outer diameter equal to 60 mm. The DTL tank1 PMQs are 45 mm long, the DTL tank2 and tank3 PMQs are 80 mm long.
 - the stems used to fix the drift tubes to the girders, with an internal layer (1.25 cm thick) of stainless steel (ST-316L) and an external layer of copper (0.25 cm thick)
 - the girders made of an aluminum alloy (AW-6082)
 - the cooling water inside the drift tubes (0.1 l of water per drift tube) and the tanks (2 l of water per metre)
 - the supports made of stainless steel (ST-37)
 - the waveguides made of stainless steel (ST-304 L)
 - the quadrupoles between the tanks are cylinders with inner bore diameter of 3.4 cm and outer diameter of 10 cm. The cylinders are 11.5 cm long. The total magnetic mass consists of magnetic low-carbon steel (90%) and copper (10%).
 - the vacuum chamber, with inner bore diameter of 3 cm and outer diameter of 3.2 cm, made of stainless steel (ST-316L)

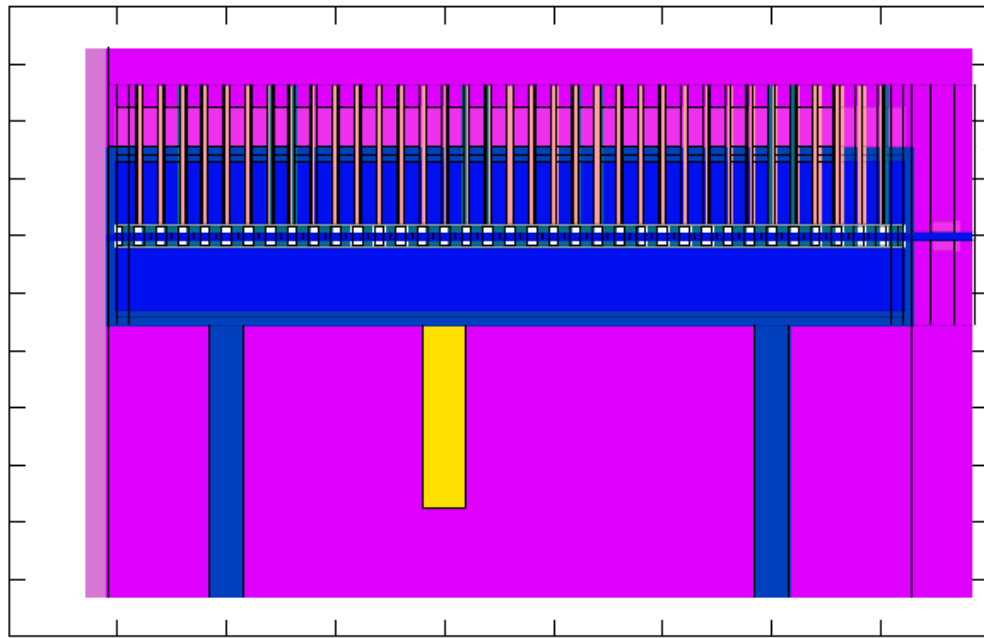


Figure 74 : FLUKA geometry plotted with Gnuplot (130): cross sectional view of the first tank of the DTL.

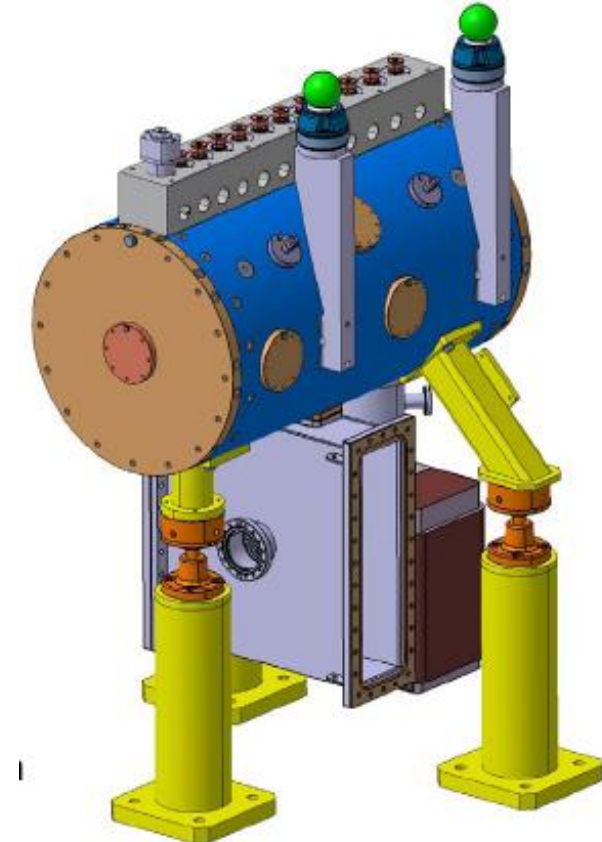


Figure 75 : 3D view of the first tank of the DTL.

- The CCDTL (Fig 76 – 77) consisting of
 - the 1.5 cm thick cavities made of stainless steel (ST-304L)
 - the 30 μm thick copper plating inside the cavity
 - two drift tubes in each cavity made of copper with inner bore diameter of 2.8 cm and outer diameter of 9.5 cm
 - the stems with an internal layer (1.25 cm thick) of stainless steel (ST-316L) and an external layer of copper (0.25 cm thick)
 - the cooling water in the tanks, in the coupling cavities and in the drift tubes. There are 2 litres of water in each module and 0.1 litres of water in each drift tube
 - the supports made of stainless steel (ST-37)
 - the waveguides made of stainless steel (ST-304 L)
 - the quadrupoles between the cavities are cylinders with inner bore diameter of 3.4 cm and outer diameter of 10 cm. The cylinders are 11.5 cm long. The total magnetic mass consists of magnetic low-carbon steel (90%) and copper (10%)
 - the coupling cavities made of stainless steel (ST-304L)
 - the vacuum chamber, with inner bore diameter of 3 cm and outer diameter of 3.2 cm, made of stainless steel (ST-316L)

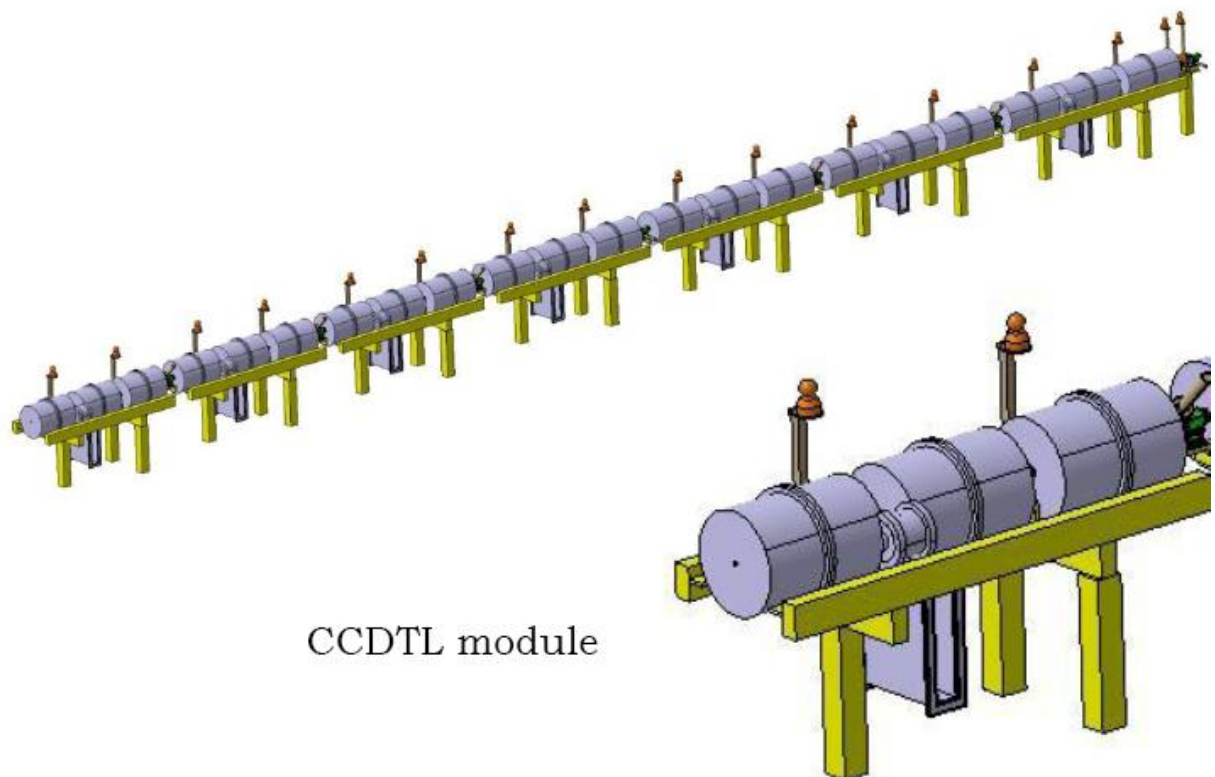


Figure 76 : 3D view of the 7 modules of the CCDTL and close-up view of the first module.

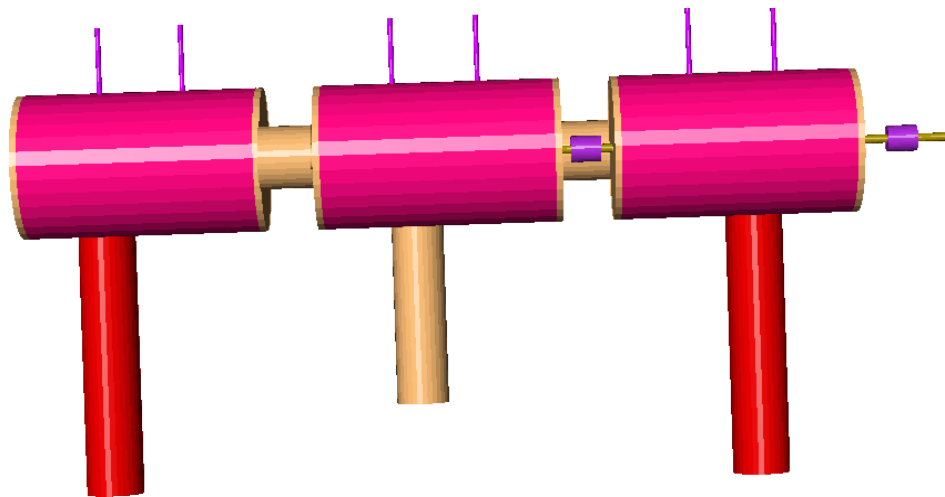


Figure 77 : FLUKA geometry plotted with SimpleGeo (128) of the first module of the CCDTL.

The PIMS (Fig. 78 – 79) consisting of

- 1.9 cm thick tanks made of copper
- 7-cell pi-mode structure consisting of discs and cylinders machined out of solid copper
- the cooling water in the copper structures (2.5 litres per tank)
- the supports made of stainless steel (ST-37)
- the waveguides made of stainless steel (ST-304 L)
- the quadrupoles between the cavities are cylinders with inner bore diameter of 3.4 cm and outer diameter of 10 cm. The cylinders are 11.5 cm long. The total magnetic mass consists of magnetic low-carbon steel (90%) and copper (10%)
- the vacuum chamber, with inner bore diameter of 3 cm and outer diameter of 3.2 cm, made of stainless steel (ST-316L)

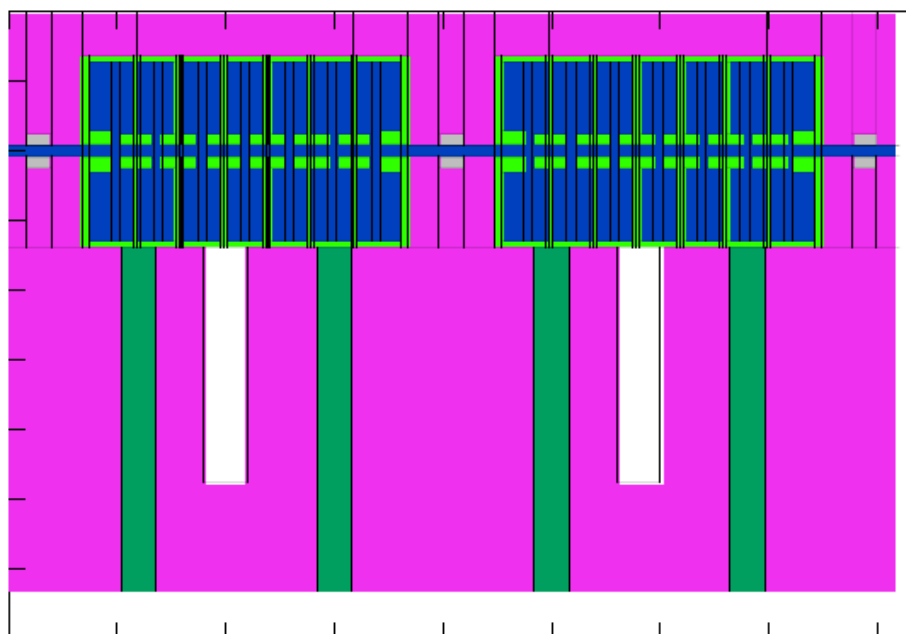


Figure 78 : FLUKA geometry plotted with Gnuplot (130): cross sectional view of two tanks of the PIMS.

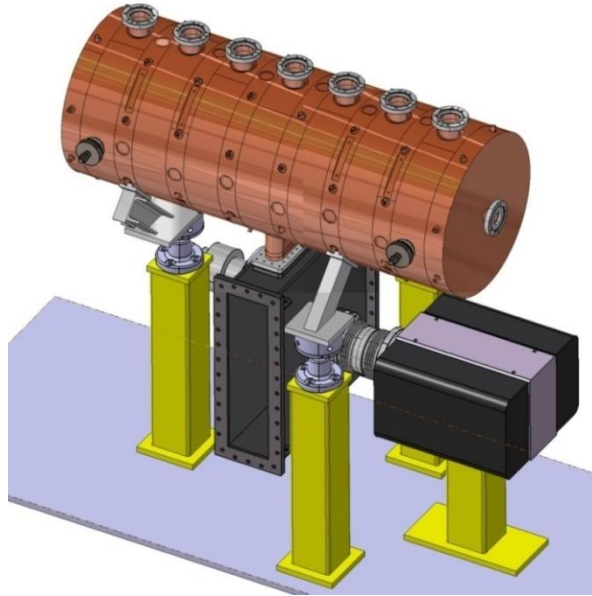


Figure 79 : Tank of the PIMS.

The materials and their compositions are listed in Table 28. The time profile of the irradiation for the FLUKA simulations includes 4 cycles of 9 month operation and 3 month shutdown period, followed by a final 9 month operating period. The residual dose rates in Linac4 were estimated at the SPL duty cycle. The simulations assumed a localized loss of 1 W in three different positions, representative of typical aperture restrictions in the various sections of Linac4: the first drift tube of the third DTL tank at 30 MeV, the quadrupole at 80 MeV within the CCDTL section and the quadrupole at 155 MeV (the last one) within the PIMS section. The ambient dose equivalent rate, $H^*(10)$, due to residual radioactivity was calculated at the height of the tanks for 6 decay times: immediately after the end of the operation and after 1 hour, 6 hours, 1 day, 1 week and 1 month.

The residual dose rates in contact with the tank of the DTL and with electromagnetic quadrupoles in the CCDTL and PIMS sections and at 1 m distance are given in Table 29. An example of the residual dose rate scoring is shown in Fig. 80, while all the dose rate plots are shown in ref. (131) and in figures 1 – 18 of the Appendix A. Whilst in the DTL the dose rates are rather low and pose no major problems from a maintenance point of view, the CCDTL and PIMS cases are more critical. Whereas the DTL quadrupole is shielded by the drift tube and by the tank, the other quadrupoles are directly accessible. Few localized spots at high energy, probably in correspondence of a quadrupole, can become rather radioactive at the end of a run at the SPL duty cycle.

An alternative layout for the CCDTL section, in which two-thirds of the EMQs are replaced by PMQ, was also studied. The PMQs are modeled as cylinders with 30 % magnetic material (the samarium-cobalt alloy in Table 28) and 70 % aluminium holder. The PMQs are cylinders with inner bore diameter equal to 40 mm and outer diameter equal to 85 mm. The CCDTL PMQs are 100 mm long. In this case the residual dose rates in contact with the PMQ body and with the coupling cavity, and at 1 meter distance are listed in Table 30. All the dose rate plots are shown in ref. (132) and in figures 19 – 24 of Appendix A. The dose rates in contact with the PMQs and at 1 m distance from the PMQs are higher than those obtained with the EMQs. Indeed the set of radionuclides produced in the PMQs is completely different from those obtained in the EMQs in the previous study, because of the different material composition (the PMQs are made of the samarium-cobalt alloy and the EMQs of low-carbon magnetic steel).

Table 28 : Materials used for the simulations of induced radioactivity and their compositions.

Material	Density (g/cm ³)	Atom composition (%)	Components
Low carbon magnetic steel	7.8	97.05 Fe, < 0.001 C, < 1.5 Si, < 1.2 Mn, < 0.05 P, < 0.0005 S and < 0.2 Al	Quadrupoles between the CCDTL cavities and the tanks of the PIMS
Samarium-Cobalt alloy	8.4	52.0 Co, 15.0 Fe, 24.0 Sm, 7.0 Cu and 2.0 Zr	Permanent magnet quadrupoles
2024-T351 aluminum alloy	2.78	92.7 Al, 0.1 Cr, 4.55 Cu, 0.5 Fe, 1.5 mg, 0.6 Mn, 0.5 Si, 0.25 Zn and 0.15 Ti	Holders of the permanent magnet quadrupoles
AW-6082 aluminum alloy	2.7	95.95 Al, 0.1 Cu, 0.2 Zn, 1.1 Si, 0.5 Fe, 0.7 Mn, 0.2 Ti, 0.9 Mg and 0.35 Cr	Girders
Copper	8.94	99.99 Cu, 0.0005 O ₂ , 0.0001 Cd, 0.0003 P, 0.0018 S, 0.0001 Zn, 0.0001 Hg, 0.001 Pb, 0.001 Se, 0.001 Te and 0.001 Bi	PIMS discs and drift tubes in the CCDTL and DTL sections
ST-52 steel	7.85	97.55 Fe, 0.22 C, 1.6 Mn, 0.55 Si, 0.04 P, 0.035 S	DTL tanks and supports of the CCDTL modules
ST-304L steel	7.8	68.5 Fe, 0.08 C, 18.8 Cr, 9.5 Ni, 2.0 Mn, 1.0 Si, 0.045 P and 0.03 S	CCDTL tanks and all the waveguides
ST-316L steel	7.8	68.5 Fe, 18.0 Cr, 1.0 Si, 14.0 Ni, 2.5 Mo, 0.045 P, 0.3 C, 0.3 S and 0.11 N	Stems and vacuum chamber
ST-37 steel	7.8	99.879 Fe, 0.055 P, 0.055 S and 0.011 N	Supports of the DTL and PIMS tanks

The radionuclide inventories after one month decay time for the most important components of the accelerator are listed in tables 31 – 34. In the DTL section the most important radionuclides responsible for the residual radioactivity in the drift tubes are ⁶⁵Zn, ⁵⁸Co, ⁶³Ni, ⁶⁰Co and ⁵⁵Fe, while the main contributors to the residual radioactivity in the PMQs are ⁵⁸Co, ⁶⁰Co, ⁵⁷Co, ⁵⁶Co, ⁶⁵Zn, ⁵⁴Mn, ⁵⁵Fe, ²²Na, ¹⁴⁷Eu, ¹⁴⁸Eu, ¹⁴⁹Eu, ¹⁵²Eu, ¹⁵⁵Eu and ¹⁴⁵Sm. In the CCDTL section equipped only with EMQs, the main radionuclides contributing to the residual radioactivity in the vacuum chamber (the loss point) are ⁵⁵Fe, ⁵⁴Mn, ⁵⁷Co, ⁵⁶Co, ⁵¹Cr, ⁴⁹V, ⁵⁸Co, ⁴⁸V, ⁸⁸Y, ⁸⁸Zr, ⁴⁶Sc, ²²Na, ³H and ⁶⁰Co, while the main contributors to the residual radioactivity in the quadrupole adjacent to the vacuum chamber are ⁵⁵Fe, ⁵⁴Mn, ⁵⁶Co, ⁵¹Cr, ⁴⁹V, ⁵⁸Co, ⁶⁵Zn, ⁶³Ni and ⁶⁰Co. In alternative layout of the CCDTL section, the main radionuclides contributing to the residual radioactivity in the vacuum chamber (the loss point) are ⁵⁵Fe, ⁵⁴Mn, ⁵⁷Co, ⁵⁶Co, ⁵¹Cr, ⁴⁹V, ⁵⁸Co, ⁴⁸V, ⁸⁸Y, ⁸⁸Zr, ⁴⁶Sc, ²²Na and ⁶⁰Co, while the main contributors to the residual activity in the PMQ adjacent to the vacuum chamber are ⁵⁵Fe, ⁵⁴Mn, ⁵⁷Co, ⁵⁸Co, ⁶⁰Co, ²²Na, ¹⁴⁹Eu, ¹⁴⁵Sm, ⁵⁶Co and ⁵⁹Fe. In the PIMS section, the most important radionuclides contributing to the residual radioactivity in the vacuum chamber are ⁵⁵Fe, ⁵⁴Mn, ⁵¹Cr, ⁴⁹V, ⁵⁷Co, ⁵⁶Co, ⁸⁸Y, ⁸⁸Zr, ⁵⁸Co, ⁴⁶Sc, ⁴⁵Ca, ³H and ⁶⁰Co, while the main contributors to the residual radioactivity in the quadrupole adjacent to the vacuum chamber are ⁵⁴Mn, ⁵¹Cr, ⁴⁹V, ⁵⁷Co, ⁵⁶Co, ⁵⁵Fe, ⁶⁵Zn, ³H, ⁶⁰Co and ⁶³Ni. The complete radionuclide inventory for all the components in the accelerator is available in refs. [(131) and (132)] and in tables 1 – 18 of Appendix A.

Table 29 : Residual dose rates in the DTL Tank3 (31 MeV), in the CCDTL (80 MeV) and in high-energy end of the PIMS (155 MeV), SPL duty cycle.

Section	Decay time	Residual dose rate in contact ($\mu\text{Sv}/\text{h}$)	Residual dose rate at 1 m distance ($\mu\text{Sv}/\text{h}$)
DTL	0	40 – 50	5 – 10
	1 day	5 – 10	0.1 – 1
	1 month	1 – 5	0.1 – 1
CCDTL	0	7000 – 8000	100 – 200
	1 day	4000 – 5000	90 – 100
	1 month	2000 – 3000	40 – 50
PIMS	0	8000 – 10000	100 – 200
	1 day	4000 – 5000	50 – 100
	1 month	1000 – 2000	30 – 40

Table 30 : Residual dose rate in the CCDTL alternative layout (80 MeV), SPL duty cycle.

Decay time	Residual dose rate in contact with the PMQ ($\mu\text{Sv}/\text{h}$)	Residual dose rate at 1 m from the PMQ ($\mu\text{Sv}/\text{h}$)	Residual dose rate in contact with the coupling cavity ($\mu\text{Sv}/\text{h}$)	Residual dose rate at 1 m from the coupling cavity ($\mu\text{Sv}/\text{h}$)
0	50000 – 60000	300 – 400	1000 – 2000	30 – 40
1 day	30000 – 40000	200 – 300	500 – 700	20 – 30
1 month	10000 – 20000	100 – 200	300 – 400	5 – 10

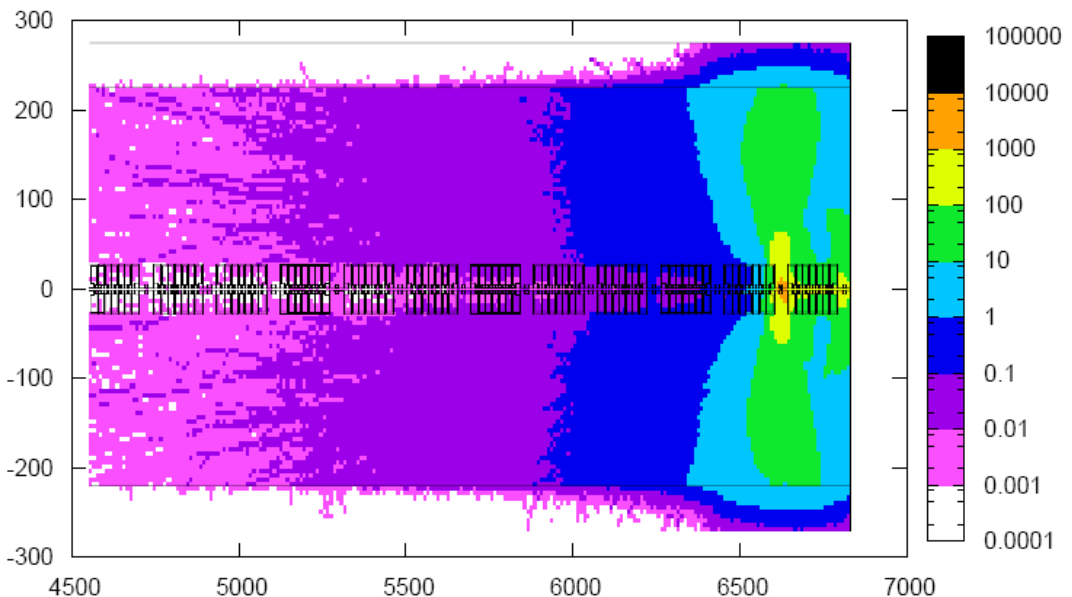


Figure 80 : Residual dose rate in the PIMS after 4 years and 9 months of operation and 1 month decay. 155 MeV, 1 W loss on the vacuum chamber. $H^*(10)$ in $\mu\text{Sv}/\text{h}$.

Table 31 : Specific activity of the most important radionuclides contributing to residual radioactivity in the main components of the DTL section of the accelerator.

Radionuclide ($t_{1/2}$)	Specific activity (Bq/g)				
	Drift tube	PMQ (a)	DTL tank	EMQ downstream of the loss point	Vacuum chamber downstream of the loss point
Na-22 (2.6 y)	-	4.8	-	-	-
Cr-51 (27.7 d)	-	-	-	-	2.88
Mn-54 (312.2 d)	-	12.2	0.35	0.48	-
Fe-55 (2.7 y)	0.97	294.7	1.47	1.03	3.3
Co-56 (78.76 d)	-	129.6	-	-	-
Co-57 (271.3 d)	-	107.2	-	-	-
Co-58 (70.8 d)	16.25	589	-	-	13
Co-60 (5.2 y)	1.97	33	-	-	-
Ni-63 (100 y)	1.2	-	-	-	-
Zn-65 (244 d)	269.4	24	-	-	-
Sm-145 (340 d)	-	26.2	-	-	-
Eu-147 (24.6 d)	-	35	-	-	-
Eu-148 (55.6 d)	-	37.5	-	-	-
Eu-149 (93.1 d)	-	29.9	-	-	-
Eu-152 (13.33 y)	-	6.8	-	-	-
Eu-155 (4.96 y)	-	3.5	-	-	-

(a) This PMQ has been modeled as a cylinder with 50% magnetic material (samarium-cobalt alloy) and 50 % aluminum holder (2024-T351 aluminum alloy).

Table 32 : Specific activity of the most important radionuclides contributing to residual radioactivity in the main components of the CCDTL section of the accelerator (equipped only with EMQs).

Radionuclide ($t_{1/2}$)	Specific activity (Bq/g)			
	Vacuum chamber	EMQ	Wall of the tank	Drift tube
H-3 (12 y)	8092	-	-	-
Na-22 (2.6 y)	2163	-	-	-
Sc-46 (83.8 d)	11473	-	12	-
V-48 (16 d)	37303	-	39.2	-
V-49 (330 d)	298396	40	336	-
Cr-51 (27.7 d)	431816	215	616	-
Mn-54 (312.2 d)	517895	2150	819	42
Fe-55 (2.7 y)	1173508	5300	1785	80
Co-56 (78.76 d)	410298	707	511	80
Co-57 (271.3 d)	296961	-	294	54
Co-58 (70.8 d)	37303	35	105	588
Co-60 (5.2 y)	812	21	2.1	60
Ni-63 (100 y)	-	9.1	-	11.5
Zn-65 (244 d)	-	18.2	-	410
Y-88 (106.6 d)	5138	-	-	-
Zr-88 (83.4 d)	4130	-	-	-

CHAPTER 5 – INDUCED RADIOACTIVITY

Table 33 : Specific activity of the most important radionuclides contributing to residual radioactivity in the main components of the PIMS section of the accelerator.

Radionuclide ($t_{1/2}$)	Specific activity (Bq/g)			
	Vacuum chamber	EMQ	Wall of the tank	Copper structures
H-3 (12 y)	19210	240	-	-
Ca-45 (163 d)	3070	-	-	-
Sc-46 (83.8 d)	24920	-	-	-
V-49 (330 d)	364980	2280	-	-
Cr-51 (27.7 d)	386930	3640	-	-
Mn-54 (312.2 d)	340280	11630	11.4	174
Fe-55 (2.7 y)	708010	22930	19.2	333.6
Co-56 (78.76 d)	192100	4050	12	282
Co-57 (271.3 d)	197850	500	69.6	1032
Co-58 (70.78 d)	26780	400	103	1004.4
Co-60 (5.2 y)	820	66	30	120
Ni-63 (100 y)	-	16	7.2	16.8
Zn-65 (244 d)	-	110	14.4	252
Y-88 (106.6 d)	9550	-	-	-
Zr-88 (83.4 d)	7440	-	-	-

Table 34 : Specific activity of the most important radionuclides contributing to residual radioactivity in the main components of the CCDTL section of the accelerator (equipped with PMQs).

Radionuclide ($t_{1/2}$)	Specific activity (Bq/g)			
	Vacuum chamber	PMQ (a)	Wall of the tank	Drift tube
Na-22 (2.6 y)	3038	224	-	-
Sc-46 (83.8 d)	15967	-	30.1	-
V-48 (16 d)	52290	-	109.2	-
V-49 (330 d)	418726	-	889	-
Cr-51 (27.7 d)	592144	-	1750	-
Mn-54 (312.2 d)	713741	224	2233	4.9
Fe-55 (2.7 y)	1601964	385	5201	12.6
Co-56 (78.76 d)	549850	93.8	1645	7
Co-57 (271.3 d)	407099	457.8	847	76.3
Co-58 (70.78 d)	51492	1281	238	118.3
Fe-59 (45 d)	-	90.3	-	-
Co-60 (5.2 y)	1113	89.6	4.2	14.7
Ni-63 (100 y)	-	-	-	3.5
Zn-65 (244 d)	-	-	-	123.9
Y-88 (106.6 d)	7084	-	-	-
Zr-88 (83.4 d)	5761	-	-	-
Sm-145 (340 d)	-	88.2	-	-
Eu-149 (93.1d)	-	30.8	-	-

(a) This PMQ has been modeled as a cylinder with 30% magnetic material (samarium-cobalt alloy) and 70 % aluminum holder (2024-T351 aluminum alloy).

5.2 Air activation in the accelerator tunnel

The track-length spectra were individually calculated by FLUKA for all air regions in the accelerator tunnel. The contribution from different regions were summed to obtain the total track-length spectra for neutrons, protons and charged pions. The yield Y_i of radionuclide i is then obtained by folding these spectra with energy-dependent partial cross-sections summed over all target nuclei and hadron components in the cascade

$$Y_i = \sum_{j,k} n_j \int \sigma_{ijk} (E) \Lambda_k (E) dE \quad (43)$$

Here n_j is the atomic concentration (per cm^3) of element j in the material and σ_{ijk} is the cumulative cross-section for the production of radionuclide i in the reaction of a particle of type k and energy E with a nucleus of element j . The quantity Λ_k is the sum of the track-lengths (in cm) of the hadrons of type k and energy E . A database with evaluated neutron, proton and charged pion interaction cross-sections which govern the conversion of the air constituents (^{14}N , ^{16}O and ^{40}Ar) into the radionuclide of interest by the various particles is available (25) and was used in a post-processing together with track-length spectra from the FLUKA simulations.

A section of the 91.5 m long accelerator tunnel was modelled with a cartesian geometry with beam direction along the z -axis. Most of the tunnel is air (density = 0.001205 g/cm^3 , volume = $1.46 \times 10^9 \text{ cm}^3$) with the following composition (weight fraction): nitrogen (75.558 %), oxygen (23.159 %) and argon (1.283 %). Taking into account the particle loss distribution described in Fig.73, the total beam loss in the tunnel is roughly 10 W. This scenario was studied for three different beam energies: 50, 100 and 160 MeV. To evaluate the worker exposure during access after shutdown the activities of airborne radionuclides have to be estimated based on the accelerator operational conditions. Assuming a continuous loss of a 10 W beam ($N_p = 1.25 \times 10^{12} \text{ protons/s}$ at 50 MeV; $N_p = 6.24 \times 10^{11} \text{ protons/s}$ at 100 MeV; $N_p = 3.9 \times 10^{11} \text{ protons/s}$ at 160 MeV), the saturation activity (A_s) for different radionuclides can be calculated from their yields: $A_s = Y N_p$. It was assumed that there is no ventilation during the operation of the accelerator and that the worker intervention lasts 1 hour. Several scenarios of irradiation and cooling times were considered. The activity for one single radionuclide after an irradiation time t_{irr} and a cooling time t_{cool} is:

$$A_0 (t_{\text{irr}}, t_{\text{cool}}) = Y N_p (1 - e^{-\lambda t_{\text{irr}}}) e^{-\lambda t_{\text{cool}}} \quad (44)$$

If the activity is mixed homogeneously in the tunnel, the activity concentration is obtained by dividing the activity by the volume of air. Both the internal exposure by inhalation and the external exposure must be evaluated. To estimate the inhalation dose received by a worker it is necessary to multiply the calculated activities by the breathing rate B_r and the inhalation activity-to-dose conversion factors e_{inh} (expressed in Sv/Bq), which in the present study were taken from the Swiss ordinance (133):

$$D_0 (t_{\text{irr}}, t_{\text{cool}}) = \frac{A_0 (t_{\text{irr}}, t_{\text{cool}}) e_{\text{inh}} B_r}{V_{\text{air}}} \quad (45)$$

The standard breathing rate for a worker is $1.2 \text{ m}^3/\text{h}$. In order to estimate the total dose per intervention, the equation

$$D_i(t) = D_0 (t_{\text{irr}}, t_{\text{cool}}) e^{-\lambda t} \quad (46)$$

must be integrated over the intervention time t_{int} . The inhalation dose received by a person intervening in the accelerator tunnel for t_{int} after a cooling time t_{cool} is:

$$D(t_{int}) = \frac{D_0(t_{irr}, t_{cool})(1 - e^{-\lambda t_{int}})}{\lambda} \quad (47)$$

The values of inhalation doses obtained for the three scenarios (50, 100 and 160 MeV proton energy), with two irradiation times (1 day and 1 week) and three waiting times (0, 10 minutes and 1 hour) are given in Table 35. Only the nuclei that give relevant contribution to the dose are listed. For the evaluation of the effective dose³ for external exposure, the conversion coefficients for air submersion listed in TABLE III-1 of ref. (134) were used. For each radionuclide, values for the organ equivalent dose coefficient h_T and for the effective dose coefficient h_E , based upon the weighting factors of the ICRP60 (135), are given in SI units. The coefficients are for air at a density of 1.2 kg m^{-3} . Both coefficients are expressed in Sv per Bq.s.m^{-3} . Note that h_E does not include the skin contribution and, being 0.01 the weighting factor for the skin, to obtain the real effective dose coefficient one must consider $h_{tot} = h_E + 0.01 h_{skin}$. To estimate the effective dose per unit time-integrated for external exposure received by the worker it is necessary to multiply the activity by h_{tot} .

In order to estimate the total effective dose per intervention, the equation

$$\frac{dD}{dt} = \frac{A(t_{irr}, t_{cool}) h_{tot} e^{-\lambda t}}{V_{air}} \quad (48)$$

must be integrated over the intervention time. The effective dose for external exposure received by a person intervening in the accelerator tunnel for t_{int} after a cooling time t_{cool} is:

$$D(t_{int}) = \frac{A(t_{irr}, t_{cool}) h_{tot} (1 - e^{-\lambda t_{int}})}{\lambda V_{air}} \quad (49)$$

The values of effective doses for external exposure obtained for the three scenarios (50, 100 and 160 MeV proton energy), with two irradiation times (1 day and 1 week) and three waiting times (0, 10 minutes and 1 hour) are given in Table 36. Only the nuclei that give a relevant contribution to the dose are listed.

The effective doses from external exposure are much higher than the inhalation doses. Nevertheless, the total dose received by a worker intervening in the tunnel is small for all energies. The dose does not change much with increasing energy, because the number of lost proton correspondingly decreases and because of the limited contribution of spallation products to the gas activation in this range of energies.

³ The effective dose, recommended by the International Commission on Radiological Protection (ICRP), is the sum of organ equivalent doses weighted by corresponding tissue weighting factors, w_T .

Table 35 : Dose received from internal exposure by a worker intervening in the Linac4 tunnel.**Inhalation dose (μSv), $\text{Ep} = 50 \text{ MeV}$, intervention time = 1 hour, 10 W total proton beam loss in the tunnel**

t_{irr}	1 day	1 day	1 day	1 week	1 week	1 week
t_{cool}	0	10 min	1 hour	0	10 min	1 hour
^{11}C	0.06	0.04	-	0.06	0.04	-
^7Be	-	-	-	0.04	0.04	0.04
^{32}P	0.01	0.01	0.01	0.06	0.06	0.06
^{33}P	-	-	-	0.01	0.01	0.01
Total dose	0.09	0.07	0.03	0.19	0.17	0.13

Inhalation dose (μSv), $\text{Ep} = 100 \text{ MeV}$, intervention time = 1 hour, 10 W total proton beam loss in the tunnel

t_{irr}	1 day	1 day	1 day	1 week	1 week	1 week
t_{cool}	0	10 min	1 hour	0	10 min	1 hour
^{11}C	0.03	0.02	-	0.03	0.02	-
^7Be	-	-	-	0.02	0.02	0.02
^{32}P	0.01	0.01	0.01	0.04	0.04	0.04
^{33}P	-	-	-	0.01	0.01	0.01
Total dose	0.04	0.04	0.02	0.10	0.09	0.08

Inhalation dose (μSv), $\text{Ep} = 160 \text{ MeV}$, intervention time = 1 hour, 10 W total proton beam loss in the tunnel

t_{irr}	1 day	1 day	1 day	1 week	1 week	1 week
t_{cool}	0	10 min	1 hour	0	10 min	1 hour
^{11}C	0.01	0.01	-	0.01	0.01	-
^{39}Cl	0.01	0.01	-	0.01	0.01	-
^7Be	-	-	-	0.01	0.01	0.01
^{32}P	0.01	0.01	0.01	0.05	0.05	0.05
^{33}P	-	-	-	0.01	0.01	0.01
Total dose	0.04	0.04	0.02	0.10	0.10	0.08

Table 36 : Effective dose received from external exposure by a worker intervening in the Linac4 tunnel.

External exposure effective dose (μSv), $E_p = 50 \text{ MeV}$, intervention time = 1 hour, 10 W proton beam loss in the tunnel

t_{irr}	1 day	1 day	1 day	1 week	1 week	1 week
t_{cool}	0	10 min	1 hour	0	10 min	1 hour
^{11}C	2.92	2.08	0.38	2.92	2.08	0.38
^{13}N	1.24	0.62	0.02	1.24	0.62	0.02
^{15}O	0.17	-	-	0.17	-	-
^{41}Ar	0.14	0.14	0.10	0.14	0.14	0.10
Total dose	4.50	2.85	0.50	4.50	2.86	0.51

External exposure effective dose (μSv), $E_p = 100 \text{ MeV}$, intervention time = 1 hour, 10 W proton beam loss in the tunnel

t_{irr}	1 day	1 day	1 day	1 week	1 week	1 week
t_{cool}	0	10 min	1 hour	0	10 min	1 hour
^{11}C	1.23	0.87	0.16	1.23	0.87	0.16
^{13}N	0.47	0.23	-	0.47	0.23	-
^{15}O	0.07	-	-	0.07	-	-
^{41}Ar	0.32	0.30	0.22	0.32	0.30	0.22
^{39}Cl	0.01	0.01	-	0.01	0.01	-
Total dose	2.11	1.43	0.40	2.11	1.44	0.40

External exposure effective dose (μSv), $E_p = 160 \text{ MeV}$, intervention time = 1 hour, 10 W proton beam loss in the tunnel

t_{irr}	1 day	1 day	1 day	1 week	1 week	1 week
t_{cool}	0	10 min	1 hour	0	10 min	1 hour
^{11}C	0.71	0.50	0.09	0.71	0.50	0.09
^{13}N	0.41	0.21	-	0.41	0.21	-
^{15}O	0.05	-	-	0.05	-	-
^{41}Ar	0.51	0.48	0.35	0.51	0.48	0.35
^{38}Cl	0.02	0.01	-	0.02	0.01	-
^{39}Cl	0.03	0.02	0.01	0.03	0.02	0.01
Total dose	1.73	1.23	0.47	1.73	1.23	0.47

5.3 Air activation in proximity of the dump

The Linac4 line is terminated with an absorber block to collect the beam during commissioning and in the event of magnet failure. The beam dump should consequently withstand the power deposited by one or more entire pulses (see Table 37 and ref. (136)). The present study considers a stack of equally-spaced thin metallic foils cooled by a forced air flow, proposed in order to enhance the core-to-air exchange surface.

All the accelerator components will be located in the Linac4 tunnel, 12 m below ground level, approximately 100 m long, 4.45 m wide and 3.20 m high. The Linac4 dump shall be situated at the intersection of the Linac4 tunnel with the Linac4 transfer line, after the bending magnet for beam delivery.

Table 37 : Summary of the LINAC4 dump irradiation scenarios considered in the present simulations. Only the commissioning and the “0-cycle” scenarios are relevant for activation estimates.

	commissioning	Scenario “0-cycle”	accident
Peak current [mA]	40	40	40
Pulse duration [μ s]	50	50	400
Repetition rate [Hz]	1	1/12	1
Duty cycle [Hz]	0.005	~0.0004	0.04
Timing	4 months 12 hours per day	9 months per year 24 hours per day	2-3 shots Once a month (max)
Total number of protons	$6.57 \cdot 10^{19}$	$2.47 \cdot 10^{19}$	$2-3 \cdot 10^{14}$
Average current [protons s^{-1}]	$6.25 \cdot 10^{12}$	$1.04 \cdot 10^{12}$	/
Irradiation time [s]	$1.05 \cdot 10^7$	$2.36 \cdot 10^7$	/

5.3.1 Simulation set-up

The simulations were performed with FLUKA [(59) and (17)] (development version FLUKA 2008). The quantities of interest are the ambient dose equivalent after different cooling times and the activities of radionuclides ejected from the Linac4 tunnel by the ventilation system during operation, as well as those present in the dump cave at the shutdown.

For an accurate description of all the nuclear processes relevant for isotope production, the evaporation of heavy fragments and the coalescence mechanism were explicitly turned on via two separated PHYSICS cards. The card DEFAULTS was used, setting defaults for precision simulations. Neutron transport below 20 MeV was performed using the multi-group approach, updated to the new 260 group library. The transport threshold for electrons/positrons and photons was 1 and 0.1 MeV, respectively, decreased by a factor of 10 for electromagnetic radiation originated by decayed nuclei at the requested cooling times.

Three scenarios have been envisaged for the LINAC4 dump irradiation (see Table 37): a 4 month commissioning, a “0-cycle” operation (planned to be of 9 months per year), and an accident case. This last is not relevant for activation estimates, but it is the most severe one from the point of view of thermo-mechanical stress induced in the dump by single shots.

In order to evaluate residual dose rates, an irradiation profile with the commissioning scenario followed by the “0-cycle” scenario after a pause of 1 month, was implemented in FLUKA via the IRRPROFI card. The pulse structure of the beam was not considered, but the average current of each scenario, preserving the integrated number of impinging protons as listed in Table 37. The

residual dose rates were calculated for two different sets of cooling times, one for each considered scenario:

Commissioning scenario: at the irradiation end (actually 1 s later, in order to prevent from falling in the irradiation period due to computational accuracy), after 1 week and after 1 month (actually 100 s before the beginning of the “0-cycle” operation for the same reason above);

“0-cycle” scenario: at the irradiation end, after 1 week, after 1 month, after 3 months and after 1 year.

The geometry model

The core of the dump is composed by a stack of 150 metallic foils, each 300 μm thick and with a 8 cm-side squared transverse section, made of a special iron alloy, whose composition is given in Table 38. The effective length is thus 4.5 cm. The foils are inter-spaced by a 3 mm gap for forced air cooling. Consequently the actual length of the dump (from the first foil to the last one, both included) is 49.2 cm. The foils were modelled through the LATTICE option: only a stack with the first 10 foils of the dump was implemented by scratch as prototype, whereas all other foils were replicas of such a prototype. The foils lies in an air chamber (see air composition in Table 39) the transverse section of which is 20 cm-side squared and centred on the beam axis (as the foils). Its length is 60 cm, starting 10 cm upstream of the first foil. No dump support was implemented since it had not yet been designed. Once a design will be available, simulations assessing its contribution to residual dose rates and air activation should be performed.

Table 38 : Composition and density of the iron alloy of the foils used in the FLUKA simulations.

Element	Weight fraction
Al	5.0 %
Cr	22.0 %
Fe	72.8 %
Y	0.1 %
Zr	0.1 %
Density: 7.22 g cm^{-3}	

Table 39 : Composition and density of the air used in the FLUKA simulations.

Element	Weight fraction
N	75.53 %
O	23.16 %
Ar	1.31%
Density : 1.225 mg cm^{-3}	

A 1.5 m-thick shielding made of concrete (the composition of which is given in Table 40) surrounds the air chamber. It is provided with a hole (40 mm in diameter, filled with air) to let the beam impinging on the dump core. Due to its size and to the proton energy, the concrete shielding was provided with an intense biasing based on region importance, in order to increase particle statistics along its walls and outside. The proton energy is 160 MeV, the energy spread and the beam divergence are negligible. Figure 81 shows a 3D view of the beam dump cave as implemented in FLUKA, with the central concrete block (the dump shielding) provided with the hole for the beam (enlarged in order to be clearly visible). The yellow arrow shows the beam direction, though, as already mentioned, in the simulations the 160 MeV proton beam is assumed to start very close to

the dump core, i.e. inside the air chamber. The concrete walls of the cave were implemented as well, in order to take into account the contribution of backscattered particles to ambient dose equivalent and air activation. The elemental composition is the same as for the dump shielding (see Table 40). Figure 82 shows a 3D view of the dump core in the air chamber surrounded by the concrete shielding.

Table 40 : Composition and density of the concrete of the shielding and the cave.

Element	Weight fraction	Element	Weight fraction	Element	Weight fraction
H	0.600 %	C	5.62 %	O	49.2875 %
Na	0.453 %	Mg	0.663 %	Al	2.063 %
Si	18.867 %	K	0.656 %	Ca	20.091 %
Fe	1.118 %	P	0.048 %	S	0.012 %
Ti	0.347 %	Mn	0.0387 %	Zn	0.0241 %
Zr	0.0074 %	Ba	0.0179 %	Pb	0.0464 %
Sr	0.399 %	Eu	0.42 ppm		
Density: 2.42 g cm ⁻³					

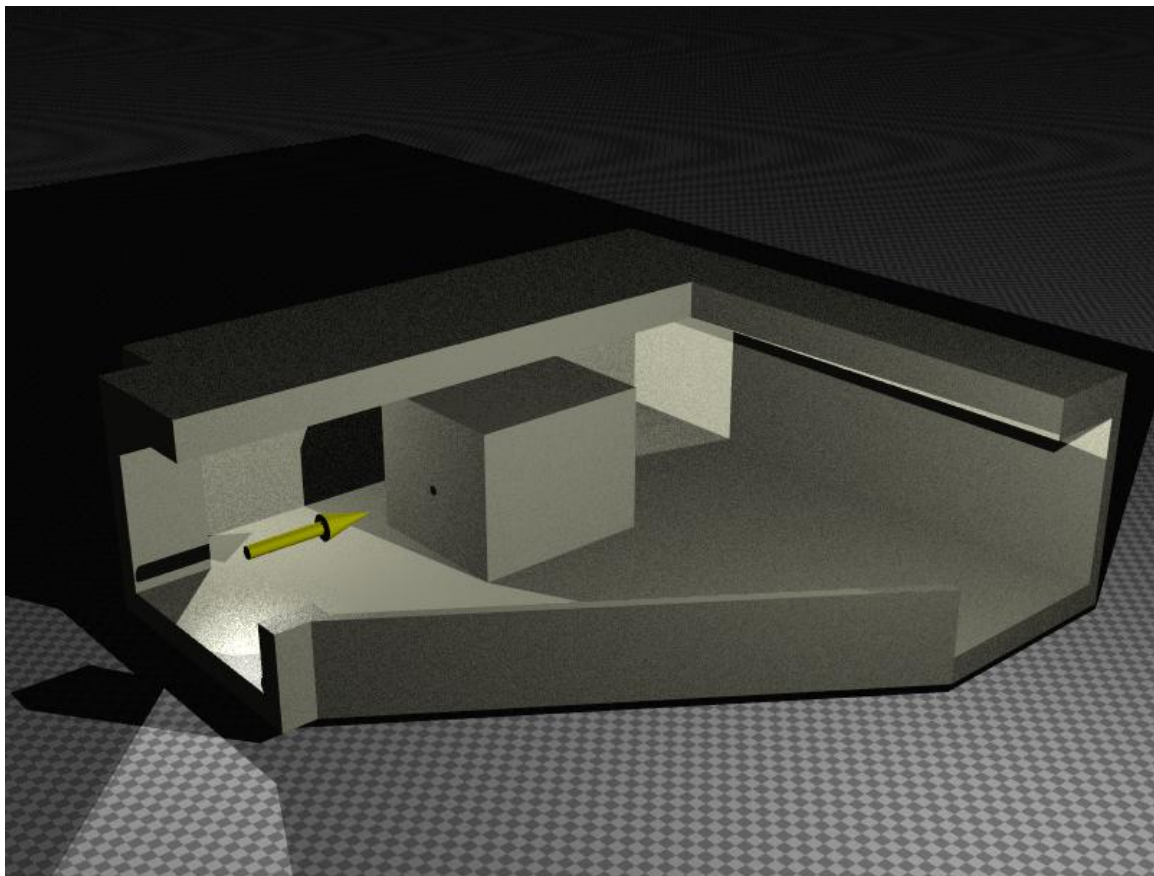


Figure 81 : The Linac4 dump cave as implemented in FLUKA, with the central concrete block for shielding the dump core. The hole for the proton beam (the axis of which is indicated by the yellow arrow) has been enlarged for being visible.

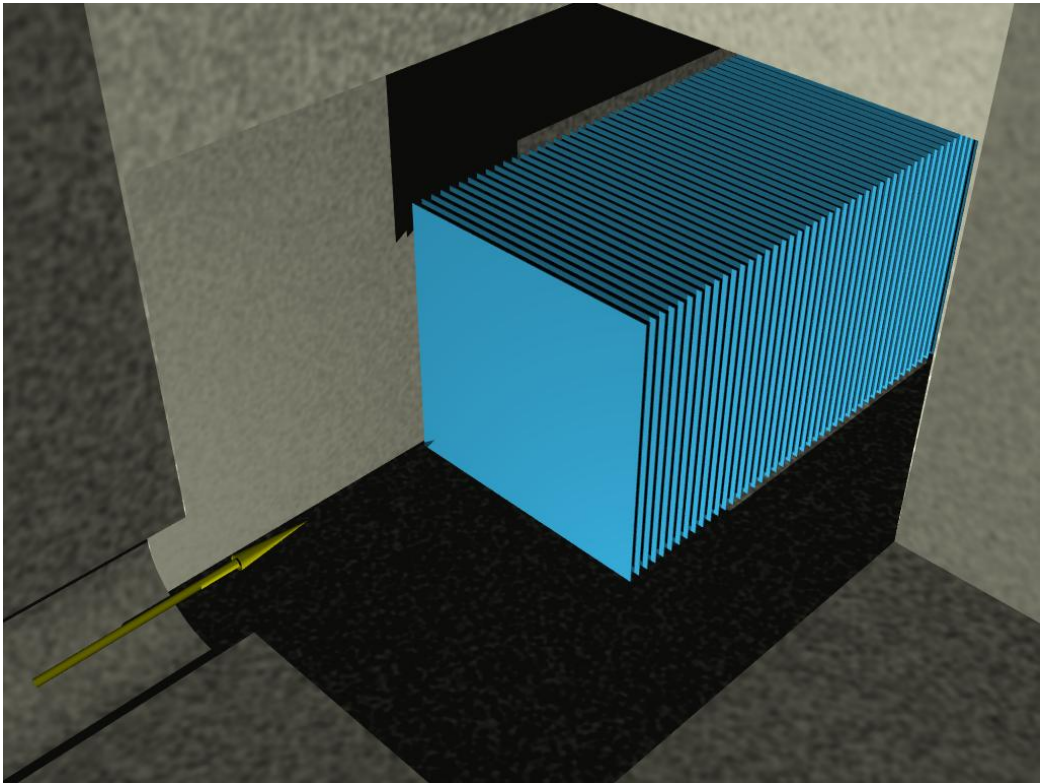


Figure 82 : FLUKA implementation of the dump core consisting of a stack of air cooled thin foils placed inside a concrete shielding block. The yellow arrow indicates the axis of the beam, coming from the upstream bending magnet (when this is switched off) through the hole in the concrete.

5.3.2 *Residual dose rate*

The residual dose rates were scored by means of a fluence detector (USRBIN card) with a Cartesian binning, covering all the volume inside the dump cave with bins of cubic shape and 10 cm-side. The special routine deq99c.f (137) was linked into the FLUKA executable in order to convert run time fluence values into ambient dose equivalent values (as invoked by the AMB74 code in the SDUM of the USRBIN card), given in pSv s^{-1} . A dedicated detector was used for each cooling time (see Section 5.3.1).

Commissioning scenario

Figure 83 shows the residual dose rates 1 month after the end of commissioning run (see Table 37 for details about this scenario) averaged over 20 cm in the vertical direction at the beam height. As expected, the highest values outside the dump shielding are in correspondence of the hole in the concrete (“upstream” location) and of the back side of the shielding (“downstream” location). The former location is heavily affected by the radiation directly coming from the activated dump, whereas the latter is affected by the activation of the concrete shielding, showing a component of fast decaying nuclei. Table 41 shows the residual dose rates in these two locations for each cooling time.

“0-cycle” scenario

Figure 84 shows the residual dose rates 3 months after a “0-cycle” operation (see Table 37 for details about this scenario), averaged over 20 cm in the vertical direction at the beam height. The highest values outside the dump shielding are at the same “upstream” and “downstream” locations as before and are listed in Table 42 as a function of cooling time. Figure 85 shows the residual dose

rates along the beam axis (averaged over $-10 \text{ cm} < x < 10 \text{ cm}$ and $-10 \text{ cm} < y < 10 \text{ cm}$) for the different cooling times. It can be seen that the dose rate, downstream of the dump shielding (where it is dominated by the residual activity of the concrete), has a very significant decrease already one week after the shutdown, and then it remains almost stable. On the contrary, where it is dominated by the residual activity in the dump core, its decrease with the cooling time is more regular.

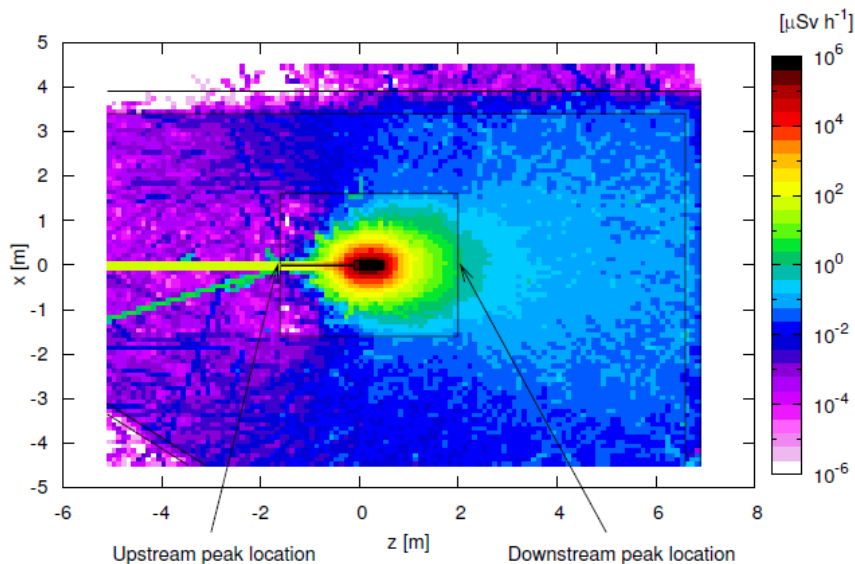


Figure 83 : Residual dose rate 1 month after the commissioning end, vertically averaged over 20 cm at the beam height.

Table 41 : Residual dose rates along the beam axis (vertically and horizontally averaged over a 20 cm side square) at the “upstream” and “downstream” locations for each cooling time after the end of commissioning.

Cooling time	Upstream location		Downstream location	
	Residual dose rate [$\mu\text{Sv h}^{-1}$]	Statistical error [%]	Residual dose rate [$\mu\text{Sv h}^{-1}$]	Statistical error [%]
1 s	470	9	180	3
1 week	174	15	1.5	4
1 month	81	9	1.2	4

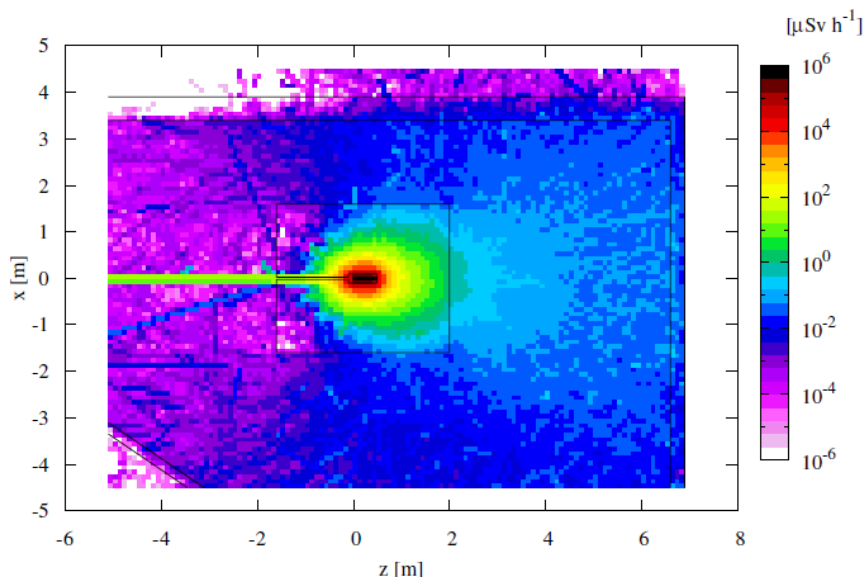


Figure 84 : Residual dose rates 3 month after a “0-cycle” operation vertically averaged over 20 cm at the beam height.

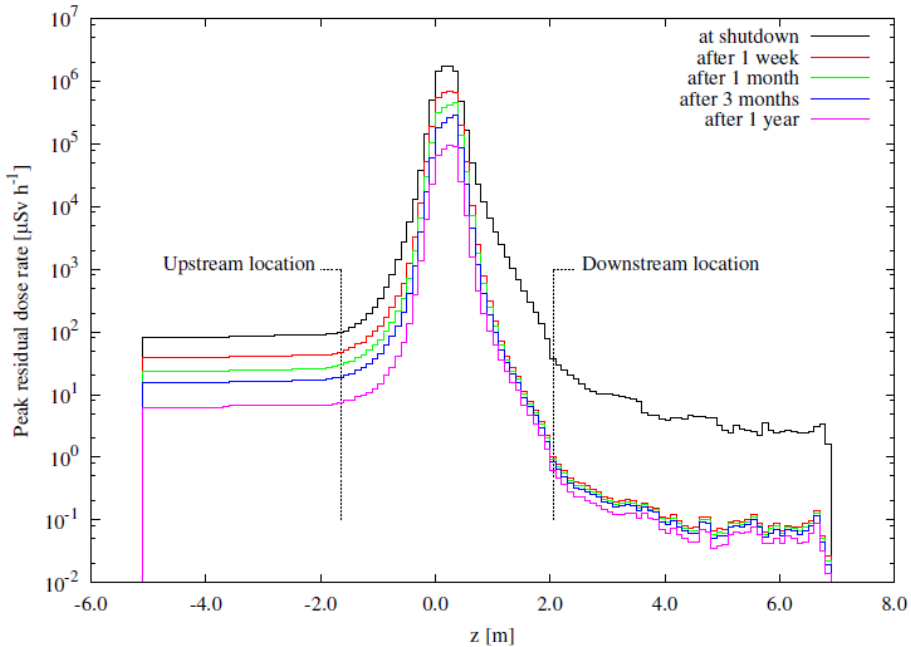


Figure 85 : Residual dose rates along the beam axis (vertically and horizontally averaged over a 20 cm side square) for the considered cooling times after the end of a “0-cycle” operation. The dashed lines indicate the shielding limits.

Table 42 : Residual dose rates along the beam axis (vertically and horizontally averaged over a 20 cm side square) at the “upstream” and “downstream” locations for each cooling time after a “0-cycle” operation.

Cooling time	Upstream location		Downstream location	
	Residual dose rate [μSv h⁻¹]	Statistical error [%]	Residual dose rate [μSv h⁻¹]	Statistical error [%]
0 s	98	10	37	3
1 week	47	15	1.0	4
1 month	29	17	0.9	4
3 months	19	18	0.8	4
1 year	7	23	0.6	4

5.3.3 Air activation

Due to the very low interaction probability of particles in air, the calculation of air activation had to be carried out in two steps. The energy distribution of hadron fluence in air was scored run time, and folded afterwards with the cross sections for radioisotope production on the target nuclei in the air compound. A dedicated set of track-length estimators was implemented in the FLUKA input file for each of the three regions containing air (the region surrounding the dump foils inside the concrete shield, the hole in the concrete shield, and the region surrounding the concrete shield). Such estimators are represented by USRTRACK cards for protons and neutrons. Most of the scored track-length is obviously located in the region inside the concrete shield, though it represents only less than 10^{-4} of the irradiated volume, corresponding to the union of the three mentioned geometry regions (about 360 m^3). As a consequence, the presence of the dump support could in principle impact the track-length spectrum and thus its effect should be checked through future simulations. The activity of a radioisotope in the dump cave at the end of the irradiation period T is given by

$$A_T = A_S (1 - \exp(-\lambda + m_{on})T) \quad (50)$$

where λ is the decay probability per unit time and m_{on} is the relative air exchange rate during irradiation, giving the fraction of the total air volume renewed per unit time. We assume that the ventilation system of the Linac4 tunnel provides a recycling of 1000 m^3 per hour out of a total air volume of 1800 m^3 . A_s is the saturation activity (138):

$$A_s = \frac{V\lambda}{\lambda+m_{on}} \sum_{P,T,j} \phi_P(E_j) \sigma_{P,T}(E_j) N_T(\Delta E)_{j,P} \quad (51)$$

where the sum has to be performed over the produced hadron species P (just protons and neutrons in our case), the target nuclear species T in air (^{12}C , ^{14}N , ^{16}O , and ^{40}Ar), and all the bins j into which the hadron energy range has been divided. V is the irradiated air volume, ϕ is the differential fluence rate (given by FLUKA in $\text{cm}^{-2} \text{ GeV}^{-1}$ per primary and to be scaled by the average proton current), σ is the production cross section for the considered radioisotope, and N_T is the number of target nuclei per unit volume, calculated from the detailed air composition given in Table 43. Table 44 and 45 (third column) list the residual activity A_T of the radioactive species present in the air at the end of commissioning.

For each radioisotope, the total amount of activity released into atmosphere all along the irradiation period T is

$$A_{on} = m_{on} A_s \left(T - \frac{1 - \exp(-(\lambda+m_{on})T)}{\lambda+m_{on}} \right) \exp(-\lambda t_{on}) \quad (52)$$

where t_{on} is the time taken by the air flux to reach the release point from the irradiated area where air is being activated. In our case t_{on} is assumed to be equal to 150 s. Table 46 (third column) gives the total activity A_{on} ejected into the external air over the 4 month commissioning.

Finally, the total amount of activity released into the atmosphere after shutdown, can be obtained by the expression

$$A_{off} = A_T \frac{m_{off}}{\lambda+m_{off}} \exp(-\lambda t_{off}) \quad (53)$$

with m_{off} and t_{off} representing the same quantities as m_{on} and t_{on} , respectively, but referred to the period following the irradiation end.

Table 43 : Air composition used in the post-processing calculation of air activation.

Molecule	Weight fraction [%]	Atomic mass [g mol ⁻¹]
CO ₂	0.05	44.0
N ₂	75.52	28.0
O ₂	23.15	32.0
Ar	1.29	40.0
Density: 1.205 mg cm ⁻³		

5.3.4 Dose to the reference population group and to a worker intervening in the tunnel after the shutdown

The environmental impact of an accelerator facility must be assessed in terms of radioactivity released in the environment and in terms of effective dose to the reference group of the population. As a complete description of the environment is not achievable and the population behaviour cannot be predicted, a conservative approach must be employed. In general the so-called screening approach is used (139) : it makes use of simplified models that overestimate the activity densities and the effective doses. When assessing the impact of air releases from the stacks, both diffusion due to the winds and deposition in environmental matrices must be considered. For the external

exposure, the effective dose must be integrated over one year. For the internal exposure, the effective dose committed during the rest of life due to inhalation and/or ingestion of radioactive substances in one year shall be evaluated. All these factors have been considered in a previous study (140) and the resulting conversion coefficients from activity to effective dose, expressed in Sv/Bq, calculated for the existing ISOLDE stack were here employed. They are based on the Swiss directive HSK-R-41 (141) and they apply to the most exposed group of the population, which consists of the border guards and their families working at the Swiss border guard station on the Route de Meyrin and living in adjacent houses.

The activity released to the external air over 4 months of commissioning was converted into the dose for exposure to the reference population group. The most exposed group of the population consists of the border guards and their families working at the Swiss border guard station on the route de Meyrin and living in the adjacent houses. Proper dose conversion coefficients for releases from the Linac4 stack are not yet available and those from the ISOLDE stack (140) had to be used. This approximation is conservative because the Linac4 building will be installed further away from the guard station with respect to the ISOLDE building. The dose conversion coefficient for adults in Table 1 of ref. (140) were used and the dose to the reference population group is listed in Table 46. The most important radionuclides contributing to the dose are ^{11}C and ^{13}N and the total dose for exposure is 0.1 μSv .

The residual activity in the area of the tunnel close to the dump after 4 months of run was used to estimate the dose received by a worker intervening after the shutdown. If the activity is mixed homogeneously in the tunnel, the activity concentration is obtained by dividing the activity by the volume of air. Both the internal exposure by inhalation and the external exposure must be evaluated. To estimate the inhalation dose, the approach described in Section 5.2 was used. It was assumed that the intervention lasts 1 hour and three possible cooling times were considered (no cooling, 10 minutes and 30 minutes). The standard breathing rate for a worker is 1.2 m^3/h and the volume of air considered is 1800 m^3 . The inhalation dose is shown in Table 44. The most important radionuclides contributing to the dose are ^{11}C , ^{38}Cl and ^{39}Cl . The total inhalation dose is 0.3 μSv in the worst case of no cooling time.

For the evaluation of the effective dose for external exposure, it was used again the approach described in Section 5.2.

The values of effective doses for external exposure received by a worker intervening in the cave for 1 hour and for three cooling times (no cooling, 10 minutes and 30 minutes) are given in Table 45. A worker intervening in the cave soon after the shutdown would receive a total effective dose for external exposure of 10.7 μSv , while a cooling time of 30 minutes would be enough to lower this value to 2.5 μSv . The most important radionuclides contributing to the effective dose for external exposure are ^{11}C , ^{13}N , ^{38}Cl and ^{39}Cl . The external exposure results to be more important than the internal irradiation by inhalation from the radiological standpoint. Nevertheless, the total dose received by a worker intervening in the tunnel is small and a cooling time of 30 minutes would lower the integrated dose to a negligible value.

Table 44 : Residual activity after 4 months and dose inhaled by a worker intervening in the tunnel.

Radio-isotope	λ (s^{-1})	Residual activity (Bq)	Committed dose (μSv) for internal exposure integrated in 1 hour starting from		
			The shutdown	10 minutes later	30 minutes later
^3H	1.80E-09	1.30E+03	3.55E-05	3.55E-05	3.55E-05
^7Be	1.50E-07	9.20E+04	2.82E-03	2.82E-03	2.82E-03
^{10}Be	1.50E-14	1.10E-03	1.39E-08	1.39E-08	1.39E-08
^{10}C	3.60E-02	2.80E+07	0.00E+00	0.00E+00	0.00E+00
^{11}C	5.70E-04	1.20E+08	2.56E-01	1.82E-01	9.18E-02
^{13}N	1.20E-03	2.10E+08	0.00E+00	0.00E+00	0.00E+00
^{14}C	3.80E-12	1.90E+01	7.35E-06	7.35E-06	7.35E-06
^{14}O	9.80E-03	3.90E+07	0.00E+00	0.00E+00	0.00E+00
^{15}O	5.70E-03	1.40E+08	0.00E+00	0.00E+00	0.00E+00
^{16}N	9.70E-02	1.10E+06	0.00E+00	0.00E+00	0.00E+00
^{17}F	1.10E-02	9.50E+02	0.00E+00	0.00E+00	0.00E+00
^{18}F	1.10E-04	1.80E+03	1.12E-04	1.04E-04	9.16E-05
^{19}O	2.60E-02	1.10E+03	0.00E+00	0.00E+00	0.00E+00
^{22}Na	8.40E-09	6.70E-01	8.93E-07	8.93E-07	8.93E-07
^{24}Na	1.30E-05	1.90E+03	6.71E-04	6.66E-04	6.56E-04
^{25}Na	1.20E-02	8.20E+03	0.00E+00	0.00E+00	0.00E+00
^{26}Al	3.00E-14	6.50E-06	6.07E-11	6.07E-11	6.07E-11
^{27}Mg	1.20E-03	2.20E+04	0.00E+00	0.00E+00	0.00E+00
^{28}Mg	9.20E-06	1.90E+02	2.15E-04	2.14E-04	2.12E-04
^{28}Al	5.20E-03	1.20E+05	0.00E+00	0.00E+00	0.00E+00
^{29}Al	1.80E-03	5.30E+04	0.00E+00	0.00E+00	0.00E+00
^{30}P	4.60E-03	1.10E+05	0.00E+00	0.00E+00	0.00E+00
^{31}Si	7.30E-05	4.40E+04	3.23E-03	3.09E-03	2.83E-03
^{32}Si	1.30E-10	3.20E-02	1.17E-06	1.17E-06	1.17E-06
^{32}P	5.60E-07	2.10E+03	4.06E-03	4.06E-03	4.06E-03
^{33}P	3.20E-07	8.70E+02	7.54E-04	7.54E-04	7.54E-04
^{34}Cl	4.50E-01	1.70E+05	0.00E+00	0.00E+00	0.00E+00
^{35}P	1.50E-02	4.60E+02	0.00E+00	0.00E+00	0.00E+00
^{35}S	9.20E-08	4.60E+02	3.68E-05	3.68E-05	3.68E-05
^{36}Cl	7.30E-14	1.20E-03	4.08E-09	4.08E-09	4.08E-09
^{37}S	2.30E-03	3.30E+04	0.00E+00	0.00E+00	0.00E+00
^{37}Ar	2.30E-07	2.50E+03	0.00E+00	0.00E+00	0.00E+00
^{38}S	6.80E-05	4.80E+03	0.00E+00	0.00E+00	0.00E+00
^{38}Cl	3.10E-04	4.40E+05	2.14E-02	1.78E-02	1.23E-02
^{38}K	1.50E-03	5.30E-04	0.00E+00	0.00E+00	0.00E+00
^{39}Cl	2.10E-04	4.80E+05	2.43E-02	2.14E-02	1.67E-02
^{39}Ar	8.20E-11	2.10E+00	0.00E+00	0.00E+00	0.00E+00
^{40}Cl	8.60E-03	2.80E+04	0.00E+00	0.00E+00	0.00E+00
^{40}K	1.70E-17	3.90E-08	7.80E-14	7.80E-14	7.80E-14
^{41}Ar	1.10E-04	6.20E+05	0.00E+00	0.00E+00	0.00E+00
Total			3.14E-01	2.33E-01	1.32E-01

Table 45 : Residual activity after 4 months and effective dose for external exposure received by a worker intervening in the tunnel.

Radio-isotope	λ (s^{-1})	Residual activity (Bq)	Effective dose (μSv) for external exposure integrated in 1 hour starting from		
			The shutdown	10 minutes later	30 minutes later
H3	1.80E-09	1.30E+03	8.61E-10	8.61E-10	8.61E-10
Be7	1.50E-07	9.20E+04	4.39E-04	4.39E-04	4.39E-04
Be10	1.50E-14	1.10E-03	3.08E-13	3.08E-13	3.08E-13
C10	3.60E-02	2.80E+07	0.00E+00	0.00E+00	0.00E+00
C11	5.70E-04	1.20E+08	5.07E+00	3.60E+00	1.82E+00
N13	1.20E-03	2.10E+08	4.78E+00	2.33E+00	5.52E-01
C14	3.80E-12	1.90E+01	1.01E-10	1.01E-10	1.01E-10
O14	9.80E-03	3.90E+07	0.00E+00	0.00E+00	0.00E+00
O15	5.70E-03	1.40E+08	6.84E-01	2.24E-02	2.39E-05
N16	9.70E-02	1.10E+06	0.00E+00	0.00E+00	0.00E+00
F17	1.10E-02	9.50E+02	0.00E+00	0.00E+00	0.00E+00
F18	1.10E-04	1.80E+03	1.48E-04	1.38E-04	1.21E-04
O19	2.60E-02	1.10E+03	0.00E+00	0.00E+00	0.00E+00
Na22	8.40E-09	6.70E-01	1.46E-07	1.46E-07	1.46E-07
Na24	1.30E-05	1.90E+03	8.20E-04	8.13E-04	8.01E-04
Na25	1.20E-02	8.20E+03	0.00E+00	0.00E+00	0.00E+00
Al26	3.00E-14	6.50E-06	1.79E-12	1.79E-12	1.79E-12
Mg27	1.20E-03	2.20E+04	0.00E+00	0.00E+00	0.00E+00
Mg28	9.20E-06	1.90E+02	2.57E-05	2.55E-05	2.53E-05
Al28	5.20E-03	1.20E+05	1.21E-03	5.36E-05	1.05E-07
Al29	1.80E-03	5.30E+04	0.00E+00	0.00E+00	0.00E+00
P30	4.60E-03	1.10E+05	6.77E-04	4.28E-05	1.72E-07
Si31	7.30E-05	4.40E+04	3.83E-05	3.67E-05	3.36E-05
Si32	1.30E-10	3.20E-02	5.63E-13	5.63E-13	5.63E-13
P32	5.60E-07	2.10E+03	2.30E-06	2.30E-06	2.30E-06
P33	3.20E-07	8.70E+02	2.54E-08	2.54E-08	2.54E-08
Cl34	4.50E-01	1.70E+05	0.00E+00	0.00E+00	0.00E+00
P35	1.50E-02	4.60E+02	0.00E+00	0.00E+00	0.00E+00
S35	9.20E-08	4.60E+02	2.91E-09	2.91E-09	2.91E-09
Cl36	7.30E-14	1.20E-03	4.06E-13	4.06E-13	4.06E-13
S37	2.30E-03	3.30E+04	0.00E+00	0.00E+00	0.00E+00
Ar37	2.30E-07	2.50E+03	6.35E-10	6.35E-10	6.34E-10
S38	6.80E-05	4.80E+03	0.00E+00	0.00E+00	0.00E+00
Cl38	3.10E-04	4.40E+05	4.23E-02	3.51E-02	2.42E-02
K38	1.50E-03	5.30E-04	3.26E-11	1.32E-11	2.19E-12
Cl39	2.10E-04	4.80E+05	5.00E-02	4.41E-02	3.43E-02
Ar39	8.20E-11	2.10E+00	4.88E-10	4.88E-10	4.88E-10
Cl40	8.60E-03	2.80E+04	0.00E+00	0.00E+00	0.00E+00
K40	1.70E-17	3.90E-08	6.60E-16	6.60E-16	6.60E-16
Ar41	1.10E-04	6.20E+05	6.76E-02	6.33E-02	5.54E-02
Sum			1.07E+01	6.09E+00	2.48E+00

Table 46 : Activity released to the external air and dose of exposure of the reference population group over 4 months.

Radioisotope	λ (s ⁻¹)	Activity released into the atmosphere (Bq)	Dose to the population (μSv)
³ H	1.80E-09	2.10E+06	1.64E-07
⁷ Be	1.50E-07	1.50E+08	4.58E-03
¹¹ C	5.70E-04	1.80E+11	4.21E-02
¹³ N	1.20E-03	2.90E+11	5.42E-02
¹⁴ C	3.80E-12	3.10E+04	3.78E-07
¹⁴ O	9.80E-03	1.40E+10	1.65E-03
¹⁵ O	5.70E-03	9.60E+10	6.66E-03
¹⁸ F	1.10E-04	2.80E+06	3.72E-06
²² Na	8.40E-09	1.10E+03	1.42E-05
²⁴ Na	1.30E-05	3.00E+06	8.58E-05
²⁵ Na	1.20E-02	2.30E+06	3.73E-08
²⁷ Mg	1.20E-03	2.90E+07	6.35E-05
²⁸ Mg	9.20E-06	3.10E+05	7.63E-06
²⁸ Al	5.20E-03	9.20E+07	2.56E-04
²⁹ Al	1.80E-03	6.60E+07	1.68E-05
³⁰ P	4.60E-03	9.10E+07	1.67E-05
³¹ Si	7.30E-05	7.10E+07	2.97E-05
³² P	5.60E-07	3.50E+06	2.67E-04
³³ P	3.20E-07	1.40E+06	1.62E-05
³⁵ P	1.50E-02	4.80E+06	2.04E-05
³⁵ S	9.20E-08	7.40E+05	7.55E-06
³⁷ S	2.30E-03	3.80E+07	1.49E-05
³⁷ Ar	2.30E-07	4.00E+06	8.04E-13
³⁸ S	6.80E-05	7.70E+06	1.97E-05
³⁸ Cl	3.10E-04	6.80E+08	5.98E-04
³⁸ K	1.50E-03	6.80E+07	8.16E-05
³⁹ Cl	2.10E-04	7.50E+08	8.33E-04
⁴⁰ Cl	8.60E-03	1.30E+07	2.26E-06
⁴¹ Ar	1.10E-04	9.80E+08	3.11E-04
Total		5.83E+11	1.12E-01

6 Conclusions

This thesis has discussed the radiation protection studies for the new 160 MeV injector linac presently under construction at CERN. The studies were carried out through a combination of Monte Carlo simulations and predictions made via analytical models.

FLUKA benchmarks

FLUKA simulations were performed to test the capability of the code in predicting induced radioactivity from intermediate energy protons. The agreement between the results of the gamma spectrometry measurements and the Monte Carlo predictions was rather good, except for ^{65}Zn . This is explained by the fact that presently the FLUKA library does not include the cross sections for neutron activation of zinc below 20 MeV. All radionuclides predicted by the simulations were detected by gamma spectrometry, except those which have low-energy photon emissions or are below the experimental detection limit.

Analytical models

FLUKA simulations were performed to test the reliability of the analytical models mostly used for the calculation of neutron streaming through ducts and labyrinths.

Two set of simulations were run, for a plane source and a point source, respectively.

In case of a plane or off-axis source, the universal transmission curves from refs. [(102) and (103)] were in agreement with the FLUKA simulations.

For a point source, preliminary simulations were performed to evaluate the dependence of the transmission factor on the shape of the cross-sectional area of the duct and on the energy of the protons impinging on the neutron-production target. The transmission factor resulted to be independent of both quantities.

Finally, FLUKA simulations were performed to estimate the attenuation of the ambient dose equivalent rate inside circular ducts of different size, representative of typical situations found in radiation protection, when the source is in direct view of the duct mouth. The simulations have shown that is not possible to define a universal transmission curve, because the transmission factor is dependent on the cross section of the duct and the equation proposed by Tesch (108) overestimates the contribution to the dose equivalent from scattered neutrons.

The curves describing the transmission factor as a function of the normalized distance were fitted through the equation $y = \frac{K\sqrt{A}}{x^{2h\sqrt{A}}}$. The fit parameters k and h decrease with increasing cross-section of the duct; their dependence on the duct area was estimated through a fit.

Shielding design

Monte Carlo simulations proved to be the appropriate method to evaluate the propagation of neutrons through the waveguide, ventilation and cable ducts placed along the accelerator, as well as in the access area, confirming preliminary estimates made with a simple analytical model.

The simulations showed that the final design of the various ducts is adequate from a radiation protection standpoint. Several configurations for the standard waveguide ducts were

investigated. In the layout finally chosen the ambient dose equivalent rate in the klystron building is expected to be less than the design value of 1 $\mu\text{Sv}/\text{h}$. The radiological impact in the low-energy section of the accelerator would raise some concern in the so-called “safe room” only in proximity of the lateral wall where the ambient dose equivalent rate is expected to be between 1 and 10 $\mu\text{Sv}/\text{h}$. Increasing the thickness of the lateral wall from 50 cm to 80 cm provides adequate reduction of the dose rate to a value less than 1 $\mu\text{Sv}/\text{h}$.

Induced radioactivity

A set of FLUKA simulations, based on a detailed geometrical model of the accelerating structures, was also performed to assess the residual dose rates in Linac4 after several years of operation and for various decay times. Two possible layouts for the CCDTL section were compared in terms of induced radioactivity. On the basis of the studies for the residual dose rates, both in contact (with the tank of the DTL or with the quadrupoles in the CCDTL and PIMS sections) and at 1 m distance, maintenance interventions on the DTL are not expected to pose major problems. Interventions on the CCDTL and on the PIMS are more critical because the expected dose rates are much higher. A proper planning of the interventions will be required and countermeasures might have to be taken, such as the use of local shields in proximity of the “hot spots” (e.g., the quadrupoles). A sufficient decay time might also be needed before an intervention can be allowed. The replacement of two-thirds of the EMQs with PMQs in CCDTL section would increase the residual dose rate in proximity of the accelerating structure.

Air activation studies, both in the accelerator tunnel and in proximity of the dump, were performed folding the particle track-lengths spectra obtained by Monte Carlo simulations with proper energy-dependent cross sections. This method was preferred to direct Monte Carlo calculations because of the low interaction probability of hadrons with air, which would have lead to very large CPU times.

In the accelerator tunnel, the doses for inhalation and external irradiation received by workers during 1-hour maintenance operation in the tunnel were estimated for different irradiation cycles and waiting times, for 50, 100 and 160 MeV proton beam energy. The doses are higher at 50 MeV because of the higher number of proton lost and because of the limited contribution of spallation products to gas activation in this energy range. The external exposure is more important than internal exposure by inhalation from the radiological standpoint.

In proximity of the dump, the activity released to the external air over 4 months of commissioning was converted into dose delivered to the reference population group. The most important radionuclides contributing to the dose are ^{11}C and ^{13}N ; the total dose due to external exposure is 0.1 μSv .

The residual radioactivity in the area of the tunnel close to the dump after 4 months of operation was used to estimate the dose received by a worker intervening soon after the accelerator is stopped. The most important radionuclides contributing to the dose are ^{11}C , ^{38}Cl and ^{39}Cl . The total inhalation dose is 0.3 μSv in the worst case of no cooling time.

A worker intervening in the tunnel soon after accelerator shutdown would receive a total effective dose for external exposure of 10.7 μSv , while a cooling time of 30 minutes would be enough to lower this value to 2.5 μSv . The most important radionuclides contributing to the effective dose for external exposure are ^{11}C , ^{13}N , ^{38}Cl and ^{39}Cl . The external exposure results to be more important than the internal irradiation by inhalation from the radiological standpoint. Nevertheless, the total

CHAPTER 6 - CONCLUSIONS

dose received by a worker intervening in the tunnel is small and a cooling time of 30 minutes would lower the integrated dose to a negligible value.

Final considerations

The present study provides complete information on beam loss assumptions, accelerator structure, material composition, and duct and maze design, in order to make the present results of sufficiently general interest and provide guidelines for similar studies for intermediate energy proton accelerators.

The capability of the FLUKA code in predicting induced radioactivity from intermediate energy protons was confirmed.

A universal expression that can be used to estimate the neutron transmission through a straight duct in direct view of the source was derived, model missing so far in literature.

Acknowledgments

I would like to express my profound gratitude to my supervisor Marco Silari (CERN) for his valuable supervision and continuous encouragement during my studies.

This thesis has benefited from the experience, the kind assistance and the support of my Swiss supervisor Aurelio Bay (EPFL).

I owe a particular debt of gratitude to François Bochud (IRA), Maurizio Vretenar, Frank Gerigk, Alessandra Lombardi, Marc Timmins and Carlo Rossi (Linac4 project at CERN).

“This research project has been supported by a Marie Curie Early Stage Research Training/ Intra-European / Research Training Network Fellowship of the European Community’s Sixth Framework Programme under contract number (MEST-CT-2005-020174-Radenv)”

Never forget friends!!! Thanks to everybody that shared with me a beer, an office, an idea, a hope, a dream and a worry and, particularly to my “scolleagues” (Stefania and Sophie), “the mind and the body”(Nuno and Giacomo), “Lazy Suzy”(Zuzana), Ludovic, Alessio and Matteo.

I would also like to thank my parents and my sister for their continuous support and encouragement during these years in Switzerland.

Finally, I would like to give my most special thank to Lidia.

Lidia, grazie a te avrò sempre una barca da scrivere ed un treno da perdere.

Appendix A - Residual dose rate plots and radionuclide inventories

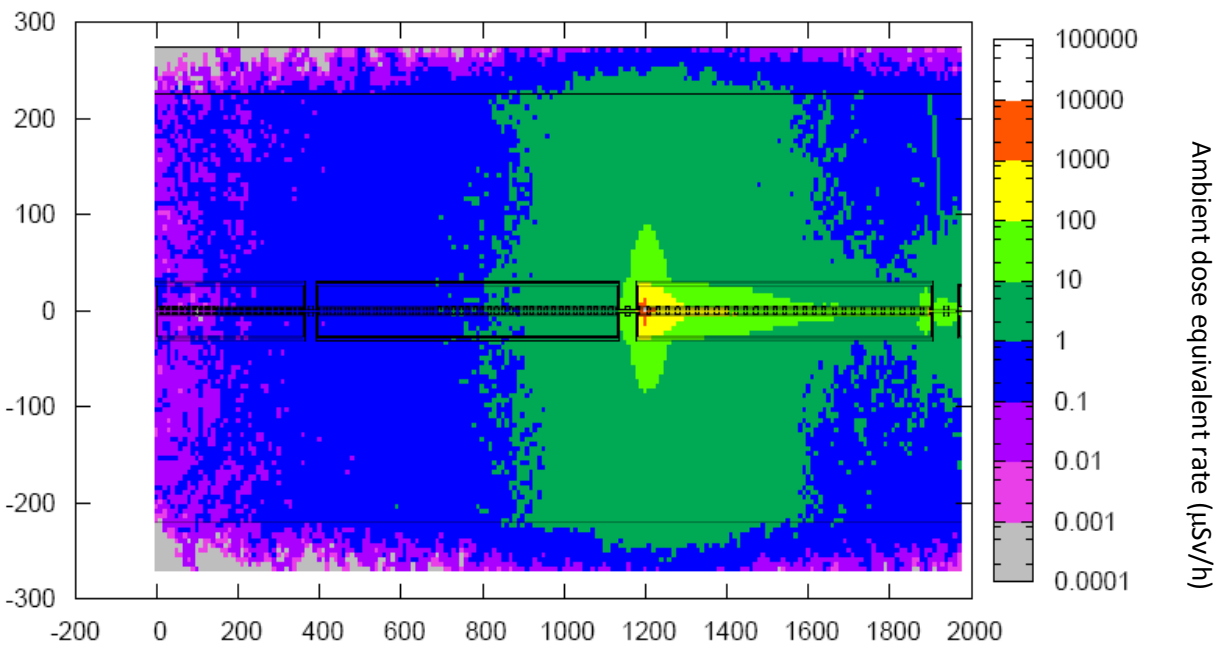


Figure 1: Residual dose rate in the DTL after 4 years and 9 months of operation and no decay. 31 MeV, 1 W loss on the drift tube. $H^*(10)$ in $\mu\text{Sv}/\text{h}$.

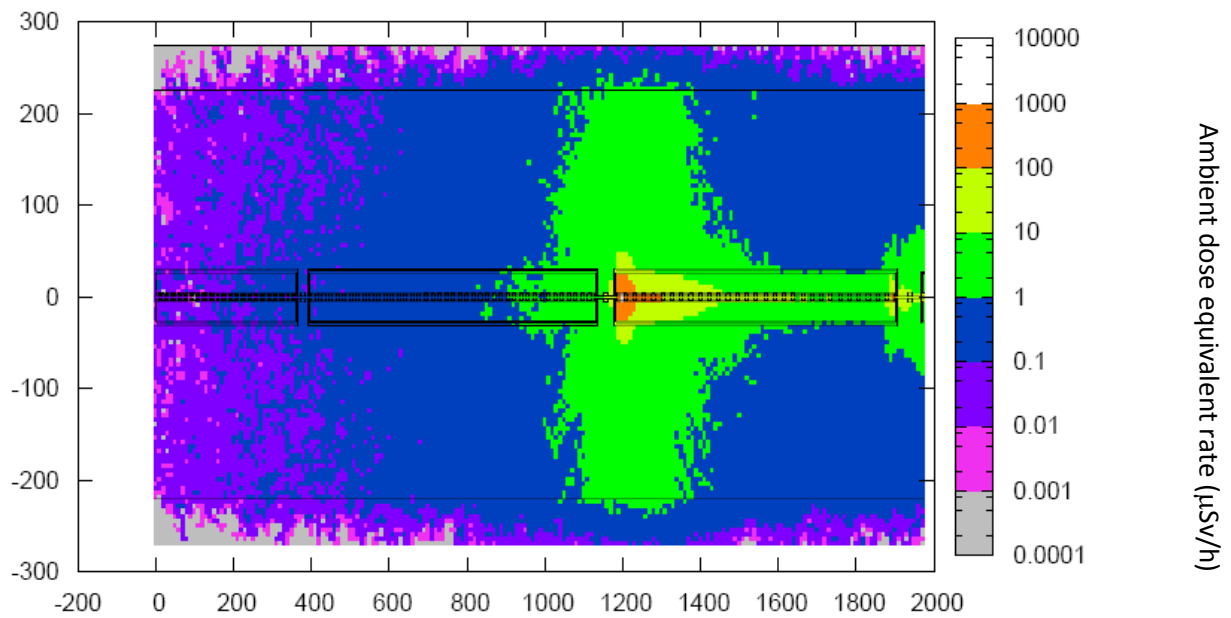


Figure 2: Residual dose rate in the DTL after 4 years and 9 months of operation and 1 hour decay. 31 MeV, 1 W loss on the drift tube. $H^*(10)$ in $\mu\text{Sv}/\text{h}$.

APPENDIX A

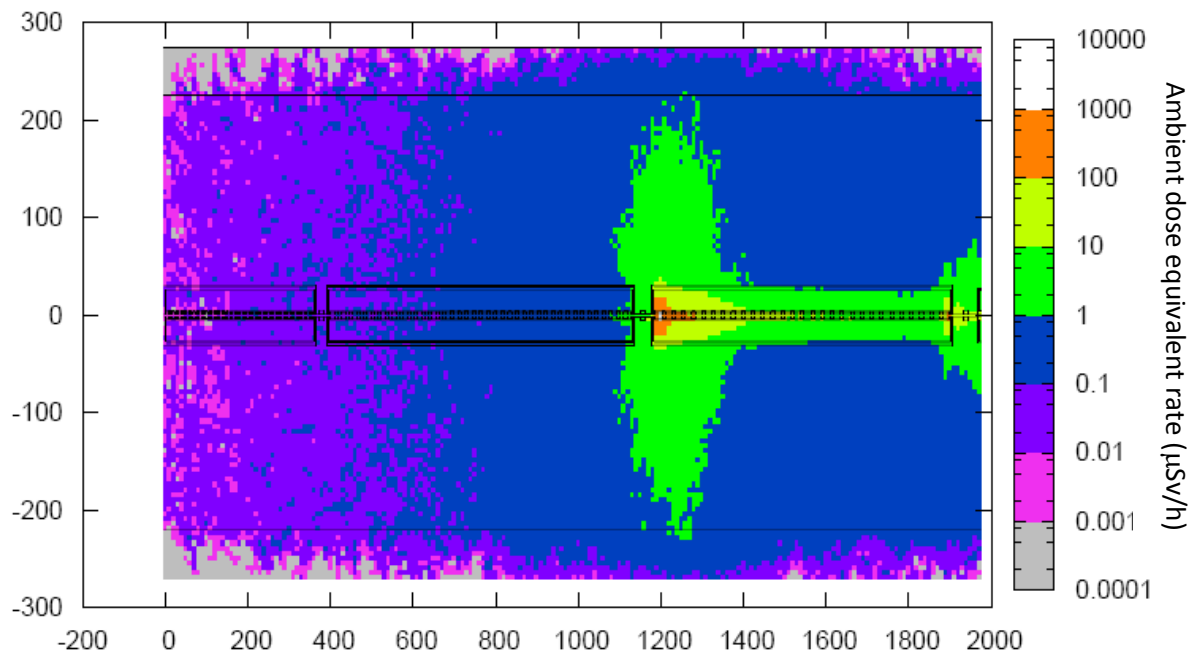


Figure 3: Residual dose rate in the DTL after 4 years and 9 months of operation and 6 hour decay. 31 MeV, 1 W loss on the drift tube. $H^*(10)$ in $\mu\text{Sv}/\text{h}$.

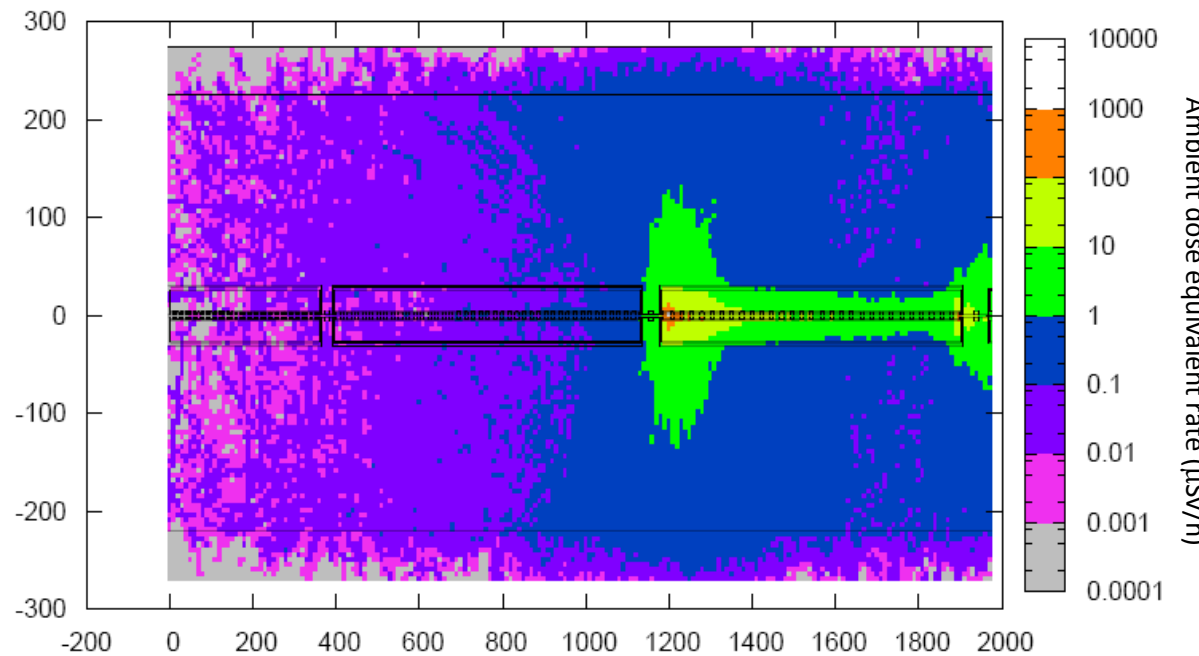


Figure 4: Residual dose rate in the DTL after 4 years and 9 months of operation and 1 day decay. 31 MeV, 1 W loss on the drift tube. $H^*(10)$ in $\mu\text{Sv}/\text{h}$.

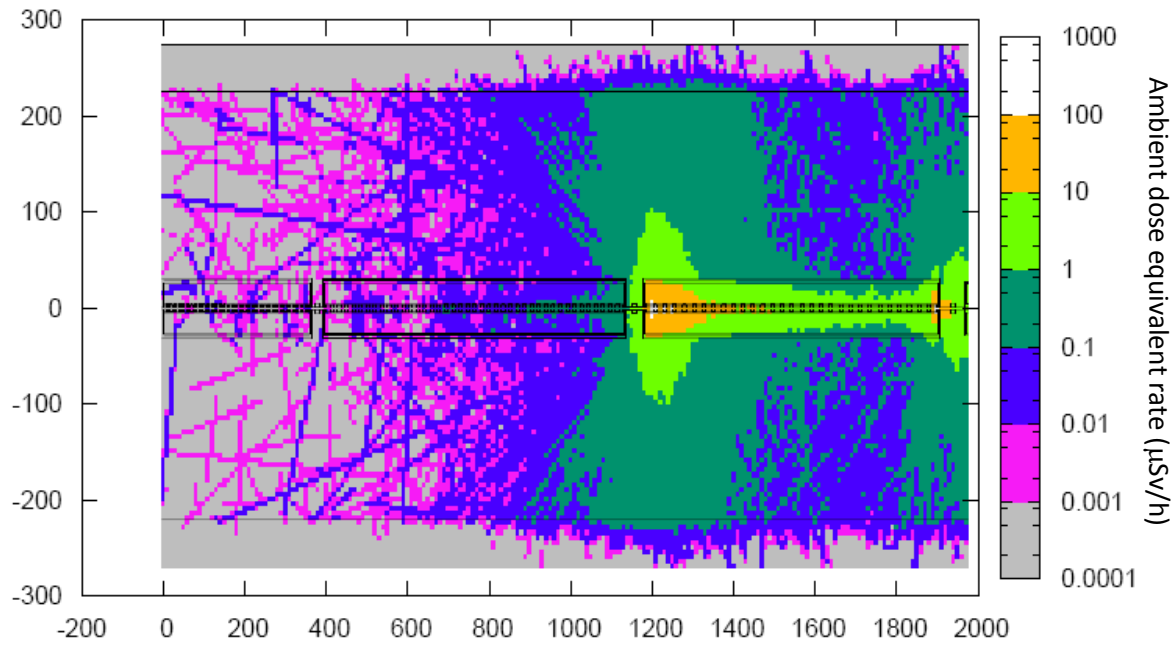


Figure 5: Residual dose rate in the DTL after 4 years and 9 months of operation and 1 week decay. 31 MeV, 1 W loss on the drift tube. $H^*(10)$ in $\mu\text{Sv}/\text{h}$.

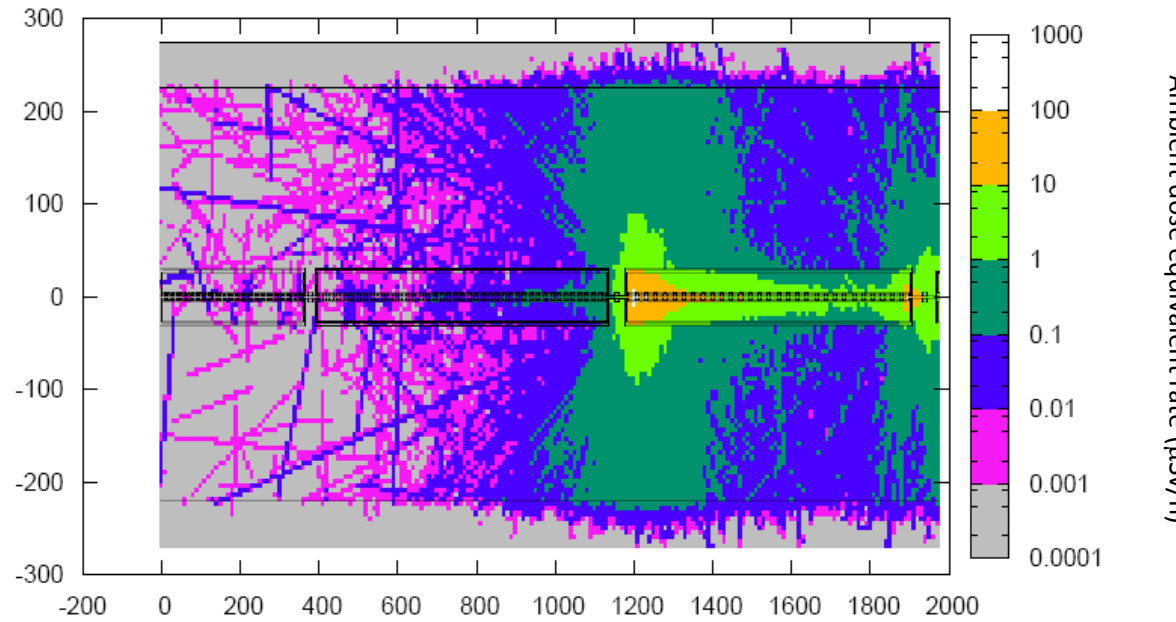


Figure 6: Residual dose rate in the DTL after 4 years and 9 months of operation and 1 month decay. 31 MeV, 1 W loss on the drift tube. $H^*(10)$ in $\mu\text{Sv}/\text{h}$.

APPENDIX A

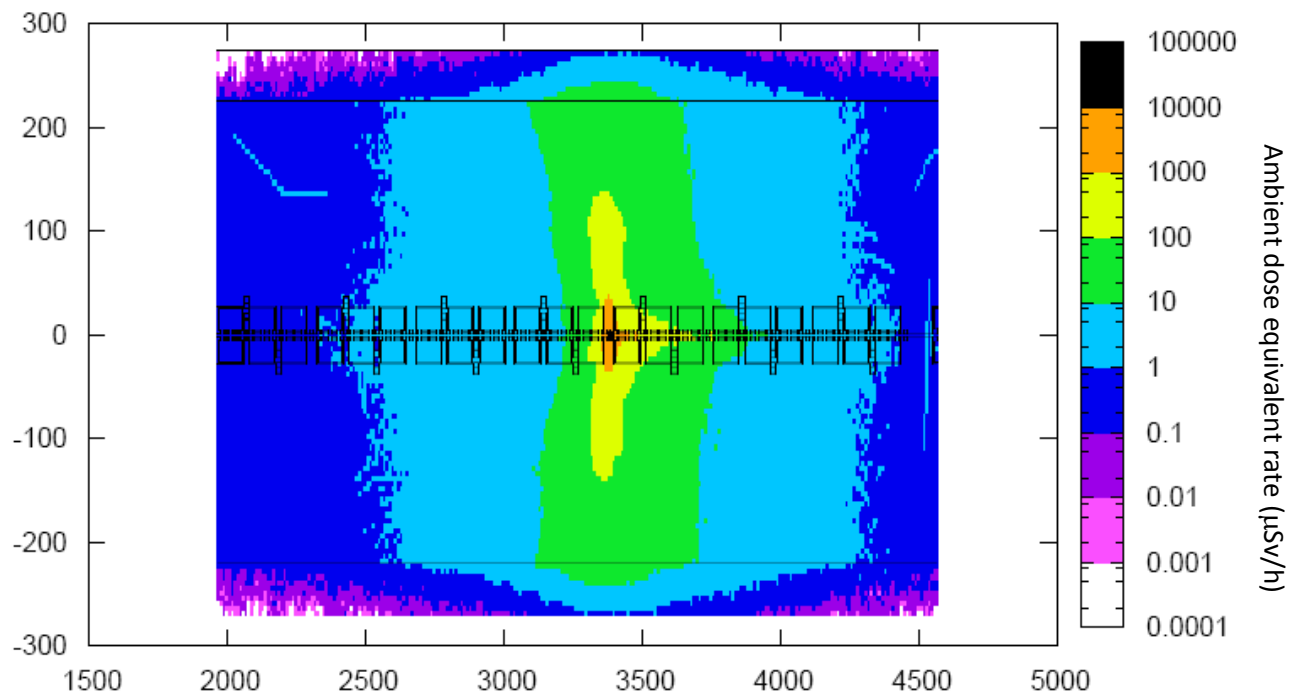


Figure 7: Residual dose rate in the CCDTL after 4 years and 9 months of operation and no decay. 80 MeV, 1 W loss on the vacuum chamber. $H^*(10)$ in $\mu\text{Sv}/\text{h}$.

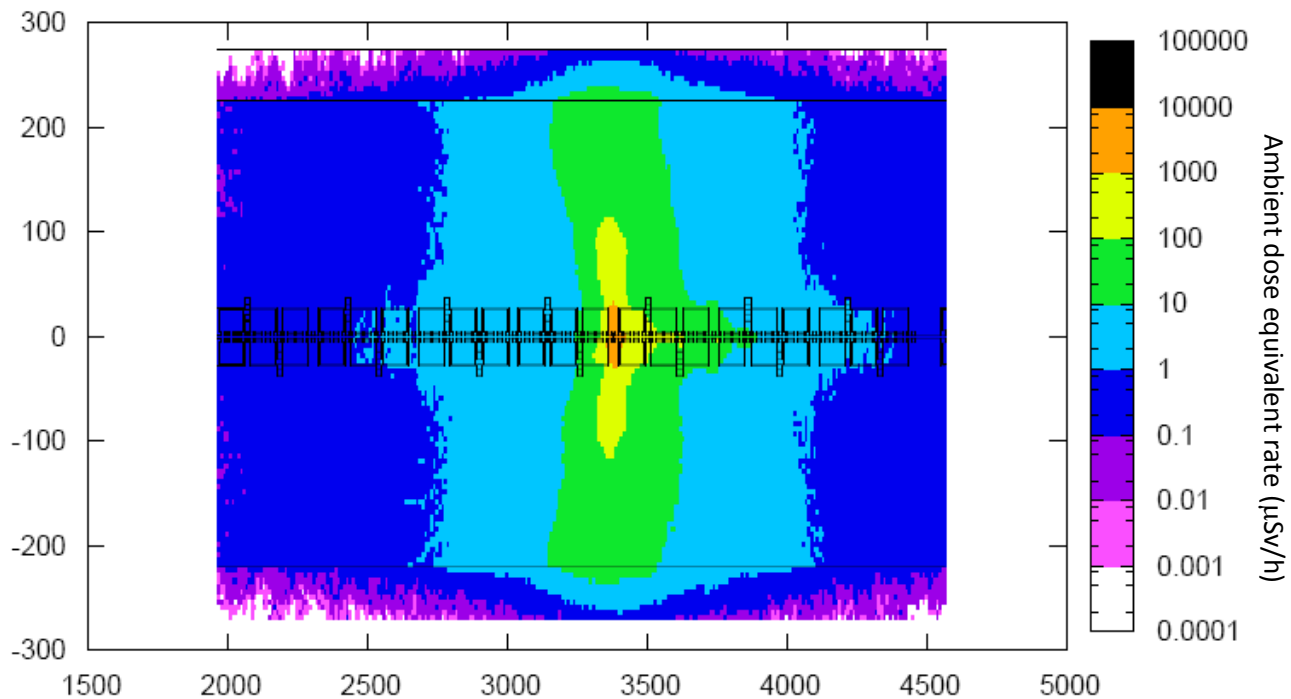


Figure 8: Residual dose rate in the CCDTL after 4 years and 9 months of operation and 1 hour decay. 80 MeV, 1 W loss on the vacuum chamber. $H^*(10)$ in $\mu\text{Sv}/\text{h}$.

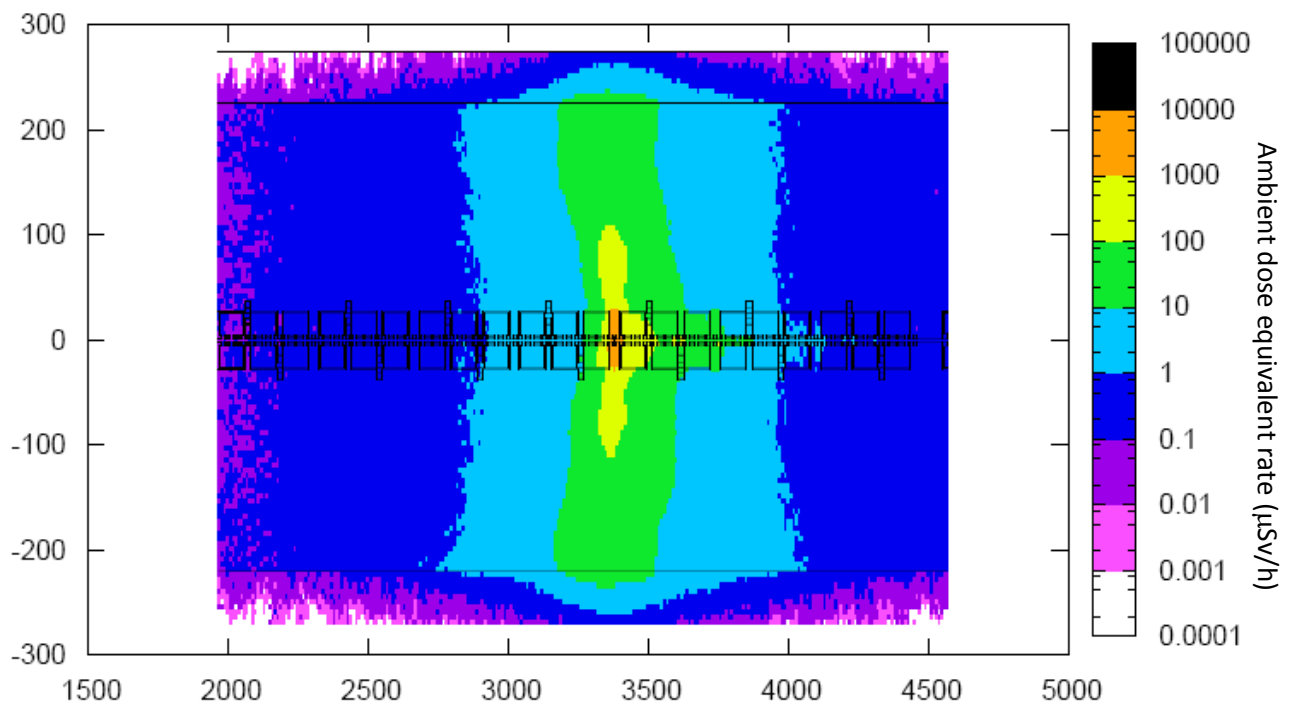


Figure 9: Residual dose rate in the CCDTL after 4 years and 9 months of operation and 6 hour decay. 80 MeV, 1 W loss on the vacuum chamber. $H^*(10)$ in $\mu\text{Sv}/\text{h}$.

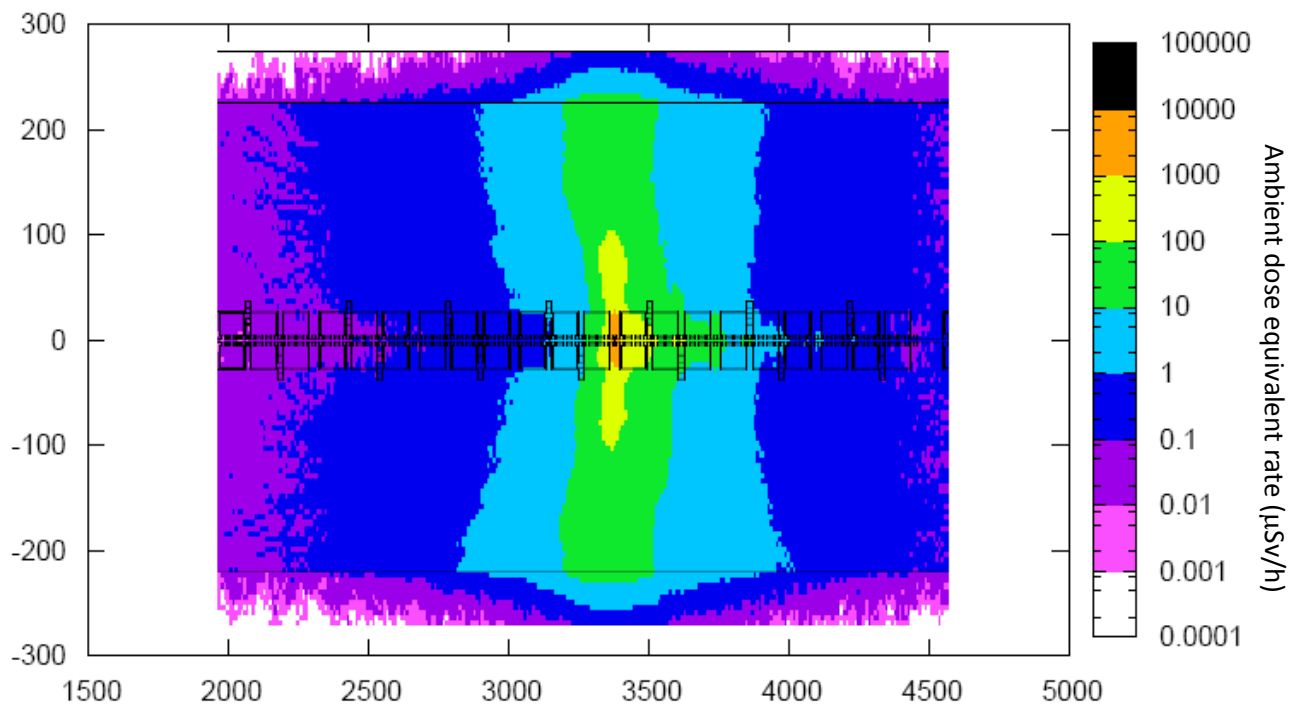


Figure 10: Residual dose rate in the CCDTL after 4 years and 9 months of operation and 1 day decay. 80 MeV, 1 W loss on the vacuum chamber. $H^*(10)$ in $\mu\text{Sv}/\text{h}$.

APPENDIX A

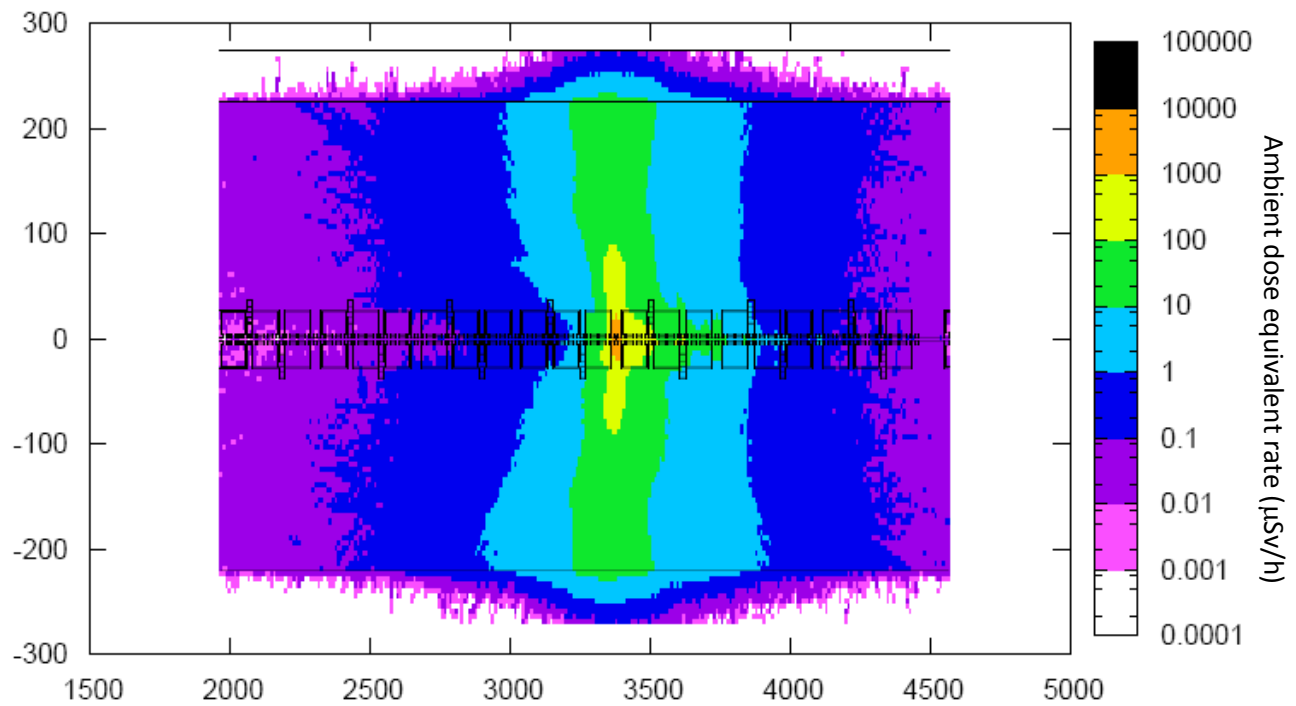


Figure 11: Residual dose rate in the CCDTL after 4 years and 9 months of operation and 1 week decay. 80 MeV, 1 W loss on the vacuum chamber. $H^*(10)$ in $\mu\text{Sv}/\text{h}$.

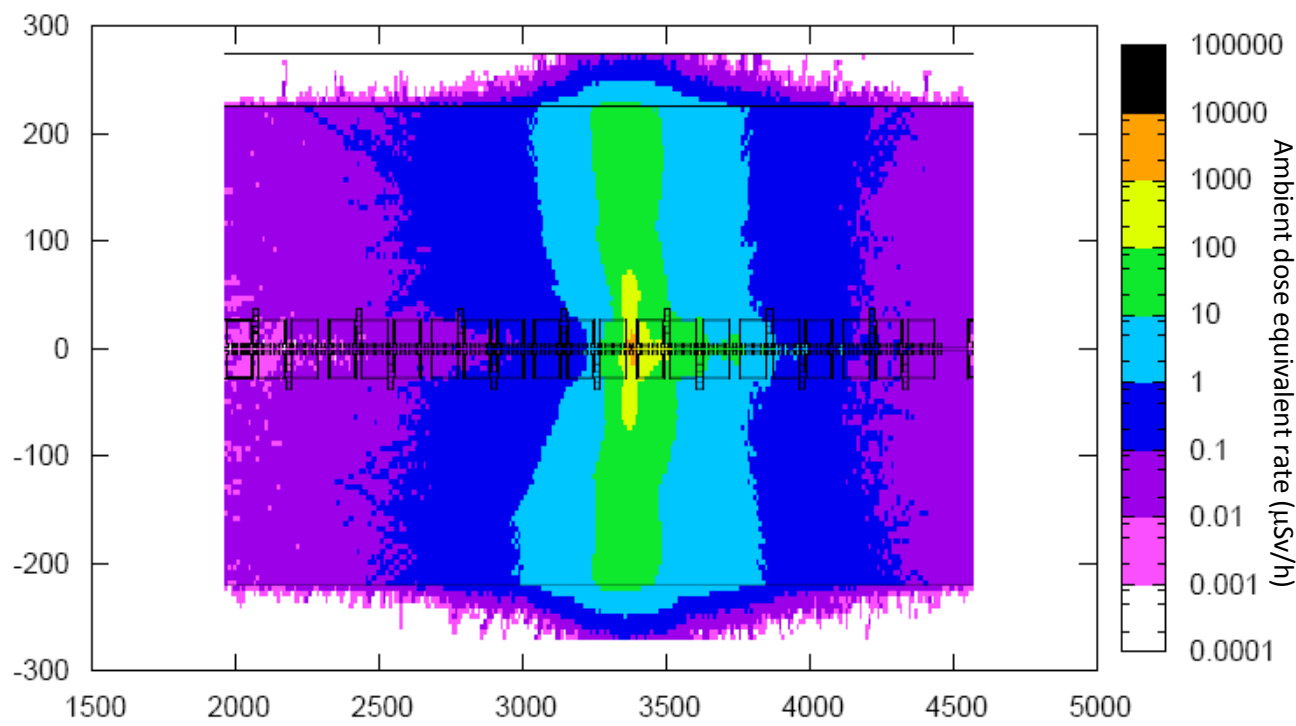


Figure 12: Residual dose rate in the CCDTL after 4 years and 9 months of operation and 1 month decay. 80 MeV, 1 W loss on the vacuum chamber. $H^*(10)$ in $\mu\text{Sv}/\text{h}$.

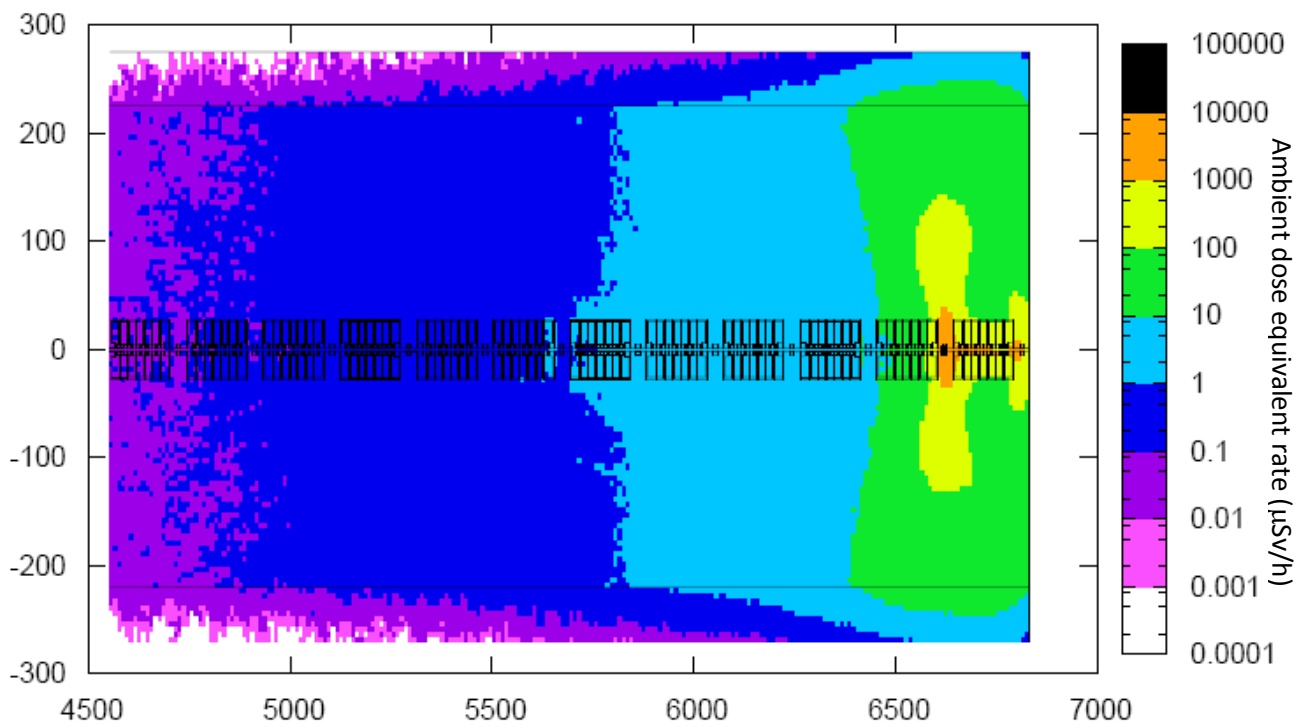


Figure 13: Residual dose rate in the PIMS after 4 years and 9 months of operation and no decay. 155 MeV, 1 W loss on the vacuum chamber. $H^*(10)$ in $\mu\text{Sv}/\text{h}$.

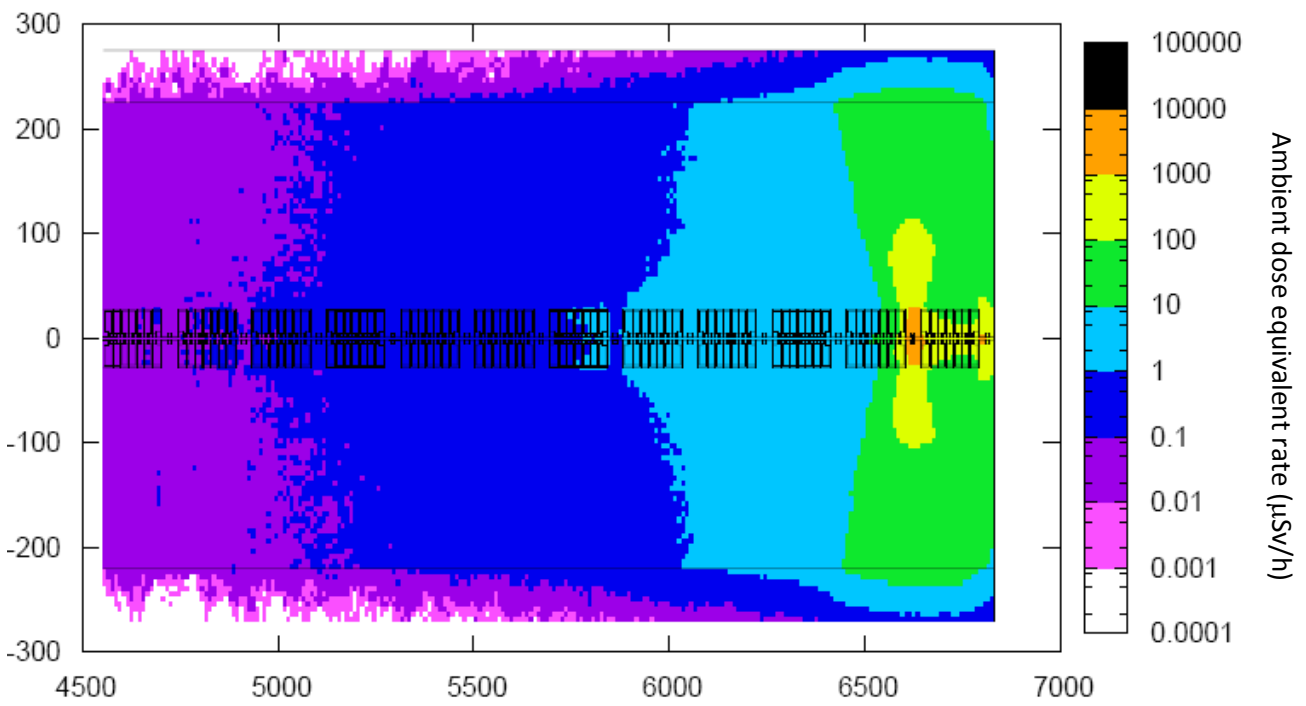


Figure 14: Residual dose rate in the PIMS after 4 years and 9 months of operation and 1 hour decay. 155 MeV, 1 W loss on the vacuum chamber. $H^*(10)$ in $\mu\text{Sv}/\text{h}$.

APPENDIX A

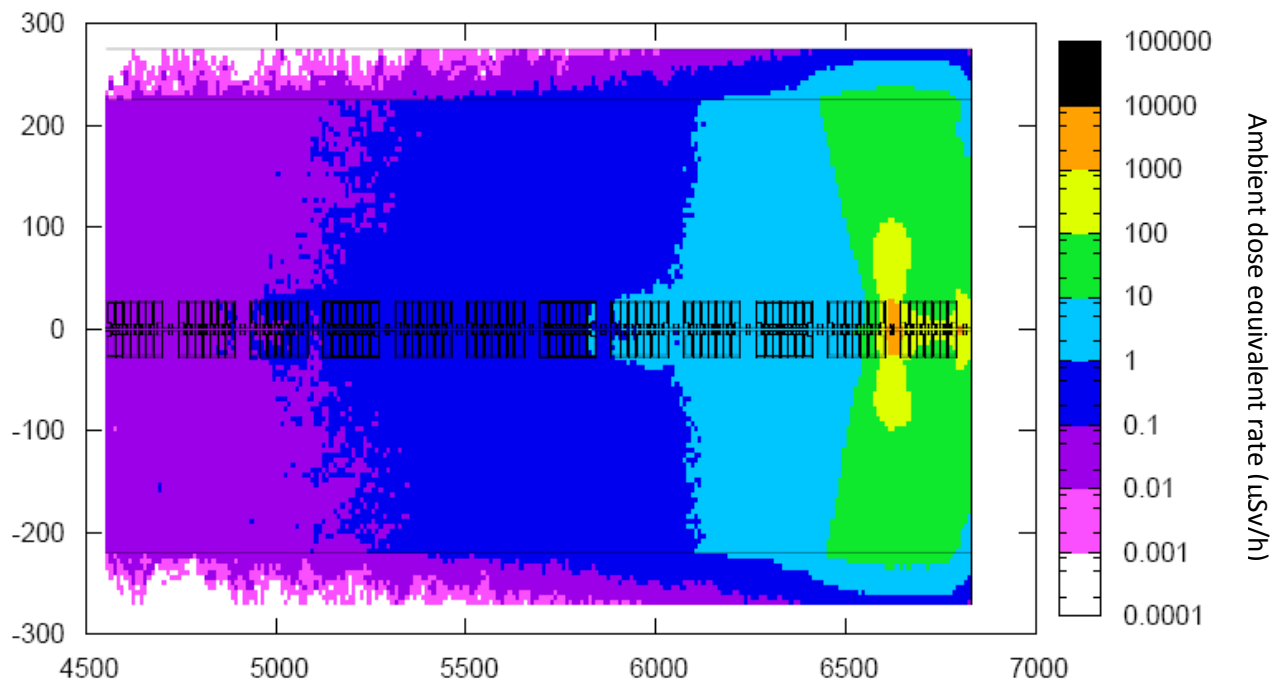


Figure 15: Residual dose rate in the PIMS after 4 years and 9 months of operation and 6 hour decay. 155 MeV, 1 W loss on the vacuum chamber. $H^*(10)$ in $\mu\text{Sv}/\text{h}$.

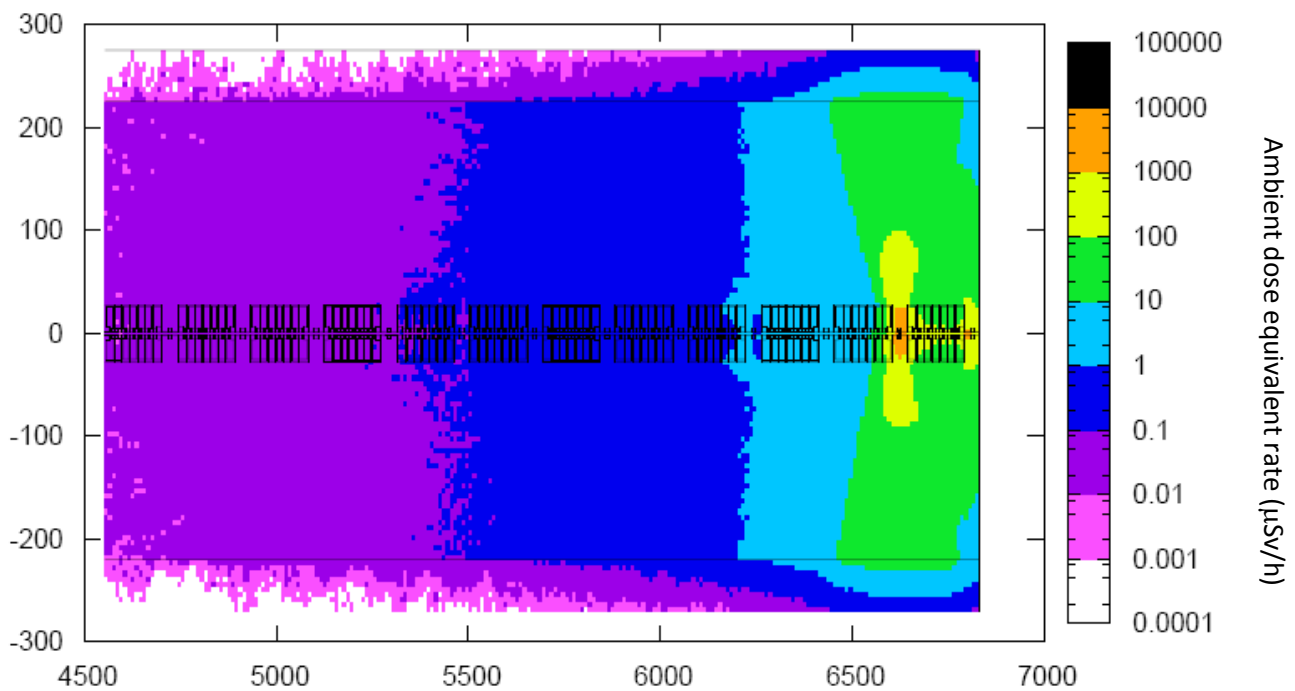


Figure 16: Residual dose rate in the PIMS after 4 years and 9 months of operation and 1 day decay. 155 MeV, 1 W loss on the vacuum chamber. $H^*(10)$ in $\mu\text{Sv}/\text{h}$.

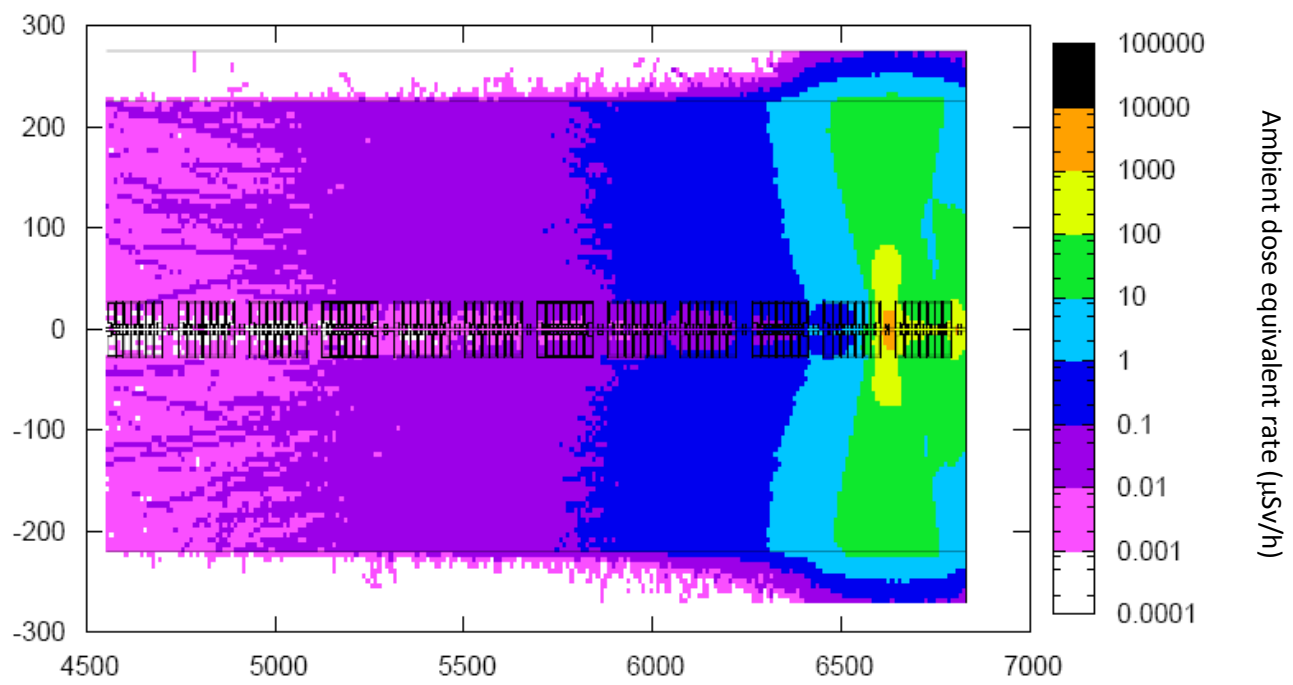


Figure 17: Residual dose rate in the PIMS after 4 years and 9 months of operation and 1 week decay. 155 MeV, 1 W loss on the vacuum chamber. $H^*(10)$ in $\mu\text{Sv}/\text{h}$.

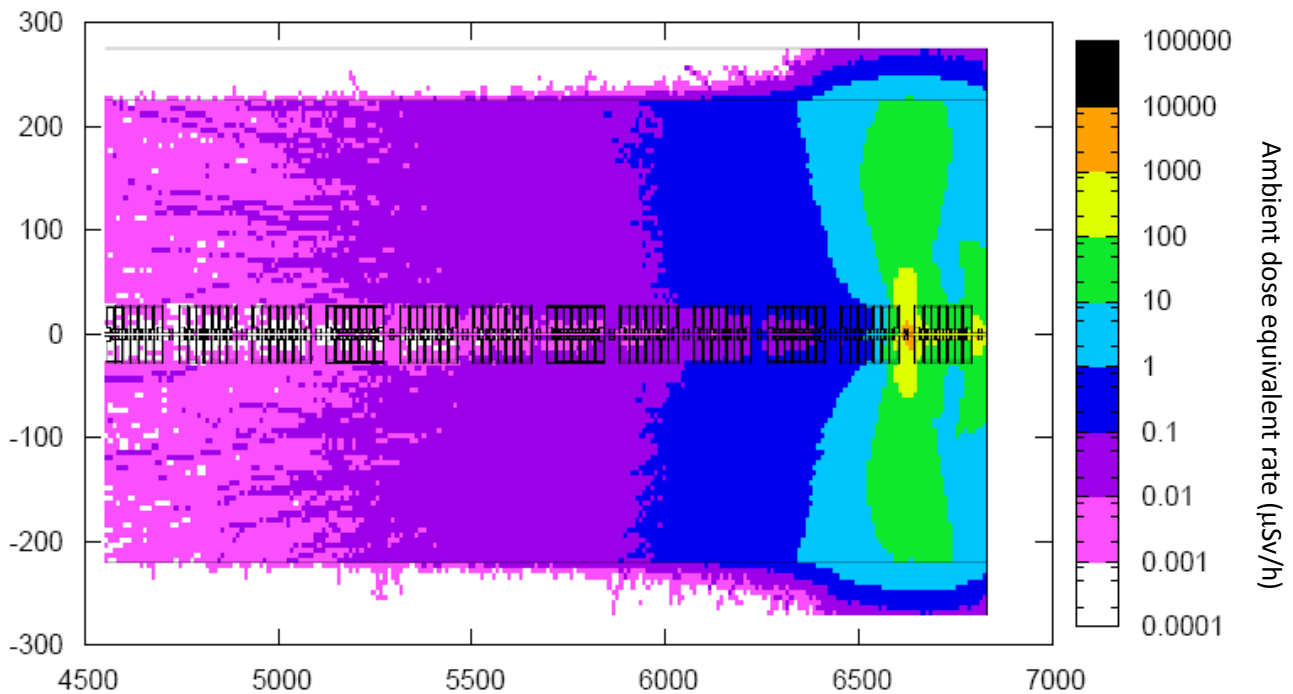


Figure 18: Residual dose rate in the PIMS after 4 years and 9 months of operation and 1 month decay. 155 MeV, 1 W loss on the vacuum chamber. $H^*(10)$ in $\mu\text{Sv}/\text{h}$.

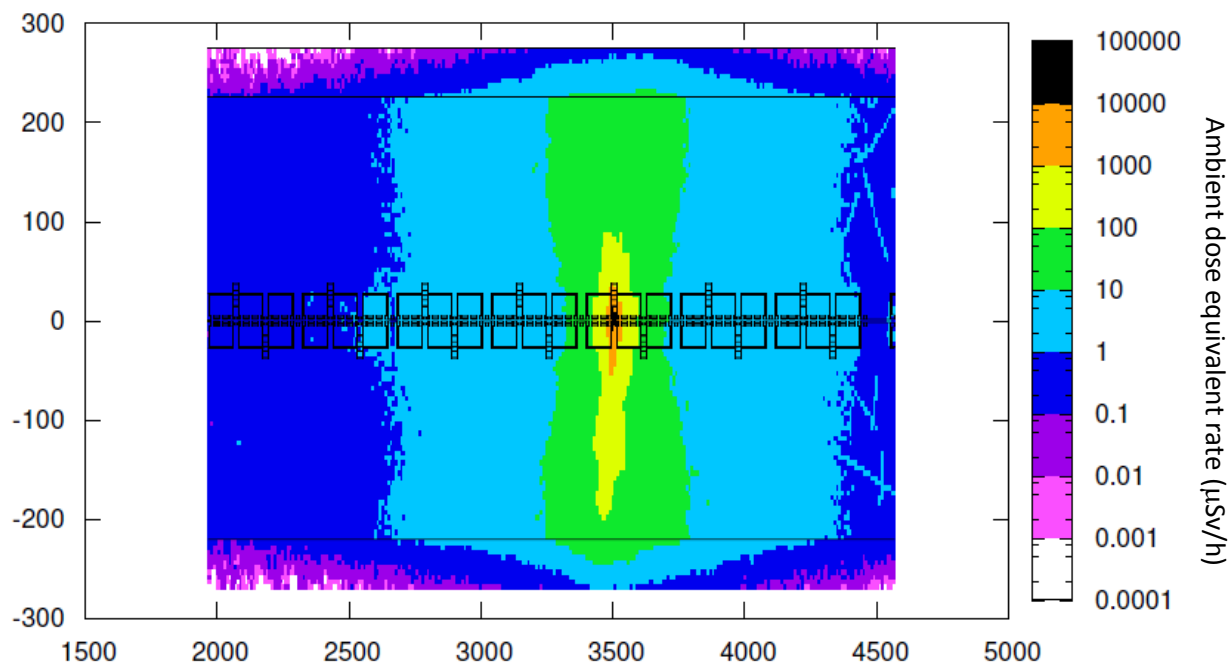


Figure 19: Residual dose rate in the alternative layout of the CCDTL after 4 years and 9 months of operation and no decay. 80 MeV, 1 W loss on the vacuum chamber. $H^*(10)$ in $\mu\text{Sv}/\text{h}$.

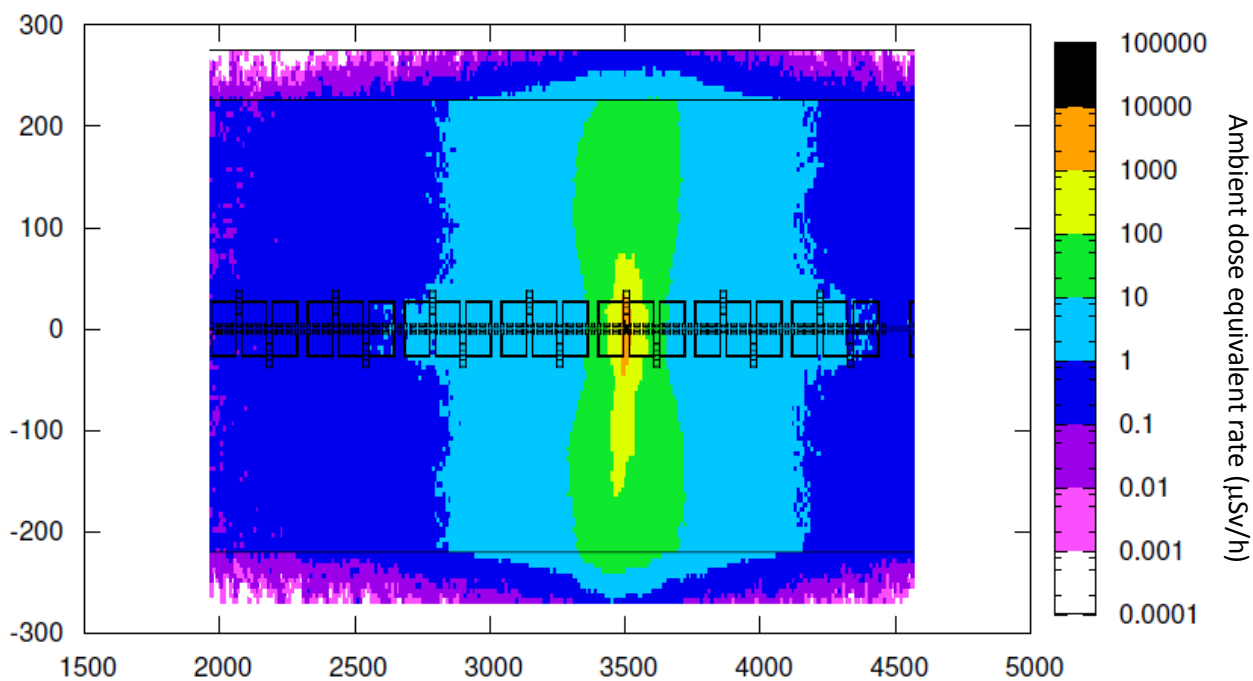


Figure 20: Residual dose rate in the alternative layout of the CCDTL after 4 years and 9 months of operation and 1 hour decay. 80 MeV, 1 W loss on the vacuum chamber. $H^*(10)$ in $\mu\text{Sv}/\text{h}$.

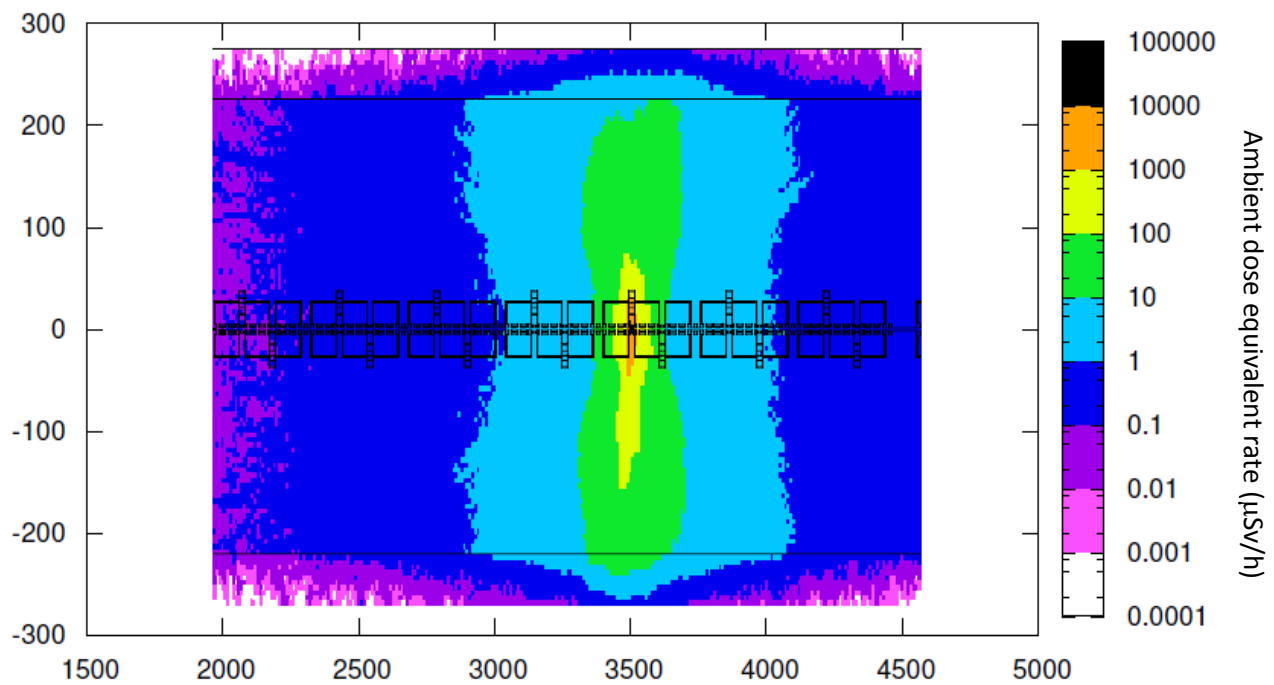


Figure 21: Residual dose rate in the alternative layout of the CCDTL after 4 years and 9 months of operation and 6 hour decay. 80 MeV, 1 W loss on the vacuum chamber. $H^*(10)$ in $\mu\text{Sv}/\text{h}$.

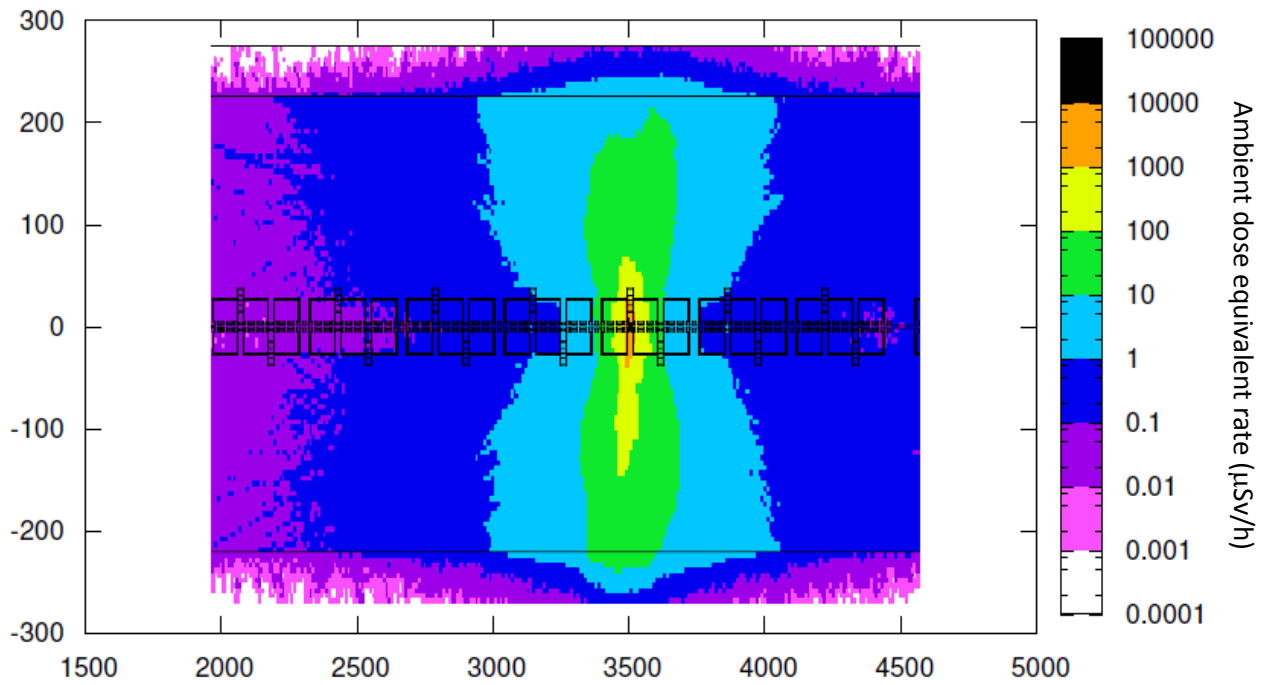


Figure 22: Residual dose rate in the alternative layout of the CCDTL after 4 years and 9 months of operation and 1 day decay. 80 MeV, 1 W loss on the vacuum chamber. $H^*(10)$ in $\mu\text{Sv}/\text{h}$.

APPENDIX A

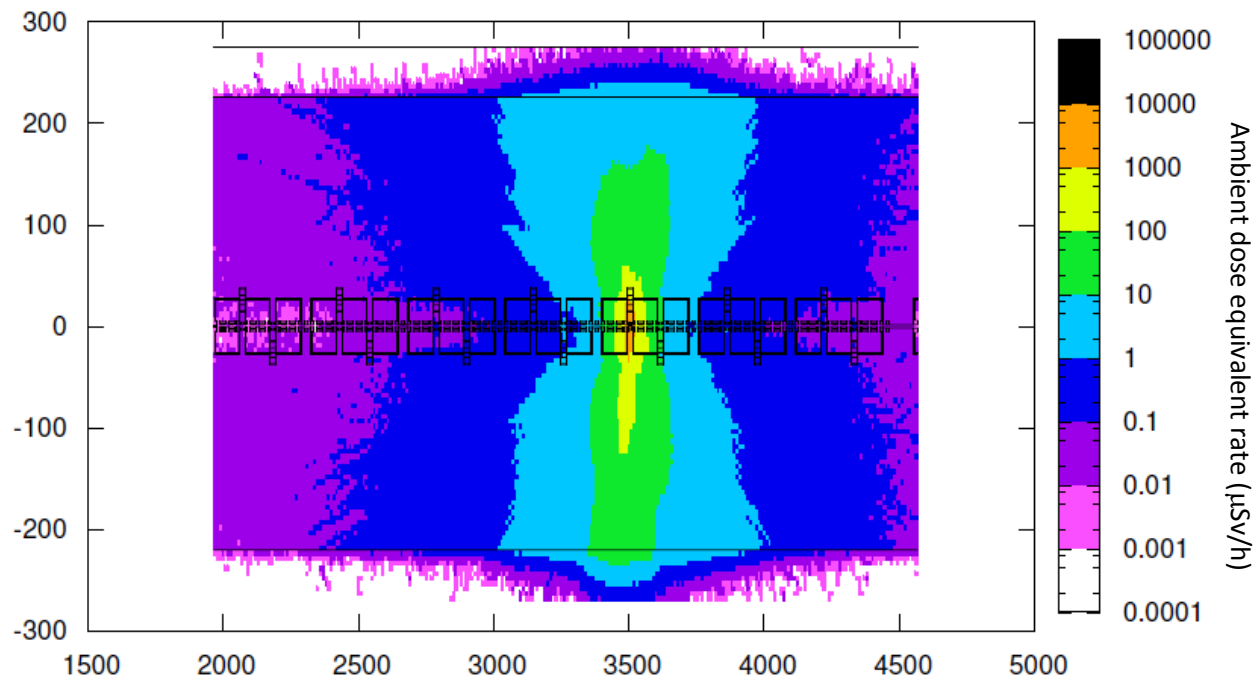


Figure 23: Residual dose rate in the alternative layout of the CCDTL after 4 years and 9 months of operation and 1 week decay. 80 MeV, 1 W loss on the vacuum chamber. $H^*(10)$ in $\mu\text{Sv}/\text{h}$.

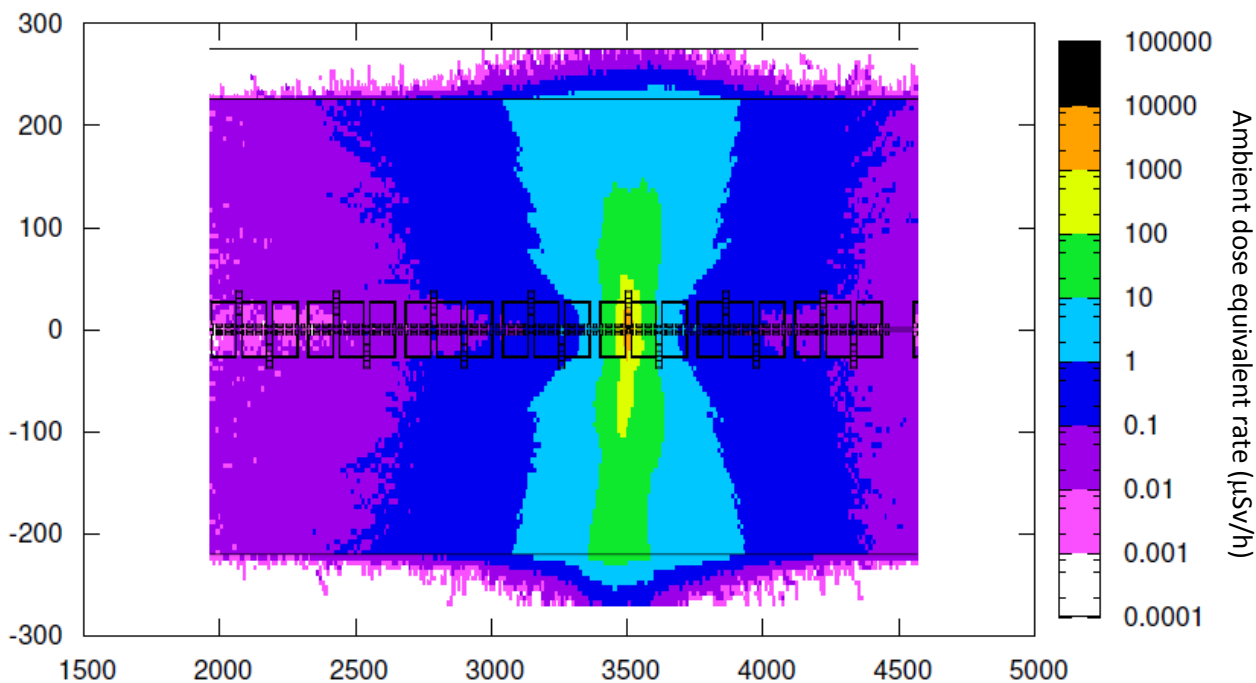


Figure 24: Residual dose rate in the alternative layout of the CCDTL after 4 years and 9 months of operation and 1 month decay. 80 MeV, 1 W loss on the vacuum chamber. $H^*(10)$ in $\mu\text{Sv}/\text{h}$.

Table 1: Specific activity of the most important radionuclides responsible for the residual radioactivity in the drift tubes of the third tank of the DTL after 1 month decay time. The LE values in the last column are the exemption limits taken from the Swiss legislation.

Radionuclide ($t_{1/2}$)	Activity after 1 month decay (Bq)	Specific activity (Bq/g)	LE (Bq/g)
Zn-65 (244 d)	6.6E7	269.4	3
Co-58 (70.8 d)	3.98E6	16.25	10
Ni-63 (100 y)	2.88E5	1.2	70
Co-60 (5.2 y)	4.84E5	1.97	1
Fe-55 (2.7 y)	2.38E5	0.97	30

Table 2: Specific activity of the main radionuclides responsible for the residual radioactivity in the PMQ of the third tank of the DTL after 1 month decay time. The LE values in the last column are the exemption limits taken from the Swiss legislation.

Radionuclide ($t_{1/2}$)	Activity after 1 month decay (Bq)	Specific activity (Bq/g)	LE (Bq/g)
Co-58 (70.8 d)	1.87E7	589	10
Eu-147 (24.6 d)	1.12E6	35	20
Eu-148 (55.6 d)	1.19E6	37.5	8
Co-60 (5.2 y)	1.05E6	33.1	1
Co-57 (271.3d)	3.4E6	107.2	50
Co-56 (78.76 d)	4.11E6	129.6	4
Fe-55 (2.7 y)	9.35E6	294.7	30
Eu-155 (4.96 y)	1.12E5	3.5	30
Eu-152 (13.33 y)	2.16E5	6.8	7
Eu-149 (93.1d)	9.47E5	29.9	100
Sm-145 (340d)	8.32E5	26.2	50
Zn-65 (244 d)	7.62E5	24	3
Mn-54 (312.2 d)	3.88E5	12.2	10
Na-22 (2.6 y)	1.53E5	4.8	3

APPENDIX A

Table 3: Specific activities after 1 month decay time in the stems (copper and stainless steel), in the DTL tank, in the girders, in the vacuum chamber, in the quadrupole between the 2nd and the 3rd tank, in the waveguide and the support closest to the loss point. The LE values in the last column are the exemption limits taken from the Swiss legislation.

Component	Radionuclide ($t_{1/2}$)	Activity after 1 month decay (Bq)	Specific activity (Bq/g)	LE (Bq/g)
Stem (copper)	Ni-63 (100 y)	1.06E3	0.04	70
	Co-60 (5.2 y)	2.16E3	0.08	1
Stem (stainless steel)	Co-58 (70.8 d)	5.87E4	1.1	10
	Co-57 (271.3 d)	1.98E4	0.37	50
	Fe-55 (2.7 y)	7.03E4	1.3	30
	Mn-54 (312.2 d)	3.16E4	0.59	10
	Fe-55 (2.7 y)	3.76E6	1.47	30
Tank	Mn-54 (312.2 d)	8.94E5	0.35	10
	Cr-51 (27.7 d)	1.41E4	0.03	300
Girder	Fe-55 (2.7 y)	5.41E3	0.01	30
	Zn-65 (244 d)	1.53E3	0.003	3
	Co-58 (70.8 d)	4.29E3	13	10
Vacuum chamber	Fe-55 (2.7 y)	1.08E3	3.3	30
	Cr-51 (27.7 d)	9.43E2	2.88	300
	Fe-55 (2.7 y)	6.49E3	1.03	30
Quadrupole	Mn-54 (312.2 d)	3.01E3	0.48	10
	Fe-55 (2.7 y)	6.27E4	0.42	30
Waveguide	Cr-51 (27.7 d)	7.26E4	0.48	300
	Mn-54 (312.2 d)	1.5E3	0.01	10
	Fe-55 (2.7 y)	1.45E5	0.97	30
Support	Mn-54 (312.2 d)	1.35E4	0.09	10

Table 4: The most important radionuclides responsible for the residual radioactivity in the vacuum chamber of the CCDTL. The LE values in the last column are the exemption limits taken from the Swiss legislation.

Radionuclide ($t_{1/2}$)	Activity after 1 month decay (Bq)	Specific activity (Bq/g)	LE (Bq/g)
Fe-55 (2.7 y)	3.2E8	1173508	30
Mn-54 (312.2 d)	1.41E8	517895	10
Co-57 (271.3 d)	8E7	296961	50
Co-56 (78.76 d)	1.1E8	410298	4
Cr-51 (27.7 d)	1.2E8	431816	300
V-49 (330 d)	8.1E7	298396	600
Co-58 (271.3 d)	1E7	37303	10
V-48 (16 d)	1E7	37303	5
Y-88 (106.6 d)	1.4E6	5138	8
Zr-88 (83.4 d)	1.1E6	4130	30
Sc-46 (83.8 d)	3.1E6	11473	7
Na-22 (2.6 y)	5.9E5	2163	3
H-3 (12 y)	2.2E6	8092	200
Co-60 (5.2 y)	2.2E5	812	1

Table 5: The most important radionuclides responsible for the residual radioactivity in the quadrupole adjacent to the vacuum chamber in the CCDTL. The LE values in the last column are the exemption limits taken from the Swiss legislation.

Radionuclide ($t_{1/2}$)	Activity after 1 month decay (Bq)	Specific activity (Bq/g)	LE (Bq/g)
Co-56 (78.76 d)	4.4E6	707	4
Fe-55 (2.7 y)	3.4E7	5300	30
Mn-54 (312.2 d)	1.5E7	2150	10
Cr-51 (27.7 d)	1.6E6	215	300
Zn-65 (244 d)	1.2E5	18.2	3
Ni-63 (100 y)	5.8E4	9.1	70
Co-60 (5.2 y)	1.3E5	21	1
Co-58 (70.78 d)	2.2E5	35	10
V-49 (330 d)	2.5E5	40	600

APPENDIX A

Table 6: Radionuclide inventory for the CCDTL wall and the nose cone closest to the loss point. The LE values in the last column are the exemption limits taken from the Swiss legislation.

Component	Radionuclide ($t_{1/2}$)	Activity after 1 month decay (Bq)	Specific activity (Bq/g)	LE (Bq/g)
CCDTL wall	Fe-55 (2.7 y)	8.5E7	1785	30
	Mn-54 (312.2 d)	3.9E7	819	10
	Co-56 (78.76 d)	2.4E7	511	4
	Co-57 (271.3 d)	1.4E7	294	50
	Co-58 (70.78 d)	5E6	105	10
	Co-60 (5.2 y)	9.2E4	2.1	1
	Cr-51 (27.7 d)	2.9E7	616	300
	V-49 (330 d)	1.6E7	336	600
	V-48 (16 d)	1.9E6	39.2	5
	Sc-46 (83.8 d)	5.7E5	12	7
Nose-cone	Co-56 (78.76 d)	4.4E6	1239	4
	Fe-55 (2.7 y)	1.5E7	4200	30
	Mn-54 (312.2 d)	6.25E6	1771	10
	Cr-51 (27.7 d)	4.5E6	1281	300
	Co-58 (70.78 d)	1.28E6	362.6	10
	Co-57 (271.3 d)	2.51E6	709	50
	V-49 (330 d)	1.64E6	462	600
	Sc-46 (83.8 d)	4.2E4	10.9	7
	Co-60 (5.2 y)	2.1E4	5.5	1

Table 7: Radionuclide inventory in the copper plating, the drift tube and the stem (copper and stainless steel) of the CCDTL. The LE values in the last column are the exemption limits taken from the Swiss legislation.

Component	Radionuclide ($t_{1/2}$)	Activity after 1 month decay (Bq)	Specific activity (Bq/g)	LE (Bq/g)
Copper plating	Zn-65 (244 d)	7.6E2	1.9	3
	Co-60 (5.2 y)	1.07E3	2.7	1
	Co-58 (70.78 d)	2.8E3	7.7	10
	Co-57 (271.3 d)	1.5E3	3.9	50
Drift tube	Zn-65 (244 d)	5E6	410	3
	Co-60 (5.2 y)	7.3E5	60	1
	Co-57 (271.3 d)	6.5E6	54	50
	Co-58 (70.78 d)	7.1E6	588	10
	Co-56 (78.76 d)	9.7E5	80	4
	Fe-55 (2.7 y)	9.7E5	80	30
	Mn-54 (312.2 d)	5.1E5	42	10
	Ni-63 (100 y)	1.25E5	11.5	70
Stem (copper)	Co-58 (70.78 d)	5.66E3	9.8	10
	Co-60 (5.2 y)	1.78E3	2.8	1
Stem (stainless steel)	Fe-55 (2.7 y)	3.94E4	60.2	30
	Co-58 (70.78 d)	1.49E4	22.4	10
	Co-57 (271.3 d)	1.05E4	16.1	50
	Mn-54 (312.2 d)	1.94E4	29.4	10
	Cr-51 (27.7 d)	1.77E4	26.6	300

APPENDIX A

Table 8: Radionuclide inventory in the vacuum chamber, the quadrupole, the coupling cavity, the waveguide and the support located downstream of the loss point in the CCDTL. The LE values in the last column are the exemption limits taken from the Swiss legislation.

Component	Radionuclide ($t_{1/2}$)	Activity after 1 month decay (Bq)	Specific activity (Bq/g)	LE (Bq/g)
Vacuum chamber	Fe-55 (2.7 y)	6.2E6	41251	30
	Co-57 (271.3 d)	1.48E6	9842	50
	Co-56 (78.76 d)	2.4E6	15778	4
	Mn-54 (312.2 d)	2.4E6	15778	10
	Cr-51 (27.7 d)	2.1E6	13972	300
	V-49 (330 d)	1.1E6	7511	600
	Co-58 (70.78 d)	1.9E5	1288	10
	V-48 (16 d)	1.4E5	910	5
	Sc-46 (83.8 d)	5.1E4	336	7
	Y-88 (106.6 d)	1.8E4	119	8
	Co-60 (5.2 y)	4.2E3	28	1
	Na-22 (2.6 y)	1.3E4	84	3
	Mn-52 (5.6 d)	2.9E4	193.2	6
Quadrupole	Fe-55 (2.7 y)	5.3E5	84	30
	Mn-54 (312.2 d)	2.5E5	37.8	10
	Co-56 (78.76 d)	3.4E4	5.5	4
Coupling cavity	Fe-55 (2.7 y)	1.3E5	12.6	30
	Mn-54 (312.2 d)	5.7E4	5.6	10
	Co-58 (70.78 d)	3.5E4	3.5	10
Waveguide	Fe-55 (2.7 y)	9.6E5	6.5	30
	Cr-51 (27.7 d)	8E5	5.6	300
	Mn-54 (312.2 d)	2.9E5	2.1	10
Support	Fe-55 (2.7 y)	3.2E6	10.5	30
	Mn-54 (312.2 d)	1.1E6	3.5	10

Table 9: Radionuclide inventory for the vacuum chamber of the PIMS. The LE values in the last column are the exemption limits taken from the Swiss legislation.

Radionuclide ($t_{1/2}$)	Activity after 1 month decay (Bq)	Specific activity (Bq/g)	LE (Bq/g)
Fe-55 (2.7 y)	2.58E8	708010	30
Mn-54 (312.2 d)	1.24E8	340280	10
Cr-51 (27.7 d)	1.41E8	386930	300
V-49 (330 d)	1.33E8	364980	600
Co-57 (271.3 d)	7.2E7	197850	50
Co-56 (78.76 d)	7E7	192100	4
Y-88 (106.6 d)	3.48E6	9550	8
Zr-88 (83.4 d)	2.71E6	7440	30
Co-58 (70.78 d)	9.76E6	26780	10
Sc-46 (83.8 d)	9.08E6	24920	7
Ca-45 (163 d)	1.12E6	3070	10
H-3 (12 y)	7E6	19210	200
Co-60 (5.2 y)	3E5	820	1

Table 10: Radionuclide inventory for the quadrupole adjacent to the vacuum chamber in the PIMS. The LE values in the last column are the exemption limits taken from the Swiss legislation.

Radionuclide ($t_{1/2}$)	Activity after 1 month decay (Bq)	Specific activity (Bq/g)	LE (Bq/g)
Co-56 (78.76 d)	3E7	4050	4
Fe-55 (2.7 y)	1.7E8	22930	30
Mn-54 (312.2 d)	8.6E7	11630	10
Cr-51 (27.7 d)	2.7E7	3640	300
Zn-65 (244 d)	7.9E5	110	3
Ni-63 (100 y)	1.2E5	16	70
Co-60 (5.2 y)	4.9E5	66	1
Co-58 (70.78 d)	3E6	400	10
Co-57 (271.3 d)	3.7E6	500	50
V-49 (330 d)	1.69E7	2280	600
H-3 (12 y)	1.75E6	240	200

APPENDIX A

Table 11: Radionuclide inventory for the left wall of the 12th tank of the PIMS and the 1.9 cm thick structures (downstream and upstream of the loss point). The LE values in the last column are the exemption limits taken from the Swiss legislation.

Component	Radionuclide ($t_{1/2}$)	Activity after 1 month decay (Bq)	Specific activity (Bq/g)	LE (Bq/g)
Left wall of the 12 th tank	Co-60 (5.2 y)	1.9E6	30	1
	Co-58 (70.78 d)	6.56E6	103	10
	Co-57 (271.3 d)	4.4E6	69.6	50
	Fe-55 (2.7 y)	1.24E6	19.2	30
	Zn-65 (244 d)	9.54E5	14.4	3
	Ni-63 (100 y)	4.77E5	7.2	70
	Co-56 (78.76 d)	7.8E5	12	4
	Mn-54 (312.2 d)	7.23E5	11.4	10
External wall of the 12 th tank	Co-58 (70.78 d)	1.1E6	19.2	10
	Co-57 (271.3 d)	5.79E5	9.6	50
	Ni-63 (100 y)	1.29E5	2.16	70
	Co-60 (5.2 y)	4.37E5	7.2	1
	Fe-55 (2.7 y)	1.42E5	2.4	30
	Mn-54 (312.2 d)	1.11E5	1.92	10
External wall of the 11 th tank	Co-58 (70.78 d)	1.85E5	3.12	10
	Co-57 (271.3 d)	9.27E4	1.56	50
	Ni-63 (100 y)	5.24E4	0.84	70
	Co-60 (5.2 y)	1.17E5	2	1
	Fe-55 (2.7 y)	2.27E4	0.36	30
	Mn-54 (312.2 d)	1.87E4	0.36	10

Table 12: Radionuclide inventory for the first nose cone of the 12th PIMS tank, the copper cylinder between the 1st and the 2nd cell of the 12th tank, the waveguide and the support closest to the loss point. The LE values in the last column are the exemption limits taken from the Swiss legislation.

Component	Radionuclide (t _{1/2})	Activity after 1 month decay (Bq)	Specific activity (Bq/g)	LE (Bq/g)
Nose-cone	Co-58 (70.78 d)	3.34E6	285.6	10
	Co-57 (271.3 d)	2.78E6	237.6	50
	Zn-65 (244 d)	6.54E5	56.4	3
	Ni-63 (100 y)	1.34E5	11.5	70
	Co-60 (5.2 y)	6.95E5	60	1
	Co-56 (78.76 d)	6.39E5	55.2	4
	Fe-55 (2.7 y)	8.9E5	75.6	30
	Mn-54 (312.2 d)	4.95E5	42	10
Copper cylinder	Co-58 (70.78 d)	3.85E6	1004.4	10
	Co-57 (271.3 d)	3.94E6	1032	50
	Zn-65 (244 d)	9.8E5	252	3
	Ni-63 (100 y)	6.6E4	16.8	70
	Co-60 (5.2 y)	4.75E5	120	1
	Co-56 (78.76 d)	1.08E6	282	4
	Fe-55 (2.7 y)	1.28E6	333.6	30
	Mn-54 (312.2 d)	6.65E5	174	10
Waveguide	Fe-55 (2.7 y)	2.22E6	14.8	30
	Mn-54 (312.2 d)	1.09E6	7.2	10
Support	Fe-55 (2.7 y)	3.74E6	25.2	30
	Mn-54 (312.2 d)	1.71E6	11.4	10

APPENDIX A

Table 13: The most important radionuclides responsible for the residual radioactivity in the vacuum chamber for the alternative layout of the CCDTL. The LE values in the last column are the exemption limits taken from the Swiss legislation.

Radionuclide ($t_{1/2}$)	Activity after 1 month decay (Bq)	Specific activity (Bq/g)	LE (Bq/g)
Fe-55 (2.7 y)	3.03E8	1601964	30
Mn-54 (312.2 d)	1.35E8	713741	10
Co-57 (271.3 d)	7.7E7	407099	50
Co-56 (78.76 d)	1.04E8	549850	4
Cr-51 (27.7 d)	1.12E8	592144	300
V-49 (330 d)	7.92E7	418726	600
Co-58 (271.3 d)	9.74E6	51492	10
V-48 (16 d)	9.89E6	52290	5
Y-88 (106.6 d)	1.34E6	7084	8
Zr-88 (83.4 d)	1.09E6	5761	30
Sc-46 (83.8 d)	3.02E6	15967	7
Na-22 (2.6 y)	5.72E5	3038	3
Co-60 (5.2 y)	2.11E5	1113	1

Table 14: Radionuclide inventory for the PMQ adjacent to the vacuum chamber for the alternative layout of the CCDTL. The LE values in the last column are the exemption limits taken from the Swiss legislation.

Radionuclide ($t_{1/2}$)	Activity after 1 month decay (Bq)	Specific activity (Bq/g)	LE (Bq/g)
Co-58 (70.8 d)	4.48E6	1281	10
Co-60 (5.2 y)	3.13E5	89.6	1
Co-57 (271.3d)	1.6E6	457.8	50
Co-56 (78.76 d)	3.3E5	93.8	4
Fe-55 (2.7 y)	1.33E6	385	30
Eu-149 (93.1d)	1.08E5	30.8	100
Sm-145 (340d)	3.08E5	88.2	50
Fe-59 (45 d)	3.16E5	90.3	10
Mn-54 (312.2 d)	7.85E5	224	10
Na-22 (2.6 y)	7.84E5	224	3

Table 15: Radionuclide inventory for the CCDTL wall and the nose-cone closest to the loss point in the alternative layout of the CCDTL. The LE values in the last column are the exemption limits taken from the Swiss legislation.

Component	Radionuclide ($t_{1/2}$)	Activity after 1 month decay (Bq)	Specific activity (Bq/g)	LE (Bq/g)
CCDTL wall	Fe-55 (2.7 y)	2.49E8	5201	30
	Mn-54 (312.2 d)	1.07E8	2233	10
	Co-56 (78.76 d)	7.88E7	1645	4
	Co-57 (271.3 d)	4.06E7	847	50
	Co-58 (70.78 d)	1.14E7	238	10
	Co-60 (5.2 y)	2.15E5	4.2	1
	Cr-51 (27.7 d)	8.38E7	1750	300
	V-49 (330 d)	4.27E7	889	600
	V-48 (16 d)	5.23E6	109.2	5
Nose-cone	Sc-46 (83.8 d)	1.43E6	30.1	7
	Co-56 (78.76)	1.64E6	462	50
	Fe-55 (2.7 y)	1.19E7	3367	30
	Mn-54 (312.2 d)	6.06E6	1715	10
	Cr-51 (27.7 d)	3.3E6	938	300
	Co-58 (70.78 d)	2.27E6	642.6	10
	Co-57 (271.3 d)	2.11E6	595	50
	V-49 (330 d)	9.11E5	257.6	600
	Sc-46 (83.8 d)	2.69E4	7.7	7
	Co-60 (5.2 y)	4.74E4	13.3	1

APPENDIX A

Table 16: Radionuclide inventory for the coupling cavity located in proximity of the loss point in the alternative layout of the CCDTL. The LE values in the last column are the exemption limits taken from the Swiss legislation.

Radionuclide ($t_{1/2}$)	Activity after 1 month decay (Bq)	Specific activity (Bq/g)	LE (Bq/g)
Fe-55 (2.7 y)	6.25E5	473.9	30
Mn-54 (312.2 d)	3.57E5	270.9	10
Co-58 (70.78 d)	4.23E5	320.6	10
Co-57 (271.3 d)	1.15E5	87.5	50

Table 17: Radionuclide inventory in the copper plating, the drift tube and the stem (copper and stainless steel) of the CCDTL (alternative layout). The LE values in the last column are the exemption limits taken from the Swiss legislation.

Component	Radionuclide ($t_{1/2}$)	Activity after 1 month decay (Bq)	Specific activity (Bq/g)	LE (Bq/g)
Copper plating	Co-60 (5.2 y)	5.6E2	1.4	1
	Co-58 (70.78 d)	2.2E3	5.6	10
	Co-57 (271.3 d)	5.9E2	1.4	50
Drift tube	Zn-65 (244 d)	1.5E6	123.9	3
	Co-60 (5.2 y)	1.77E5	14.7	1
	Co-57 (271.3 d)	9.22E5	76.3	50
	Co-58 (70.78 d)	1.43E6	118.3	10
	Co-56 (78.76 d)	8.16E4	7	4
	Fe-55 (2.7 y)	1.51E5	12.6	30
	Mn-54 (312.2 d)	5.99E4	4.9	10
	Ni-63 (100 y)	4.35E4	3.5	70
Stem (copper)	Co-58 (70.78 d)	3.35E3	5.6	10
	Co-60 (5.2 y)	1.68E3	2.8	1
Stem (stainless steel)	Fe-55 (2.7 y)	3.75E4	56.7	30
	Co-58 (70.78 d)	1.79E4	27.3	10
	Co-57 (271.3 d)	1.25E4	18.9	50
	Mn-54 (312.2 d)	2.17E4	32.9	10
	Cr-51 (27.7 d)	1.77E4	26.6	300

Table 18: Radionuclide inventory in the vacuum chamber, the PMQ, the waveguide and the support located downstream of the loss point in the CCDTL (alternative layout). The LE values in the last column are the exemption limits taken from the Swiss legislation.

Component	Radionuclide ($t_{1/2}$)	Activity after 1 month decay (Bq)	Specific activity (Bq/g)	LE (Bq/g)
Vacuum chamber	Fe-55 (2.7 y)	9.7E3	51.1	30
	Co-57 (271.3 d)	1.78E3	9.1	50
	Co-56 (78.76 d)	1.7E3	9.1	4
	Mn-54 (312.2 d)	2.9E3	15.4	10
	Cr-51 (27.7 d)	3.3E3	17.5	300
	Co-60 (5.2 y)	5.58E2	2.8	1
PMQ	Co-60 (5.2 y)	7.23E4	20.7	1
Waveguide	Fe-55 (2.7 y)	1.88E6	12.5	30
	Cr-51 (27.7 d)	1.01E6	6.7	300
	Mn-54 (312.2 d)	8.14E5	5.4	10
Support	Fe-55 (2.7 y)	1.7E6	5.6	30
	Mn-54 (312.2 d)	3.9E5	1.4	10

Bibliography

1. *NCRP Report No 144, Radiation protection for particle accelerator facilities, National Council on Radiation Protection and Measurements.* 2007.
2. **Sullivan, A. H.** *A guide to radiation and radioactivity levels near high energy proton accelerators.* Ashford, Kent : Nuclear Techology Publishing, 1992.
3. **Evans, R. D.** *The atomic nucleus.* New York : McGraw-Hill Book Company, 1969.
4. **Richard-Serre, F. D. et Measday, C.** *Loss of protons by nuclear interactions in various materials.* CERN Yellow Report 69-17. 1969.
5. **Bertini, H. W.** *Low energy intranuclear cascade calculation.* Physical Review 131. 1963.
6. **Chen, K, et al.** *A Monte Carlo simulation of intranuclear cascades.* Physical Review 166 (1968) 949.
7. **Metropolis, N., et al.** *Monte Carlo Calculations on intranuclear cascades.* Physical Review 110 (1958) 185.
8. **Broome, T, et al.** *Particle distribution around a copper beam stop for 72 MeV protons.* Health Physics 44 (1983) 487.
9. **Cierjacks, S., et al.** *High energy particle spectra from spallation targets.* Proc. 5th Mtg on Advanced Neutron Sources, Julich (1981) 215.
10. **Nakamura, T., et al.** *Neutron production from thick targets of carbon, iron, copper and lead by 30 and 52 MeV protons.* Nuclear Science and Engineering 83 (1983) 444.
11. **Alsmille, R., G., et al.** *Calculated neutron production by 190 to 268 MeV protons in a water cooled tantalum target.* Nuclear Science and Engineering 80 (1982) 452.
12. **Fullwood, R., et al.** *Neutron production by medium-energy protons on heavy metal targets.* Los Alamos Scientific Lab., Los Alamos, NM : Rep. LA-4789, 1972.
13. **Tesch, K.** A simple estimation of the lateral shielding for proton accelerators in the energy range 50 to 1000 MeV. Radiation Protection Dosimetry, 1985, Vol. 11, 3, pp. 165 – 172.
14. **Alsmiller, R. G., Leimdorfer, Jr. et Barish, J.** *Analytic representation of non-elastic cross-sections and particle emission spectra from nucleon-nucleus collisions in the energy range 25 - 400 MeV.* Oak Ridge Natl. Lab., Oak Ridge, TN : Rep. ORNL-4046, 1967.
15. *NCRP Report No 38, Protection against neutron radiation, National Council on Radiation Protection and Measurements.* 1971.
16. **Moritz, L. E.** Radiation protection at low energy proton accelerators. Nuclear Technology Publishing, 2001, Vol. 96, 4, pp. 297 - 309.

17. **Fassò, A., et al.** *FLUKA: a multi-particle transport code.* CERN-2005-10 (2005), INFN/TC_05/11, SLAC-R-773.
18. **Fassò, A., et al.** *The physics models of FLUKA: status and recent developments.* Computing in High Energy and Nuclear Physics 2003 Conference, La Jolla, CA, USA, March 24 - 28, 2003.
19. **Moyer, B. J.** Evaluation of the shielding required for the improved Bevatron. UCRL-9769, 1961.
20. **Stapleton, G. B., O'Brien, K. et Thomas, R. H.** Accelerator skyshine. Tyger, Tyger, Burning Bright. Part. Accel. 44(1), 1 - 15 , 1994.
21. **Barish, Jr., Childs, R. L. et Alsmiller, R. G.** Skyshine at neutron energies less than 400 MeV. Part. Accel. 11, 131-141, 1981.
22. *NCRP Report No 123, Screening models for releases of radionuclides to atmosphere, surface water and ground, National Council on Radiation Protection and Measurements.* 1996.
23. **Gollon, P. J.** *Production of radioactivity by particle accelerators.* IEEE Trans. Nucl. Sci. NS-23, 1395-1398. 1976.
24. **Sullivan, A. H. et Overton, T. R.** *Time variation of the dose rate from radioactivity induced in high-energy particle accelerators.* Health Physics 11, 1101-1105. 1965.
25. **Huhtinen, M.** *Determination of cross-sections for assessment of air activation at LHC.* CERN Internal Report CERN/TIS-RP/TM/97-29. 1997.
26. **Stevenson, G. R.** *Induced activity in accelerator structures, air and water.* Radiation Protection Dosimetry Vol.96, No. 1 - 4, pp. 373 - 380. 2001.
27. **Garoby, R., et al.** *Preliminary Accelerator Plans for Maximizing the Integrated LHC Luminosity.* CERN-AB-2006-018.
28. **Gerigk, F. et Vretenar, M.** *Linac4 Technical Design Report.* CERN-AB-2006-084.
29. **Gerigk, F.** *The SPL study group, conceptual design of the SPL II a high power superconducting H-linac at CERN.* CERN-2006-006.
30. *LHC Design Report, Volume III, The LHC Injector Chain,* CERN-2004-003.
31. **Boussard, D., et al.** *Preliminary parameters of a proton linac using the LEP2 RF system when decommissioned.* SL-RF Technical Note 96-4.
32. **Vretenar, M et Garoby, R.** *Proposal for a 2 GeV linac injector for the CERN PS.* s.l. : PS/RF/Note 96-27.
33. **Vretenar, M.** *Conceptual design of the SPL, a high power superconducting H- linac at CERN.* : CERN-2000-012.
34. **Vretenar, M.** *Linear accelerator designs for the upgrade of the CERN proton injector complex (LINAC4, SPL).* s.l. : CARE-Conf-2007-002-HIPPI, 2007.

BIBLIOGRAPHY

35. *EURISOL Design study.*
36. **Benedikt, M., et al.** *Potential for neutrino and radioactive beam physics of the foreseen upgrades of the CERN.* CERN-AB-2006-019-PAF.
37. **Gruber, P.** *The Study of a European Neutrino Factory Complex.* CERN/PS/2002-080(PP), CERN-NUFACT 122.
38. **Alba, M.** *Feasibility Study of Accumulator and Compressor for the 6-bunches SPL-based Proton Driver.* CERN-AB-2008-060. 2008.
39. **Lombardi, A. M.** *End-to-End Beam Dynamics for CERN Linac4.* Geneva : Tech. Rep. CERN-AB-2007-001 / CARE-Conf-06-039-HIPPI, CERN, August 2006.
40. **Gerigk, F, et al.** *RF Structures for Linac4.* s.l. : PAC07, Albuquerque.
41. **Vretenar, M., et al.** *Development Status of the Pi-Mode Accelerating Structure (PIMS) for Linac4, to be published.*
42. **Baldy, J. L., et al.** *Site layout of the new proposed hadrons injector chain at CERN.* CERN-AB-2007-061-PAF.
43. **Lombardi, A. M., et al.** *Loss Control and Steering Strategy for the CERN LINAC4.* s.l. : CERN-AB-2007-033 .
44. **Mauro, E., Silari, M. et Vincke, H.** *Radiological interferences between the SPL tunnel and existing underground and surface structures,* CERN-SC-2007-083-RP-TN. 2007.
45. **Peters, J.** *The HERA RF-Volume Source.* PAC05 Conf. Proc. 2005.
46. **Kuchler, D., et al.** *Towards an H- Rf Source for Future CERN Accelerator Projects.* Proc. 11th International Symposium on Production of negative Ions and Beams, AIP 195, 121. 2006.
47. **Peters, J.** *The HERA RF-driven Multicusp H- Ion Source.* s.l. : Proc. 11th International Symposium on Production and Neutralization of negative Ions and Beams, AIP 195, 79, 2006.
48. **Rossi, C., et al.** *The Radiofrequency Quadrupole accelerator for the Linac4, to be published.*
49. **Mathot, S.** *RFQ Vacuum Brazing at CERN.* Genova, Italy : EPAC08.
50. **Ramberger, S., et al.** *Drift tube linac design and prototyping for the CERN Linac4, to be published.*
51. **Stovall, J.** *Low and Medium Energy Beam Acceleration in High Intensity Linacs.* Lucerne, Switzerland : Proc. EPAC 2004, pp.108-112, 2004.
52. **Lapostolle, P. M. et Septier, L.** *Linear accelerators.* Amsterdam : North-Holland, 1970.
53. **Moretti, A., et al.** *Effects of high solenoidal magnetic fields on rf accelerating cavities.* Phys. Rev. ST Accel. Beams 8(2005) 7, p. 072001.
54. **Gerigk, F, et al.** *Development of a cell-coupled drift tube Linac (CCDTL) for Linac4.* s.l. : to be published.

55. **Billen, J., et al.** A new RF structure for intermediate-velocity particles. *Proceedings of the 1994 Linear Accelerator Conference, Tsukuba, Japan, August 21 -26, 1994.*

56. **Wilson, I. et Henke, H.** The LEP main ring accelerating structure. *CERN-89-09.* November 1989.

57. **Gerigk, F, et al.** Development status of the pi-mode accelerating structure (PIMS) for Linac4. s.l. : to be published.

58. **Ranft, J.** 33 years of high energy radiation Monte Carlo calculations in Europe as seen from CERN. *Proceedings of SARE-2, CERN-TIS-RP/97-05.* 1997.

59. **Battistoni G., et al.** The FLUKA code: Description and benchmarking. *Proceedings of the Hadronic Shower Simulation Workshop 2006, Fermilab 6--8 September 2006, M. Albrow, R. Raja eds.,AIP Conference Proceeding 896, 31-49.* 2007.

60. **Cullen D. E., et al.** *EPDL97: the Evaluated Photon Data Library, '97 Version. UCRL-50400, Vol. 6.*

61. **Antonelli, M., et al.** *Proc. VI Int. Conf. on Calorimetry in High Energy Physics (Calor 96), Frascati. Physics Series Vol. VI , pp. 561-570.* 1997.

62. **Battistoni, G., et al.** *Nuclear Instruments and Methods A394 , 136-145,* 1997.

63. **Ferrari A., et al.** *Nuclear Instruments and Methods B71, 412-426.* 1992.

64. **Fassò A., et al.,** Proceedings of SARE-3, KEK report Proceedings 97-5, 32. H. Hirayama ed. 1997.

65. **Sihver, L., et al.** *Jpn. J. Med. Phys. 18, I.* 1998.

66. **Sommerer F., et al.,** *Physics in Medicine and Biology 51, 4385.* 2006.

67. **Ferrari, A. et Sala, P. R.** Proceedings of Workshop on Nuclear Reaction Data and Nuclear Reactors Physics, Design and Safety, 2, 424. A. Gandini, G. Reffo eds. 1998.

68. **Battistoni G., et al.** Proc. 11th Int. Conf. on Nuclear Reaction Mechanisms, 126,483. Ric. Scient. ed Ed. Perm. Suppl., E. Gadioli ed. 2006.

69. **Capella, A., et al.** *Physics Reports 236, 225.* 1994.

70. **Glauber, R. J. et Matthiae, G.** *Nuclear Physics B21, 135.* 1970.

71. **Gribov, V. N.** Sov. Phys. JETP 29, 483. 1969.

72. **Ferrari, A. et Sala, P. R.** Proc. MC93 Int. Conf. on Monte-Carlo Simulation in High-Energy and Nuclear Physics. World Scientific ed., 277. 1994.

73. **Scobel, W. et al.** *Physical Review C41, 2010,* 1990.

74. **Ishibashi, et al.** *Nuclear Science and Technology 32, 827,* 1995.

75. **Franz, J., Koncz, P. et Rossle, E.** *Nuclear Physics A510, 774.* 1990.

76. **Enqvist T., et al.** *Nuclear Physics A 686 481.* 2001.

BIBLIOGRAPHY

77. **Birattari C., et al.** *Radiation Protection Dosimetry* 76, 135, 1988.

78. **Brugger M., et al.** *Radiation Protection Dosimetry* 116, 12-15, 2005.

79. **Fassò, A., et al.** A comparison of FLUKA simulations with measurements of fluence and dose in calorimeter structures. *Nuclear Instruments & Methods A*, 332, 459-468. 1993.

80. **Andriamonje S., et al.** Experimental determination of the energy generated in nuclear cascades by a high energy beam. *Physics Letter B*, 348 697-709. 1995.

81. **Arnould, H., et al.** Experimental verification of neutron phenomenology in lead and transmutation by adiabatic resonance crossing in accelerator driven systems. *Physics Letter B*, 458 167-180. 1999.

82. **Abánades, A., et al.** Results from the TARC experiment: spallation neutron phenomenology in lead and neutron-driven nuclear transmutation by adiabatic resonance crossing. *Nuclear Instruments & Methods A*, 478, 577-730, 2002.

83. **Nakamura T., et al.** Intercomparison of Neutron Transmission Benchmark Analyses for Iron and Concrete shields in low, intermediate and high energy Proton Accelerator Facilities. *Proceedings of the 3rd "Specialists" Meeting on Shielding Aspects of Accelerators, Targets & Irradiation Facilities (SATIF-3), Tohoku University, Sendai, Japan, May 12-13 1997. OECD/NEA, OECD documents, ISBN 92-64-16071-X, 151-182.* 1998.

84. **Birattari C., et al.** Measurements and characterization of high energy neutron fields. *Nuclear Instruments & Methods A*, 338, 534-543. 1994.

85. —. Measurements and simulations in high energy neutron fields. *Proceedings of the 2nd "Specialists" Meeting on Shielding Aspects of Accelerators, Targets & Irradiation Facilities (SATIF-2), CERN-Geneva October 12-13 1995. OECD/NEA, OECD documents, ISBN 92-64-15287-3, 171-197.* 1996.

86. **Hajek M., et al.** Comparison of measurements with active and passive Bonner sphere spectrometers. *2000 International Conference on Nuclear Science and Technology: Supporting Sustainable Development Worldwide, 12-16 Nov. 2000, Washington, DC. USA. Trans. Am. Nucl. Soc. 2000, 83, 263-265.* 2000.

87. Thesis dissertations by: E. De Ponti (Academic year 1992-1993), M. Magugliani (Academic year 1994-1995), T. Rancati (Academic year 1995-1996), E. Nava (Academic year 1996-1997). Università degli Studi di Milano : unpublished.

88. **Ferrari, A., Pelliccioni, M. et Pillon, M.** Fluence to effective dose and effective dose equivalent conversion coefficients for photons from 50 keV to 10 GeV. *Radiation Protection Dosimetry* 67, n° 4, 245-251. 1996.

89. —. Fluence to effective dose and effective dose equivalent conversion coefficients for electrons from 5 MeV to 10 GeV. *Radiation Protection Dosimetry* 69, n° 2, 97-104. 1997.

90. —. Fluence to effective dose conversion coefficients for protons from 5 MeV to 10 TeV. *Radiation Protection Dosimetry* 71, n° 2, 85-91. 1997.

91. —. Fluence to effective dose conversion coefficients for neutrons up to 10 TeV. *Radiation Protection Dosimetry* 71, n° 3, 165-173. 1997.

92. —. Fluence to effective dose conversion coefficients for muons. *Radiation Protection Dosimetry* 74, n° 4, 227-233. 1997.

93. —. Fluence to effective dose conversion coefficients for negatively and positively charged pions. *Radiation Protection Dosimetry* 80, n° 4, 361-370. 1998.

94. **Ferrari, A. et Pelliccioni, M.** On the Conversion Coefficients for Cosmic Ray Dosimetry. *Radiation Protection Dosimetry*, 104, 211-220. 2003.

95. **Biaggi, M., et al.** Physical and biophysical characteristics of a fully modulated 72 MeV therapeutic proton beam: model predictions and experimental data. *Nuclear Instruments & Methods B*, 159, 89-100. 1999.

96. **Ballarini, F., et al.** Estimating mixed field effects: an application supporting the lack of a non-linear component for chromosome aberration induction by neutrons. *Radiation Protection Dosimetry* 103, 19-27. 2003.

97. **Ballarini, F., et al.** Role of shielding in modulating the effects of solar particle events: Monte Carlo calculation of absorbed dose and DNA complex lesions in different organs. *Advances in Space Research*, 34(6), 1338-1346. 2004.

98. National Bronze & Metals, Inc., Houston, Texas, USA.

99. Table of Isotopes . New York : Ed. by R.B. Firestone ,Wiley, 1996.

100. **Mauro, E. et Silari, M.** An estimate of the activation of patient-specific collimators used in proton therapy. *IEO-ARC Project Note* 2. 2008.

101. —. Calcolo approssimato del numero di protoni richiesto per fornire una dose predeterminata ad un volume bersaglio mediante terapia adronica. *IEO-ARC Project Note* 3. 2008.

102. **Goebel, K., et al.** *Evaluating dose rates due to neutron leakage through the access tunnels of the SPS. CERN Lab II-RA/Note/75-10.* 1975.

103. **Thomas, R. H. et Stevenson, G. R.** Radiological safety aspects of the operation of proton accelerators. Vienna:IAEA : Technical Report Series No. 283, 1988.

104. **Cohen, M. O., et al.** *SAM-CE: A Three-Dimensional MonteCarlo Code for Solution of the Forward Neutron and Forward and Adjoint Gamma-Ray Transport Equations.* Springfield, Virginia : DNA-2830-F, Rev. B (National Technical Information Service), 1973.

105. **Maerker, R. E. et Cain, V. R.** *AMC: A Monte Carlo Code Utilizing the Albedo Approach for Calculating Neutron and Capture Gamma-Ray Distributions in Rectangular Concrete Ducts.* Oak Ridge National Laboratory, Oak Ridge, Tennessee : ORNL-3964, 1967.

106. **D'Hombres, M. M., et al.** *Propagation des Neutrons dans les Tunnels d'Accès à un Accélérateur de Haute Energie à Protons.* Centre d'Etudes Nucléaires de Saclay, Saclay, France : R-3491, 1968.

BIBLIOGRAPHY

107. **Stevenson, G. R. et Fassò, A.** *A Comparison of a Morse Calculation of Attenuation in a Concrete-lined Duct with Experimental Data from the CERN SPS.* CERN Divisional Report TIS-RP/185/CF. 1987.
108. **Tesch, K.** The attenuation of the neutron dose equivalent in a labyrinth through an accelerator shield. Part. Acc. 12, 169.
109. *NCRP Report No 51, Radiation Protection Design Guidelines for 0.1 - 100 MeV Particle Accelerator Facilities, National Council on Radiation Protection and Measurements.* 1977.
110. **Maerker, R. E. et Muckenthaler, F. J.** Monte-Carlo Calculations, using the Albedo Concept, of the Fast-neutron Dose Rates along the Center Lines of One- and Two-legged Square Concrete Open Ducts and Comparison with Experiment. *Nuclear Science and Engineering* 27 (1967) 423 .
111. —. *Neutron fluxes in concrete ducts arising from incident epicadmium neutrons: calculations and experiments.* *Nuclear Science and Engineering* 27 (1967) 423-432.
112. **Gollon, P. J. et Awschalom, M.** Design of penetrations in hadron shield. *IEEE Trans. Nucl. Sci.* 18 (1971) 741 - 745.
113. **Maerker, R. E. et Muckenthaler, F. J.** Calculation and measurement of the fast-neutron differential dose albedo for concrete. *Nuclear Science and Engineering* 30 (1967) 340.
114. **Cossairt, J. D., et al.** Radiation measurements in a labyrinth penetration at a high energy proton accelerator. *Health Physics* 49 (1985) 907 - 917.
115. **Cossairt, J. D.** *Radiation physics for personnel and environmental protection, Rev. 9B.* Batavia, Illinois : Fermi National Accelerator Laboratory Report TM-1834, 2007.
116. **Nakane, Y., et al.** *Intercomparison of neutron transmission benchmark analyses for iron and concrete shield in low, intermediate and high energy proton accelerator facilities.* Tohoku University, Sendai, Japan : Proceedings of the 3rd "Specialists" meeting on shielding aspects of accelerators, targets & irradiation facilities (SATIF-3), May 12-13 1997, published by OECD/NEA, OECD documents, ISBN 92-64-16071-X (1998) 151 – 182.
117. **Mauro, E. et Silari, M.** Attenuation of neutrons through ducts and labyrinths, submitted for publication in *Nuclear Instruments and Methods A*.
118. —. *Radiation protection studies for a high-power 160 MeV proton linac.* *Nuclear Instruments and Methods A, in press.*
119. **Gaborit, J. C., Silari, M. et Ulrici, L.** *Radiation levels in the CERN Large Electron Positron collider during the LEP 2 phase (68 - 105 GeV).* *Nuclear Instruments and Methods A* 565 (2006) 333 - 350.
120. **Silari, M. et Vincke, H.** *Shielding proposal for the SPL front end.* CERN-TIS-2003-002-RP-TN. 2003.
121. **Magistris, M. et Silari, M.** *Preliminary shielding design of Linac4.* CERN-SC-2005-011-RP-TN. 2005.
122. —. *Preliminary shielding design of Linac4. Top shielding and induced radioactivity.* CERN-SC-2005-050-RP-TN. 2005.

123. **Magistris, M., Mauro, E. et Silari, M.** *Complementary shielding calculation for Linac4 in the South Hall.* CERN-SC-2006-060-RP-TN. 2006.

124. —. *Radiation protection considerations for the installation of Linac4 in the existing Linac2 building.* CERN-SC-2007-031-RP-TN. 2007.

125. —. *Radiation protection studies for the front-end of the 3.5 GeV SPL.* Pocatello, Idaho, USA : Eighth international Topical Meeting on Nuclear Applications and Utilization of Accelerator Conference(AccApp07), 30 July - 2 August 2007.

126. **Agosteo, S., et al.** Shielding data for 100 - 250 MeV proton accelerators: Double differential neutron distributions and attenuation in concrete. *Nuclear Instruments and Methods in Physics Research Section B* 265 (2007) pp. 581 -598.

127. *Safety Code F, Radiation Protection, CERN.* November 2006.

128. **Theis, C., et al.** *Interactive three dimensional visualization and creation of geometries for Monte Carlo calculations.* *Nuclear Instruments and Methods A* 562, 827 - 829. 2006.

129. **Lombardi, A. M., et al.** *Loss management and alignment tolerances for the CERN Linac4, in preparation.*

130. **Williams, T. et Kelley, C.** *Gnuplot, an interactive plotting program.*

131. **Mauro, E. et Silari, M.** *Residual dose rates and induced radioactivity in the Linac4 tunnel.* CERN-SC-2008-069-RP-TN. 2008.

132. —. *Residual dose rates and induced radioactivity in the Linac4 tunnel for an alternative layout of the CCDTL section.* CERN-SC-2008-090-RP-TN. 2008.

133. *Swiss Legislation on Radiological Protection (Ordonnance sur la Radioprotection), ORaP of 22nd June 1994.* state 4th April 2000.

134. **Eckerman, K. F. et Ryman, J. C.** *External Exposure to Radionuclides in Air, Water and Soil.* Washington DC : Federal Guidance Report No. 12, EPA 402-R-93-081, Environmental Protection Agency, 1993.

135. *ICRP Publication 60, 1990 Recommendations of the International Commission on Radiological Protection.* *Annals of the ICRP* Vol. 21, No. 1 – 3. 1991.

136. **Cerutti, F., et al.** *Study of energy deposition and activation for the Linac4 dump,* CERN-SC-2008-085-RP-TN. 2008.

137. **Roesler, S. et Stevenson, G. R.** *deq99.f - A FLUKA user-routine converting fluence into effective dose and ambient dose equivalent.* CERN-SC-2006-070-RP-TN. 2006.

138. **Birattari, C., et al.** *Neutron Activation of Air by a Biomedical Cyclotron and an Assessment of Dose to Neighbourhood Populations.* *Radiation Protection Dosimetry*, Vol. 14, Issue 4, pp. 311 - 319. 1986.

BIBLIOGRAPHY

139. **Vojtyla, P.** *Models for Assessment of the Environmental Impact of Radioactive Releases from CERN Facilities.* CERN-SC-2005-005-IE. 2005.
140. —. *Dose Conversion Coefficients for Exposure of the Reference Population Group to Radionuclides in Air Released from the ISOLDE Facility.* CERN-SC-2008-001-IE-TN. 2008.
141. *Hauptabteilung fur die Sicherheit der Kernanlagen (HSK), Berechnung der Strahlenexposition in der Umgebung aufgrund von Emissionen radioaktiver Stoffe aus Kernanlagen.* s.l. : HSK-R-41/d, July 1997.

Publications

1. **Magistris M., Mauro E. and Silari M.**, *Radiation protection studies for the front-end of the 3.5 GeV SPL at CERN*, Proceedings of the Eighth International Topical Meeting on Nuclear Applications and Utilization of Accelerators (AccApp' 07) – Pocatello, Idaho – July 29 – August 2, 2007, published by the American Nuclear Society, pp 37 - 44.
2. **Mauro E., Silari M. and Vincke H.**, *Radiation protection studies for the new CERN injector complex*, Proceedings of the 11th International Conference on Radiation Shielding (ICRS-11)– Callaway Gardens, Pine Mountain, Georgia, USA – April 13 – 18, 2008, accepted for Publication by Nuclear Technology, Vol. 168, Oct. 2009 (uncorrected proof).
3. **Mauro E. and Silari M.**, *Radiation protection studies for a high-power 160 MeV proton linac*, Nucl. Instr. and Meth. A (2009), doi:10.1016/j.nima.2009.03.250.
4. **Mauro E. and Silari M.**, *Attenuation of neutrons through ducts and labyrinths*, Nucl. Instr. and Meth. A (2009), doi:10.1016/j.nima.2009.06.045.

RADIATION PROTECTION STUDIES FOR THE FRONT-END OF THE 3.5 GEV SPL AT CERN

Matteo Magistris, Egidio Mauro* and Marco Silari

* Corresponding author: Tel.+41227675280; E-mail address: egidio.mauro@cern.ch

CERN, CH-1211 Geneve 23, Switzerland

CERN is presently designing a Superconducting Proton Linac (SPL) accelerating H^- ions to energy of 3.5 GeV and beam power of up to 4 MW. The ultimate goal of this accelerator is the production of intense neutrino beams. The SPL is also intended to replace the present CERN injectors, the 50 MeV linac and the 1.4 GeV booster used for injecting into the 26 GeV proton synchrotron (PS). A conceptual design has also recently been started to replace the PS with a new 50 GeV synchrotron. The design of the first 160 MeV section of the SPL is well along as is the shielding study, which has been focused on three possible scenarios: the installation in an existing hall, in the building housing the present linac and in a future purpose-built tunnel (which will be referred to as "green field" solution). A shielding design was first carried out via analytical calculations. Next, extensive Monte Carlo simulations with the latest version of the FLUKA code were performed to investigate the propagation of neutrons in the existing buildings and to evaluate the environmental impact.

1. Introduction

A 160 MeV H^- linear accelerator, called Linac4 [1], is being designed at CERN to replace the present 50 MeV linac (Linac2) as injector to the Proton Synchrotron Booster (PSB). Linac4 will provide the conditions to double the intensity of the beam from the PSB. Moreover, this new linac constitutes an essential component of any of the envisaged LHC upgrade scenarios and could open the way to future extensions of the CERN accelerator complex. In one of these upgrade scenarios, Linac4 would be used as the front-end of the future multi-GeV, multi MW superconducting Proton Linac (SPL) [2,3]. The SPL is intended to produce intense neutrino beams and to replace the 1.4 GeV PSB injecting into the 26 GeV Proton Synchrotron (PS). A conceptual design was also recently started to replace the PS with a new 50 GeV synchrotron (called PS2). In this case the SPL will inject protons into PS2. The layout of these new

LHC injectors is shown in Fig. 1

The design of Linac4 is well advanced and its main parameters are based on the requirements for PSB injection. It will operate at 2 Hz, with a peak current of 40 mA and a pulse length of 0.4 ms. These parameters correspond to approximately 0.1% duty cycle and 0.032 mA average current or 2×10^{14} protons per second, which is equivalent to 5.1 kW beam power at the top energy of 160 MeV.

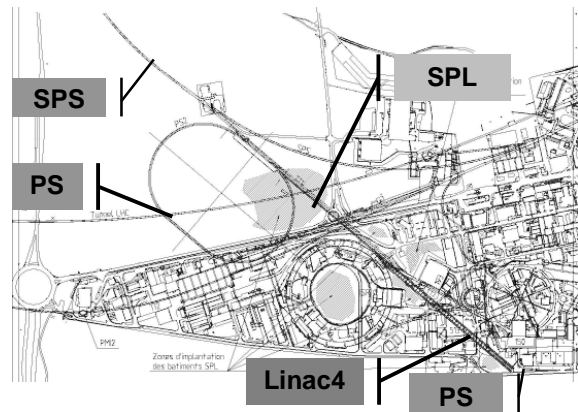


Fig 1: New LHC injector project.

The overall architecture of Linac4 is schematically shown in Fig. 2. The ion source is followed by a Radio Frequency Quadrupole (RFQ), a chopper line and the main linear accelerator structure. Three types of accelerating structures bring the energy to 160 MeV: a Drift Tube Linac (DTL) up to 40 MeV, a Cell-Coupled Drift Tube Linac (CCDTL) up to 90 MeV and finally a Side Coupled Linac (SCL) to the final energy. A long transfer line equipped with debunching and collimation sections connects Linac4 to the existing Linac2 transfer line. Three possible scenarios for the installation of the Linac4 were studied:

- 1) the installation in an existing hall;
- 2) the installation in the building housing the present linac with little additional shielding to the existing structure;
- 3) a green field solution.

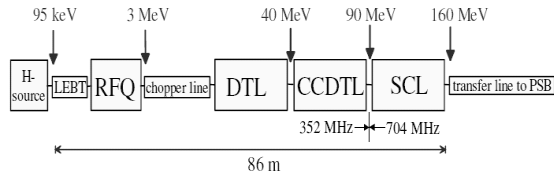


Fig 2: Schematic view of Linac4.

The shielding design for Linac4 in an existing hall has been studied in a previous paper[4]. This paper describes the Monte Carlo simulations performed to assess the effectiveness of the additional shielding needed in the second scenario, to optimize the waveguides ducts and to estimate the possible inhalation dose received by the workers from air activation in the green field solution.

2. Installation of Linac4 in an existing building with additional shielding

In modern linear accelerators, the design maximum beam loss is below 1 W/m. Losses below this threshold generate very low values of induced radioactivity such that hands-on maintenance on the accelerator is still possible. The beam dynamics and the apertures in Linac4 have been optimised to keep losses below 1 W/m at the SPL having a beam duty cycle of 5 %. The same loss level was also taken as guideline for the shielding calculations of Linac4 as the injector for PSB. This assumption leads to a safety factor of about 50, which is the ratio of the SPL and PSB duty cycles. Therefore, the proposed shielding design is appropriate for Linac4 to be used as the injector to PSB and it is rather conservative as used for the front-end of SPL.

In reality beam losses will not be equally distributed along the accelerator, but will typically occur in the aperture restrictions of quadrupoles. Other critical spots are the bending sections of the transfer line, where particles outside the energy acceptance of the bending will be lost on the vacuum chamber. In order to have a realistic loss configuration, in the following it is assumed that constant losses of 10 W every 10 m occur at selected points along the accelerator. In terms of shielding requirements this loss distribution is approximately equivalent to a uniform loss of 1 W/m.

As shown in Fig. 3, one the most critical issues with the installation of Linac4 in the existing building is its proximity to the ion injector Linac3. At present Linac3 is shielded from the Linac2 radiation by "molasse" with a density of 2.4 g/cm³ which has the following composition: O (49,5%), Si (19,8%), Al (6,4%), K (1,8%), Fe (3,9%), Mg (3,2%), Na (0,5%),

Ca (9,3%), Mn (0,1%) and C (5%). This is used at 3 to 6 m thickness, depending on location. The section of Linac4 which is closest to Linac3 is where the energy increases from 140 to 160 MeV.

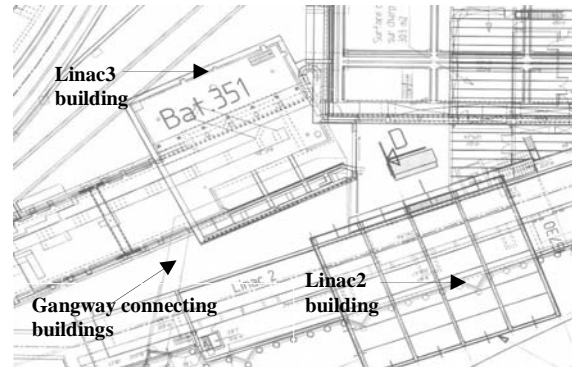


Fig 3: Schematic overview of the Linac2 and Linac3 buildings.

The high energy section and the transfer line of Linac4 were precisely modelled with the radiation transport code FLUKA [5,6]. The earth shielding separating the accelerator from Linac3 was implemented in FLUKA with the actual thickness. A 40 cm thick layer of concrete was added to the adjacent Linac2 wall to enhance the shielding.

Fig. 4 shows the geometry implemented in the simulation: the high energy section, the transfer line and the technical gallery of Linac4, the Linac3 external wall and the earth between the two accelerators.

The layout of the simulation includes the following structures (heights are given with reference to the tunnel floor):

- The part of the building housing the high energy (140-160 MeV) section of the accelerator, consisting of
 - the 14 m long, 3.5 m wide and 3.5 m high accelerator tunnel, with the 100 cm thick concrete shield on the left side, an additional 40 cm thick concrete shield on the right side (i.e., towards Linac3), the 100 cm thick concrete roof (the accelerator beam axis is at 126 cm height)
 - the 14 m long technical gallery on the left side of the accelerator at 170 cm height
 - the 30 cm thick concrete wall on the left side of the technical gallery
 - the 30 cm thick concrete floor of the accelerator tunnel
 - the building roof made of iron (1 cm thickness, 10.6 m height)
- The measurement tunnel, which corresponds to the first part of the transfer line, consisting of

- the 8.6 m long, 3.5 m wide and 6.1 m high measurement tunnel, with the 100 cm thick concrete shield on the left side, an additional 40 cm thick concrete shield on the right side and the 100 cm thick concrete roof
- the 30 cm thick concrete floor
- the 8.6 m long, 1.5 m wide and 5.5 m high tunnel on the left side of the measurement tunnel with the 20 cm thick concrete roof and the 20 cm thick concrete wall
- the earth above these tunnels, up to 650 cm height in the first metre and 750 cm height in the remaining 7.6 metres (consequently the first metre of the measurement tunnel is not underground).
- The second part of the transfer tunnel (i.e., downstream of the measurement tunnel), consisting of
- the 3.3 m long, 3.5 m wide and 2.5 m high initial section, with the 100 cm thick concrete shield on the left side, an additional 40 cm thick concrete shield on the right side, the 100 cm thick concrete roof
- the 30 cm thick concrete floor
- the 5.5 m high and 6.3 m wide part of this building housing the tunnel with a 20 cm thick concrete roof and a 20 cm thick concrete left wall
- the earth up to 750 cm height.
- The building housing the linac3 accelerator and the earth between the two accelerators, consisting of
- the wall of the building 50 cm thick, made of concrete and tilted with respect to the shield on the right side of the Linac2 accelerator tunnel
- the first part of the Linac3 building (closest to the first 10 metres of the Linac2 tunnel), which is 750 cm high and it is not underground, while the second part (closest to the final part of the accelerator and the transfer line) is 570 cm high and it is underground
- the earth between the two buildings, defined as a tilted plane with respect to the floor of the accelerator. The plane reaches a maximum height of 610 cm in the first 14 metres, it is 650 cm high between 14 and 15 metres and 750 cm high in the remaining part.

The same FLUKA geometry was used for two separate sets of simulations, namely to predict the prompt radiation in Linac3 near the high energy section (140 MeV) and near the transfer line (160 MeV) of Linac4.

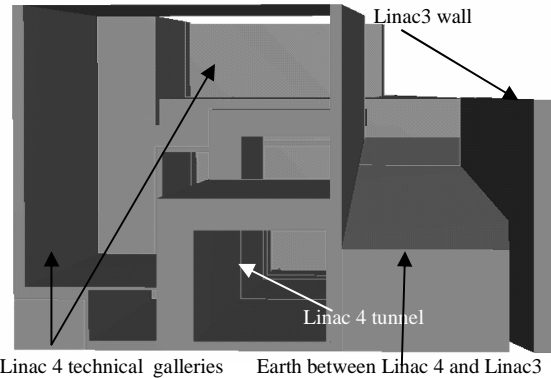


Fig 4: FLUKA geometry plotted with SimpleGeo [7]: cross sectional view of the Linac4 building and the wall of Linac3 building. The view is looking downstream of the tunnel, towards the high-energy end of the linac.

Beam losses were simulated as a 10 W proton beam hitting a $5 \times 5 \times 5 \text{ cm}^3$ copper target, which represents a magnet coil or yoke. Copper was chosen as representative of other materials with similar density (e.g., iron and stainless steel).

The first set of simulations was dedicated to study the stray radiation in the part of the Linac3 building close to the 140 MeV section of the Linac4. The ambient dose equivalent rate $H^*(10)$ was scored both on the ground floor of the Linac3 building - in the technical gallery - and at an height between 490 cm and 570 cm - on the upper floor. The dose rate is expected to be less than $1 \mu\text{Sv/h}$ in the technical gallery and up to $100 \mu\text{Sv/h}$ on the upper floor of the Linac3 building (Fig. 5). The reason for such a high dose rate can be ascribed to the insufficient amount of earth shielding between these two buildings (Fig. 4)

In the second set of simulations, the stray radiation in the part of the Linac3 building close to the transfer line of Linac4 was studied. The ambient dose equivalent rate $H^*(10)$ was scored in the Linac3 building on the ground floor, on the first floor and at an height between 730 cm and 810 cm. The latter location corresponds to the roof of the building, where the gangway connecting the two buildings is situated. In this part of the building, the dose rate in the technical gallery is less than $0.1 \mu\text{Sv/h}$ and on the gangway on the first floor is less than $1 \mu\text{Sv/h}$. The simulations predict that the radiation level on the gangway is particularly high: the maximum dose rate is $100 \mu\text{Sv/h}$. This value is unacceptable because the gangway is accessible to the members of the public (Fig. 6).

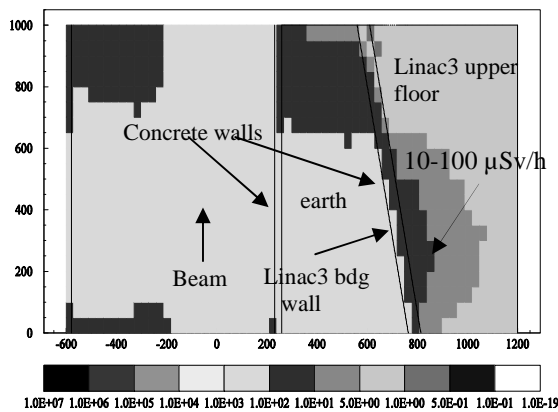


Fig 5 : Beam loss in a $5 \times 5 \times 5$ cm 3 copper target, 10 W, 140 MeV. Top cross sectional view of the Linac4 tunnel and of the Linac3 building. $H^*(10)$ in $\mu\text{Sv/h}$ at 530 cm, on the upper floor of the Linac3 building.

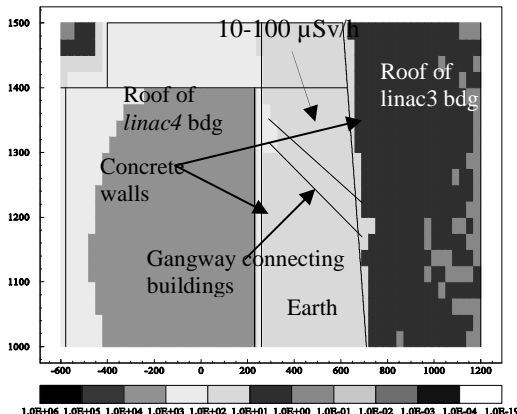


Fig 6: Beam loss in a $5 \times 5 \times 5$ cm 3 copper target, 10 W, 160 MeV. Top cross sectional view of the Linac4 tunnel and of Linac3 building. $H^*(10)$ in $\mu\text{Sv/h}$ at 760 cm above the hall floor where the gangway connecting the two buildings is located.

3. Waveguides duct studies for the green field solution

In the green field solution the Linac4 tunnel will be placed underground, so that the direct stray radiation is attenuated by the earthen shielding. The linac will effectively be shielded by about 4 m of earth plus about 1 m of concrete. The klystrons will be installed in an auxiliary tunnel located on the top of the linac tunnel and will be connected to the linac by waveguides running through ducts traversing the shielding. The first radiological simulation performed for the green field solution concerns the propagation

of neutrons through the waveguides ducts.

In the present design both the linac tunnel and the klystron tunnel are underground. The klystron gallery will be designed as a supervised radiation area according to CERN radiation Safety Manual [8] and the dose rate must be kept below 3 $\mu\text{Sv/h}$. The shielding calculations were performed for the worst-case scenario (160 MeV, 10 W point losses every 10 m).

The stray radiation in the klystron tunnel is mainly given by the addition of two terms, the radiation propagating through the shield and the radiation streaming through the waveguides ducts. This study evaluates the minimum required earth thickness between the accelerator tunnel and the klystron tunnel and optimizes the number, cross-sectional area and length of the waveguides ducts.

For a point source calculation, the ambient dose equivalent rate $H^*(10)$ past the lateral shield approximates to

$$H = \frac{H_{\pi/2} e^{-\frac{d}{\lambda}}}{r^2}$$

where r is the distance from the radiation source to the exposure point of interest, $H_{\pi/2}$ is the source term for 90 degrees emission, d is the shield thickness and λ is the attenuation length of the shielding material. The parameter r was assigned a value of 4 m. By scaling the values as in the Thomas and Stevenson book [9] to the losses in Linac4, it is found that at 160 MeV the source term for a 90 degrees emission is 1290 mSv/h and the attenuation length in concrete is 24.9 cm.

The concrete thickness required to reduce the dose equivalent rate down to 3 $\mu\text{Sv/h}$ is 254 cm. A safety factor of 3 in a shielding design is usually recommended. This can be obtained by increasing the concrete shielding by 1.1λ , which leads to a 280 cm thickness of concrete. The minimum earth thickness required can approximately be assessed by simply scaling the thickness for concrete by the ratio of the densities of the two materials (taken as 1.8 g/cm 3 for earth and 2.35 g/cm 3 for concrete). Actually, the value used for the earth density should be regarded as conservative for local soil, a density of 2 g/cm 3 being probably a more realistic figure. With this simplification, 280 cm of concrete are approximately equivalent to 370 cm of earth, from the point of view of radiation attenuation. As mentioned above, the shield is made of 100 cm of concrete plus 390 cm of earth and it is sufficient to reduce the dose-rate below 0.1 $\mu\text{Sv/h}$.

Several Monte Carlo simulations were performed

to evaluate the transmission of neutrons through the waveguides ducts in order to assess the feasibility of grouping several waveguides in larger ducts. The cross-sectional area of the waveguides is $700 \times 250 \text{ mm}^2$. Two possible configurations for the ducts were studied :

- 1) several 200 cm long (in the beam direction) ducts, each one housing 2 waveguides,
- 2) one single 90 m long rectangular well housing all the 18 waveguides.

In both cases a three-legged configuration was considered. The width of the second leg increases from 40 cm to 60 cm in its upper part. The layout of the geometry used in the simulation is shown in Fig. 7

As shown in Fig. 8, for the 200 cm long duct in the most critical case the radiation streaming into the klystron tunnel is between 0.1 and 0.5 $\mu\text{Sv}/\text{h}$. For the 90 m long rectangular well the dose streaming into the klystron tunnel can reach a maximum value between 1 and 3 $\mu\text{Sv}/\text{h}$ (Fig. 9).

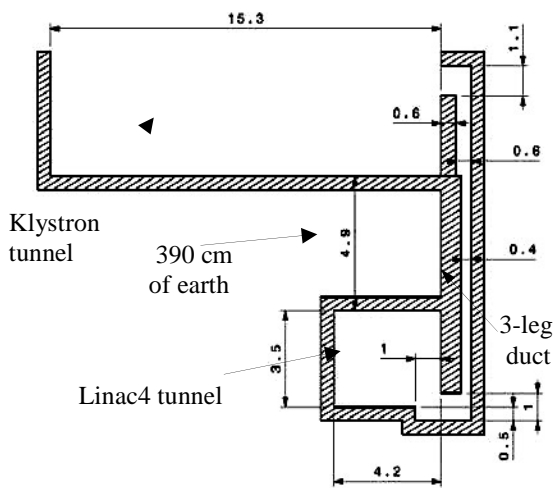


Fig 7: Layout of the geometry implemented in the simulation (linac tunnel, three-legged waveguides ducts and klystron tunnel).

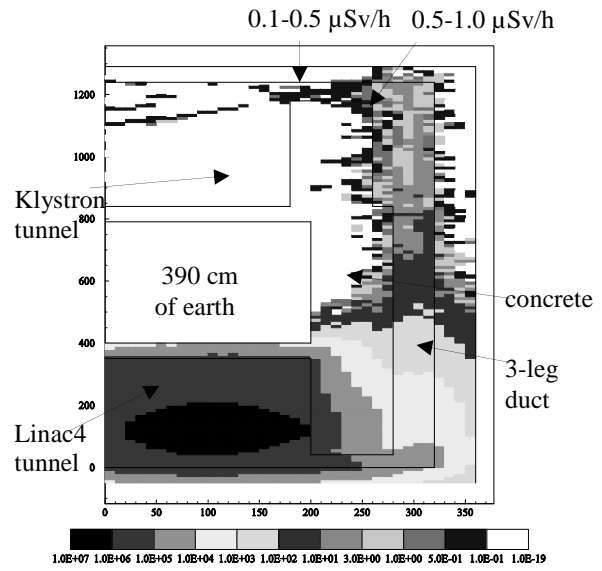


Fig 8: Beam loss in a $5 \times 5 \times 5 \text{ cm}^3$ copper target, 10 W, 160 MeV. Cross sectional view of the Linac4 tunnel, the 2 m long duct housing two waveguides and the klystron tunnel. $H^*(10)$ in $\mu\text{Sv}/\text{h}$.

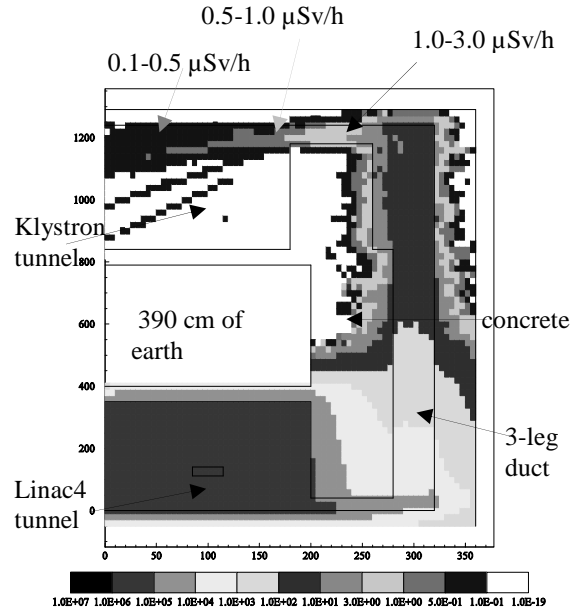


Fig 9: Beam loss in a $5 \times 5 \times 5 \text{ cm}^3$ copper target, 10 W, 160 MeV. Cross sectional view of the Linac4 tunnel, the 90 m long well housing all the waveguides and the klystron tunnel. $H^*(10)$ in $\mu\text{Sv}/\text{h}$.

4. Air activation

Three methods are commonly used for estimating induced radioactivity: 1) the multiplication of the density of inelastic interactions (“stars”) with pre-determined conversion factors, 2) the folding of particle track-length spectra with evaluated isotope production cross sections and 3) the explicit Monte Carlo calculation of isotope production from hadronic interaction models. The choice of the method depends on the case to be studied. Conversion factors from star densities are typically used for preliminary estimates and for bulk materials. Folding of track-lengths with energy-dependent cross sections is usually applied to low-density (e.g. gaseous) materials, as long as reliable experimental cross sections are available. The explicit calculation, which is relatively time-consuming, can assess the self-absorption in solids with complex geometry and the build-up and decay of radioactivity under arbitrary irradiation cycles. However, it fails in predicting induced radioactivity in gases due to the very low interaction probability.

The second approach was retained for the determination of air activation in the Linac4 tunnel. The track-length spectra were individually calculated by FLUKA for all air regions in the accelerator tunnel. The contribution from different regions were summed to obtain the total track-length spectra for neutrons, protons and charged pions. The yield Y_i of radionuclide i is then obtained by folding these spectra with energy-dependent partial cross-sections summed over all target nuclei and hadron components in the cascade

$$Y_i = \sum_{j,k} n_j \int \sigma_{ijk}(E) \Lambda_k(E) dE$$

Here n_j is the atomic concentration (per cm^3) of element j in the material and σ_{ijk} is the cumulative cross-section for the production of radionuclide i in the reaction of a particle of type k and energy E with a nucleus of element j . The quantity Λ_k is the sum of the track-lengths (in cm) of the hadrons of type k and energy E . A database with evaluated neutron, proton and charged pion interaction cross-sections which govern the conversion of the air constituents (^{14}N , ^{16}O and ^{40}Ar) into the radionuclide of interest by the various particles is available [10] and was used in a post-processing together with track-length spectra from the FLUKA simulations.

A section of the 91.5 m long accelerator tunnel was modelled with a cartesian geometry with beam direction along the z -axis. Most of the tunnel is air (density=0.001205 g/ cm^3 , volume=1.46x10 9 cm^3) with the following composition (weight fraction): nitrogen

(75.558 %), oxygen (23.159 %) and argon (1.283 %). Assuming a beam loss of 1 W/m and a tunnel length of 90 m, the total beam loss in the tunnel is 90 W. This scenario was studied for three different beam energies: 50, 100 and 160 MeV. To evaluate the worker exposure during access after shutdown, the activities of airborne radionuclides have to be estimated based on the accelerator operating conditions. Assuming a continuous loss of a 90 W beam ($N_p=1.12 \cdot 10^{13}$ protons/s at 50 MeV; $N_p=5.62 \cdot 10^{12}$ protons/s at 100 MeV; $N_p=3.51 \cdot 10^{12}$ protons/s at 160 MeV), the saturation activity (A_s) for different radionuclides can be calculated from their yields: $A_s = Y N_p$. It was assumed that there is no ventilation during the operation and that the worker intervention lasts 1 hour. Several scenarios of irradiation and cooling times were considered. The activity for one single radionuclide after an irradiation time t_{irr} and a cooling time t_{cool} is:

$$A_0(t_{\text{irr}}, t_{\text{cool}}) = Y N_p (1 - e^{-\lambda t_{\text{irr}}}) e^{-\lambda t_{\text{cool}}}$$

If the activity is mixed homogeneously in the tunnel, the activity concentration is obtained by dividing the activity by the volume of air. To estimate the inhalation dose received by a worker it is necessary to multiply the calculated activities by the breathing rate B_r and the inhalation activity-to-dose conversion factors e_{inh} (expressed in Sv/Bq), which in the present study were taken from the Swiss ordonnance [11]:

$$D_0(t_{\text{irr}}, t_{\text{cool}}) = \frac{A_0(t_{\text{irr}}, t_{\text{cool}}) e_{\text{inh}} B_r}{V_{\text{air}}}$$

The standard breathing rate for a worker is 1.2 m^3/h . In order to estimate the total dose per intervention, the equation

$$D(t) = D_0(t_{\text{irr}}, t_{\text{cool}}) e^{-\lambda t}$$

should be integrated over the intervention time t_{int} . The inhalation dose received by a person intervening in the accelerator tunnel for t_{int} after a cooling time t_{cool} is:

$$D(t_{\text{int}}) = \frac{D_0(t_{\text{irr}}, t_{\text{cool}}) (1 - e^{-\lambda t_{\text{int}}})}{\lambda}$$

The values of inhalation doses obtained for the three scenarios (50, 100 and 160 MeV proton energy), with two irradiation times (1 day and 1 week) and three waiting times (0, 10 minutes and 1 hour) are given in Table 1. Only the nuclei that give relevant contribution to the dose are listed.

Table 1: Inhalation dose received by a worker intervening in the Linac4 tunnel.

Inhalation dose (μSv), Ep = 50 MeV, intervention time = 1 hour, 90 W total proton beam loss in the tunnel						
t_{irr}	1 day	1 day	1 day	1 week	1 week	1 week
t_{cool}	0	10 min	1 hour	0	10 min	1 hour
^{11}C	5.63E-01	4.01E-01	7.33E-02	5.63E-01	4.01E-01	7.33E-02
^{38}Cl	2.34E-02	1.94E-02	7.66E-03	2.34E-02	1.94E-02	7.66E-03
^{39}Cl	2.35E-02	2.07E-02	1.11E-02	2.35E-02	2.07E-02	1.11E-02
^7Be	5.20E-02	5.20E-02	5.20E-02	3.50E-01	3.50E-01	3.50E-01
^{32}P	9.45E-02	9.45E-02	9.44E-02	5.75E-01	5.75E-01	5.74E-01
^{33}P	1.72E-02	1.72E-02	1.71E-02	1.11E-01	1.11E-01	1.11E-01
^{35}S	4.33E-03	4.33E-03	4.33E-03	2.96E-02	2.96E-02	2.96E-02
Total dose	7.83E-01	6.14E-01	2.64E-01	1.69E+00	1.52E+00	1.17E+00

Inhalation dose (μSv), Ep = 100 MeV, intervention time = 1 hour, 90 W total proton beam loss in the tunnel						
t_{irr}	1 day	1 day	1 day	1 week	1 week	1 week
t_{cool}	0	10 min	1 hour	0	10 min	1 hour
^{11}C	2.37E-01	1.69E-01	3.08E-02	2.37E-01	1.69E-01	3.08E-02
^{38}Cl	2.43E-02	2.02E-02	7.97E-03	2.43E-02	2.02E-02	7.97E-03
^{39}Cl	4.52E-02	3.99E-02	2.14E-02	4.52E-02	3.99E-02	2.14E-02
^7Be	2.21E-02	2.21E-02	2.21E-02	1.49E-01	1.49E-01	1.49E-01
^{32}P	6.10E-02	6.09E-02	6.08E-02	3.71E-01	3.70E-01	3.70E-01
^{33}P	1.10E-02	1.10E-02	1.10E-02	7.14E-02	7.13E-02	7.13E-02
^{35}S	2.41E-03	2.41E-03	2.41E-03	1.65E-02	1.65E-02	1.65E-02
^{14}C	1.61E-03	1.61E-03	1.61E-03	1.13E-02	1.13E-02	1.13E-02
Total dose	4.08E-01	3.30E-01	1.60E-01	9.30E-01	8.52E-01	6.82E-01

Inhalation dose (μSv), Ep = 160 MeV, intervention time = 1 hour, 90 W total proton beam loss in the tunnel						
t_{irr}	1 day	1 day	1 day	1 week	1 week	1 week
t_{cool}	0	10 min	1 hour	0	10 min	1 hour
^{11}C	1.37E-01	9.75E-02	1.78E-02	1.37E-01	9.75E-02	1.78E-02
^{38}Cl	4.43E-02	3.67E-02	1.45E-02	4.43E-02	3.67E-02	1.45E-02
^{39}Cl	8.62E-02	7.61E-02	4.08E-02	8.62E-02	7.61E-02	4.08E-02
^7Be	1.63E-02	1.63E-02	1.63E-02	1.10E-01	1.10E-01	1.10E-01
^{32}P	7.03E-02	7.02E-02	7.01E-02	4.27E-01	4.27E-01	4.26E-01
^{33}P	1.28E-02	1.28E-02	1.28E-02	8.25E-02	8.25E-02	8.24E-02
^{35}S	3.59E-03	3.59E-03	3.58E-03	2.45E-02	2.45E-02	2.45E-02
^{14}C	2.54E-03	2.54E-03	2.54E-03	1.78E-02	1.78E-02	1.78E-02
Total dose	3.83E-01	3.23E-01	1.84E-01	9.44E-01	8.83E-01	7.44E-01

5. Conclusions

In dealing with the installation of Linac4 in the present Linac2 building, it was not possible to use a simple analytical model for the estimation of the radiation levels due to the complexity of the geometry. Extensive Monte Carlo simulations proved to be the appropriate method to evaluate the transmission of stray radiation from Linac4 to Linac3. The FLUKA simulations predict that the installation of Linac4 in the Linac2 building would raise concern about the dose rate in two critical areas of Linac3: on the gangway connecting the two buildings and on the upper floor of the Linac3 building, where the dose equivalent rate can reach a maximum value of 100 $\mu\text{Sv}/\text{h}$. The existing amount of earth and the additional 40 cm thick layer of concrete between Linac3 and Linac4 are inadequate for reducing the dose rate to a value compatible with the CERN Safety Code [8] in all occupied areas.

The FLUKA simulations for the waveguides ducts for the green field solution lead to the conclusion that a 90 m long well housing all of the waveguides is a feasible solution. Slight modifications to the geometry could further reduce the ambient dose equivalent rate in the occupied areas.

Air activation studies were also performed for the green field solution, folding the particle track-lengths spectra obtained by Monte Carlo simulations with proper energy-dependent cross sections. This method was preferred to direct Monte Carlo calculations because of the low interaction probability of hadrons with air, which would have lead to very large central processing unit (CPU) times. The inhalation dose received by workers during 1-hour maintenance operation in the tunnel was estimated for different irradiation cycles and waiting times, for 50, 100 and 160 MeV proton beam energy. The doses are similar at the three energies. They are slightly higher at 50 MeV because of the higher number of proton lost and because of the limited contribution of spallation products to gas activation in this energy range.

- [3] F. Gerigk et al., Conceptual design of the SPL II, CERN Yellow Report 2006-006 (2006).
- [4] M. Magistris and M. Silari, Prompt radiation, shielding and induced radioactivity in a high-power 160 MeV proton linac. Nuclear Instruments and Methods A 562, 967-971, 2006.
- [5] A. Fassò, A. Ferrari, J. Ranft, and P.R. Sala, FLUKA: a multi-particle transport code, CERN-2005-10 (2005), INFN/TC_05/11, SLAC-R-773.
- [6] A. Fassò, A. Ferrari, S. Roesler, P.R. Sala, G. Battistoni, F. Cerutti, E. Gadioli, M.V. Garzelli, F. Ballarini, A. Ottolenghi, A. Empl and J. Ranft, The physics models of FLUKA: status and recent developments, Computing in High Energy and Nuclear Physics 2003 Conference (CHEP2003), La Jolla, CA, USA, March 24-28, 2003, (paper MOMT005), eConf C0303241 (2003), arXiv:hep-ph/0306267.
- [7] C. Theis, K.H. Buchegger, M. Brugger, D. Forkel-Wirth, S. Roesler and H. Vincke, Interactive three dimensional visualization and creation of geometries for Monte Carlo calculations, Nucl. Instrum. and Meth. A 562, 827-829 (2006).
- [8] CERN Safety Code F, Radiation Protection (November 2006).
- [9] R.H. Thomas and G.R. Stevenson, Radiological safety aspects of the operation of proton accelerators, Technical report n. 283, International Atomic Energy Agency, Vienna (1988).
- [10] M. Huhtinen, Determination of Cross Sections for Assessment of Air Activation at LHC, CERN/TIS-RP/TM/96-29 (1997).
- [11] Swiss Legislation on Radiological Protection (Ordonnance sur la Radioprotection, ORaP) of 22 June 1994 (state 4 April 2000).

REFERENCES

- [1] L. Arnaudon et al, Linac4 Technical Design Report, M. Vretenar and F. Gerick, Editors, CERN-2006-AB-084 (2006).
- [2] B. Autin et al., Conceptual design of the SPL, a high power superconducting H^- linac at CERN, CERN Yellow Report 2000-012 (2000).

RADIATION PROTECTION STUDIES FOR THE NEW CERN INJECTOR COMPLEX

RADIATION PROTECTION

KEYWORDS: *shielding design, radiation protection, proton machine*

EGIDIO MAURO,* MARCO SILARI, and HEINZ VINCKE
CERN, CH-1211 Geneve 23, Switzerland

Received April 10, 2008

Accepted for Publication July 22, 2008

CERN is at present designing a new chain of accelerators to replace the present Proton Synchrotron (PS) complex: a 160-MeV room-temperature linear accelerator (linac) (Linac4) to replace the present 50-MeV linac injector, a 3.5-GeV superconducting proton linac (SPL) to replace the 1.4-GeV PS booster, and a 50-GeV synchrotron to replace the 26-GeV PS. Linac4 has been funded, and civil engineering will start soon, while the SPL is in an advanced stage of design. Beyond injecting into the future 50-GeV PS, the ultimate goal of the SPL is to generate a 4-MW beam to produce intense neutrino beams. The radiation protection design is driven by the latter requirement. This work summarizes the radiation protection studies conducted so far for Linac4. The calculations of the shielding, access maze, ducts for cables, waveguides, and ventilations were performed with the FLUKA Monte Carlo code, complemented by analytical estimates.

The overall architecture of Linac4 is schematically shown in Fig. 1. The ion source is followed by a radio-frequency quadrupole (RFQ), a chopper line, and the main linac structure. Three types of accelerating structures bring the energy up to 160 MeV: a drift tube linac (DTL) up to 50 MeV, a cell-coupled DTL (CCDTL) up to 102 MeV, and finally a pi-mode structure (PIMS) to the final energy. A long transfer line equipped with debunching and collimation sections connects Linac4 to the existing Linac2 transfer line.

Four possible locations were considered for the site of Linac4:

1. an existing hall (the radiation protection aspects are discussed in Refs. 4 through 7)
2. the building housing the present linac with a substantial reinforcement of the existing shielding (solution soon abandoned for cost reasons)
3. the building housing the present linac with little additional shielding to the existing structure^{8,9}
4. a future purpose-built tunnel.

Various configurations of the civil engineering of this latest option were investigated. The radiation protection aspects of an earlier scheme are discussed in Ref. 9.

This paper discusses the radiation protection aspects of the final configuration of the fourth scenario, evaluating in particular the propagation of neutrons through the waveguide ducts placed along the accelerator, the ventilation duct, and the access area at the low-energy end of the linac, by Monte Carlo simulations with the FLUKA radiation transport code^{10,11} (version 2006.3b, March 2007). The accuracy of this code for the radiation protection issues and, in particular, for the shielding design has been proven through several benchmarks.¹²

II. INSTALLATION OF LINAC4 IN A FUTURE PURPOSE-BUILT TUNNEL

In modern linacs, the design maximum beam loss is below 1 W/m. Losses below this threshold generate

I. INTRODUCTION

A new proton linear accelerator (linac) (Linac4) is being designed at CERN to replace the present Linac2 injecting protons at 50 MeV into the proton synchrotron (PS) booster (PSB). Linac4 will deliver H^- ions at a kinetic energy of 160 MeV (Ref. 1), and it is also conceived for use as the front end of a future multi-giga-electron-volt, multi-megawatt superconducting proton linac^{2,3} (SPL). For its use as PSB injector, Linac4 will operate at 2 Hz, with a peak current of 40 mA and a pulse length of 0.4 ms. These parameters correspond to 0.08% beam duty cycle and 0.032-mA average current or 2×10^{14} protons/s, equivalent to a beam power of 5.1 kW at the top energy of 160 MeV.

*E-mail: egidio.mauro@cern.ch

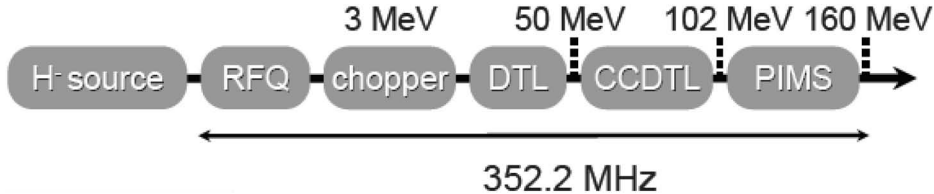


Fig. 1. Schematic view of Linac4.

values of induced radioactivity such that hands-on maintenance on the machine is still possible. The beam dynamics and the apertures in Linac4 have been optimized to keep losses below 1 W/m at the SPL beam duty cycle of 5%. The same loss level was also taken as a guideline for the shielding calculations of Linac4 as injector for the PSB. Since the accelerator designers expect that losses scale proportionally with duty cycle, this assumption leads to a safety factor of about 50 (the ratio of the SPL and PSB duty cycles). Therefore, the proposed shielding design is appropriate for Linac4 used as the front end of the SPL, and it is rather conservative as injector to the PSB. In reality beam losses will not be equally distributed along the machine but will typically occur in the aperture restrictions of quadrupoles. In order to have a realistic loss configuration, in the following it is assumed that constant losses of 10 W every 10 m occur at selected points along the machine. In terms of shielding requirements, this loss distribution is approximately equivalent to a uniform loss of 1 W/m (Refs. 13 and 14).

The Linac4 tunnel will be located underground, at a depth sufficient to shield the direct stray radiation produced during the accelerator operation. In the first design the linac was at a depth such that it was effectively shielded by 435 cm of earth plus ~ 1 m of concrete. Subsequently, with the aim to minimize the interference of the SPL with surface buildings and existing tunnels nearby,¹⁵ the Linac4 and SPL tunnels were lowered by 2.5 m. Klystrons will be installed in an auxiliary building located on the surface on top of the linac tunnel and will be connected to the linac by waveguides running through ducts traversing the shielding.

III. RADIATION SHIELDING

The klystron building will be classified as a supervised radiation area according to CERN Safety Code F (Ref. 16), where a maximum ambient dose equivalent rate of 3 μ Sv/h can be accepted. However, because of the thin walls separating this building from the public area, 1 μ Sv/h has been taken as the design value for the calculations. The shielding calculations were performed for the worst-case scenario for routine operation of the machine (160 MeV, 10-W point losses every 10 m). The minimum earth thickness required between the machine tunnel and the kly-

tron building, simply evaluated with a point-source line-of-sight model, is 370 cm. Thus, even the original 435 cm of earth plus 100 cm of concrete are largely sufficient to reduce the ambient dose equivalent rate due to stray radiation through the shield to well below the value for public exposure of 0.5 μ Sv/h. Given the fact that the linac tunnel was further lowered by 2.5 m, it was decided that detailed Monte Carlo simulations were not necessary to confirm the adequacy of the bulk shielding.

IV. NEUTRONS STREAMING THROUGH THE WAVEGUIDE DUCTS

The first radiological study was focused on the propagation of neutrons through the waveguide ducts. Along the accelerator the distance between the waveguides decreases with increasing energy. The worst-case scenario in the high-energy section was studied. The stray radiation in the klystron building is mainly given by the addition of two terms: the radiation traversing the shield and the radiation streaming through the waveguide ducts. As stated above, the shield, 100 cm of concrete plus 685 cm of earth, is largely sufficient to shield the direct radiation. Thereby, to optimize the computing time, in the simulations the particles were not transported through the earth. Several simulations were performed to optimize the number, cross-sectional area, and length of the legs of the ducts. The final three-legged configuration studied is shown in Table I.

The geometry implemented in the simulation includes two parallel ducts separated by 280 cm of earth (density 1.8 g/cm³) plus 20 cm of concrete corresponding to the

TABLE I
Layout of the Standard Waveguide Ducts

	Section (cm ²)	Length (cm)
First leg (vertical)	90 × 90	755
Second leg (horizontal)	90 × 90	250
Third leg (vertical)	100 × 90	145

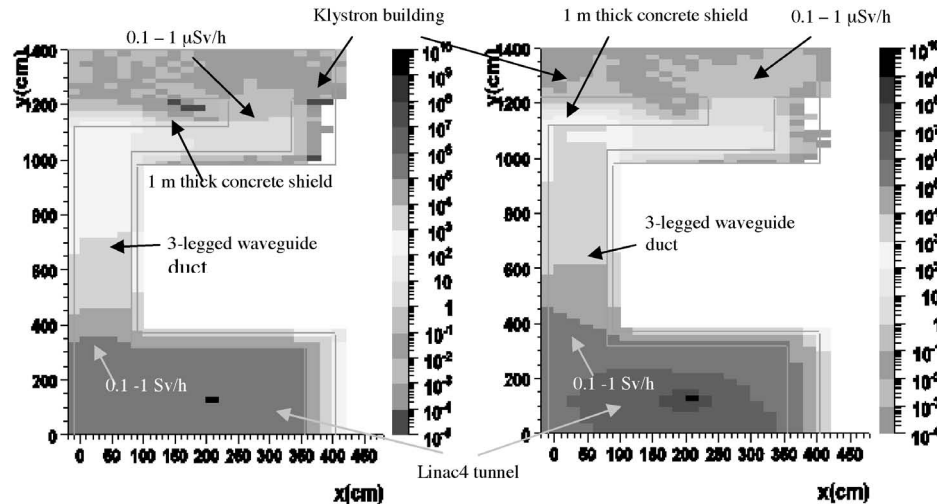


Fig. 2. Neutrons streaming through a pair of waveguide ducts, spaced by 2.8 m. Beam loss in a $5 \times 5 \times 5$ -cm 3 copper target, 10 W, 160 MeV, placed in front of the downstream duct. Cross-sectional view of the Linac4 tunnel and the three-legged duct. $H^*(10)$ in $\mu\text{Sv}/\text{h}$. Left: Dose rate in the upstream duct. Right: Dose rate in the downstream duct. 2

thickness of the duct walls. The target simulating a beam loss was a cube of 5-cm side, made of copper, placed in front of the mouth of the second (downstream) duct. The simulations showed that the stray radiation in the klystron building on top of the first leg is expected to be $<0.1 \mu\text{Sv}/\text{h}$, while the radiation streaming out of the third leg is between 0.1 and 1 $\mu\text{Sv}/\text{h}$. The radiation on top of the first leg of the second duct and that streaming out of the third leg are both expected between 0.1 and 1 $\mu\text{Sv}/\text{h}$ (Fig. 2). These radiation levels are below the design value of 1 $\mu\text{Sv}/\text{h}$.

V. ACCESS MAZE, VENTILATION, AND CABLE DUCTS AT THE LOW-ENERGY END OF THE LINAC

A detailed geometry was implemented in the FLUKA simulation to study the radiological impact in the low-energy section of the accelerator. An initial simulation was performed to estimate the radiation backscattered from a beam loss point at the end of the low-energy section (10 W, 11 MeV) into the access area, where the lift and the staircase are located, and to evaluate the need for an access maze. The geometry implemented in the simulation includes a simplified model of the accelerator tunnel and of the access area. The simulations showed that without the maze the radiation streaming into the low-energy access area is expected to be between 10 and 100 $\mu\text{Sv}/\text{h}$ (Fig. 3). A 100-cm-thick concrete wall was thus implemented in this area to create a maze and to reduce the radiation streaming through the lift and the staircase.

A second simulation, including this maze in the geometry, was performed to estimate the radiation in the occupied areas near the low-energy section of Linac4. The layout of the simulation (Fig. 4) includes the follow-

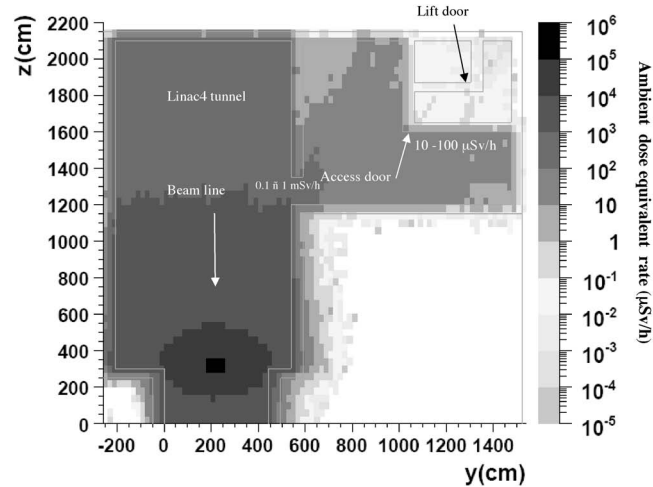


Fig. 3. Neutrons streaming into the ground floor of the Linac4 tunnel. Beam loss in a $5 \times 5 \times 5$ -cm 3 copper target, 10 W, 11 MeV, placed at the end of the low-energy section of the accelerator. Cross-sectional view of the Linac4 tunnel and of the low-energy access area. $H^*(10)$ in $\mu\text{Sv}/\text{h}$. 2

ing structures (heights are given with reference to the tunnel floor):

1. the accelerator tunnel
2. the so-called “safe room” at a height of 3.5 m
3. the galleries on the first and second floors located at a height of 7.6 and 12.1 m, respectively
4. the ventilation shaft and the cable duct located at the beginning of the accelerator tunnel

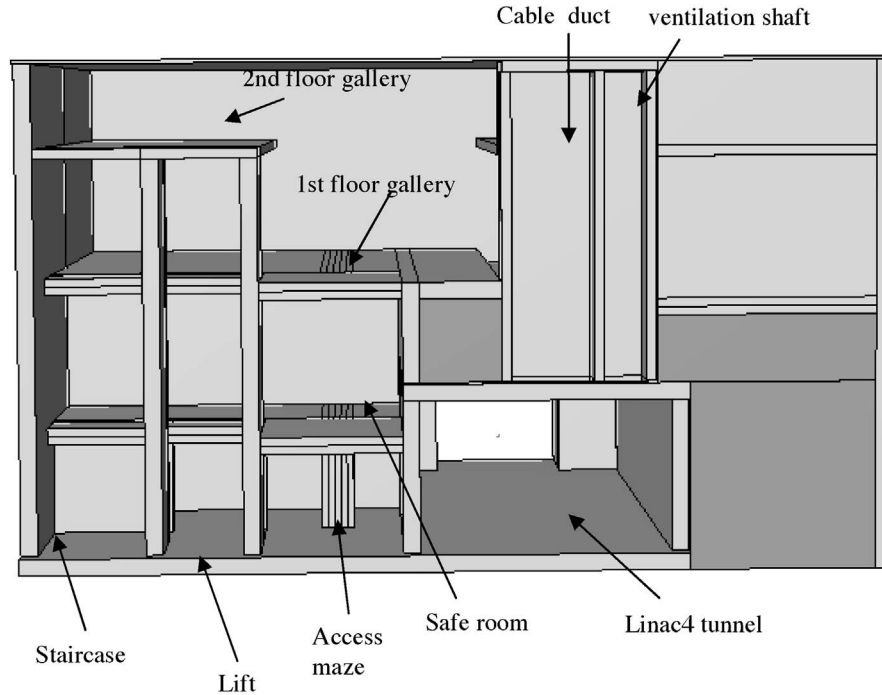


Fig. 4. FLUKA geometry plotted with SimpleGeo (Ref. 17). Cross-sectional view of the low-energy section of Linac4. The view looks downstream of the tunnel, toward the high-energy end of the accelerator.

5. the low-energy access area with the lift, the staircase, and the maze designed to reduce the radiation streaming through these shafts
6. the target, a 5-cm-side cube, made of copper and located at the end of the low-energy section (energy of 11 MeV).

A beam loss of 10 W at the energy of 11 MeV was simulated, and the backscattered radiation was estimated. The setup of an access maze by the addition of the 100-cm-thick wall is expected to reduce the dose rate in the access area to a value of $<0.1 \mu\text{Sv/h}$ (Fig. 5). The radiation in the safe room is expected to be between 1 and $10 \mu\text{Sv/h}$ just in the proximity of the 50-cm-thick lateral wall of the room, while everywhere else in the room is expected to be $<1 \mu\text{Sv/h}$ (Fig. 6). The radiation in the gallery on the first floor is expected to be well below $1 \mu\text{Sv/h}$ (Fig. 7).

VI. VENTILATION DUCT AT THE END OF THE ACCELERATOR

The ventilation duct is located at the end of the accelerator tunnel downstream of the beam dump (Fig. 8). The three-legged configuration described in Table II was implemented in the FLUKA geometry. In this scenario it was assumed that the shielding of the dump is such to create in its surroundings a stray radiation field equiva-

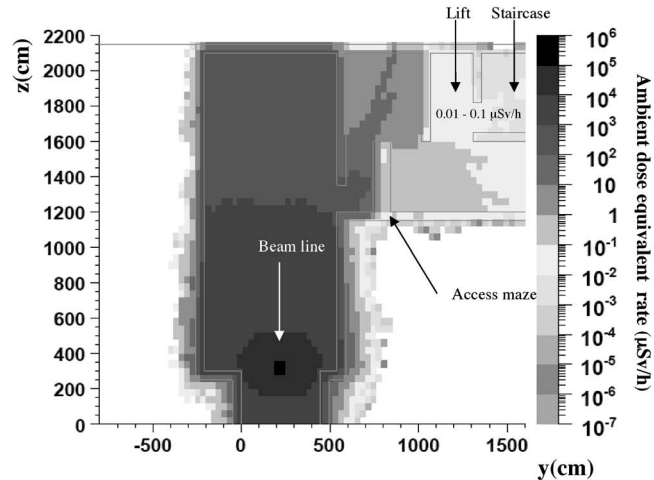


Fig. 5. Neutrons streaming into the ground floor of the Linac4 tunnel. Beam loss in a $5 \times 5 \times 5\text{-cm}^3$ copper target, 10 W, 11 MeV, placed at the end of the low-energy section of the accelerator. Cross-sectional view of the Linac4 tunnel and of the access area with the addition of the maze. $H^*(10)$ in $\mu\text{Sv/h}$.

lent to an unshielded 10-W loss (as everywhere else in Linac4). This is the radiation source used to assess the radiation transmitted through the duct. The duct mouth is located 5.35 m downstream of the beam loss point. The

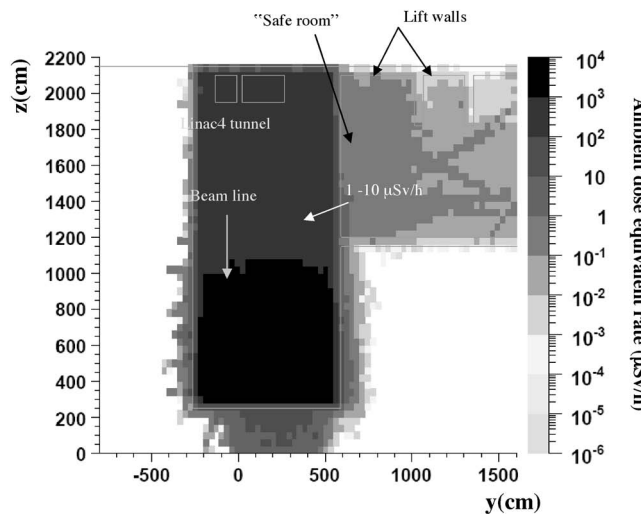


Fig. 6. Neutrons streaming into the safe room. Beam loss in a $5 \times 5 \times 5$ -cm 3 copper target, 10 W, 11 MeV, placed at the end of the low-energy section of the accelerator. Top cross-sectional view of the safe room at the height of 3.5 m with respect to the tunnel floor. $H^*(10)$ in $\mu\text{Sv}/\text{h}$.

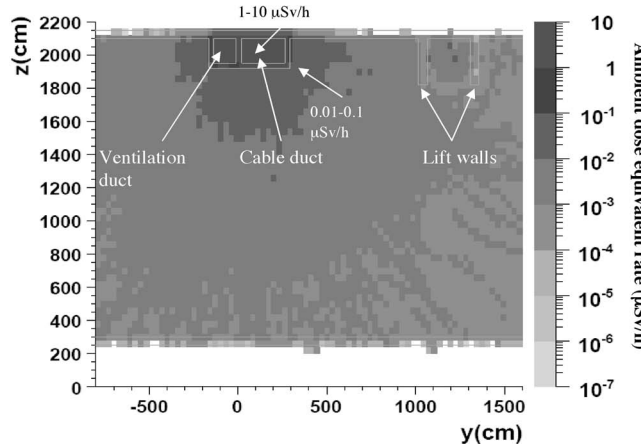


Fig. 7. Neutrons streaming into the gallery on the first floor. Beam loss in a $5 \times 5 \times 5$ -cm 3 copper target, 10 W, 11 MeV, placed at the end of the low-energy section of the accelerator. Top cross-sectional view of the gallery on the first floor in the Linac4 tunnel at a height of 7.6 m. $H^*(10)$ in $\mu\text{Sv}/\text{h}$.

simulations show that the radiation in the upper floor is expected to be between 0.1 and 1 $\mu\text{Sv}/\text{h}$ (Fig. 9).

VII. CONCLUSIONS

This paper has discussed the radiation protection studies for the installation of Linac4 in a future purpose-built

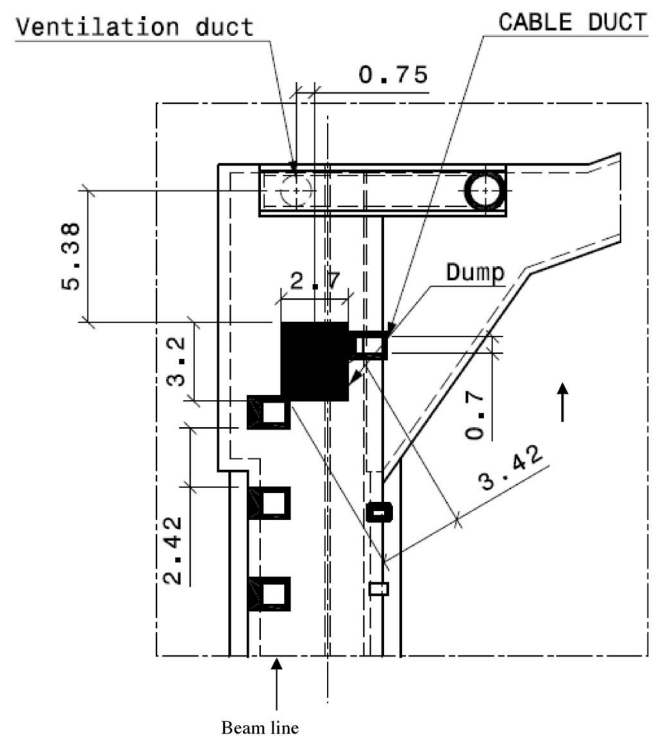


Fig. 8. Top cross-sectional view of the high-energy section of Linac4 with the ventilation duct placed downstream of the dump at the end of the tunnel.

TABLE II
Layout of the High-Energy Ventilation Duct

	Section	Length
First leg (vertical)	Circular with diameter of 125 cm	0.2 m
Second leg (horizontal)	Squared with a side of 120 cm	7.67 m
Third leg (vertical)	Circular with diameter of 125 cm	7.2 m

tunnel. Monte Carlo simulations proved to be the appropriate method to evaluate the propagation of neutrons through the waveguide, ventilation and cable ducts placed along the accelerator, and in the access area, confirming preliminary estimates made with a simple model. The simulations show that the design of the various ducts as presented in this paper is adequate from a radiation protection standpoint. Several configurations for the standard waveguide ducts were investigated, and in the final layout the ambient dose equivalent rate in the klystron building is expected to be $<1 \mu\text{Sv}/\text{h}$, the design value. The radiological impact in the low-energy section of the accelerator would raise some concern in the so-called safe

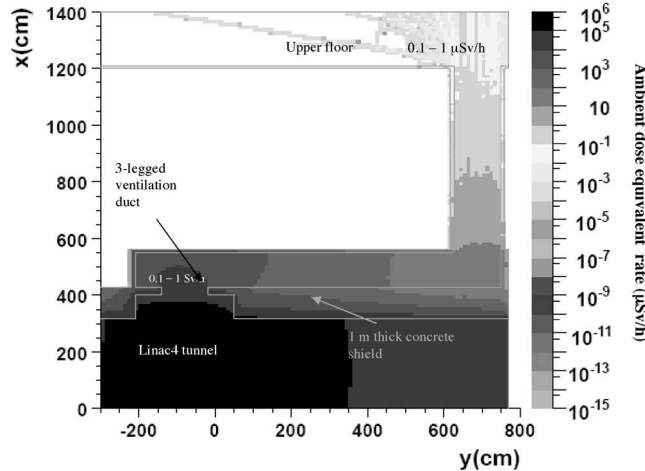


Fig. 9. Neutrons streaming through the ventilation duct. Beam loss in a $5 \times 5 \times 5$ -cm 3 copper target, 10 W, 160 MeV, placed in correspondence to the dump. Cross-sectional view of the Linac4 tunnel, the three-legged ventilation duct, and the ventilation building above. $H^*(10)$ in $\mu\text{Sv}/\text{h}$.

room only in the proximity of the lateral wall where the ambient dose equivalent rate is expected to be between 1 and $10 \mu\text{Sv}/\text{h}$. Increasing the thickness of the lateral wall from 50 to 80 cm provides adequate reduction of the dose rate to a value $<1 \mu\text{Sv}/\text{h}$. In the high-energy section the ambient dose equivalent rate in the ventilation building on the surface is expected to be $<1 \mu\text{Sv}/\text{h}$. The radiation protection studies will now continue with the design of the dump at the end of the linac and with the assessment of the induced radioactivity in the accelerator components, cooling water, and tunnel air.

ACKNOWLEDGMENT

This work was supported by MARIE CURIE project No. 21074 (RADENV).

REFERENCES

1. L. ARNAUDON et al., "Linac 4 Technical Design Report," CERN-2006-AB-084, M. VRETENAR and F. GERICK, Eds., CERN (2006).
2. B. AUTIN et al., "Conceptual Design of the SPL, A High Power Superconducting H⁻ Linac at CERN," Yellow Report 2000-012, CERN (2000).
3. F. GERIGK et al., "Conceptual Design of the SPL II," Yellow Report 2006-006, CERN (2006).
4. M. SILARI and H. VINCKE, "Shielding Proposal for the SPL Front End," CERN-TIS-2003-002-RP-TN, CERN (2003).
5. M. MAGISTRIS and M. SILARI, "Preliminary Shielding Design of Linac 4," CERN-SC-2005-011-RP-TN, CERN (2005).
6. M. MAGISTRIS and M. SILARI, "Preliminary Shielding Design of Linac 4. Top Shielding and Induced Radioactivity," CERN-SC-2005-050-RP-TN, CERN (2005).
7. M. MAGISTRIS, E. MAURO, and M. SILARI, "Complementary Shielding Calculation for Linac 4 in the South Hall," CERN-SC-2006-060-RP-TN, CERN (2006).
8. M. MAGISTRIS, E. MAURO, and M. SILARI, "Radiation Protection Considerations for the Installation of Linac4 in the Existing Linac2 Building," CERN-SC-2007-031-RP-TN, CERN (2007).
9. M. MAGISTRIS, E. MAURO, and M. SILARI, "Radiation Protection Studies for the Front-End of the 3.5 GeV SPL," *Proc. 8th Int. Topl. Mtg. Nuclear Applications and Utilization of Accelerators (AccApp'07)*, Pocatello, Idaho, July 29–August 2, 2007, American Nuclear Society (2007).
10. A. FASSO', A. FERRARI, J. RANFT, and P. R. SALA, "FLUKA: A Multi-Particle Transport Code," CERN-2005-10 (2005), INFN/TC_05/11, SLAC-R-773, CERN/Istituto Nazionale di Fisica Nucleare/Stanford Linear Accelerator Center.
11. A. FASSO', A. FERRARI, S. ROESLER, P. R. SALA, G. BATTISTONI, F. CERUTTI, E. GADIOLI, M. V. GARZELLI, F. BALLARINI, A. OTTOLENGHI, A. EMPL, and J. RANFT, "The Physics Models of FLUKA: Status and Recent Developments," *Proc. Conf. Computing in High Energy and Nuclear Physics (CHEP2003)*, La Jolla, California, March 24–28, 2003, University of California, San Diego/Stanford Linear Accelerator Center (2003).
12. Y. NAKANE, Y. SAKAMOTO, K. HAYASHI, and T. NAKAMURA, "Intercomparison of Neutron Transmission Benchmark Analyses for Iron and Concrete Shields in Low, Intermediate and High Energy Proton Accelerator Facilities," *Proc. 3rd Specialists' Mtg. Shielding Aspects of Accelerators, Targets and Irradiation Facilities (SATIF-3)*, Tohoku University, Sendai, Japan, May 12–13 1997, p. 151, Organization for Economic Cooperation and Development/Nuclear Energy Agency (1998).
13. S. AGOSTEO and M. SILARI, "Preliminary Shielding Calculations for a 2 GeV Superconducting Proton Linac," TIS-RP/TM/2001-028, CERN (2001).
14. E. MAURO and M. SILARI (to be published).
15. E. MAURO, M. SILARI, and HZ. VINCKE, "Radiological Interferences Between the SPL Tunnel and the Existing Underground and Surface Structures," CERN-SC-2007-083-RP-TN, CERN (2007).
16. "Safety Code F, Radiation Protection," CERN (Nov. 2006).
17. C. THEIS, K. H. BUCHEGGER, M. BRUGGER, D. FORKEL-WIRTH, S. ROESLER, and H. VINCKE, "Interactive Three Dimensional Visualization and Creation of Geometries for Monte Carlo Calculations," *Nucl. Instrum. Methods A*, **562**, 827 (2006).



Contents lists available at ScienceDirect

Nuclear Instruments and Methods in Physics Research A

journal homepage: www.elsevier.com/locate/nima

Review

Radiation protection studies for a high-power 160 MeV proton linac

Egidio Mauro ^{*}, Marco Silari

CERN, CH-1211 GENEVA 23, Switzerland

ARTICLE INFO

Article history:

Received 6 March 2009

Accepted 29 March 2009

Keywords:

Linac

Radioactivity

FLUKA

CERN

Shielding

Accelerator

ABSTRACT

CERN is presently designing a new chain of accelerators to replace the present Proton Synchrotron (PS) complex: a 160 MeV room-temperature H⁻ linac (Linac4) to replace the present 50 MeV proton linac injector, a 3.5 GeV Superconducting Proton Linac (SPL) to replace the 1.4 GeV PS **Booster** (PSB) and a 50 GeV synchrotron (named PS2) to replace the 26 GeV PS. Linac4 has been funded and the civil engineering work started in October 2008, whilst the SPL is in an advanced stage of design. Beyond injecting into the future 50 GeV PS, the ultimate goal of the SPL is to generate a 4 MW beam for the production of intense neutrino beams. The radiation protection design is driven by the latter requirement. This work summarizes the radiation protection studies conducted for Linac4. FLUKA Monte Carlo simulations, complemented by analytical estimates, were performed to evaluate the propagation of neutrons through the waveguide, ventilation and cable ducts placed along the accelerator, to estimate the radiological impact of the accelerator in its low-energy section, where the access area is located, and to calculate the induced radioactivity in the air and in the components of the accelerator. The latter study is particularly important for maintenance interventions and final disposal of radioactive waste. Two possible layouts for the CCDTL section of the machine were considered in order to evaluate the feasibility, from the radiological standpoint, of replacing electromagnetic quadrupoles with permanent magnet quadrupoles with a high content of cobalt.

© 2009 Elsevier B.V. All rights reserved.

Contents

1. Introduction	1
2. Beam loss assumptions	2
3. Radiation shielding	3
4. Neutrons streaming through the waveguide ducts	4
4.1. First layouts: first duct close to the loss point	5
4.2. First layouts: ducts housing one waveguide (interspaced by 1 m of earth plus 20 cm of concrete)	5
4.3. First layouts: ducts housing two waveguides (interspaced by 280 cm of earth plus 20 cm of concrete)	6
4.4. Final layout	6
5. Access maze, ventilation and cable ducts at the low-energy end of the linac	6
6. Induced radioactivity in the main components of the accelerator	8
6.1. Air activation	12
7. Conclusions	15
Acknowledgements	17
References	17

1. Introduction

A new proton linac (Linac4) has been designed at CERN to replace the present Linac2 injecting protons at 50 MeV into the PS

Booster (PSB). Linac4 will deliver H⁻ ions with a kinetic energy of 160 MeV [1] and it is also conceived for use as the front-end of a future multi-GeV, multi-MW Superconducting Proton Linac (SPL) [2,3]. Fig. 1 shows a view of the CERN Linac-PSB-PS complex, indicating the position of Linac4 and of the future extension to the SPL. For its use as a PSB injector, Linac4 will operate at 2 Hz, with a peak current of 40 mA and a pulse length of 0.4 ms. These

* Corresponding author. Tel.: +41 22 7673535; fax: +41 22 7679360.

E-mail addresses: egidio.mauro@cern.ch, egidiomanuro@yahoo.it (E. Mauro).

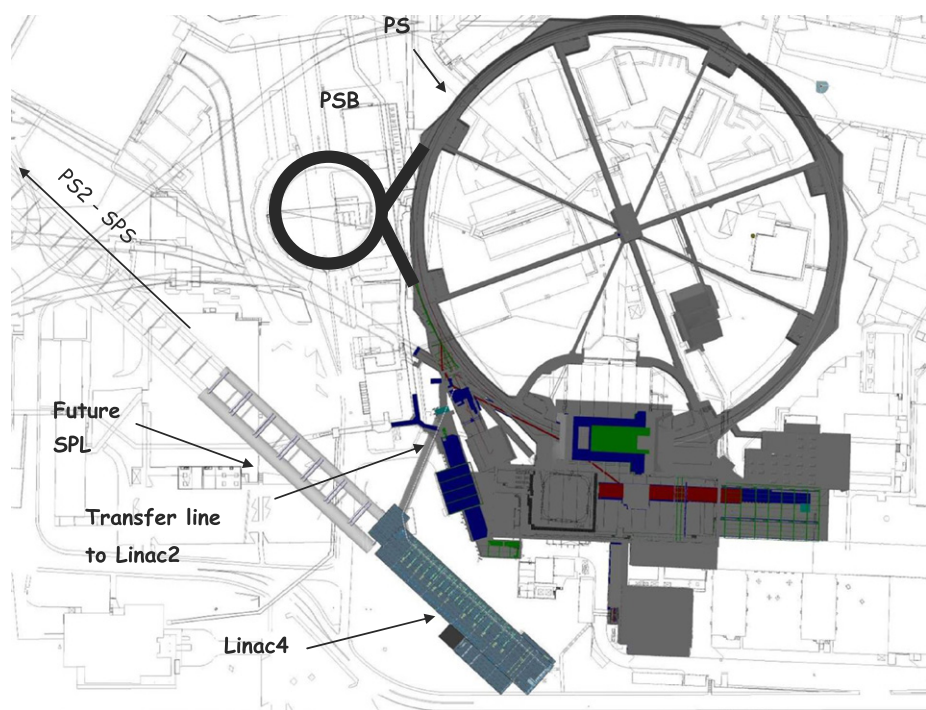


Fig. 1. View of the PS complex at CERN, showing the position of Linac4.

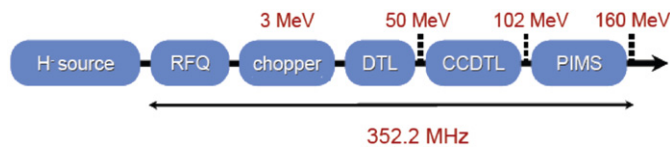


Fig. 2. Schematic view of Linac4.

parameters correspond to 0.08% beam duty cycle and 0.032 mA average current or 2×10^{14} protons/s, equivalent to a beam power of 5.1 kW at 160 MeV.

The overall architecture of Linac4 is schematically shown in Fig. 2. The ion source is followed by a Radio Frequency Quadrupole (RFQ), a chopper line and the main linac. Three types of accelerating structures raise the energy to 160 MeV: a Drift Tube Linac (DTL) up to 50 MeV, a Cell-Coupled Drift Tube Linac (CCDTL) up to 102 MeV and a Pi-Mode Structure (PIMS) to the final energy. A long transfer line equipped with debunching and collimation sections connects Linac4 to the existing Linac2 transfer line.

Over the past few years, four possible locations were investigated for the site of Linac4:

- (1) an existing hall (the radiation protection aspects are discussed in Refs. [4–7]);
- (2) the building housing the present Linac2 with a substantial reinforcement of the existing shielding (solution soon abandoned for cost reasons);
- (3) the building housing the present Linac2 with little additional shielding the existing structure [8,9];
- (4) a future purpose-built tunnel, for which various options were investigated. The radiation protection aspects of an earlier scheme are discussed in Ref. [9].

This paper discusses the radiation protection aspects of the final configuration of the fourth scenario, the solution finally adopted and which is now under construction. Particular attention was

devoted to evaluating the propagation of neutrons through the waveguide ducts and through the access area at the low-energy end of the linac. The induced radioactivity in the components of the accelerator and in the air of the tunnel was estimated by Monte Carlo simulations with the particle transport code FLUKA [10,11] (version 2006.3b, March 2007) for various beam energies and several decay times. The accuracy of this code for use in radiation protection has been proven through several benchmarks (see, for example, Refs. [11,12]). The paper provides complete information on beam loss assumptions, accelerator structure, material composition, and duct and maze design, in order to make the present results of sufficiently general interest and provide guidelines for similar studies for intermediate-energy proton accelerators.

2. Beam loss assumptions

In modern linear accelerators, the design maximum beam loss is normally below 1 W/m. Losses below this threshold usually generate values of induced radioactivity such that hands-on maintenance on the machine is still possible. The beam dynamics and the apertures in Linac4 have been optimized to keep losses below 1 W/m at the SPL duty cycle of 5%. The same loss level was also taken as guideline for the shielding calculations of Linac4 as injector for the PSB. Since the accelerator designers expect that losses scale proportionally with duty cycle, this assumption leads to a large safety factor of about 50 (the ratio of the SPL and PSB duty cycles). Therefore the proposed shielding design is appropriate for Linac4 used as front-end of the SPL and it is rather conservative as injector to the PSB.

In reality, beam losses will not be equally distributed along the machine, but will typically occur in the aperture restrictions of quadrupoles. In order to have a realistic loss configuration, in the following it is assumed that constant losses of 10 W every 10 m occur at selected points along the machine. In terms of shielding requirements, this loss distribution is approximately equivalent to

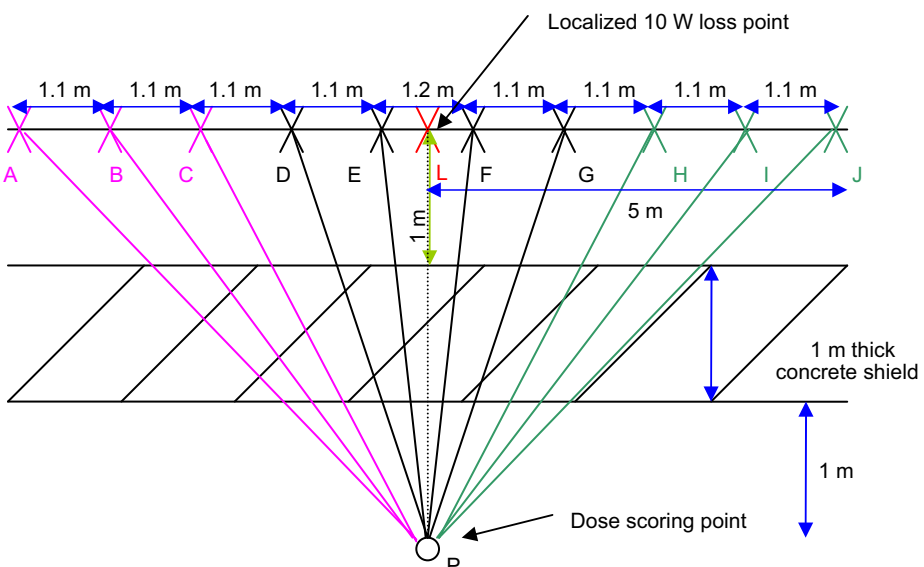


Fig. 3. Simplified model for the comparison between a continuous beam loss and a localized beam loss 10 times higher.

Table 1
Ambient dose equivalent rates for a continuous beam loss of 1 W/m and a localized loss of 10 W.

Loss-point	Distance source-scoring point P (m)	Effective shield thickness d (cm)	Angle (deg.)	λ for concrete (cm)	Source term (Sv m ² /proton)	Ambient dose equivalent H (Sv/proton)	Ambient dose equivalent rate $H^*(10)$ (Sv/h)
A	6.10	174	35.01	32.42	5.52E-16	6.84E-20	1.03E-05
B	5.23	150	42.00	32.01	3.73E-16	1.28E-19	1.93E-05
C	4.47	128	51.57	31.44	2.19E-16	1.88E-19	2.85E-05
D	3.88	111	64.52	30.67	1.06E-16	1.90E-19	2.88E-05
E	3.54	101	80.95	29.69	4.24E-17	1.11E-19	1.68E-05
F	3.54	101	99.09	28.61	1.54E-17	3.55E-20	5.37E-06
G	3.88	111	115.52	27.63	6.14E-18	7.40E-21	1.12E-06
H	4.47	128	128.48	26.86	2.98E-18	1.28E-21	1.94E-07
I	5.23	150	138.05	26.29	1.74E-18	2.16E-22	3.26E-08
J	6.10	174	145.04	25.87	1.18E-18	3.75E-23	5.67E-09
Total ambient dose equivalent and dose equation rate from the 10 W loss points						7.30E-19	1.10E-04
10W loss point	3.5	100	90.00		29.15	2.56E-17	6.75E-20
	1.02E-04						

a uniform loss of 1 W/m. The validity of this approximation can be proved through a simplified model in which the 1 W/m continuous loss is represented through 10 aligned 1 W loss points equally spaced over a total distance of 10 m and the localized 10 W loss point is placed in the middle of this ideal line (Fig. 3). As an example, the contributions to the ambient dose equivalent rate at point P beyond the shield of the 10 W losses and of the 10 W localized loss are compared at the proton energy of 150 MeV. Let us consider the distance of the localized source from the inner surface of the concrete wall to be equal to 1 and consider a 1-m-thick shield. The attenuation through the shield of the ambient dose equivalent is described through the classical two-parameter formula (see, for example, Ref. [13,14]):

$$H(E_p, \theta, d/\lambda) = \frac{H_0(E_p, \theta)}{r^2} \exp\left[-\frac{d}{\lambda(\theta)g(\alpha)}\right] \quad (1)$$

where H is the ambient dose equivalent beyond the shield, E_p is the proton energy, r is the distance between the radiation source (the target stopping the protons) and the scoring position, θ is the angle between the direction \vec{r} and the beam axis, H_0 is the source term, d is the shield thickness, $\lambda(\theta)$ is the attenuation length for the given shielding material at emission angle θ , and α is the angle between the direction \vec{r} and the normal to the shield surface. The

function $g(\alpha) = 1$ for a spherical geometry and $g(\alpha) = \cos \alpha$ in all other cases. The ambient dose equivalent rate can be calculated multiplying the ambient dose equivalent by the number of protons per hour. At the energy of 150 MeV the number of lost protons per hour is 1.5×10^{14} for 1 W beam loss. Attenuation lengths and source terms as a function of proton energy E_p and emission angle θ were taken from Ref. [14]. As shown in Table 1, the contributions to the ambient dose equivalent rate in point P of the 10 W losses and of the localized 10 W loss are 1.10×10^{-4} and 1.02×10^{-4} Sv/h, respectively. Therefore, the approximation used in the present study is correct.

3. Radiation shielding

The Linac4 tunnel will be located underground, at a depth sufficient to shield the direct stray radiation produced during the accelerator operation. In the first design the linac was at a depth such that it was effectively shielded by 430 cm of earth plus about 1 m of concrete. Subsequently, with the aim to minimize the interference of the future SPL with surface buildings and existing tunnels nearby [15], the Linac4 and SPL tunnels were lowered by 2.5 m. The klystrons will be installed in an auxiliary building

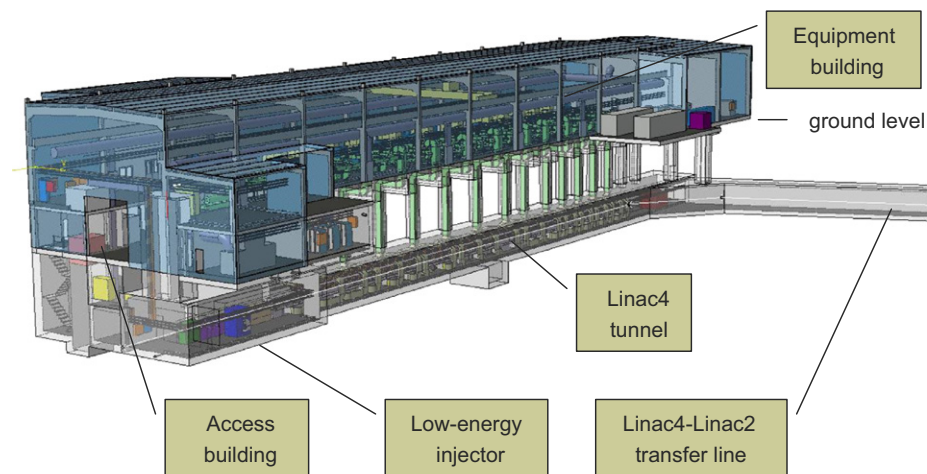


Fig. 4. The Linac4 layout showing the underground accelerator tunnel, the transfer line towards the PS and the surface building housing the klystrons and ancillary equipment.

Table 2
Classification of radiation areas according to CERN radiation safety code.

Type of area	Maximum annual effective dose (mSv)	Maximum ambient dose equivalent rate ($\mu\text{Sv}/\text{h}$)
Non-designated	1	0.5
Supervised	6	3
Simple controlled	20	10

located on the surface on top of the linac tunnel and will be connected to the linac by waveguides running through ducts traversing the shielding. The final layout is depicted in Fig. 4.

The basic assumptions for the shielding design are the classification of radiation areas (Table 2) and the beam loss pattern (position and intensity of the losses) for routine operation and accidental conditions. The linac tunnel is underground, while the klystron building is on the surface on top of the tunnel. The klystron building will be classified as a supervised radiation area ($3 \mu\text{Sv}/\text{h}$ guideline value for the dose rate) according to CERN Radiation Safety Code [16] but, because of the thin walls separating this building from the public area, $1 \mu\text{Sv}/\text{h}$ has been taken as design value for the calculations. The shielding calculations were performed for the worst-case scenario for routine operation (160 MeV, 10 W point losses every 10 m). Because the linac is at such a depth, one can verify by using a simple point-source line-of-sight model that the earth thickness between the machine tunnel and the klystron building is indeed sufficient as bulk shield. For a point source and 90° emission expression (1) approximates to

$$H = \frac{H_{\pi/2} \exp(-d/\lambda)}{r^2} \quad (2)$$

where r is the distance from the radiation source to the exposure point of interest, $H_{\pi/2}$ and λ are the source term and attenuation length of the shielding material for 90° emission, and d is the shield thickness. Both $H_{\pi/2}$ and λ increase with increasing beam energy. The distance r is about 8 m. Data from Refs. [13,14] were used to estimate the source term and the attenuation length in ordinary concrete at 160 MeV. The estimated concrete thicknesses required to reduce the dose equivalent rate down to $1 \mu\text{Sv}/\text{h}$ are 250 and 190 cm. The 25% discrepancy is acceptable considering that the two sets of data are derived from totally independent assumptions and calculation approaches (data from Ref. [13] are based on analytical models and data from Ref. [14] from Monte

Carlo simulations with the latest version of the FLUKA code) and 20 yr apart. The “real” thickness required for the shielding is probably closer to the value estimated from Ref. [14], but the thickest shield was here chosen as a conservative assumption. A safety factor of 3 in a shielding design is usually recommended. This can be obtained by increasing the concrete shielding by 1.1, which leads to a 280 cm thickness of concrete. The equivalent earth thickness can approximately be assessed by simply scaling the thickness for concrete by the ratio of the densities of the two materials, taken as 1.8 g/cm^3 for earth and 2.35 g/cm^3 for concrete. This value of earth density should be regarded as conservative for CERN local soil, a density of 2 g/cm^3 being probably a more realistic figure. With this simplification, 280 cm of concrete is approximately equivalent to 370 cm of earth, from the point of view of radiation attenuation. Thus even the original 435 cm of earth plus 100 cm of concrete are largely sufficient to reduce the ambient dose equivalent rate due to stray radiation through the shield to well below the value for public exposure of $0.5 \mu\text{Sv}/\text{h}$. Given the fact that the linac tunnel was further lowered by 2.5 m, it was decided that detailed Monte Carlo simulations were not necessary to confirm the adequacy of the bulk shielding.

4. Neutrons streaming through the waveguide ducts

The first radiological study was focused on the propagation of neutrons through the waveguide ducts from the linac tunnel to the surface klystron building. Along the accelerator the distance between the waveguides decreases with increasing energy. The worst-case scenario in the high-energy section was studied. The stray radiation in the klystron building is mainly given by the addition of two terms, the radiation traversing the shield and the radiation streaming through the waveguide ducts. As the bulk shield is largely sufficient to shield the direct radiation, in the simulations the particles were not transported through the earth in order to optimize the computing time. Several simulations were performed to optimize the number, cross-sectional area and length of the legs of the ducts. The first calculations for the waveguide ducts were performed before the linac tunnel was finally lowered by 2.5 m. Sections 4.1–4.3 discuss these first studies, while Section 4.4 refers to the final layout.

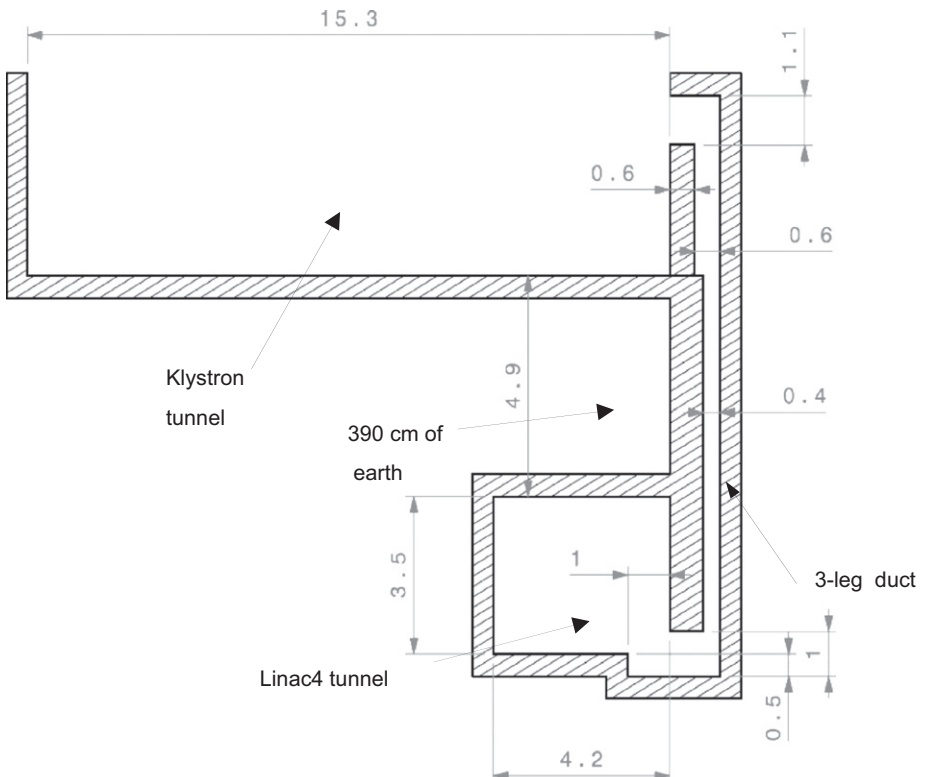


Fig. 5. Layout of the geometry implemented in the simulation (linac tunnel, three-leg waveguide ducts and klystron tunnel).

Table 3

Layout of the waveguide duct for two possible scenarios: a duct housing two waveguides and a long well housing all the 18 waveguides (Section 4.1 of text).

	Height (cm)	Length (cm)	Width in beam direction (cm)
First leg (horizontal)	40 cm	100	200 or 9000
Second leg (vertical)	40 cm in the lower section and 60 cm in the upper section	1150	200 or 9000
Third leg (horizontal)	40 cm	110	200 or 9000

4.1. First layouts: first duct close to the loss point

The ducts housing the waveguides were originally designed according to the three-leg configuration shown in Fig. 5 and described in Table 3, dictated by an early design of the facility in which the klystrons were located in an underground tunnel just below ground level. The cross-sectional area of the waveguides is $700 \times 250 \text{ mm}^2$ and two possible layouts for the ducts were investigated:

- (1) several 200-cm-long (in the beam direction) ducts, each one housing two waveguides;
- (2) one single 90-m-long rectangular well housing all the 18 waveguides.

The target where the beam is lost was simulated by a $5 \times 5 \times 5 \text{ cm}^3$ copper block placed at beam height, 126 cm above the floor of the tunnel and 86 cm above the opening of the duct. A beam loss of 10 W at the maximum energy (160 MeV) was assumed. The importance biasing technique was used to improve

the transport of the neutrons through the three legs of the duct and to kill those crossing the bulk shield.

As shown in Fig. 6 (left), for the 200-cm-long duct in the most critical case the radiation streaming into the klystron tunnel is between 0.1 and 0.5 $\mu\text{Sv}/\text{h}$. For the 90-m-long rectangular well the dose streaming into the klystron tunnel can reach a maximum value between 1 and 3 $\mu\text{Sv}/\text{h}$ (Fig. 6, right).

4.2. First layouts: ducts housing one waveguide (interspaced by 1 m of earth plus 20 cm of concrete)

In the next design phase, the klystrons were moved to a surface building (the configuration finally adopted). The ducts housing the waveguides connecting the klystrons to the RF cavities were designed according to the three-leg configuration described in Table 4. The ducts have two reductions in size, at the beginning and at the end of the first vertical leg, respectively, where the width is reduced from 75 to 30 cm.

In correspondence to the waveguides the shield is made of 100 cm of concrete plus 360 cm of earth with an additional 50-cm-thick concrete layer over the horizontal leg (the vertical dimension of the duct is 25 cm) (Fig. 7). The geometry implemented in the simulation includes two parallel ducts separated by 100 cm of earth plus 20 cm of concrete corresponding to the thickness of the duct walls (Fig. 7, right). The target where the beam is lost was simulated by a $5 \times 5 \times 5 \text{ cm}^3$ copper block placed in front of the mouth of the second (downstream) duct. A beam loss of 10 W at the maximum energy of 160 MeV was assumed. The simulations showed that the radiation streaming into the klystron building directly from the first leg of the first duct, beyond the 50-cm-thick concrete shield, is expected to be between 0.1 and 1 $\mu\text{Sv}/\text{h}$. For both ducts the radiation streaming out of the third leg is less than 0.1 $\mu\text{Sv}/\text{h}$ (Fig. 8). However, the radiation streaming into the klystron building from the first leg of the second duct beyond the 50-cm-thick concrete shield is expected between 1 and 10 $\mu\text{Sv}/\text{h}$.

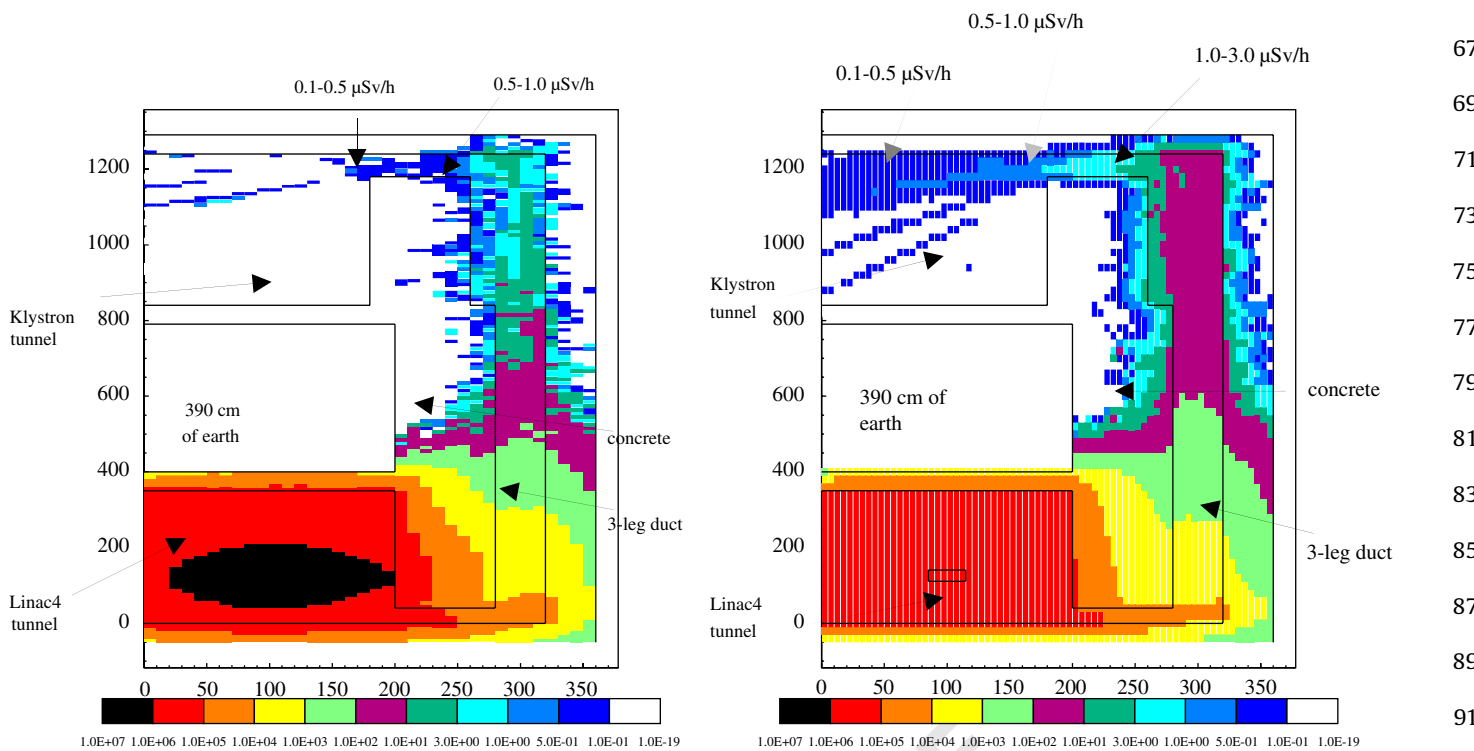


Fig. 6. Beam loss in a $5 \times 5 \times 5$ cm 3 copper target, 10W, 160 MeV. Left: cross-sectional view of the Linac4 tunnel, the 2-m-long duct housing two waveguides and the klystron tunnel. Right: cross-sectional view of the Linac4 tunnel, the 90-m-long well housing all the waveguides and the klystron tunnel. $H^*(10)$ in $\mu\text{Sv}/\text{h}$.

Table 4
Layout of the waveguide ducts (Section 4.2 of text).

	Section (cm 2)	Length (cm)
First leg (vertical)	75 \times 75	460
Second leg (horizontal)	25 \times 70	400
Third leg (vertical)	25 \times 70	50

This radiation level is so high that a different solution had to be studied.

4.3. First layouts: ducts housing two waveguides (interspaced by 280 cm of earth plus 20 cm of concrete)

With the aim of grouping two waveguides in a single duct, a new three-leg configuration was designed (Table 5). The concrete shield over the horizontal leg was increased from 50 to 100 cm. Two parallel waveguide ducts are now spaced by 2.80 m of earth plus 20 cm of concrete corresponding to the thickness of the duct walls (Fig. 9). Several configurations regarding the size, the material and the position of the target were studied by FLUKA simulations: the resulting radiation levels are given in Table 6. The results are comparable and the level of radiation is acceptable for the classification of the klystron building as a supervised area. The results for the last scenario described in Table 6 are also depicted in Fig. 10.

4.4. Final layout

The civil engineering design has been subsequently modified lowering the linac4 tunnel by 2.5 m because of radiation safety aspects related to the future SPL [15]. The waveguide duct design has also been changed, increasing the length of the first leg by

2.5 m, increasing the cross-section of the first two legs and shortening the horizontal leg by 50 cm. The new three-leg configuration is described in Table 7.

The target, a cube of 5 cm side made of copper, was placed in front of the mouth of the second (downstream) duct. The simulations showed that the stray radiation in the klystron building on top of the first leg is expected to be less than 0.1 $\mu\text{Sv}/\text{h}$, while the radiation streaming out of the third leg is between 0.1 and 1 $\mu\text{Sv}/\text{h}$. The radiation on top of the first leg of the second duct and that streaming out of the third leg are both expected between 0.1 and 1 $\mu\text{Sv}/\text{h}$ (Fig. 11).

5. Access maze, ventilation and cable ducts at the low-energy end of the linac

A detailed geometry was implemented in the FLUKA simulation to study the radiological impact in the low-energy section of the accelerator. This part of the Linac4 tunnel is particularly important for two reasons: first it includes the shafts housing the cables and the ventilation system and second it is close to the access shaft containing the staircases and the lift. An initial simulation was performed to estimate the radiation backscattered from a beam loss point at the end of the low-energy section (10 W, 11 MeV) into the access area, where the lift and the staircases are located, and to evaluate the need for an access maze. The geometry implemented in the simulation includes a simplified model of the accelerator tunnel and of the access area. The simulations showed that without maze the radiation streaming into the access area is expected between 10 and 100 $\mu\text{Sv}/\text{h}$ (Fig. 12). A 100-cm-thick concrete wall was thus added in this area to create a maze and to reduce the radiation streaming through the lift and the staircases and reaching the surface.

A second simulation, including this maze in the geometry, was performed to estimate the radiation in the occupied areas nearby the low-energy section of Linac4. The layout of the simulation

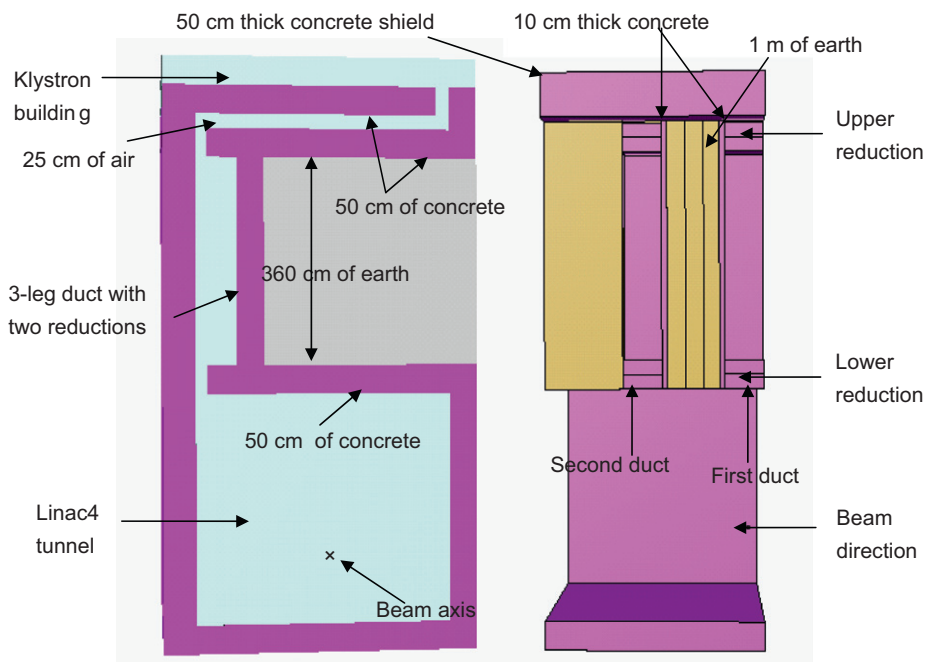


Fig. 7. FLUKA geometry plotted with SimpleGeo [17]: cross-sectional and lateral views of the Linac4 tunnel, the two three-leg ducts and the floor of the klystron building.

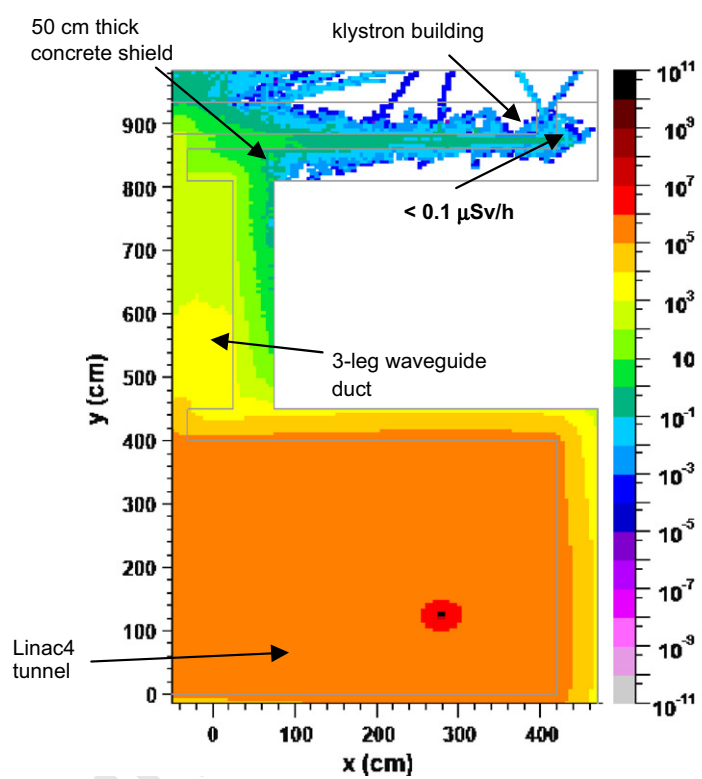


Fig. 8. Neutrons streaming through a pair of waveguide ducts spaced by 1 m. Beam loss in a $5 \times 5 \times 5 \text{ cm}^3$ copper target, 10 W, 160 MeV, placed in front of the downstream duct. Cross-sectional view of the Linac4 tunnel, the three-leg duct and the floor of the klystron building. $H^*(10)$ in $\mu\text{Sv}/\text{h}$. Left: Dose rate in the upstream duct. Right: Dose rate in the downstream duct. Note the different scale for x and y directions.

(Fig. 13) includes the following structures (heights are given with reference to the tunnel floor):

- the accelerator tunnel;
- the so-called "safe room" at a height of 3.5 m;
- the galleries on the first and second floor located at a height of

7.6 and 12.1 m, respectively;

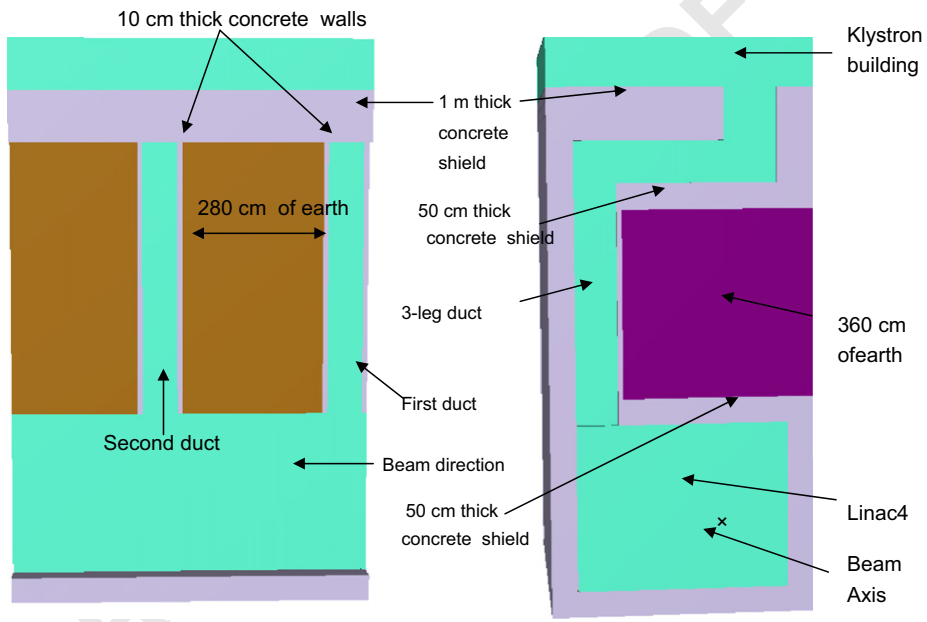
- the ventilation shaft and the cable duct located at the beginning of the accelerator tunnel;
- the access area with the lift, the staircases and the maze designed to reduce the radiation streaming through these shafts;

1 • the target, a 5 cm side cube, made of copper and located at the
 3 end of the low-energy section (energy of 11 MeV).

5 A beam loss of 10 W at the energy of 11 MeV was simulated and
 7 the backscattered radiation estimated. The setup of an access
 9 maze by the addition of the 100-cm-thick wall reduces the dose
 11 rate in the access area to less than 0.1 $\mu\text{Sv}/\text{h}$ (Fig. 14). The radiation
 13 in the “safe room” is expected to be between 1 and 10 $\mu\text{Sv}/\text{h}$ just
 15 in proximity of the 50-cm-thick lateral wall of the room, while
 17 everywhere else in the room is less than 1 $\mu\text{Sv}/\text{h}$ (Fig. 15). The
 19 radiation in the gallery on the first floor is well below 1 $\mu\text{Sv}/\text{h}$ (Fig.
 21 16).

19 **Table 5**
 Layout of the waveguide ducts (Section 4.3 of text).

	Section (cm 2)	Length (cm)
First leg (vertical)	80 × 70	500
Second leg (horizontal)	80 × 70	285
Third leg (vertical)	100 × 90	140



51 **Fig. 9.** FLUKA geometry plotted with SimpleGeo [17]: lateral and cross-sectional views of the Linac4 tunnel, the two three-leg ducts housing two waveguides and the klystron building.

53 **Table 6**

55 Dose rates for several configurations of size, material and position of the target in the waveguide duct studies (Section 4.3 of text)

Target dimension	Target material	Position of the target	Dose rate streaming out of the first leg (first duct) ($\mu\text{Sv}/\text{h}$)	Dose rate streaming out of the third leg (first duct) ($\mu\text{Sv}/\text{h}$)	Dose rate streaming out of the first leg (second duct) ($\mu\text{Sv}/\text{h}$)	Dose rate streaming out of the third leg (second duct) ($\mu\text{Sv}/\text{h}$)
5 cm × 5 cm × 5 cm	Copper	In between the two ducts	<0.1	0.1–1	0.1–1	0.1–1
5 cm × 5 cm × 30 cm (beam direction)	Iron	In between the two ducts	<0.1	0.1–1	0.1–1	0.1–1
5 cm × 5 cm × 5 cm	Copper	In front of the second duct mouth	<0.1	0.1–1	0.1–1	0.1–1
20 cm × 20 cm × 5 cm	Copper	In front of the second duct mouth	<0.1	0.1–1	0.1–1	0.1–1

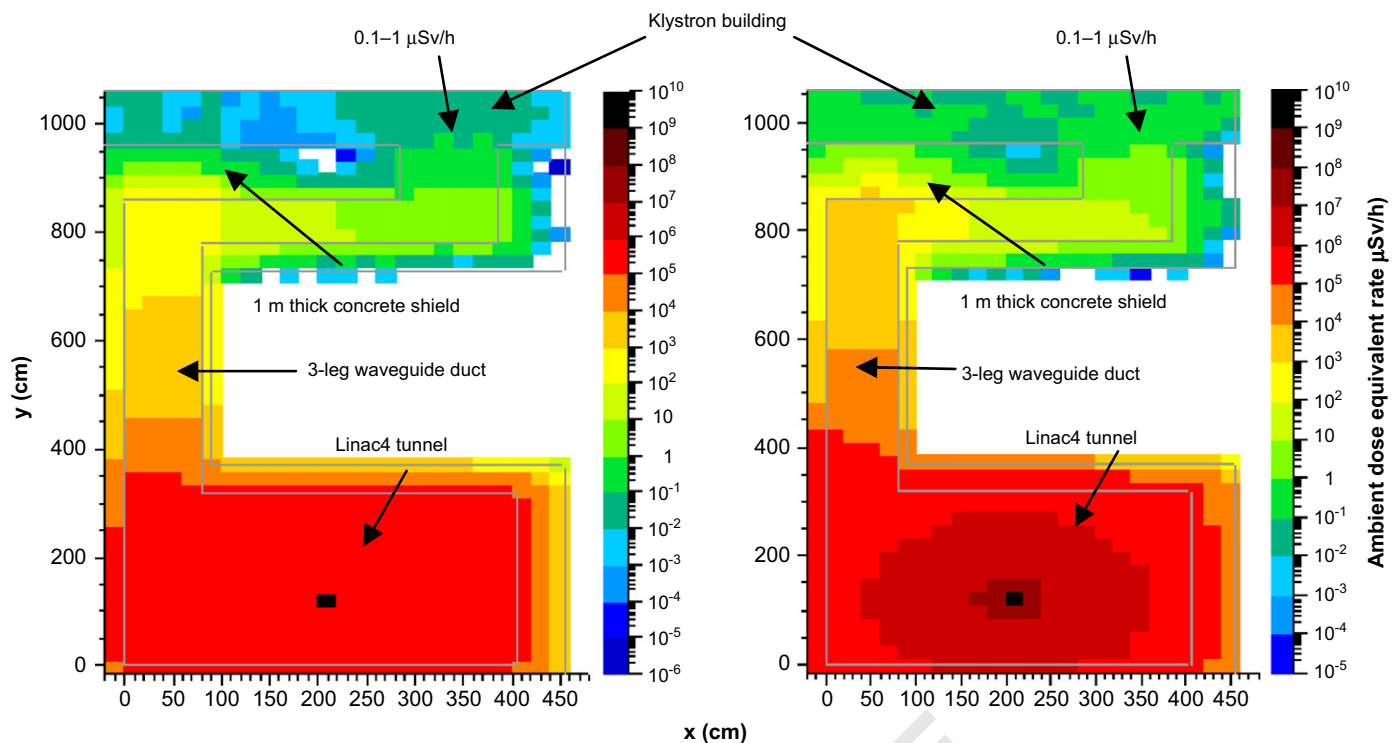


Fig. 10. Neutrons streaming through a pair of waveguide ducts spaced by 2.8 m. Beam loss in a $20 \times 20 \times 5 \text{ cm}^3$ copper target, 10 W, 160 MeV, placed in front of the downstream duct. Cross-sectional view of the Linac4 tunnel and the three-leg duct. $H^*(10)$ in $\mu\text{Sv}/\text{h}$. Left: Dose rate in the upstream duct. Right: Dose rate in the downstream duct. Note the different scale for x and y directions.

Table 7
Layout of the waveguide ducts (Section 4.4 of text).

	Section (cm^2)	Length (cm)
First leg (vertical)	90 × 90	755
Second leg (horizontal)	90 × 90	250
Third leg (vertical)	100 × 90	145

interventions and final disposal of radioactive waste. Equipment activation in the Linac4 area will be produced by particle losses. The main causes of particle loss in a linear accelerator are collisions between accelerated particles escaping from the fields generated for controlling the focusing and the acceleration, and the metallic walls of the vacuum chamber. The analysis of particle losses (carried out by the Linac4 design team) and induced radioactivity was done at the highest possible operating beam current, corresponding to the full SPL duty cycle. Several measures have been applied in the design of Linac4 to minimize the beam losses [18,19]. After the optimization process, a set of multiparticle calculations with random errors have been performed in order to determine the particle loss distribution and their values expected in Linac4. The results for the worst-case computation are shown in Fig. 17 extracted from Refs. [18,19].

The beam losses are concentrated in 22 “hot spots” along the machine. The lost beam power ranges from 0.03 to 0.92 W (worst case, at the end of the CCDTL section). The actual error distribution in the real machine is unpredictable, and the number, position and intensity of the hot spots will be different from the simulated ones. However, taking the worst case over 1500 (for the DTL) and 700 (for the rest of the machine) random error distributions instead of the average is considered a conservative assumption covering against all possible real cases.

To assess the residual dose rates in the Linac4 tunnel, a series of FLUKA calculations were performed, using a detailed geometrical model of the accelerating structures, based on the current linac layout.

The geometry implemented in the simulations includes the following structures:

- The DTL (Fig. 18) made of three accelerating cavities over a length of 18.7 m. The RF cavities are 520 mm in diameter with drift tubes of 90 mm diameter and 20 mm beam aperture. The three DTL cavities consist of 2, 4 and 4 sections of about 1.8 m each, are equipped with 35, 41 and 29 drift tubes, respectively, and are stabilized with postcouplers. The drift tubes are equipped with permanent magnet quadrupoles (PMQ), used as focusing elements, with an FFDD lattice in cavity 1 and an FD lattice in cavities 2 and 3. PMQs have the advantage of small size at medium magnetic gradients without the need for current supply wires or power converters. The PMQs of the first tank of the DTL are modeled in the simulations as cylinders with 90% magnetic material (a samarium–cobalt alloy) and 10% aluminum holder, whereas those of the second and third tanks have 50% magnetic material and 50% aluminum. The PMQs are cylinders with inner bore diameter equal to 22 mm and outer diameter equal to 60 mm. The DTL tank1 PMQs are 45 mm long, the DTL tank2 and tank3 PMQs are 80 mm long. To ease matching for beam currents below nominal, electromagnetic quadrupoles (EMQ) are placed in each of the inter-tank sections.
- The CCDTL (Fig. 19) made of seven modules of three-cavity DTL-like accelerating tanks, connected by off-axis coupling cells bridging the focusing quadrupoles. Each cavity is equipped with two drift tubes and the electromagnetic quadrupoles are placed between the cavities. An alternative layout, in which two-thirds of the EMQs are replaced by PMQs, was also studied. In the latter layout the PMQs are modeled as

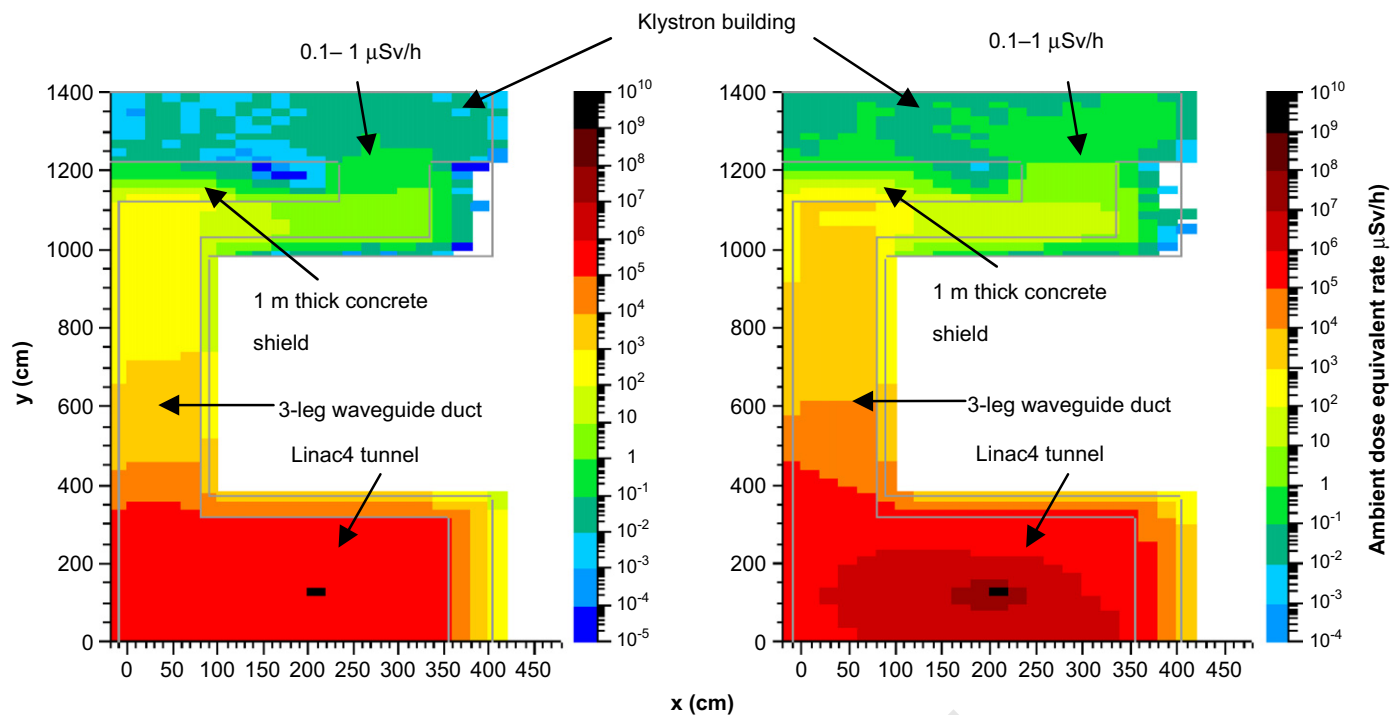


Fig. 11. Neutrons streaming through a pair of waveguide ducts spaced by 2.8 m. Beam loss in a $5 \times 5 \times 5 \text{ cm}^3$ copper target, 10 W, 160 MeV, placed in front of the downstream duct. Cross-sectional view of the Linac4 tunnel and the three-leg duct. $H^*(10)$ in $\mu\text{Sv/h}$. Left: Dose rate in the upstream duct. Right: Dose rate in the downstream duct. Note the different scale for x and y directions.

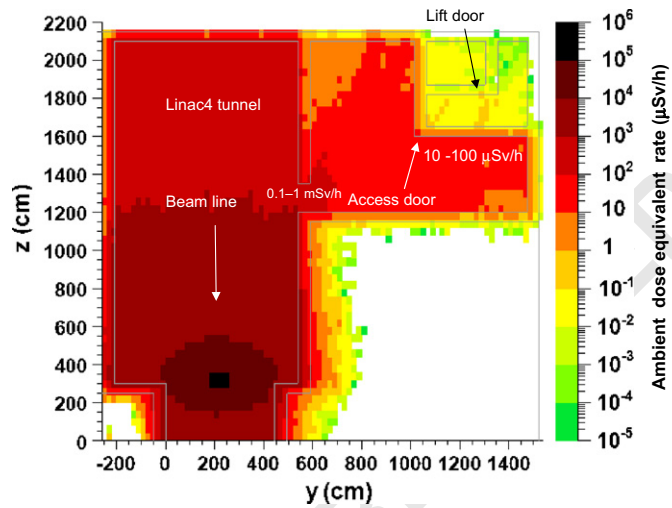


Fig. 12. Neutrons streaming on the ground floor of the Linac4 tunnel. Beam loss in a $5 \times 5 \times 5 \text{ cm}^3$ copper target, 10 W, 11 MeV, placed at the end of the low-energy section of the accelerator. Cross-sectional view of the Linac4 tunnel and of the access area. $H^*(10)$ in $\mu\text{Sv/h}$.

cylinders with 30% magnetic material (a samarium-cobalt alloy) and 70% aluminum holder. The PMQs are cylinders with inner bore diameter equal to 40 mm and outer diameter equal to 85 mm. The CCDTL PMQs are 100 mm long. The overall length of this accelerating structure is 23.4 m. • The PIMS (Fig. 20) made of a sequence of 12 seven-cell accelerating cavities of the Pi-Mode Structure type. The structure consists of discs and cylinders which are machined out of solid copper blocks. The cell length is the same within a cavity, but changes from cavity to cavity according to the beam velocity profile. The electromagnetic quadrupoles are placed

between the cavities. The overall length of this accelerating structure is 22 m.

The materials and their compositions are listed in Table 8. The time profile of the irradiation for the FLUKA simulations includes four cycles of 9-month operation and 3-month shutdown period, followed by a final 9-month operating period. The residual dose rates in Linac4 were estimated at the SPL duty cycle. The simulations assumed a localized loss of 1 W in three different positions, representative of typical aperture restrictions in the various sections of Linac4: the first drift tube of the third DTL tank at 30 MeV, the quadrupole (electromagnetic or permanent magnet according to the layout considered) at 80 MeV within the CCDTL section and the quadrupole at 155 MeV (the last one) within the PIMS section. The ambient dose equivalent rate, $H^*(10)$, due to residual radioactivity was calculated at the height of the tanks for six decay times: immediately after the end of the operation and after 1 h, 6 h, 1 d, 1 week and 1 month.

The residual dose rates in contact with the tank of the DTL and with electromagnetic quadrupoles in the CCDTL and PIMS sections and at 1 m distance are given in Table 9. An example of the residual dose rate scoring is shown in Fig. 21. Whilst in the DTL the dose rates are rather low and pose no major problems from a maintenance point of view, the CCDTL and PIMS cases are more critical. Whereas the DTL quadrupole is shielded by the drift tube and by the tank, the other quadrupoles are directly accessible. Few localized spots at high energy, probably in correspondence of a quadrupole, can become rather radioactive at the end of a run at the SPL duty cycle.

In the alternative layout for the CCDTL section (using PMQs instead of EMQs), the residual dose rates in contact with the PMQ body and with the coupling cavity, and at 1 m distance are listed in Table 10. The dose rates in contact with the PMQs and at 1 m distance from the PMQs are higher than those obtained with the EMQs. Indeed the set of radionuclides produced in the PMQs is

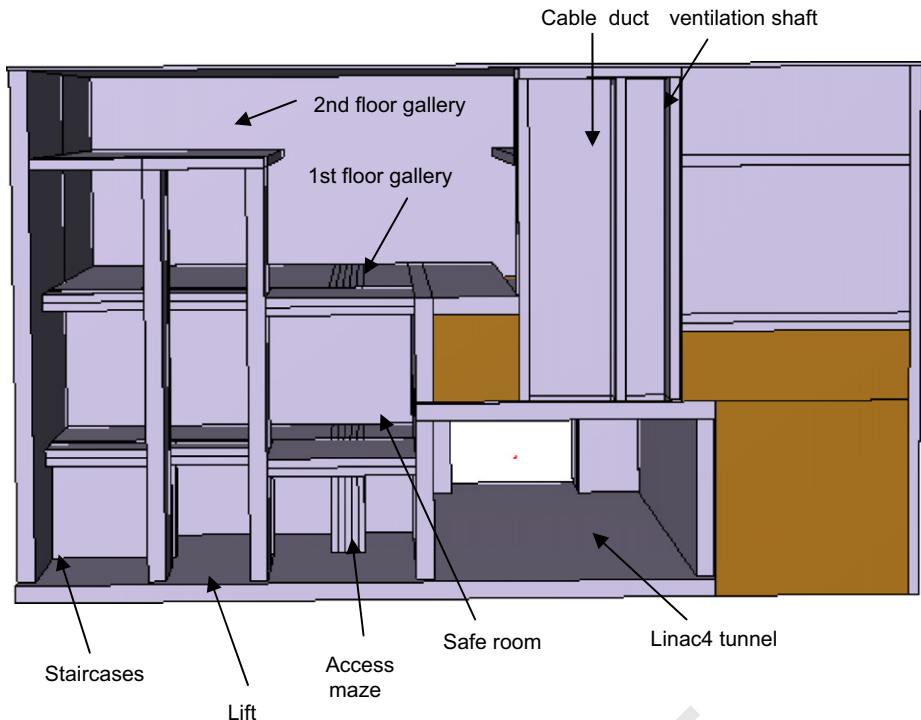


Fig. 13. FLUKA geometry plotted with SimpleGeo [17]. Cross-sectional view of the low-energy section of Linac4. The view looks downstream in the tunnel, towards the high-energy end of the accelerator.

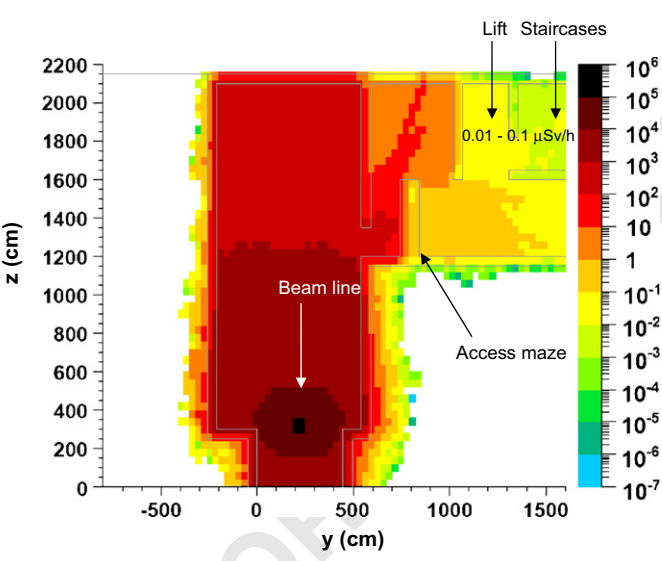


Fig. 14. Neutrons streaming into the ground floor of the Linac4 tunnel. Beam loss in a $5 \times 5 \times 5 \text{ cm}^3$ copper target, 10 W, 11 MeV, placed at the end of the low-energy section of the accelerator. Cross-sectional view of the Linac4 tunnel and of the access area with the addition of the maze. $H^*(10)$ in $\mu\text{Sv}/\text{h}$.

completely different from those obtained in the EMQs in the previous study, because of the different material composition (the PMQs are made of the samarium-cobalt alloy and the EMQs of low-carbon magnetic steel).

The radionuclide inventories after 1-month decay time for the most important components of the accelerator are listed in Tables 11–14. In the DTL section the most important radionuclides responsible for the residual radioactivity in the drift tubes are ^{65}Zn , ^{58}Co , ^{63}Ni , ^{60}Co and ^{55}Fe , while the main contributors to the residual radioactivity in the PMQs are ^{58}Co , ^{60}Co , ^{57}Co , ^{56}Co , ^{65}Zn ,

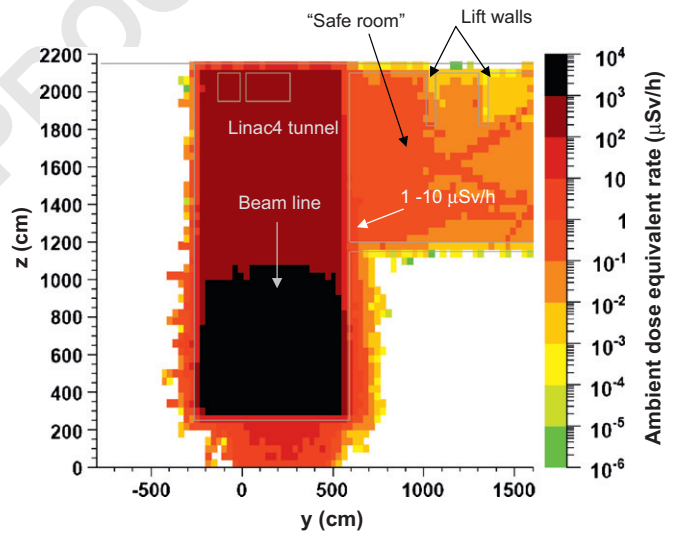


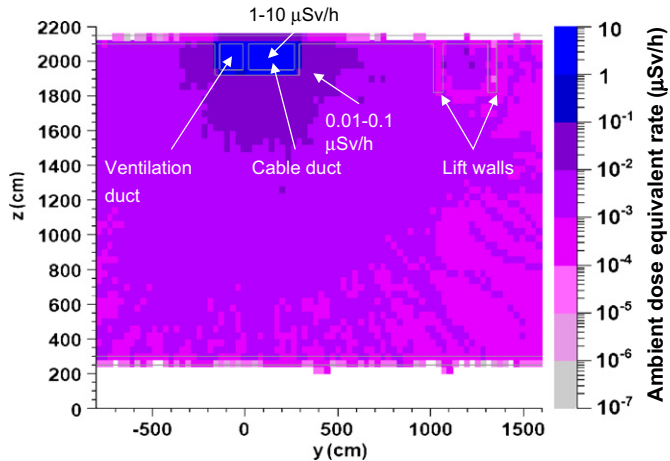
Fig. 15. Neutrons streaming into the "safe room". Beam loss in a $5 \times 5 \times 5 \text{ cm}^3$ copper target, 10 W, 11 MeV, placed at the end of the low-energy section of the accelerator. Top cross-sectional view of the "safe room" at the height of 3.5 m with respect to the tunnel floor. $H^*(10)$ in $\mu\text{Sv}/\text{h}$.

^{54}Mn , ^{55}Fe , ^{22}Na , ^{147}Eu , ^{148}Eu , ^{149}Eu , ^{152}Eu , ^{155}Eu and ^{145}Sm . In the CCDTL section equipped only with EMQs, the main radionuclides contributing to the residual radioactivity in the vacuum chamber (the loss point) are ^{55}Fe , ^{54}Mn , ^{57}Co , ^{56}Co , ^{51}Cr , ^{49}V , ^{58}Co , ^{48}V , ^{88}Y , ^{88}Zr , ^{46}Sc , ^{22}Na , ^{3}H and ^{60}Co , while the main contributors to the residual radioactivity in the quadrupole adjacent to the vacuum chamber are ^{55}Fe , ^{54}Mn , ^{56}Co , ^{51}Cr , ^{49}V , ^{58}Co , ^{65}Zn , ^{63}Ni and ^{60}Co . In alternative layout of the CCDTL section, the main radionuclides contributing to the residual radioactivity in the vacuum chamber (the loss point) are ^{55}Fe , ^{54}Mn , ^{57}Co , ^{56}Co , ^{51}Cr , ^{49}V , ^{58}Co , ^{48}V , ^{88}Y , ^{88}Zr , ^{46}Sc , ^{22}Na and ^{60}Co , while the main contributors to the

1 residual activity in the PMQ adjacent to the vacuum chamber are
 2 ^{55}Fe , ^{54}Mn , ^{57}Co , ^{58}Co , ^{60}Co , ^{22}Na , ^{149}Eu , ^{145}Sm , ^{56}Co and ^{59}Fe . In
 3 the PIMS section, the most important radionuclides contributing
 4 to the residual radioactivity in the vacuum chamber are ^{55}Fe ,
 5 ^{54}Mn , ^{51}Cr , ^{49}V , ^{57}Co , ^{56}Co , ^{88}Y , ^{88}Zr , ^{58}Co , ^{46}Sc , ^{45}Ca , ^{3}H and ^{60}Co ,
 6 while the main contributors to the residual radioactivity in the
 7 quadrupole adjacent to the vacuum chamber are ^{54}Mn , ^{51}Cr , ^{49}V ,
 8 ^{57}Co , ^{56}Co , ^{58}Co , ^{55}Fe , ^{65}Zn , ^{3}H , ^{60}Co and ^{63}Ni . The complete
 9 radionuclide inventory for all the components in the accelerator is
 10 available in Refs. [20,21].

11 6.1. Air activation

15 The track-length spectra were individually calculated by FLUKA
 17 for all air regions in the accelerator tunnel. The contribution from
 19 different regions was summed to obtain the total track-length
 spectra for neutrons, protons and charged pions. The yield Y_i of
 radionuclide i is then obtained by folding these spectra with

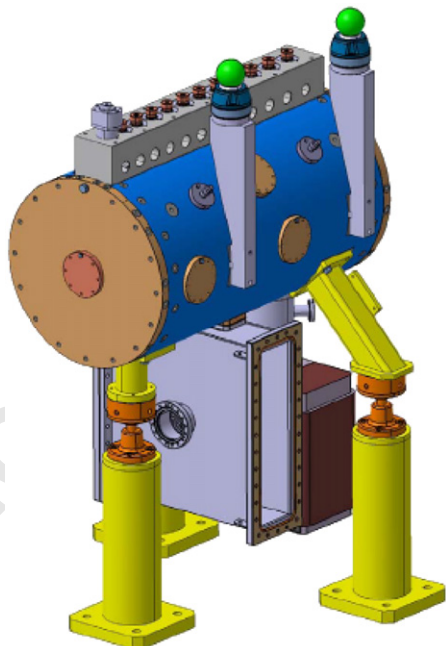


37 **Fig. 16.** Neutrons streaming into the gallery on the first floor. Beam loss in a
 39 $5 \times 5 \times 5 \text{ cm}^3$ copper target, 10W, 11 MeV, placed at the end of the low-energy
 41 section of the accelerator. Top cross-sectional view of the gallery on the first floor
 43 in the Linac4 tunnel at a height of 7.6 m. $H^*(10)$ in $\mu\text{Sv}/\text{h}$.

1 energy-dependent partial cross-sections summed over all target
 2 nuclei and hadron components in the cascade

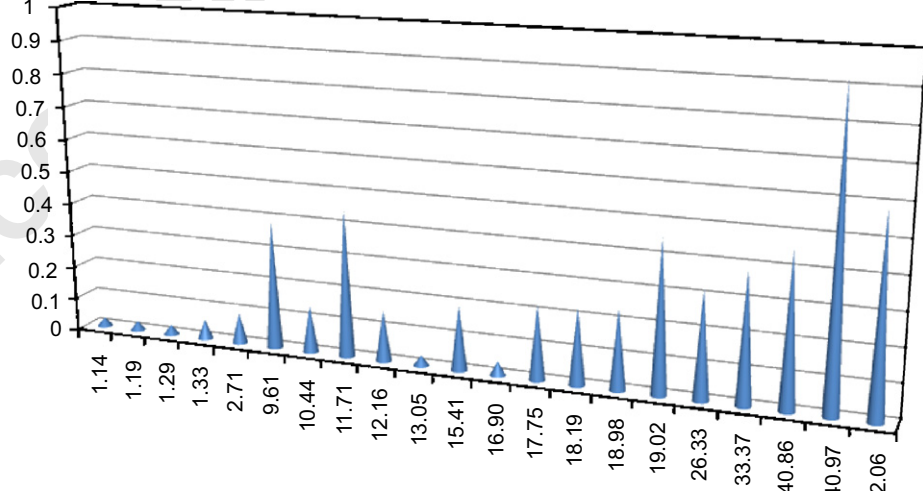
$$13 Y_i = \sum_{j,k} n_j \int \sigma_{ijk}(E) \Lambda_k(E) dE \quad (3)$$

15 where n_j is the atomic concentration (per cm^3) of element j in the
 17 material and σ_{ijk} is the cumulative cross-section for the produc-
 19 tion of radionuclide i in the reaction of a particle of type k and
 21 energy E with a nucleus of element j . The quantity Λ_k is the sum of
 23 the track-lengths (in cm) of the hadrons of type k and energy E . A
 25 database with evaluated neutron, proton and charged pion
 27 interaction cross-sections that govern the conversion of the air
 29 constituents (^{14}N , ^{16}O and ^{40}Ar) into the radionuclide of interest



105 **Fig. 18.** 3D view of the first tank of the DTL.

107 Power lost (watt) vs z (m),
 109 40 mA, 6% duty cycle, worst case, steererson
 111 quad alignment 0.1 mm 1 sigma gaussian, beam error
 113 0.3 mm 0.3 mrad gaussian



115 **Fig. 17.** Lost beam power along Linac4, from the entrance of the DTL (3 MeV) to the end of the PIMS (160 MeV). Losses are localized; the plot shows position and intensity of
 117 the loss points in the presence of errors, for the worst case, at 6% duty cycle [18,19].

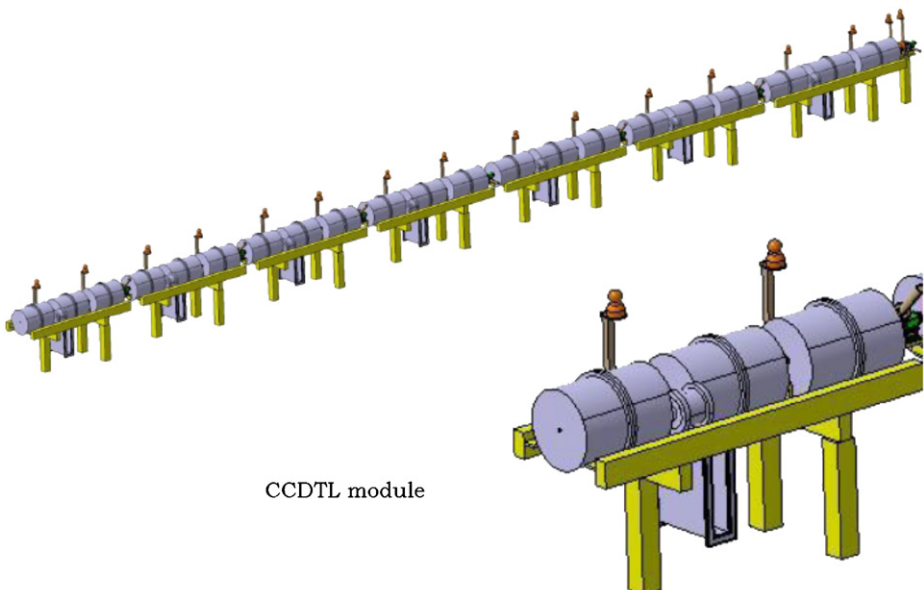


Fig. 19. 3D view of the seven modules of the CCDTL and close-up view of the first module.

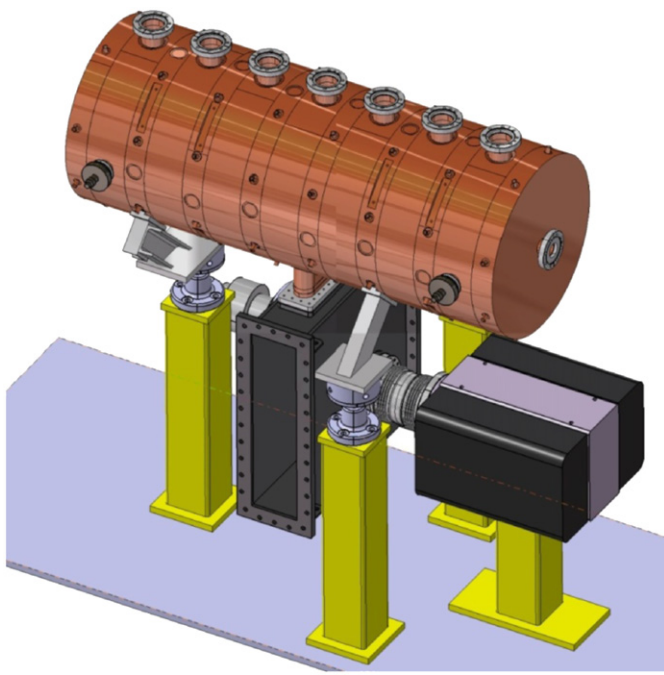


Fig. 20. Tank of the PIMS.

by the various particles is available [22] and was used in a post-processing together with track-length spectra from the FLUKA simulations.

A section of the 91.5-m-long accelerator tunnel was modeled with a cartesian geometry with beam direction along the z-axis. Most of the tunnel is air (density = 0.001205 g/cm³, volume = 1.46×10^9 cm³) with the following composition (weight fraction): nitrogen (75.558%), oxygen (23.159%) and argon (1.283%). Taking into account the particle loss distribution described in Fig. 17, the total beam loss in the tunnel is roughly 10 W. This scenario was studied for three different beam energies: 50, 100 and 160 MeV. To evaluate the worker exposure during access after shutdown, the activities of airborne radionuclides

have to be estimated based on the accelerator operational conditions. Assuming a continuous loss of a 10 W beam ($N_p = 1.25 \times 10^{12}$ protons/s at 50 MeV; $N_p = 6.24 \times 10^{11}$ protons/s at 100 MeV; $N_p = 3.9 \times 10^{11}$ protons/s at 160 MeV), the saturation activity (A_s) for different radionuclides can be calculated from their yields: $A_s = Y N_p$. It was assumed that there is no ventilation during the operation of the accelerator and that the worker intervention lasts 1 h. Several scenarios of irradiation and cooling times were considered. The activity for one single radionuclide after an irradiation time t_{irr} and a cooling time t_{cool} is

$$A_0(t_{irr}, t_{cool}) = Y N_p (1 - e^{-\lambda t_{irr}}) e^{-\lambda t_{cool}} \quad (4)$$

If the activity is mixed homogeneously in the tunnel, the activity concentration is obtained by dividing the activity by the volume of air. Both the internal exposure by inhalation and the external exposure must be evaluated. To estimate the inhalation dose received by a worker, it is necessary to multiply the calculated activities by the breathing rate B_r and the inhalation activity-to-dose conversion factors e_{inh} (expressed in Sv/Bq), which in the present study were taken from the Swiss ordonnance [23]:

$$D_0(t_{irr}, t_{cool}) = \frac{A_0(t_{irr}, t_{cool}) e_{inh} B_r}{V_{air}} \quad (5)$$

The standard breathing rate for a worker is 1.2 m³/h. In order to estimate the total dose per intervention, the equation

$$D_i(t) = D_0(t_{irr}, t_{cool}) e^{-\lambda t} \quad (6)$$

must be integrated over the intervention time t_{int} . The inhalation dose received by a person intervening in the accelerator tunnel for t_{int} after a cooling time t_{cool} is

$$D(t_{int}) = \frac{D_0(t_{irr}, t_{cool}) (1 - e^{-\lambda t_{int}})}{\lambda} \quad (7)$$

The values of inhalation doses obtained for the three scenarios (50, 100 and 160 MeV proton energy), with two irradiation times (1 d and 1 week) and three waiting times (0, 10 min and 1 h) are given in Table 15. Only the nuclei that give relevant contribution to the dose are listed.

For the evaluation of the effective dose for external exposure, the conversion coefficients for air submersion listed in TABLE III-1 of Ref. [24] were used. For each radionuclide, values for the organ

1 **Table 8**

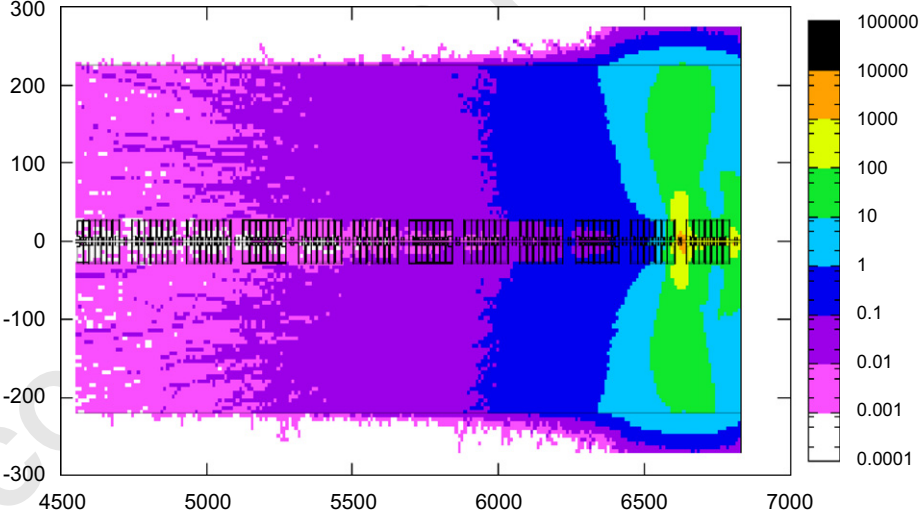
3 Materials used for the simulations of induced radioactivity and their compositions.

Material	Density (g/cm ³)	Atom composition (%)	Components
Low carbon magnetic steel	7.8	97.05 Fe, <0.001 C, <1.5 Si, <1.2 Mn, <0.05 P, <0.0005 S and <0.2 Al	Quadrupoles between the CCDTL cavities and the tanks of the PIMS
Samarium–cobalt alloy	8.4	52.0 Co, 15.0 Fe, 24.0 Sm, 7.0 Cu and 2.0 Zr	Permanent magnet quadrupoles
2024-T351 aluminum alloy	2.78	92.7 Al, 0.1 Al, 4.55 Cu, 0.5 Fe, 1.5 mg, 0.6 Mn, 0.5 Si, 0.25 Zn and 0.15 Ti	Holders of the permanent magnet quadrupoles
AW-6082 aluminum alloy	2.7	95.95 Al, 0.1 Cu, 0.2 Zn, 1.1 Si, 0.5 Fe, 0.7 Mn, 0.2 Ti, 0.9 Mg and 0.35 Cr	Girders
Copper	8.94	99.99 Cu, 0.0005 O ₂ , 0.0001 Cd, 0.0003 P, 0.0018 S, 0.0001 Zn, 0.0001 Hg, 0.001 Pb, 0.001 Se, 0.001 Se and 0.001 Bi	PIMS discs and drift tubes in the CCDTL and DTL sections
ST-52 steel	7.85	97.55 Fe, 2.2 C, Mn 1.6, 0.55 Si, 0.04 P, 0.035 S	DTL tanks and supports of the CCDTL modules
ST-304L steel	7.8	68.5 Fe, 0.08 C, 18.8 Cr, 9.5 Ni, 2.0 Mn, 1.0 Si, 0.045 P and 0.03 S	CCDTL tanks and all the waveguides
ST-316L steel	7.8	68.5 Fe, 18.0 Cr, 1.0 Si, 14.0 Ni, 2.5 Mo, 0.045 P, 0.3 C, 0.3 S and 0.11 N	Stems and vacuum chamber
St-37 steel	7.8	99.879 Fe, 0.055 P, 0.055 S and 0.011 N	Supports of the DTL and PIMS tanks

21 **Table 9**

23 Residual dose rates in the DTL Tank3 (31 MeV), in the CCDTL (80 MeV) and in high-energy end of the PIMS (155 MeV), SPL duty cycle.

Section	Decay time	Residual dose rate in contact (μSv/h)	Residual dose rate at 1 m distance (μSv/h)
DTL	0	40–50	5–10
	1 d	5–10	0.1–1
	1 month	1–5	0.1–1
CCDTL	0	7000–8000	100–200
	1 d	4000–5000	90–100
	1 month	2000–3000	40–50
PIMS	0	8000–10000	100–200
	1 d	4000–5000	50–100
	1 month	1000–2000	30–40

57 **Fig. 21.** Residual dose rate in the PIMS after 4 yr and 9 months of operation and 1-month decay. 155 MeV, 1 W loss on the vacuum chamber. $H^*(10)$ in $\mu\text{Sv}/\text{h}$.59 **Table 10**

61 Residual dose rate in the CCDTL alternative layout (80 MeV), SPL duty cycle.

Decay time	Residual dose rate in contact with the PMQ (μSv/h)	Residual dose rate at 1 m from the PMQ (μSv/h)	Residual dose rate in contact with the coupling cavity (μSv/h)	Residual dose rate at 1 m from the coupling cavity (μSv/h)
0	50,000–60,000	300–400	1000–2000	30–40
1 d	30,000–40,000	200–300	500–700	20–30
1 month	10,000–20,000	100–200	300–400	5–10

Table 11

Specific activity of the most important radionuclides contributing to residual radioactivity in the main components of the DTL section of the accelerator.

Radionuclide ($t_{1/2}$)	Specific activity (Bq/g)				
	Drift tube	PMQ ^a	DTL tank	EMQ downstream of the loss point	Vacuum chamber downstream of the loss point
Na-22 (2.6 yr)	–	4.8	–	–	–
Cr-51 (27.7 d)	–	–	–	–	2.88
Mn-54 (312.2 d)	–	12.2	0.35	0.48	–
Fe-55 (2.7 yr)	0.97	294.7	1.47	1.03	3.3
Co-56 (78.76 d)	–	129.6	–	–	–
Co-57 (271.3 d)	–	107.2	–	–	–
Co-58 (70.8 d)	16.25	589	–	–	13
Co-60 (5.2 yr)	1.97	33	–	–	–
Ni-63 (100 yr)	1.2	–	–	–	–
Zn-65 (244 d)	269.4	24	–	–	–
Sm-145 (340 d)	–	26.2	–	–	–
Eu-147 (24.6 d)	–	35	–	–	–
Eu-148 (55.6 d)	–	37.5	–	–	–
Eu-149 (93.1 d)	–	29.9	–	–	–
Eu-152 (13.33 yr)	–	6.8	–	–	–
Eu-155 (4.96 yr)	–	3.5	–	–	–

^a This PMQ has been modeled as a cylinder with 50% magnetic material (samarium–cobalt alloy) and 50% aluminum holder (2024-T351 aluminum alloy).

Table 12

Specific activity of the most important radionuclides contributing to residual radioactivity in the main components of the CCDTL section of the accelerator (equipped only with EMQs).

Radionuclide ($t_{1/2}$)	Specific activity (Bq/g)			
	Vacuum chamber	EMQ	Wall of the tank	Drift tube
H-3 (12 yr)	8092	–	–	–
Na-22 (2.6 yr)	2163	–	–	–
Sc-46 (83.8 d)	11,473	–	12	–
V-48 (16 d)	37,303	–	39.2	–
V-49 (330 d)	298,396	40	336	–
Cr-51 (27.7 d)	431,816	215	616	–
Mn-54 (312.2 d)	517,895	2150	819	42
Fe-55 (2.7 yr)	1,173,508	5300	1785	80
Co-56 (78.76 d)	410,298	707	511	80
Co-57 (271.3 d)	296,961	–	294	54
Co-58 (271.3 d)	37,303	35	105	588
Co-60 (5.2 yr)	812	21	2.1	60
Ni-63 (100 yr)	9.1	9.1	–	11.5
Zn-65 (244 d)	18.2	18.2	–	410
Y-88 (106.6 d)	5138	–	–	–
Zr-88 (83.4 d)	4130	–	–	–

equivalent dose coefficient h_T and for the effective dose coefficient h_E , based upon the weighting factors of the ICRP60 [25], are given in SI units. The coefficients are for air at a density of 1.2 kg m^{-3} .

Both coefficients are expressed in Sv/Bq s m^{-3} . Note that h_E does not include the skin contribution and, 0.01 being the weighting factor for the skin, to obtain the real effective dose coefficient one must consider $h_{\text{tot}} = h_E + 0.01 h_{\text{skin}}$. To estimate the effective dose per unit time-integrated for external exposure received by the worker, it is necessary to multiply the activity by h_{tot} .

In order to estimate the total effective dose per intervention, the equation

$$\frac{dD}{dt} = A(t_{\text{int}}, t_{\text{cool}})h_{\text{tot}}e^{-\lambda t} \quad (8)$$

must be integrated over the intervention time. The effective dose for external exposure received by a person intervening in the accelerator tunnel for t_{int} after a cooling time t_{cool} is

$$D(t_{\text{int}}) = \frac{A(t_{\text{int}}, t_{\text{cool}})h_{\text{tot}}(1 - e^{-\lambda t_{\text{int}}})}{\lambda} \quad (9)$$

Table 13

Specific activity of the most important radionuclides contributing to residual radioactivity in the main components of the PIMS section of the accelerator.

Radionuclide ($t_{1/2}$)	Specific activity (Bq/g)			
	Vacuum chamber	EMQ	Wall of the tank	Copper structures
H-3 (12 yr)	19,210	240	–	–
Ca-45 (163 d)	3070	–	–	–
Sc-46 (83.8 d)	24,920	–	–	–
V-49 (330 d)	364,980	2280	–	–
Cr-51 (27.7 d)	386,930	3640	–	–
Mn-54 (312.2 d)	340,280	11,630	11.4	174
Fe-55 (2.7 yr)	708,010	22,930	19.2	333.6
Co-56 (78.76 d)	192,100	4050	12	282
Co-57 (271.3 d)	197,850	500	69.6	1032
Co-58 (70.78 d)	26,780	400	103	1004.4
Co-60 (5.2 yr)	820	66	30	120
Ni-63 (100 yr)	–	16	7.2	16.8
Zn-65 (244 d)	–	110	14.4	252
Y-88 (106.6 d)	9550	–	–	–
Zr-88 (83.4 d)	7440	–	–	–

The values of effective doses for external exposure obtained for the three scenarios (50, 100 and 160 MeV proton energy), with two irradiation times (1 d and 1 week) and three waiting times (0, 10 min and 1 hour), are given in Table 16. Only the nuclei that give a relevant contribution to the dose are listed.

The effective doses from external exposure are much higher than the inhalation doses. Nevertheless, the total dose received by a worker intervening in the tunnel is small for all energies. The dose does not change much with increasing energy, because the number of lost proton correspondingly decreases and because of the limited contribution of spallation products to the gas activation in this range of energies.

7. Conclusions

This paper has discussed the radiation protection studies for the new CERN 160 MeV injector linac presently under construction. Monte Carlo simulations proved to be the appropriate method to evaluate the propagation of neutrons through the waveguide, ventilation and cable ducts placed along the accel-

1 **Table 14**

3 Specific activity of the most important radionuclides contributing to residual
 5 radioactivity in the main components of the CCDTL section of the accelerator
 7 (equipped with PMQs).

Radionuclide ($t_{1/2}$)	Specific activity (Bq/g)			
	Vacuum chamber	PMQ ^a	Wall of the tank	Drift tube
Na-22 (2.6 yr)	3038	224	–	–
Sc-46 (83.8 d)	15967	–	30.1	–
V-48 (16 d)	52290	–	109.2	–
V-49 (330 d)	418726	–	889	–
Cr-51 (27.7 d)	592144	–	1750	–
Mn-54 (312.2 d)	713741	224	2233	4.9
Fe-55 (2.7 yr)	1601964	385	5201	12.6
Co-56 (78.76 d)	549850	93.8	1645	7
Co-57 (271.3 d)	407099	457.8	847	76.3
Co-58 (70.78 d)	51492	1281	238	118.3
Fe-59 (45 d)	–	90.3	–	–
Co-60 (5.2 yr)	1113	89.6	4.2	14.7
Ni-63 (100 yr)	–	–	–	3.5
Zn-65 (244 d)	–	–	–	123.9
Y-88 (106.6 d)	7084	–	–	–
Zr-88 (83.4 d)	5761	–	–	–
Sm-145 (340 d)	–	88.2	–	–
Eu-149 (93.1 d)	–	30.8	–	–

25 ^a This PMQ has been modeled as a cylinder with 30% magnetic material
 27 (samarium–cobalt alloy) and 70% aluminum holder (2024-T351 aluminum alloy).

29 **Table 15**

31 Dose received from internal exposure by a worker intervening in the Linac4 tunnel.

$t_{\text{irr.}}$	1 d	1 d	1 d	1 week	1 week	1 week
$t_{\text{cool.}}$	0	10 min	1 h	0	10 min	1 h
Inhalation dose (μSv), $\text{Ep} = 50 \text{ MeV}$, intervention time = 1 h, 10 W total proton beam loss in the tunnel						
¹¹ C	0.06	0.04	–	0.06	0.04	–
⁷ Be	–	–	–	0.04	0.04	0.04
³² P	0.01	0.01	0.01	0.06	0.06	0.06
³³ P	–	–	–	0.01	0.01	0.01
Total dose	0.09	0.07	0.03	0.19	0.17	0.13
Inhalation dose (μSv), $\text{Ep} = 100 \text{ MeV}$, intervention time = 1 h, 10 W total proton beam loss in the tunnel						
¹¹ C	0.03	0.02	–	0.03	0.02	–
⁷ Be	–	–	–	0.02	0.02	0.02
³² P	0.01	0.01	0.01	0.04	0.04	0.04
³³ P	–	–	–	0.01	0.01	0.01
Total dose	0.04	0.04	0.02	0.10	0.09	0.08
Inhalation dose (μSv), $\text{Ep} = 160 \text{ MeV}$, intervention time = 1 h, 10 W total proton beam loss in the tunnel						
¹¹ C	0.01	0.01	–	0.01	0.01	–
³⁹ Cl	0.01	0.01	–	0.01	0.01	–
⁷ Be	–	–	–	0.01	0.01	0.01
³² P	0.01	0.01	0.01	0.05	0.05	0.05
³³ P	–	–	–	0.01	0.01	0.01
Total dose	0.04	0.04	0.02	0.10	0.10	0.08

53 **Table 16**

55 Effective dose received from external exposure by a worker intervening in the Linac4 tunnel.

$t_{\text{irr.}}$	1 d	1 d	1 d	1 week	1 week	1 week
$t_{\text{cool.}}$	0	10 min	1 h	0	10 min	1 h
External exposure effective dose (μSv), $\text{Ep} = 50 \text{ MeV}$, intervention time = 1 h, 10 W proton beam loss in the tunnel						
¹¹ C	2.92	2.08	0.38	2.92	2.08	0.38
¹³ N	1.24	0.62	0.02	1.24	0.62	0.02
¹⁵ O	0.17	–	–	0.17	–	–
⁴¹ Ar	0.14	0.14	0.10	0.14	0.14	0.10
Total dose	4.50	2.85	0.50	4.50	2.86	0.51
External exposure effective dose (μSv), $\text{Ep} = 100 \text{ MeV}$, intervention time = 1 h, 10 W proton beam loss in the tunnel						
¹¹ C	1.23	0.87	0.16	1.23	0.87	0.16
¹³ N	0.47	0.23	–	0.47	0.23	–
¹⁵ O	0.07	–	–	0.07	–	–

57 erator, as well as in the access area, confirming preliminary estimates made with a simple analytical model. A comparison of the attenuation in ducts and mazes obtained by the “universal” transmission curves of Ref. [13] and by Monte Carlo simulations has shown that under given circumstances the former provides sufficiently accurate results. A detailed comparison between the two methods will be the subject of a forthcoming article. The simulations showed that the final design of the various ducts is adequate from a radiation protection standpoint. Several configurations for the standard waveguide ducts were investigated and in the final layout the ambient dose equivalent rate in the klystron building is expected to be less than 1 $\mu\text{Sv/h}$, the design value. The radiological impact in the low-energy section of the accelerator would raise some concern in the so-called “safe room” only in proximity of the lateral wall where the ambient dose equivalent rate is expected to be between 1 and 10 $\mu\text{Sv/h}$. Increasing the thickness of the lateral wall from 50 to 80 cm provides adequate reduction of the dose rate to a value less than 1 $\mu\text{Sv/h}$.

59 A set of FLUKA simulations, with a detailed geometrical model of the accelerating structures, was also performed to assess the residual dose rates in Linac4 after several years of operation and for various decay times. Two possible layouts for the CCDTL section were compared in terms of induced radioactivity. On the basis of the studies for the residual dose rates, both in contact (with the tank of the DTL or the quadrupoles in the CCDTL and PIMS sections) and at 1 m distance, maintenance interventions on

Table 16 (continued)

t_{irr}	1 d	1 d	1 d	1 week	1 week	1 week
t_{cool}	0	10 min	1 h	0	10 min	1 h
⁴¹ Ar	0.32	0.30	0.22	0.32	0.30	0.22
³⁹ Cl	0.01	0.01	–	0.01	0.01	–
Total dose	2.11	1.43	0.40	2.11	1.44	0.40
External exposure effective dose (μSv), $E_p = 160\text{ MeV}$, intervention time = 1 h, 10W proton beam loss in the tunnel						
¹¹ C	0.71	0.50	0.09	0.71	0.50	0.09
¹³ N	0.41	0.21	–	0.41	0.21	–
¹⁵ O	0.05	–	–	0.05	–	–
⁴¹ Ar	0.51	0.48	0.35	0.51	0.48	0.35
³⁸ Cl	0.02	0.01	–	0.02	0.01	–
³⁹ Cl	0.03	0.02	0.01	0.03	0.02	0.01
Total dose	1.73	1.23	0.47	1.73	1.23	0.47

the DTL are not expected to pose major problems. Interventions on the CCDTL and the PIMS are more critical because the expected dose rates are much higher. A proper planning of the interventions will be required and countermeasures might have to be taken, such as the use of local shields in proximity to the “hot spots” (e.g., the quadrupoles). A sufficient decay time might also be needed before an intervention can be allowed. The replacement of two-thirds of the EMQs with PMQs in CCDTL section would increase the residual dose rate in proximity of the accelerating structure.

Air activation studies were also performed folding the particle track-lengths spectra obtained by Monte Carlo simulations with proper energy-dependent cross-sections. This method was preferred to direct Monte Carlo calculations because of the low interaction probability of hadrons with air, which would have led to very large CPU times. The doses for inhalation and external irradiation received by workers during 1-hour maintenance operation in the tunnel were estimated for different irradiation cycles and waiting times, for 50, 100 and 160 MeV proton beam energy. The doses are higher at 50 MeV because of the higher number of proton lost and because of the limited contribution of spallation products to gas activation in this energy range. The external exposure results to be more important than the internal irradiation by inhalation from the radiological standpoint.

Acknowledgements

The authors wish to thank Yves Cuvet, Alessandra Lombardi, Stephan Maury, Carlo Rossi, Marc Timmins and Maurizio Vretenar of the Linac4 design team, for providing all machine and civil engineering data needed for the present study and for useful discussions.

References

- [1] L. Arnaudon, et al., in: M. Vretenar, F. Gerigk, (Eds.), Linac 4 Technical Design Report, CERN-2006-AB-084, 2006.
- [2] B. Autin, et al., Conceptual design of the SPL, a high power superconducting H^- linac at CERN, CERN Yellow Report 2000-012, 2000.
- [3] F. Gerigk, et al., Conceptual design of the SPL II, CERN Yellow Report 2006-006, 2006.
- [4] M. Silari, H. Vincke, Shielding proposal for the SPL front end, CERN-TIS-2003-002-RP-TN, 2003.
- [5] M. Magistris, M. Silari, Preliminary shielding design of Linac 4, CERN-SC-2005-011-RP-TN, 2005.
- [6] M. Magistris, M. Silari, Preliminary shielding design of Linac 4. Top shielding and induced radioactivity, CERN-SC-2005-050-RP-TN, 2005.
- [7] M. Magistris, E. Mauro, M. Silari, Complementary shielding calculation for Linac 4 in the South Hall, CERN-SC-2006-060-RP-TN, 2006.
- [8] M. Magistris, E. Mauro, M. Silari, Radiation protection considerations for the installation of Linac4 in the existing Linac2 building, CERN-SC-2007-031-RP-TN, 2007.
- [9] M. Magistris, E. Mauro, M. Silari, Radiation protection studies for the front-end of the 3.5 GeV SPL, in: Eight International Topical Meeting on Nuclear Applications and Utilization of Accelerator Conference (AccApp07), Pocatello, Idaho, USA, 30 July–2 August, 2007.
- [10] A. Fasso', A. Ferrari, J. Ranft, P.R. Sala, FLUKA: a multi-particle transport code, CERN-2005-10, 2005, INFN/TC_05/11, SLAC-R-773.
- [11] G. Battistoni, S. Muraro, P.R. Sala, F. Cerutti, A. Ferrari, S. Roesler, A. Fassò, J. Ranft, The FLUKA code: description and benchmarking, in: M. Albrow, R. Raja (Eds.), in: Proceedings of the Hadronic Shower Simulation Workshop 2006, Fermilab 6–8 September 2006, AIP Conference Proceedings, vol. 896, 2007, pp. 31–49.
- [12] Y. Nakane, Y. Sakamoto, K. Hayashi, T. Nakamura, Intercomparison of neutron transmission benchmark analyses for iron and concrete shields in low, intermediate and high energy proton accelerator facilities, in: Proceedings of the Third “Specialists” Meeting on Shielding Aspects of Accelerators, Targets & Irradiation Facilities (SATIF-3), Tohoku University, Sendai, Japan, May 12–13, 1997, published by OECD/NEA, OECD documents, ISBN:92-64-16071-X, 1998, pp. 151–182.
- [13] R.H. Thomas, G.R. Stevenson, Radiological safety aspects of the operation of proton accelerators, Technical Report No. 283, International Atomic Energy Agency, Vienna, 1988.
- [14] S. Agosteo, M. Magistris, A. Mereghetti, M. Silari, Z. Zajacova, Nucl. Instr. and Meth. Phys. Res. B 265 (2) (2007) 581.
- [15] E. Mauro, M. Silari, H. Vincke, Radiological interferences between the SPL tunnel and the existing underground and surface structures, CERN-SC-2007-083-RP-TN, 2007.
- [16] Safety Code F, Radiation Protection, CERN, November 2006.
- [17] C. Theis, K.H. Buchegger, M. Brugger, D. Forkel-Wirth, S. Roesler, H. Vincke, Nucl. Instr. and Meth. A 562 (2006) 827.
- [18] A.M. Lombardi, J.B. Lallement, E. Sargsyan, S. Lanzone, G. Bellodi, M. Eshraqi, B. Hadorn, Loss Control and Steering Strategy for the CERN Linac4, AB-Note-2007-033 ABP, 2007.
- [19] A.M. Lombardi, J.B. Lallement, E. Sargsyan, S. Lanzone, G. Bellodi, M. Eshraqi, B. Hadorn, Loss Management and Alignment Tolerances for the CERN Linac4, in preparation.
- [20] E. Mauro, M. Silari, Residual dose rates and induced radioactivity in the Linac4 tunnel, CERN-SC-2008-069-RP-TN, 2008.
- [21] E. Mauro, M. Silari, Residual dose rates and induced radioactivity in the Linac4 tunnel for an alternative layout of the CCDTL section, CERN-SC-2008-069-RP-TN, 2008.
- [22] M. Huhtinen, Determination of Cross Sections for Assessment of Air Activation at LHC, CERN/TIS-RP/TM/96-29, 1997.
- [23] Swiss Legislation on Radiological Protection (Ordonnance sur la Radio-protection, ORaP) of 22 June 1994 (state 4 April 2000).
- [24] K.F. Eckerman, J.C. Ryman, External exposure to radionuclides in air, water and soil, Federal Guidance Report No. 12, EPA 402-R-93-081, Environmental Protection Agency, Washington, DC, 1993.
- [25] International Commission on Radiological Protection, “1990 Recommendations of the International Commission on Radiological Protection”. ICRP Publication 60, Ann. ICRP 21(1–3) (1991).



Contents lists available at ScienceDirect

Nuclear Instruments and Methods in Physics Research A

journal homepage: www.elsevier.com/locate/nima

Attenuation of neutrons through ducts and labyrinths

Egidio Mauro, Marco Silari *

CERN, 1211 Geneva 23, Switzerland

ARTICLE INFO

Article history:

Received 18 May 2009

Received in revised form

15 June 2009

Accepted 18 June 2009

Keywords:

Proton accelerator

Neutron streaming

Radiation protection

Labyrinth

Duct

ABSTRACT

Monte Carlo simulations have been performed for the attenuation of neutron radiation produced at proton accelerators through ducts and labyrinths of various design, and the results are compared with the predictions made by analytical expressions available in the literature. The results show that the so-called universal transmission curves are an appropriate and simple tool applicable in many situations, when the radiation source is not in direct view of the duct mouth. This is not the case for point sources located in front of the duct. The simulations showed that it is not possible to apply the same models because the transmission factor is strongly dependent on the cross-sectional area of the duct. A universal expression has been derived to estimate the neutron transmission through a straight duct of length d and cross-sectional area A in direct view of the source, which only depends on A and on a small set of numerical coefficients.

© 2009 Published by Elsevier B.V.

1. Introduction

Accelerator shielding is not limited to the calculation of barriers, but includes assessment of groundshine, skyshine and roof shielding as well as design of ducts and mazes (labyrinths) penetrating the shielding walls. Ducts and labyrinths serve as access path for control and power cables, ventilation pipes, waveguides for RF power, cooling and cryogenic lines as well as for personnel and equipment access. At the same time they also represent a leakage path for radiation, especially neutrons, and must be properly designed in order not to compromise the shielding effectiveness of the barriers. This paper discusses the attenuation of neutrons and the dominant secondary radiation at proton accelerators. Ducts and mazes can be very large: an example of an extreme case is represented by the access shafts leading to the underground areas of Large Hadron Collider (LHC) of CERN, which are up to 20 m in diameter and more than 100 m in depth. Monte Carlo simulations are the best tool for calculating radiation streaming through ducts and labyrinths. However, the design of labyrinths with right-angle bends (curved tunnels are less common and are not addressed in this paper) can often be performed to a sufficient level of accuracy by simple analytical expressions or so-called universal transmission curves. Nonetheless, whereas the simple models available in the literature often provide sufficiently accurate results for cases in which the radiation source is not in direct view of the duct mouth, this is not the case for point sources located in front of the mouth. This paper

compares results from Monte Carlo simulations and from analytical expressions available in the literature for a number of practical cases. The aim is to confirm the suitability of the simple models for plane sources and point sources off-axis, and to propose a better expression for estimating the attenuation for neutrons sources located in direct view of the duct mouth.

2. Analytical models

Universal transmission curves (Figs. 1 and 2) are the so-called depth in a duct or in a maze leg d , is normalized to its cross-sectional area A , and thus expressed as a function of $d/A^{1/2}$. They were obtained in the 1970s with the aim to evaluate the dose rates due to neutron leakage through the access tunnels of the CERN Super Proton Synchrotron (SPS) and other similar access ways to the experimental areas [1,2]. The tunnel penetration was estimated using the codes SAM-CE [3], AMC [4] and ZEUS [5] and experimental data were used both to check the results of the computations and for extrapolating directly to tunnels of roughly similar dimensions.

A parametric form of the transmission curves has later been derived by Stevenson and Fassò [6] for the case of an off-axis source to facilitate pocket-calculator estimations. The transmission T in the first and the second leg is given by

$$T = 1/(1 + 2.5D^{0.17}D^{1.7} + 0.79D^3) \quad (1)$$

and

$$T = 1/[1 + 2.8D(1.57)^{d+2}] \quad (2)$$

where $D = d/A^{1/2}$.

* Corresponding author. Tel.: +41 22 7673937.

E-mail address: marco.silari@cern.ch (M. Silari).

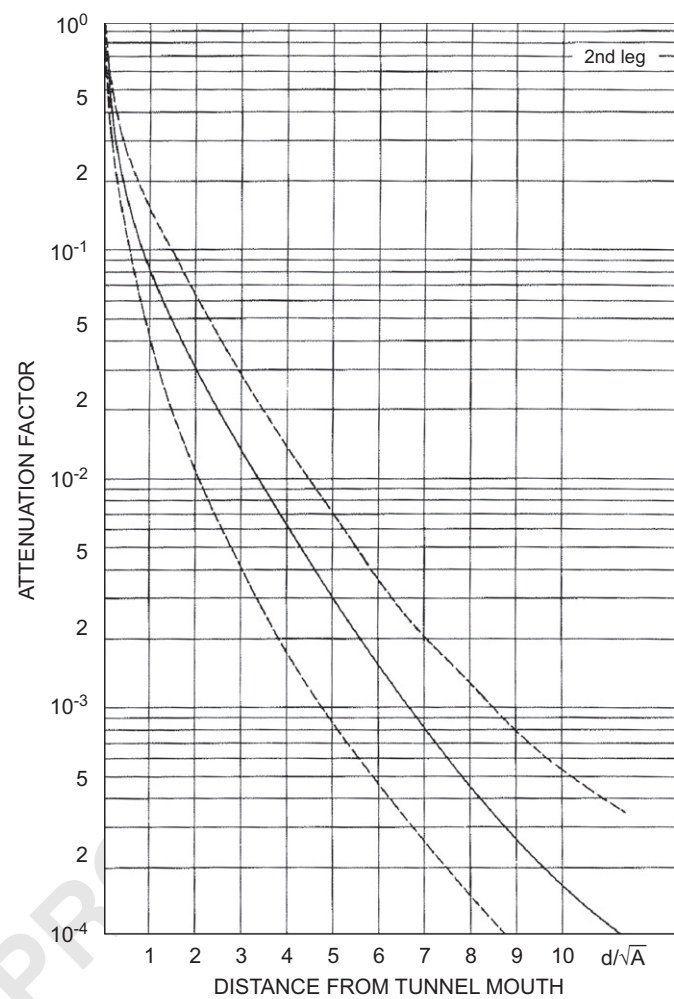
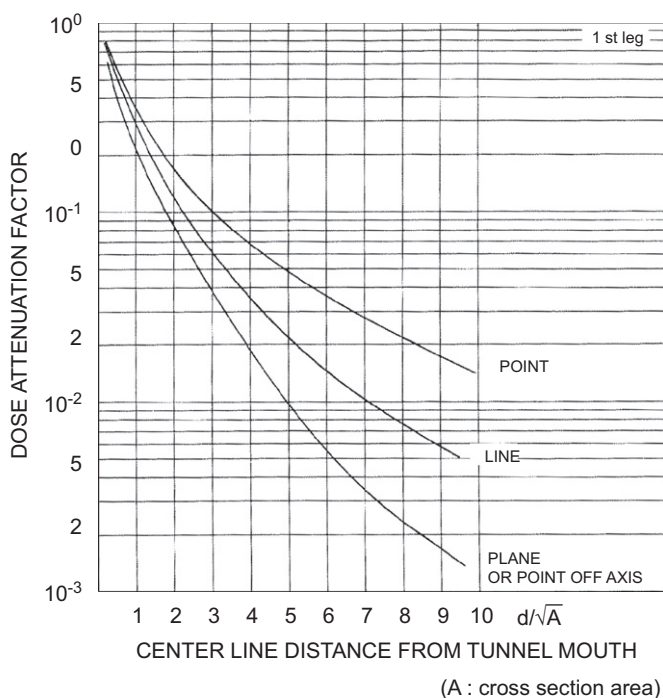


Fig. 1. Universal transmission curves for the first leg of a labyrinth (from Ref. [1]).

Tesch [7] has developed a very simple approach to the problem of dose equivalent rate attenuation by multi-legged labyrinths at proton accelerators that are typical of personnel passage ways of approximately 2 m^2 cross-section. Based on the experimental data for the transmission of Am-Be neutrons in concrete lined labyrinths, and on the similarity between the neutron spectra in the second leg of a labyrinth from either an Am-Be source and from high-energy protons stopped in a target, he proposed an empirical formula for describing the transmission of the dose equivalent. The equation for the first leg (as presented in Ref. [8]) is an inverse-square law, modified by a simple in-scattering factor of two, in the section of the labyrinth in direct view of the source

$$H(r_1) = 2H_0(a)a^2r_1^{-2} \quad (3)$$

where $H(r_1)$ is the dose equivalent, in the first leg, at a distance r_1 from the source, a is the distance from the source to the mouth of the first leg and $H_0(a)$ is the dose equivalent at the mouth of the first leg. This formula does not accommodate the expected scaling with the square root of the tunnel aperture and is best used for labyrinths with relatively large cross-sectional areas (about 2 m^2) used for personnel access. The expression for the succeeding legs is the sum of two exponentials:

$$H(r_i) = \frac{e^{-r_i/0.45} + 0.022A_i^{1.3}e^{-r_i/2.35}}{1 + 0.022A_i^{1.3}} H_0 \quad (4)$$

where r_i is the distance into the i th leg in meters, H_0 is the dose equivalent at the entrance of the i th leg and A_i is the cross-sectional area of the maze in m^2 .

NCRP Report 51 [9] provides guidelines for designing ducts and labyrinths for proton accelerators of energies below 100 MeV, using an empirical and conservative approach based on the work of Maerker and Muckenthaler [10,11] built on the use of the albedo concept, where the reflecting properties of the concrete are determined in great detail. In practice, for a multi-legged maze, it is assumed that beyond the second leg all neutrons at the entrance of the duct have thermal energies. Transmission factors are given for thermal neutrons through a straight duct and for

two- and three-legged ducts from which one can calculate the dose equivalent at the exit once the neutron fluence rate incident on the inner aperture of the maze is known.

Gollon and Awschalom [12] have reported a number of Monte Carlo calculations of the attenuation of the neutron fluence in labyrinths using the albedo program ZEUS [5]. In this program monoenergetic neutrons (3 or 4 MeV) were scattered at random angles from the walls of "typical" labyrinths using the albedo parameters of Maerker and Muckenthaler [10,13]. The calculations were used for a three-legged labyrinth and the calculated labyrinth attenuation resulted to be insensitive to the neutron energy.

Cossairt et al. [14] made measurements at the Tevatron at Fermilab in a four-legged labyrinth. The labyrinth gave access to the accelerator tunnel in which 400 GeV protons struck an aluminium target located in front of the mouth of the first leg, which was perpendicular to the beam direction. In Ref. [15], the experimental measurement of Ref. [14] were compared with calculations based on the work of Goebel et al. [1], Gollon and Awschalom [12] and Tesch [7]. The calculated transmission curves are in fair agreement with the measured data. Neutron spectral measurements also showed that the spectrum in the second leg of the labyrinth is dominated by thermal neutrons.

Tanaka et al. [16] carried out a radiation streaming experiment at the Takasaki Ion Accelerator Facility for Advanced Radiation

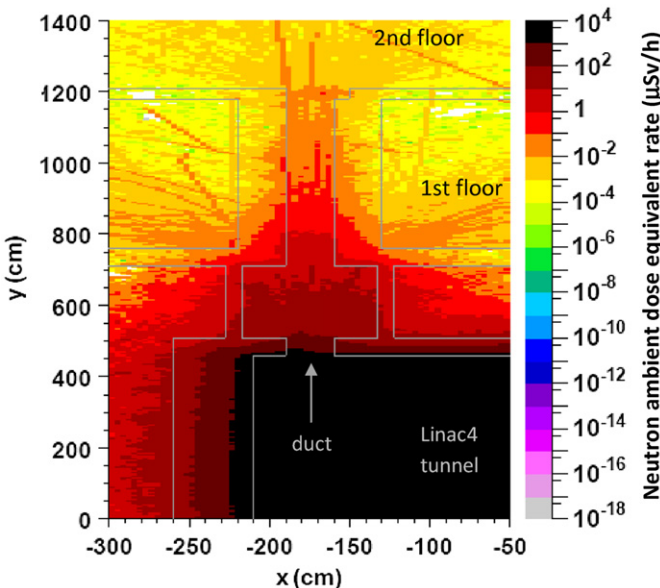


Fig. 3. Neutron streaming through the low-energy waveguide duct (see Table 1) calculated with FLUKA.

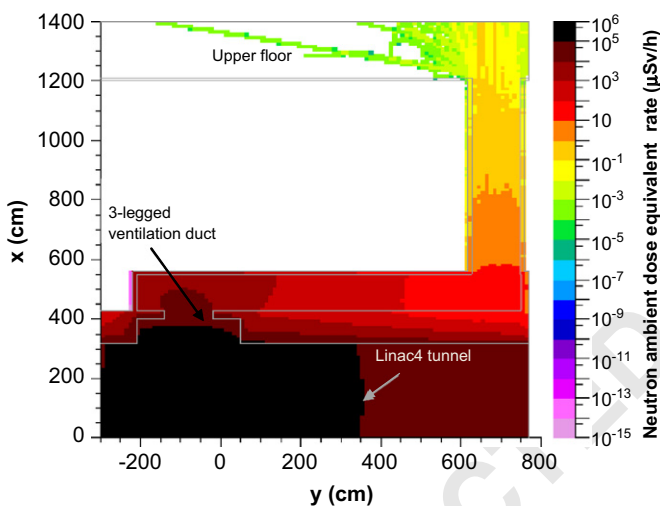


Fig. 4. Neutron streaming through the ventilation ducts (see Table 2) calculated with FLUKA.

Application at the Japan Atomic Energy Research Institute using a neutron source produced by a copper target irradiated with protons of 68 MeV energy. The access way consisted of a three-legged labyrinth. The neutron dose equivalent rates inside the labyrinth were measured with Bonner Spheres and rem counters. The experimental data were compared with the results obtained with Tesch's (Eqs. (3) and (4)) and Nakamura and Uwamino's formulae [17,18]. The latter formula assumes that the attenuation in the labyrinth obeys a simple $1/r^2$ law. They found that in general both formulae are applicable to estimate the neutron dose equivalent due to neutron streaming through the labyrinth.

A good summary of calculations and measurements of the transmission of neutrons through ducts and labyrinths at higher energy accelerator can be found in Refs. [2,8]. According to several experiments, most of the dose equivalent transmission is due to 1–20 MeV source neutrons. If the tunnel is to be designed from known or expected beam losses, instead of a defined dose equivalent rate at the tunnel entrance, one has to determine the neutron yield in the 1–20 MeV range from the effective source.

This yield may then be converted to dose equivalent using appropriate conversion coefficients. When a point source is in full view of the back end of the duct, a simple inverse-square law can be used to determine the neutron fluence at the duct exit. An appropriate coefficient to convert the apparent neutron fluence to dose equivalent is 20 fSv m^2 [2]. It should nonetheless be stressed that the $1/r^2$ law for the attenuation of neutrons from a point source in front of a duct is only approximately true. How close it is actually followed also depends on the scattering material around the source (the beam loss point), e.g. the presence of nearby or back walls, and on the cross-sectional area of the duct, as it will be shown below.

The geometric and angular distribution of the neutrons source and its position with respect to the maze mouth considerably affect the attenuation factor provided by the first leg of the maze. However, after the first bend the neutrons essentially lose "memory" of their original spectrum. For the second and subsequent legs of a labyrinth, the position of the source (plane or point off-axis, linear or point on-axis) is no longer relevant. This reflects into a single universal curve (Fig. 2). The energy of the proton beam causing the neutron emission is also not much relevant when considering the attenuation provided by the second and subsequent legs of the maze, especially for emission at 90° .

The latest generation of Monte Carlo codes allows fast and accurate calculation of particle transport and interaction with matter. In this paper the reliability of the analytical or semi-empirical curves of Goebel et al. [1,2] and Tesch [7] was tested through comparisons with simulations made with the latest version (2006.3b, March 2007) of the particle transport code FLUKA [19,20]. The accuracy of this code for radiation protection applications and in particular for shielding design has been demonstrated through several benchmarks (see, for examples, Refs. [20,21]).

3. Comparison of Monte Carlo simulations with the universal curves

The recent radiation protection studies performed for the new CERN injector presently under construction, a 160 MeV proton linac called Linac4 [22], required designing various types of penetrations for RF waveguides, cables and ventilation pipes. The linac will be installed in an underground tunnel whereas klystron and other services will be housed in a surface building on top of the linac. The accelerator is at sufficient depth that assessment of bulk shielding was straightforward, whilst neutrons streaming through various apertures in the shielding represented one of the major radiological issues to be tackled. These penetrations were partly designed by Monte Carlo simulations with the FLUKA code [19,20] and partly with the universal curves of Refs. [1,2]. These studies were subsequently extended and employed for a detailed comparison of the attenuation provided by these curves and the Monte Carlo predictions, for point and plane or point off-axis sources, which is the aim of this paper.

3.1. Plane or point off-axis source

Three configurations were investigated: a single, straight duct made of four sections of variable sizes and shapes (rectangular and circular), and two types of three-legged labyrinths. The duct geometries as implemented in the FLUKA simulations are shown in Figs. 3–5 taken from Ref. [22] and are described in Tables 1–3. The first configuration (Figs. 3 and 6 and Table 1), which we call low-energy waveguide duct, is for housing the 3 MeV waveguides for the Radio Frequency Quadrupole (RFQ): the neutron source

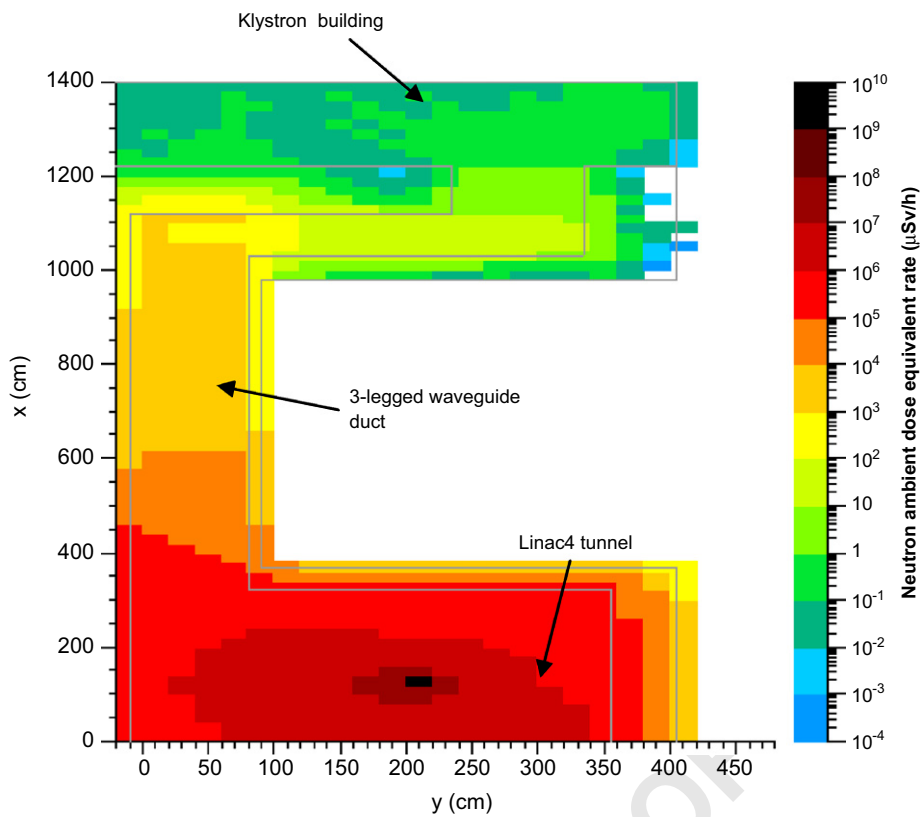


Fig. 5. Neutron streaming through the high-energy waveguide ducts (see Table 3) calculated with FLUKA.

Table 1
Layout of the low-energy waveguide ducts.

Section of the duct	Length
Rectangular (30 cm × 70 cm)	0–50 cm
Cylindrical with diameter of 85 cm	50–250 cm
Rectangular (30 cm × 70 cm)	250–720 cm
Rectangular (40 cm × 70 cm)	720–750 cm

Table 2
Layout of the ventilation duct.

Section	Length
First leg (vertical)	Circular with diameter of 125 cm
Second leg (horizontal)	Squared with a side of 120 cm
Third leg (vertical)	Circular with diameter of 125 cm

Table 3
Layout of the high-energy waveguide ducts.

Section (cm ²)	Length (cm)
First leg (vertical)	90 × 90
Second leg (horizontal)	90 × 90
Third leg (vertical)	100 × 90

was generated by a 11 MeV proton beam lost on a 5 × 5 × 5 cm³ copper block placed 2.65 m downstream of the mouth of the duct and 3.8 m off-axis. The second configuration (Figs. 4 and 7 and Table 2) is a labyrinth housing the ventilation duct at the high-

energy end of the linac. Here neutrons were produced by a 160 MeV proton beam lost on a 5 × 5 × 5 cm³ copper block placed 5.35 m upstream of the mouth of the maze and 80 cm off-axis. The third configuration (Fig. 5 and Table 3, see also Ref. [22]) is a maze for housing the waveguides at the high-energy end of the linac. The neutron source was generated by 160 MeV protons lost on a 5 × 5 × 5 cm³ copper block placed at the same longitudinal distance in the tunnel as the maze mouth, but 1.8 m off-axis. Important biasing techniques were used to improve the transport of neutrons through the three legs of the labyrinths and to kill those crossing the bulk shield in order to save computing time (see Ref. [22] for more details).

Figs. 3–5 plot the neutron transport through the ducts and labyrinths as simulated by FLUKA. The value of the neutron ambient dose equivalent rate from the FLUKA simulations at the mouth of the ducts was used as a source value for estimating the attenuation provided by the duct and labyrinths via the universal transmission curves of Goebel et al. (Figs. 1 and 2). The transmission curve for the first leg of a labyrinth for a plane (or point off-axis) source was used for the four sections of the low-energy waveguide duct. Fig. 8 compares the transmission calculated with the universal curves and the FLUKA simulations as a function of the total normalized distance in the duct. For the three-legged configurations, the transmission curves for the first (plane source model) and the subsequent legs were used. The comparison between universal curves and Monte Carlo simulations is shown in Figs. 9 and 10. In all cases, the agreement between simple model and Monte Carlo simulations is rather good.

The same universal curves are also appropriate for much larger ducts. An example is the attenuation of neutrons generated by high-energy electrons and positrons by one of the access shafts of the former CERN Large Electron Positron Collider (LEP). Fig. 11 from Ref. [23] shows the attenuation of neutron radiation in the

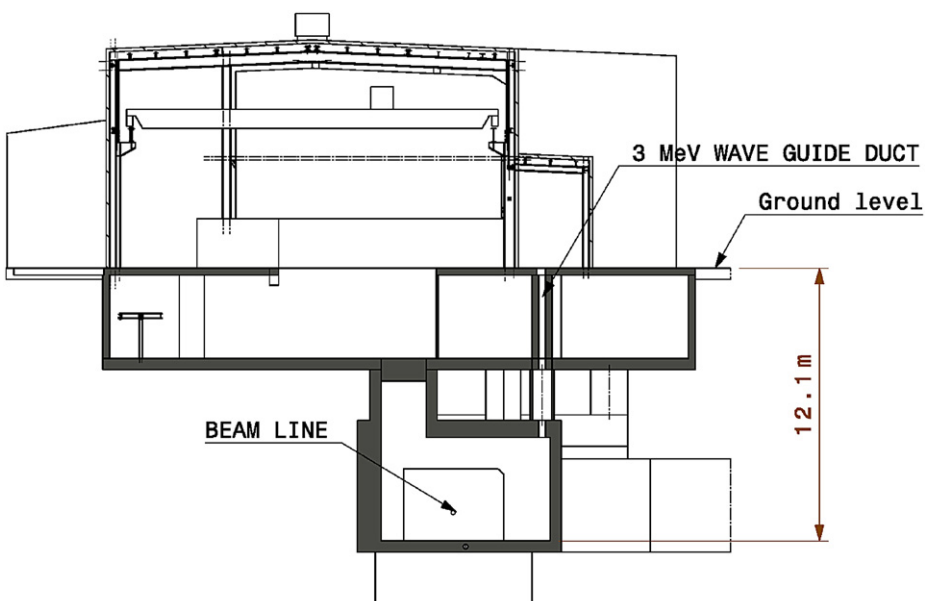


Fig. 6. Cross-sectional view of the low-energy end of the Linac4 tunnel, the 3 MeV waveguide duct and the two upper floors (looking downstream in the tunnel). Note that this view is a reversed view with respect to Fig. 3, as it looks downstream in the tunnel whereas Fig. 3 looks upstream.

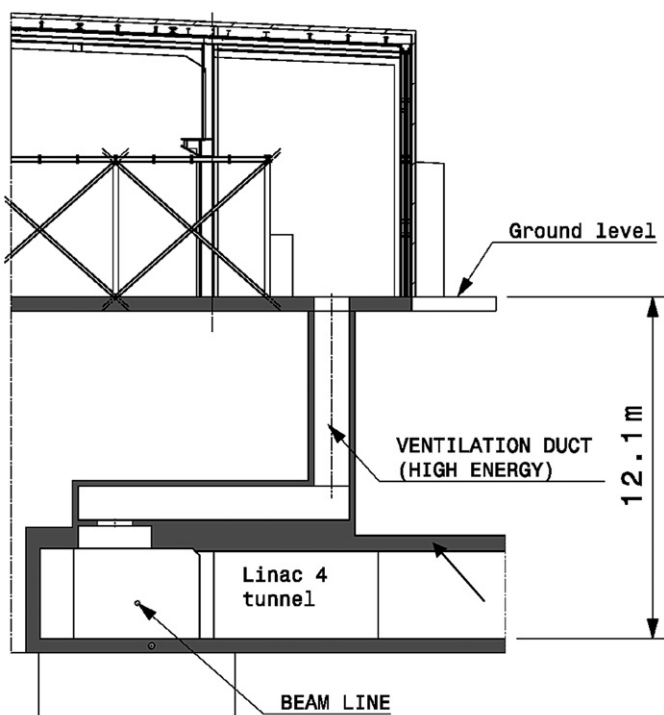


Fig. 7. Cross-sectional view of the Linac4 tunnel, the three-legged ventilation duct and the ventilation building on top.

PM18 shaft (80 m deep and 14 m in diameter, max $d/A^{1/2}$ 6.5) determined experimentally at three LEP energies (94.5, 100 and 103 GeV). PM18 was located on top of the positron injection region, where neutrons were produced by beam losses on the injection components. The dose attenuation measurements were performed with bubble detectors (model BD PND from Bubble Technology Industries, Chalk River, Ontario, Canada) suspended on the shaft axis from the surface all the way down to the bottom. The experimental values are compared with the transmission curves for a neutron plane source and a neutron line

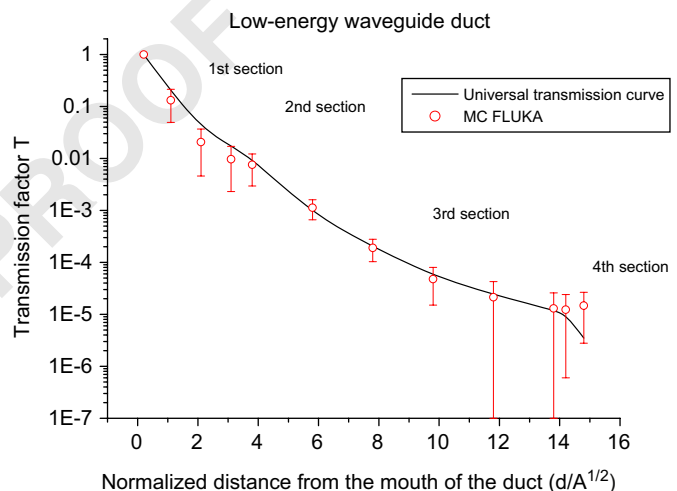


Fig. 8. Transmission of neutrons through a straight duct made of four sections of variable sizes, calculated with the universal transmission curve of Refs. [1,2] and by Monte Carlo simulations (see Table 1 and Fig. (1)). The slightly lower statistical uncertainty associated with the last two values as compared to the previous ones at large depth in the duct could be due to a biasing artifact.

source. The latter better seems to fit the experimental data, which is coherent with the beam loss scheme. The beam losses at injection remained constant over the years as shown by the relative similarity of the data points at the three energies.

3.2. Point source

A point source on-axis, i.e. a localized beam loss in direct view of the duct aperture, represents a worst case and, although it may be less of a common situation than the previous case, it must also be considered. The results of Monte Carlo simulations of the propagation of neutrons through a long duct were compared with predictions made by the model of Tesch [7] and Goebel et al. [1,2].

First, the dependence of the transmission factor on the shape of the cross-sectional area of the duct and on the energy of the protons impinging on the neutron production target was inves-

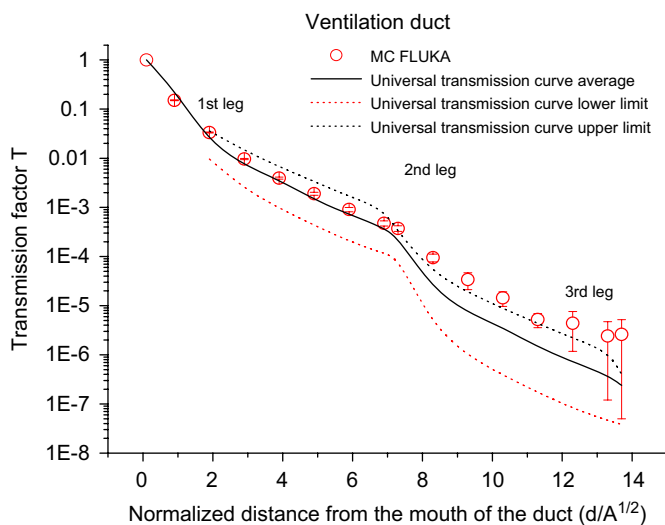


Fig. 9. Transmission of neutrons through a three-legged labyrinth (Table 2 and Fig. 2) calculated with the universal transmission curve of Refs. [1,2] and by Monte Carlo simulations. The dotted lines for the second and third leg indicate appropriate confidence limits as explained in Refs. [1,2].

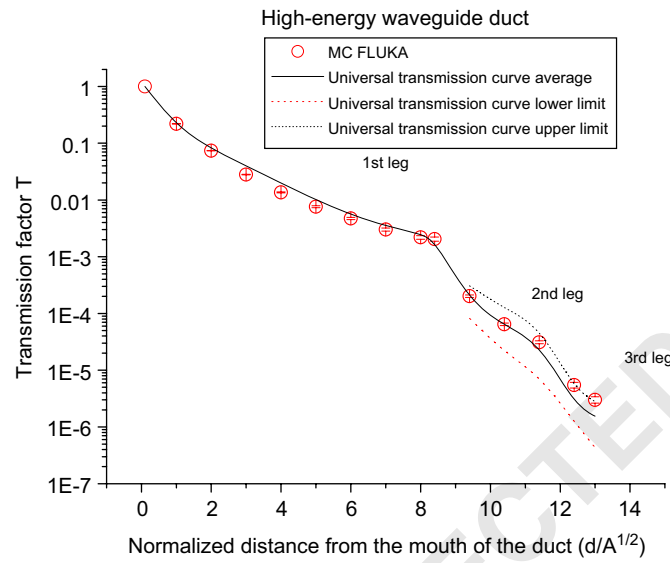


Fig. 10. Transmission of neutrons through a three-legged labyrinth (Table 3 and Fig. 3) calculated with the universal transmission curve of Refs. [1,2] and by Monte Carlo simulations. The dotted lines for the second and third leg indicate appropriate confidence limits, as explained in Refs. [1,2].

tigated. For the former study, a 160 MeV proton beam hit a cylindrical copper target (5 cm long and 5 cm in radius) placed at 2 m distance from the duct with the beam direction perpendicular to the duct. For the same cross-sectional area (1 m^2) a circular and a squared aperture were considered, scoring the ambient dose equivalent rate along the duct. The transmission factor as a function of the normalized distance inside the duct is plotted in Fig. 12. There is no appreciable difference between the two curves. The present result is in agreement with older calculations made, with a different code, by Gollon and Awschalom [12], who estimated the attenuation of the neutron fluence by straight ducts with the same cross-sectional area and different height-to-width ratio.

Keeping constant the shape of the duct, Monte Carlo simulations were then performed at three proton energies (50, 160 and 300 MeV). The proton beam hit a cylindrical copper target (5 cm in

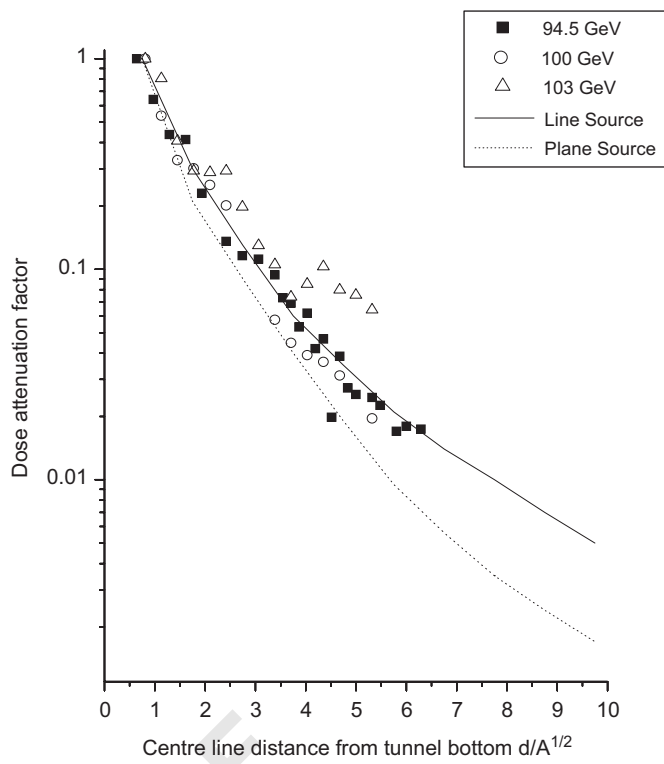


Fig. 11. Attenuation of neutron radiation in the access shaft PM18 (14 m in diameter and 80 m in depth) of the CERN Large Electron Positron collider (LEP) measured at three electron beam energies (94.5, 100 and 103 GeV per beam); d is the distance from the bottom end of the pit and A is the cross-sectional area of the pit. The uncertainty on the measurements is $\pm 30\%$. The attenuation for a neutron plane source and a neutron line source is shown for comparison (from Ref. [23]).

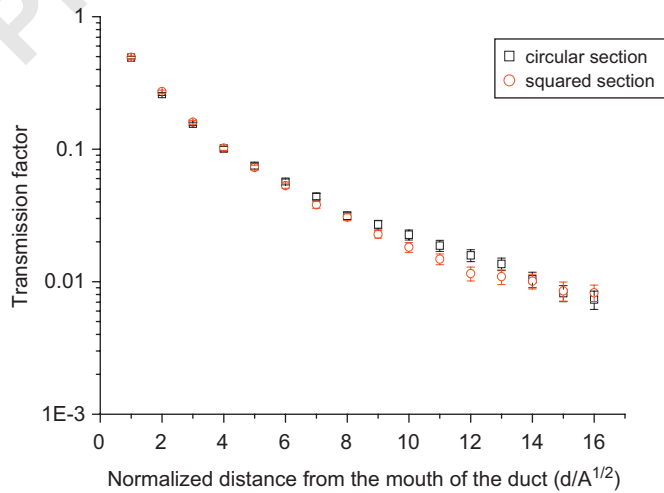


Fig. 12. Neutron transmission factor as a function of normalized distance in ducts with the same cross-sectional area and different shapes.

radius, 5 cm long for 50 and 160 MeV, 10 cm long for 300 MeV) placed at 2 m distance from the mouth of the duct. Fig. 13 shows the transmission factor as a function of the normalized distance inside the duct for the three proton energies. Again the curves show no appreciable difference, confirming that the energy of the proton beam has no major influence on the attenuation of the secondary neutrons in the duct, as mentioned above.

Finally, FLUKA simulations were performed to estimate the attenuation of the ambient dose equivalent rate inside circular ducts of different sizes (Table 4), representative of typical

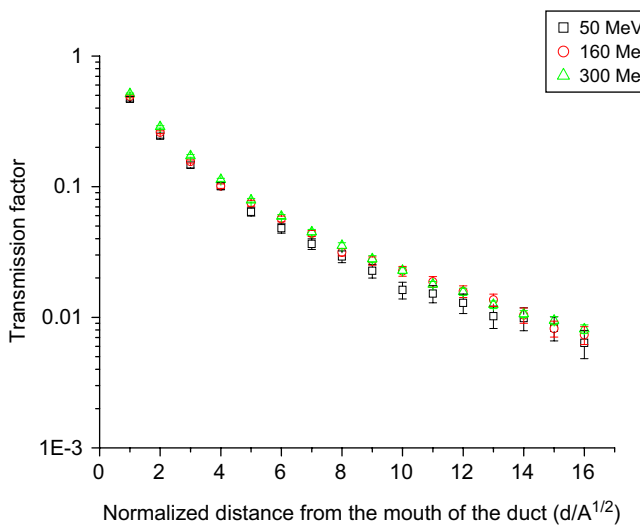


Fig. 13. Attenuation by a straight duct of neutrons produced by proton beams of different energies.

Table 4

Typical cross-sectional area for circular ducts and mazes according to their use.

Cross-section (m ²)	$A^{1/2}$ (m)	Diameter (cm)	Use
0.07	0.26	30	Cables, cooling, cryogenics
0.28	0.53	60	RF waveguides, cooling, cryogenics
1	1.0	110	RF waveguides, ventilation
4	2.0	225	Access of personnel and services
9	3.0	340	Access of personnel and equipment

situations found in radiation protection. A localized loss was assumed in front of the mouth of the duct. The comparison among transmission factors for the five ducts as predicted by the FLUKA simulations, evaluated by the universal curves for a point source of Ref. [2], by the inverse-square law and by the equation proposed by Tesch [7] is shown in Fig. 14.

The results of Fig. 14 clearly show that it is not possible to define a generic transmission curve for the point source case. The inverse-square law completely fails for ducts of small cross-sectional area, is approximately correct for the 1 m² case up to a depth of about 7 d/A^{1/2}, and underestimates at low d/A^{1/2} and overestimates at larger depths for ducts of larger cross-sectional areas. This is possibly because this law does not take into account the varying contributions of the scattered neutrons along the duct. With increasing distance, this scattering contribution first increases and then decreases because of the absorption in air. The equation proposed by Tesch [7] overestimates the contribution to the ambient dose equivalent from scattered neutrons. In fact, Tesch's equation seems to be applicable only far inside the duct and is totally inconsistent at the mouth.

The five transmission curves obtained from the Monte Carlo simulations can be fitted by

$$T = (kA^{1/2})(d/A^{1/2})^{-2hA^{1/2}} \quad (5)$$

where $A^{1/2}$ is in meters and the exponential quantifies the deviation from the inverse-square law. The parameters k and h are given in Table 5 for the five curves of Fig. 14. Since the dependence of k and h on $A^{1/2}$ is rather regular (both parameters decreasing with increasing $A^{1/2}$), it can be represented by the fits shown in Figs. 15 and 16:

$$k = k_1 A^{-k_2/2} \quad (6a)$$

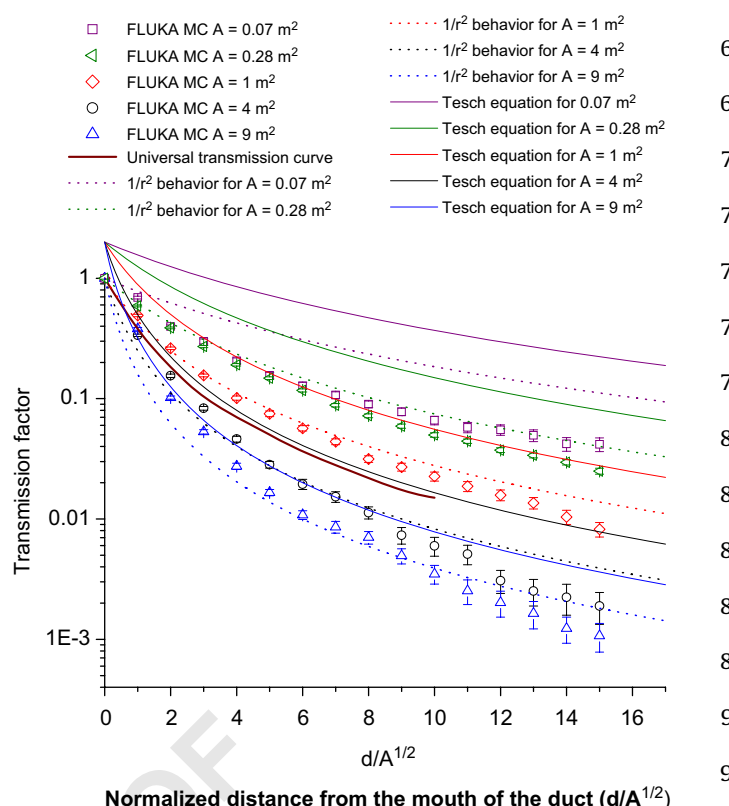


Fig. 14. Transmission of neutrons through a single duct for a point source on-axis, calculated with the universal transmission curves of Refs. [1,2], the Tesch equation (Eq. (3)), the inverse-square law and by FLUKA Monte Carlo simulations for five different cross sections.

Table 5

Fit parameters k and h calculated for five cross-sections of the duct.

	$A^{1/2}$ (m)				
	0.26	0.53	1.0	2.0	3.0
k (m ⁻¹)	4.18	1.70	0.76	0.39	0.17
h (m ⁻¹)	2.38	1.18	0.78	0.56	0.36

$$h = h_1 A^{-h_2/2} \quad (6b)$$

with k_1 , k_2 , h_1 , h_2 given in Table 6. The neutron transmission through a straight duct of length d and cross-sectional area A in direct view of the source can thus be estimated from expression 5, with the parameters k and h calculated by expressions (6) and Table 6, for any given cross-sectional area A .

4. Discussion

Expression (5) can be used directly with the parameters of Table 5 for straight ducts with dimensions as given in Table 4, or together with the parameters given by expressions (6) and Table 6 for ducts of intermediate size. A penetration in a shield is usually orthogonal to the circulating beam direction (as e.g. for both linear and circular accelerators installed in a tunnel), and thus the neutron component generated by the beam loss and streaming through the duct is mainly the evaporation component rather than the direct neutron component. Therefore expression (5) is expected to be valid over a wide range of energies, and is applicable at both low (MeV), intermediate (tens or hundreds of MeV) and high-energy (GeV) particle accelerator facilities.

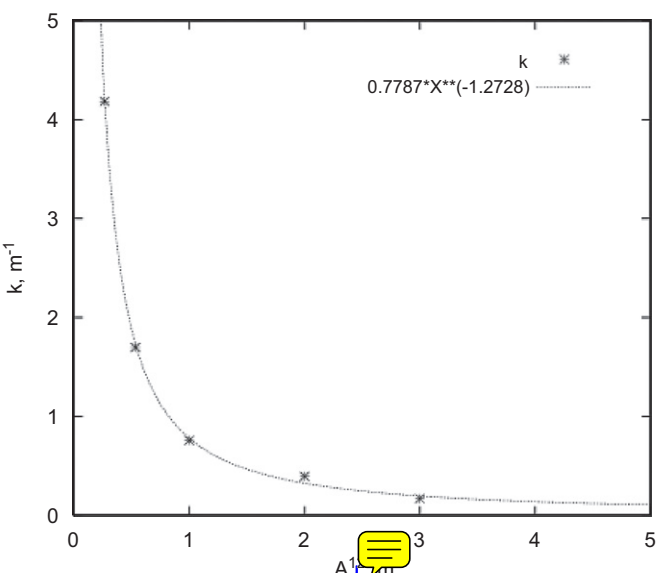


Fig. 15. Fit parameter k as a function of $A^{1/2}$ fitted through the equation $y = 0.7787x^{-1.2728}$.

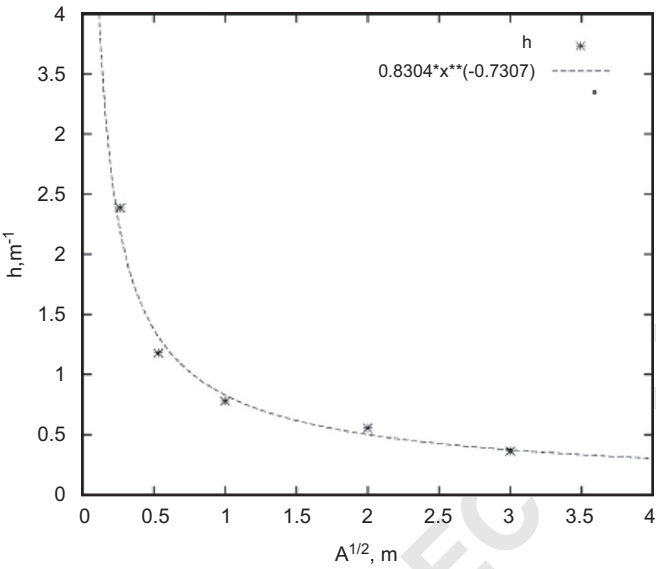


Fig. 16. Fit parameter h as a function of $A^{1/2}$ fitted through the equation $y = 0.8304x^{-0.7307}$.

Table 6
Fit parameters k_1 , k_2 , h_1 , h_2 to be used in Eqs. (7a and b).

k_1	k_2	h_1	h_2
1.7787	1.2728	0.8304	0.7307

It may be redundant but still worth stressing that neutron attenuation data *cannot* be used to estimate the attenuation of electromagnetic radiation. A duct or a labyrinth is much more effective in attenuating photon radiation than neutrons. As an example, measurements of the attenuation by the LEP PM18 shaft of photons produced by electrons/positrons beams with energy varying from 45 to 103 GeV have shown that the same duct in orders of magnitude is more effective to attenuate photons than neutrons (see Fig. 12 of Ref. [23]). The measurements also indicated a constant reduction in the photon attenuation factor

(in other words, a constant increase in the transmission of radiation) with increasing electron beam energy, i.e. with increasingly harder photon spectra. As discussed above, this dependence on the original spectrum is much less pronounced with neutrons, in particular for the second and subsequent legs.

Although the present study has focused on the transmission of neutrons produced by proton accelerators, we have seen that the information on the original energy distribution is lost rather rapidly during the propagation in the first leg – because of scattering and attenuation – and is no longer relevant from the second leg onwards. Therefore, it can reasonably be expected that these same attenuation data are equally applicable to neutrons produced at electron accelerators (where a large fraction of the neutrons are expected from the giant dipole resonance in the few MeV region), certainly for the second and subsequent legs, and most likely also in the first leg (as shown in Fig. 11), or at least after a sufficient depth.

5. Conclusions

This paper has discussed Monte Carlo simulations performed to test the reliability of the analytical models commonly used to estimate the attenuation of the neutron ambient dose equivalent through ducts and labyrinths at particle accelerators. Separate simulations were run for a plane or point off-axis source and a point source on-axis. For the former case, the FLUKA simulations have confirmed that the universal transmission curves of Ref. [1,2] are an appropriate and simple tool applicable in many situations and over a wide energy range, from low (MeV) to intermediate (tens or hundreds of MeV) to high-energy (GeV) accelerators.

For a point source off-axis, simulations were first performed to evaluate the dependence of the transmission factor on the shape of the cross-sectional area of the duct and on the energy of the protons impinging on the neutron production target. The transmission factor resulted to be independent of both quantities. Subsequent simulations were performed to estimate the attenuation provided by circular ducts of different size, representative of typical situations found at accelerators. The results clearly show that it is not possible to define a generic curve because the transmission factor is strongly dependent on the cross-sectional area of the duct. The expression proposed in Ref. [7] overestimates the contribution to the *equivalent dose* from the scattered neutrons. The universal curve of Refs. [1,2] is also not generally applicable. A “universal” expression – also expected to be applicable over a wide range of energies – has been derived to estimate the neutron transmission through a straight duct of length d and cross-sectional area A in direct view of the source, which only depends on A and on a small set of numerical coefficients.

Acknowledgements

The authors wish to thank Stefan Roesler for useful discussion on the manuscript and Marc Timmins for providing Figs. 6 and 7.

References

- [1] K. Goebel, G.R. Stevenson, J.T. Routti, H.G. Vogt, Evaluating dose rates due to neutron leakage through the access tunnels of the SPS, CERN Lab II-RA/Note/75-10, 1975.
- [2] R.H. Thomas, G.R. Stevenson, Radiological safety aspects of the operation of proton accelerators, IAEA Technical Report Series No. 283, IAEA, Vienna, 1988.
- [3] M.O. Cohen, W. Guber, E.S. Troubetzkoy, H. Lichtenstein, H.A. Steinberg, SAMCE: a three-dimensional MonteCarlo code for solution of the forward neutron and forward and adjoint gamma-ray transport equations, DNA-2830-F, Rev. B, National Technical Information Service, Springfield, Virginia, 1973.

[4] R.E. Maerker, V.R. Cain, AMC: a Monte Carlo code utilizing the Albedo approach for calculating neutron and capture gamma-ray distributions in rectangular concrete ducts, ORNL-3964, Oak Ridge National Laboratory, Oak Ridge, Tennessee, 1967.

[5] M.M. D'Hombres, C. Devillers, F. Gervaise, B. De Sereville, P. Tardy-Joubert, Propagation des Neutrons dans les Tunnels d'Accès à un Accélérateur de Hume Energie à Protons, R-3491, Centre d'Etudes Nucléaires de Saclay, Saclay, France, 1968.

[6] G.R. Stevenson, A. Fassò, A comparison of a Morse calculation of attenuation in a concrete-lined duct with experimental data from the CERN SPS, CERN Divisional Report TIS-RP/185/CF, 1987.

[7] K. Tesch, Part. Accel. 12 (1982) 169.

[8] National Council on Radiation Protection and Measurements, Radiation protection for particle accelerator facilities, NCRP Report No. 144, 2003.

[9] National Council on Radiation Protection and Measurements, Radiation protection design guidelines for 0.1–100 MeV particle accelerator facilities, NCRP Report 51, Bethesda, MD, NCRP, 1977.

[10] R.E. Maerker, F.J. Muckenthaler, Nucl. Sci. Eng. 27 (1967) 423.

[11] R.E. Maerker, F.J. Muckenthaler, Nucl. Sci. Eng. 30 (1967) 340.

[12] P.J. Gollon, M. Awschalom, IEEE Trans. Nucl. Sci. NS-18 (1971) 741.

[13] R.E. Maerker, F.J. Muckenthaler, Nucl. Sci. Eng. 22 (1965) 455.

[14] J.D. Cossairt, J.G. Couch, A.L. Elwyn, W.S. Freeman, Health Phys. 49 (1985) 907.

[15] J.D. Cossairt, Radiation physics for personnel and environmental protection, Rev. 9B, Fermi National Accelerator Laboratory Report TM-1834, Batavia, IL, 2007.

[16] Su. Tanaka, H. Nakashima, Y. Sakamoto, Y. Nakane, S. Meigo, Sh. Tanaka, T. Nakamura, M. Takada, T. Kurosawa, H. Hirayama, N. Nakao, Y. Uwamino, M. Imamura, K. Shin, Health Phys. 81 (2001) 406.

[17] T. Nakamura, Y. Uwamino, Radioisotopes 35 (1986) 51 (in Japanese).

[18] Y. Uwamino, T. Nakamura, T. Okubo, A. Hara, Med. Phys. 13 (1986) 374.

[19] A. Fassò, A. Ferrari, J. Ranft, P.R. Sala, FLUKA: a multi-particle transport code, CERN-2005-10, INFN/TC_05/11, SLAC-R-773, 2005.

[20] G. Battistoni, S. Muraro, P.R. Sala, F. Cerutti, A. Ferrari, S. Roesler, A. Fassò, J. Ranft, The FLUKA code: description and benchmarking, in: M. Albrow, R. Raja (Eds.), Proceedings of the Hadronic Shower Simulation Workshop 2006, Fermilab, 6–8 September 2006, AIP Conference Proceeding 896, 2007, pp. 31–49.

[21] Y. Nakane, Y. Sakamoto, K. Hayashi, T. Nakamura, Intercomparison of neutron transmission benchmark analyses for iron and concrete shields in low, intermediate and high energy proton accelerator facilities, in: Proceedings of the 3rd "Specialists" Meeting on Shielding Aspects of Accelerators, Targets and Irradiation Facilities (SATIF-3), Tohoku University, Sendai, Japan, May 12–13 1997, published by OECD/NEA, OECD documents, 1998, pp. 151–182, ISBN:92-64-16071-X.

[22] E. Mauro, M. Silari, ~~Radiation protection studies for a high-power 160 MeV proton linac~~, Nucl. Instr. and Meth. A, *in press*.

[23] J.C. Gaborit, M. Silari, L. Ulrici, Nucl. Instr. and Meth. A 565 (2006) 333.

23 25 27 29 31 33 35 37 39 41

Curriculum Vitae

EGIDIO MAURO

PERSONAL DETAILS

Via Istria 65 egidio.mauro@yahoo.it
74100 Taranto
Italy Tel +393497219600
Italian Date of birth:12-10-1979

EDUCATION

April 2007 – Today EPFL - Ecole Polytechnique Federale de Lausanne, Lausanne, Switzerland
PhD in High Energy Physics

Main Subjects: Particle Physics, Radiation protection, Medical physics, Accelerator Physics

Dissertation: "Radiation protection studies for CERN Linac4/SPL accelerator complex"

March 2005 – May 2006 I.U.S.S (University Institute for Advanced Studies) ,Pavia, Italy
Master in Tecnologie Nucleari e Radiazioni Ionizzanti

Main subjects: Industrial Applications of the Ionising Radiations, Radioisotopes Techniques, Environmental Radiochemistry, Radioprotection, Decommissioning of Nuclear Facilities

September 1998 – July 2004 University of Bari
Laurea in Fisica

Final mark : 110/110 with distinction

Main subjects: Particle Physics, Theoretical Physics, Nuclear Physics, Nuclear and Subnuclear Physics Laboratory.

Dissertation: "Dalitz plot analysis of the decay $D^+ \rightarrow K^-\pi^+\pi^+$ $e^- D^+ \rightarrow K^+K^-\pi^+$ in the BaBar experiment in SLAC" a study of CP-violation in these decays using Dalitz plot analysis and a research about the κ scalar meson existence

September 1993- July 1998 Liceo Scientifico Battaglini, Taranto
Diploma di maturità scientifica
Final mark: 60/60

Main subjects: Physics, English, Italian, Maths, Chemistry

WORK EXPERIENCE

June 2009 – Today NUCLECO, Rome, Italy

- Radiological characterization of radioactive wastes coming from nuclear power plants, industrial facilities, research centres and hospitals.

September 2006 – May 2009 CERN (European Organization for Nuclear Research)

- 3 years Marie Curie fellow in the project RADENV with the aim to study the radiological impact of the future accelerators of CERN on the personnel and on the environment with the combination of calculation via Monte Carlo codes simulation (FLUKA) and benchmark experiments. The work includes the shielding design, the estimate of the propagation of neutrons through the ventilation, cable and waveguide ducts placed along the accelerator and the calculation of the induced radioactivity in the air and in the components of the accelerator.
- Participation in an experimental activity concerning the study of the response of neutron radiation detectors, namely rem counters and Bonner Sphere spectrometers, in a reference high-energy stray radiation field in one of the Cern experimental areas

October 2005 – April 2006 LENA (Laboratorio di Energia Nucleare Applicata), Università di Pavia

- Radiological characterization of solid wastes coming from the nuclear reactor facility with the aim of evaluating the possible correlation between long-lives pure beta emitters radio-nuclides (i.e. ^{55}Fe , ^{59}Ni , ^{63}Ni) and nuclides directly measurable by gamma-ray spectrometry (i.e. ^{60}Co);
- Neutron flux calculation and activation evaluation in solid material by means of Monte Carlo Code simulations (MCNP4b);
- Low background gamma-ray spectrometry measurements;
- Analysis of different materials (traces and ultra-traces determination) by means of Instrumental Neutron Activation Analysis (INAA)
- Contribution in writing some procedures of the Health Physics Area of LENA for the radiometric controls of solid materials and waste.

JOURNALS AND CONFERENCE PROCEEDINGS

- E. Mauro and M. Silari, *Radiation protection studies for the front-end of the 3.5 GeV SPL at CERN*, Proceedings of the Eighth International Topical Meeting on Nuclear Applications and Utilization of Accelerator Conference (AccApp07), Pocatello (Idaho), 30 July – 2 August, 2007, American Nuclear Society (2007), pp. 37 – 44.
- E. Mauro, M. Silari and H. Vincke, *Radiation protection studies for the new CERN injector complex* Proceedings of the 11th International Conference on Radiation Shielding (ICRS11), Pine Mountain (Georgia), April 13 – 18, 2008, accepted for publication by Nuclear Technology, Vol. 168, Oct. 2009.
- E. Mauro and M. Silari, *Radiation protection studies for a high-power 160 MeV proton linac*, Nuclear Instruments and Methods A, in press.

RELEVANT SKILLS

IT Skills

Operating system: Windows and Linux
Word processing: Microsoft Word and LaTex
Monte Carlo codes: FLUKA and MCNP
Programming language: Fortran 77 and C++
Office Package: Powerpoint, Excel, Access, Outlook
HTML

Languages

Mother tongue: Italian

English: advanced (written and oral)

French: intermediate (written and oral)

Interests

Tourism, Music, Sports, Reading